Characterization of Photonuclear Collisions and the Search for Quark-Gluon Plasma

by

Sruthy Jyothi Das

B.S.M.S, Indian Institute of Science Education and Research Pune, 2019

A thesis submitted to the

Faculty of the Graduate School of the

University of Colorado in partial fulfillment

of the requirements for the degree of

Doctor of Philosophy

Department of Physics

2024

Committee Members:

Jamie Nagle, Chair

Dennis Perepelitsa

Paul Romatschke

Alysia Marino

Ben Brown

Das, Sruthy Jyothi (Ph.D., Physics)

Characterization of Photonuclear Collisions and the Search for Quark-Gluon Plasma

Thesis directed by Prof. Jamie Nagle

Ultra-relativistic heavy-ion collisions create tiny droplets of Quark-Gluon Plasma (QGP), a hot, dense state of matter where quarks and gluon are in a deconfined state. Experiments at the CERN Large Hadron Collider have observed the presence of this strongly interacting matter in Pb+Pb collisions and, interestingly, in small collision systems like p + Pb and pp. This raised many important questions in the field, particularly: What is the smallest system that is necessary to create a tiny droplet of QGP? Photonuclear collisions, a subset of Ultra Peripheral Collisions (UPCs), are one such exotic small system and occur when the electromagnetic field of one nucleus acts as a photon and breaks apart the other nucleus. The ATLAS Collaboration has recently observed flow-like features, a QGP signature suggesting the collective expansion of the fluid in photonuclear collisions. Thus, it is imperative to check these events for other potential QGP signatures, including radial flow, strangeness enhancement, and enhanced production of baryons relative to mesons. Furthermore, modeling photonuclear collisions is particularly challenging due to their extremely asymmetric nature and the fluctuating photon energies between events.

This dissertation presents two new measurements of photonuclear collisions using 5.02 TeV Pb+Pb data collected in 2018 by ATLAS, with a dedicated photo-nuclear event trigger. The first measurement reports unidentified-charged-hadron yields, and the second measurement provides the identified-hadron yields, such as K^0_S, Λ, and Ξ^-, in Pb+Pb UPCs. The yields are shown as a function of pseudorapidity and transverse momentum in different categories of event multiplicity. The results are compared with 5.02 TeV p+Pb data collected in 2016 by ATLAS at the same event multiplicities. Additionally, they are compared with calculations by the DPMJET Monte Carlo model and hydrodynamic-based models. These comparisons enable detailed characterizations of photonuclear collision properties and evaluate the potential formation of small QGP droplets.

Dedication

I dedicate this thesis to my parents, Jyothi Arjunan and Muralidas Sundaram. Thank you for constantly supporting me on this journey to become the first "Dr." in the entire family.

Acknowledgements

This thesis is a testament to the significant progress I have achieved in my journey as a budding scientist, showcasing my learning, hardships, and resilience along the way.

Firstly, I would like to thank my two advisors, Prof. Jamie Nagle and Prof. Dennis Perepelitsa. I am deeply grateful to my advisor, Jamie, for his detailed systematic methods to approach even the most challenging physics problems and his notable way of explaining complex ideas simply. I am grateful to Dennis for his boundless curiosity and the excitement he brings to the learning process. I can proudly say that both of them have imparted these qualities to the scientist in me.

Secondly, to my dearest colleagues, thank you for the numerous coffee walks, lunch quests, and countless physics discussions: Postdocs - JaeBeom Park, Yeonju Go, Chris McGinn, Ran Bi, Qipeng Hu; Graduate students - Sam Liechty, Joey Clement, Daniel Lis, Berenice Garcia, Jeff Ouellette, Blair Seidlitz, Kurt Hill; and all my Undergrad colleagues. I am particularly grateful to Blair Seidlitz, for guiding me to think critically, and always being available for discussions. My special thanks to Berenice Garcia, for the cherished memories and your immense support. I am grateful to my mentors in ATLAS, for providing continuous guidance on analyses: Peter Steinberg, Martin Rybar, Aaron Angerami, Thorsten Kuhl, Fernando Barreiro, and Mariusz Przbycien.

Finally, I would like to thank my dearest friends and family. To Harikrishna, thank you for always being my rock and unwavering support. Sankalp and Sanaa, your friendship has brought countless memories and enriching discussions. Swathy, you have been an incredible sister, offering me strength and encouragement when needed. And to my parents, Jyothi and Muralidas, thank you for believing in me. I wouldn't be here today without your support.

Contents

Chapter

Tables

Table

Figures

Figure

Chapter 1

Introduction

For a few microseconds following the Big Bang, the temperature and energy density of the universe were so extreme that the fundamental particles that make up nuclear matter, such as quarks and gluons, could not remain bound together in hadrons. The universe existed in a state of "quark-gluon plasma" (QGP), essentially a soup of unbound quarks and gluons [1]. To replicate these earliest moments of the universe, scientists have collided heavy nuclei at energy scales of TeV, giving birth to the field of heavy-ion physics.

The nuclear collision experiments conducted at CERN in Europe and Brookhaven National Laboratory (BNL) in the United States are primarily aimed at studying nuclear matter under extreme conditions, with the potential to create droplets of QGP. Early results from the Relativistic Heavy Ion Collider (RHIC) at BNL and the Large Hadron Collider (LHC) at CERN have uncovered that the matter produced in head-on, ultra-relativistic collisions of heavy elements, such as gold (Au) or lead (Pb), as illustrated in Figure 1.1, exhibit characteristics of a nearly perfect fluid [2]. This fluidity is characterized by the remarkably low shear viscosity to entropy density ratio η/s of the QGP; the lowest value of any matter observed so far in nature [3]. These results motivated employing relativistic hydrodynamics to theoretically describe the expansion of QGP from the initial-state energy deposition in the collision to final-state particle formation.

Within the framework of relativistic, viscous hydrodynamics, one of the properties indicating the existence of QGP is the presence of large azimuthal anisotropic distributions of particle momenta, characterized by anisotropic flow coefficients, v_2 [4]. This effect manifests in particles'

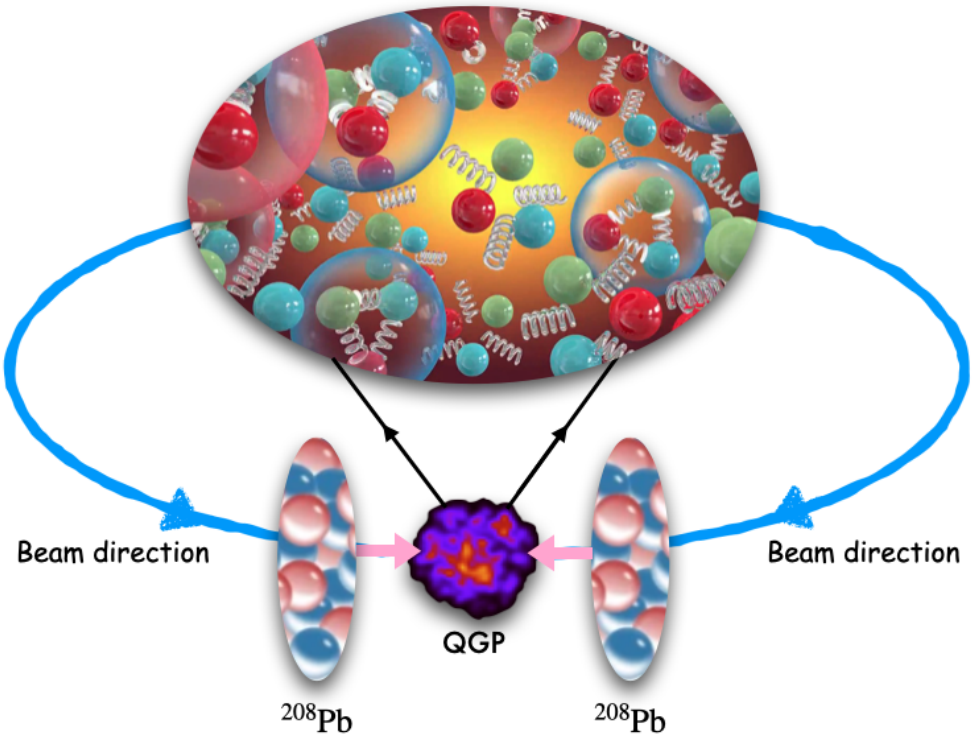

Figure 1.1: A schematic illustration of a Pb+Pb collision at the LHC, producing a hot-dense matter called quark–gluon plasma (QGP), reaching temperatures of a few trillion Kelvin. The colored spheres and springs inside the oval box are representations of quarks and gluons forming the QGP.

uneven distribution along the azimuthal space in the transverse plane relative to the impact parameter direction. It arises from the larger pressure gradient formed along the x-axis compared to the y-axis (for example), resulting from the almond-shaped geometry of the overlapping region in a collision, as shown in Figure 1.2. This observation of collective flow in experiments helped to characterize the quark-gluon plasma as a fluid, exhibiting behavior consistent with predictions of a strongly coupled medium.

The first observable proposed to detect the presence of QGP was strangeness enhancement during nuclear collisions [5]. Particles that contain at least one strange quark, in other words, those that carry the quantum number of strangeness, are called strange particles. The commonly found strange particles are K^0_S, Λ, and Ξ. The matter surrounding us is mostly created from up and down quarks. Any observed strange quarks or antiquarks in experiments must be newly created from

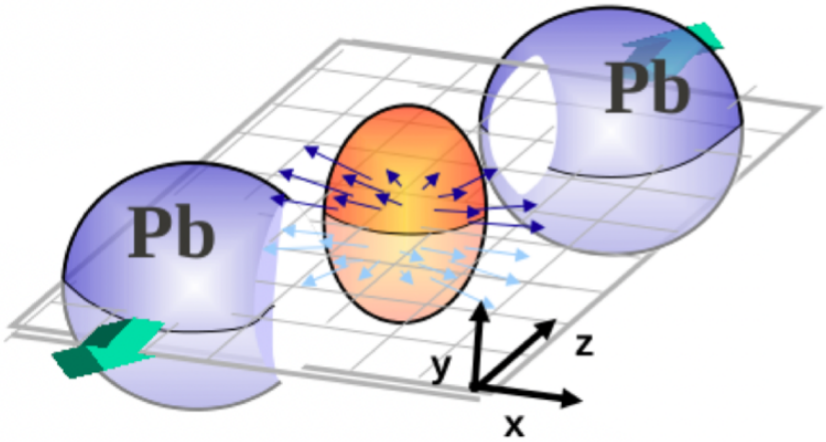

Figure 1.2: Almond-shaped geometry of the overlapping region in a heavy-ion collision results in an uneven distribution of particles in the azimuthal space.

the kinetic energy of colliding nuclei, with gluons acting as catalysts. The abundance of strange quarks in the medium from the thermal production mechanism is a signature of the existence of the deconfined phase of matter. It is crucial to note that particle production through perturbative Quantum Chromodynamics (pQCD) always occurs. Additionally, an increase in the production of baryons relative to mesons at intermediate transverse momenta, observed in QGP environments like heavy-ion collisions, remains poorly understood [6].

Smaller collision systems, such as proton-proton (pp) collisions, are used as a reference to heavy-ion collisions to distinguish the properties that emerge from the interaction of particles in heavy-nuclei collisions. More recently, the collective flow-like behavior has been observed in smaller systems [7]. These observations were quite surprising to the field, as it was previously thought that a smaller collision system would not have enough energy density or number of particles to produce a medium that can behave like a fluid. This has prompted questions about the minimum size of the system necessary to create a QGP droplet. Therefore, studying the properties of smaller collision systems is essential for investigating the properties of QGP.

One such fascinating smallest system produced at LHC is photon-lead collisions, as shown in Figure 1.3. When ultra-relativistic beams of lead nuclei collide, the electric field of one lead nucleus acts as a flux of photons capable of breaking apart the other nucleus. The unaffected nucleus

continues its path, with no hadronic interaction between the nuclei. These collisions, known as ultraperipheral collisions (UPC) [8, 9], or more specifically, photonuclear collisions (γ+Pb), occur when the impact parameters between the incoming nuclei are sufficiently large.

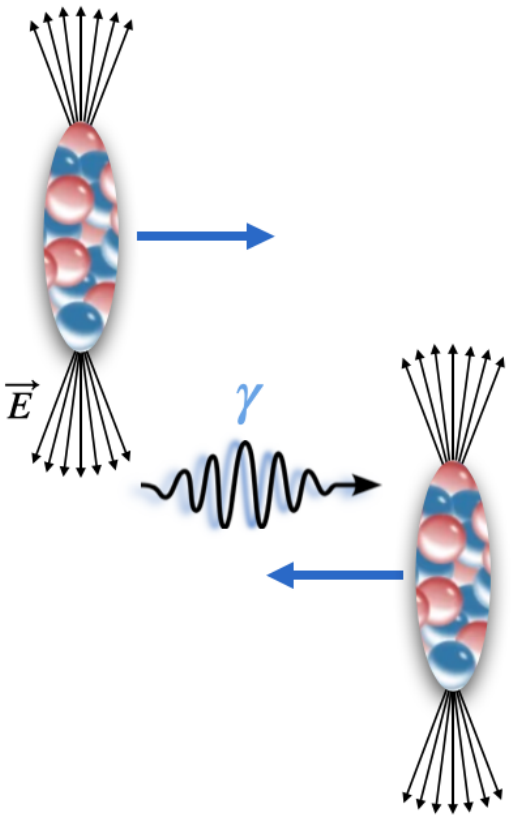

Figure 1.3: A schematic illustration of ultraperipheral collision, where the electric field of one colliding nucleus acts as a flux of photons, breaking apart the other nucleus.

Previously, UPC physics was explored through Deep Inelastic Scattering (DIS) measurements using the Hadron-Electron Ring Accelerator (HERA), the only electron-proton collider to date. However, with recent technological advancements, higher-energy machines like RHIC and LHC have begun studying particle production in powerful force fields, known by the physics of ultra-peripheral collisions. Photonuclear collisions at LHC have the capacity to achieve ten times the energies available at HERA and 30 times higher than those available at fixed-target experiments at accelerators like CERN SPS. The current and upcoming results from RHIC and LHC indicate that UPC has the potential to make substantial contributions to different areas of nuclear physics,

including the search for new physics processes that are not accessible in hadronic collisions. In addition, these contributions will benefit the future era of the Electron-Ion Collider (EIC), which has physics similar to UPC. EIC resembles HERA as a true electron-hadron DIS collider but parallels the LHC UPC program by utilizing nuclei as the target.

The ATLAS experiment at LHC particularly excels at UPC measurements, given its sophisticated trigger system designed to collect UPC events with significantly reduced contamination from hadronic collision events. They have measured flow coefficients in photonuclear collisions, providing the first evidence for the existence of QGP in such collisions [10]. This serves as a clear motivation to search photonuclear collisions for more QGP-like signals such as radial hydrodynamic flow [2], strangeness enhancement [11], baryon/meson enhancement [12], or other signals of collectivity that have been observed in heavy-ion collisions.

However, analyzing photonuclear collisions poses more complex challenges, such as constraining the energy distribution of the photons involved in these collisions. In the simplest case, a photon can act as a point-like particle interacting with a parton in the lead nucleus. In a more complex scenario, a photon may fluctuate into a vector meson, such as a ρ meson, which then interacts with the lead nucleus. These events will have an overall rapidity boost in the center-of-mass frame in the direction of the nucleus, depending on the ρ meson energy. To perform detailed characterizations of photonuclear collisions and determine whether tiny QGP droplets may form, data is compared with calculations based on the dual-parton model and hydrodynamics. Differences between data and theory calculations in basic kinematic observables of charged hadrons, such as the pseudorapidity η and transverse momentum p_{T}, if present, can better constrain the photon energy distribution in such collisions.

This thesis reports on two new ultra-peripheral collisions (UPC) measurements in 2018 Pb+Pb 5.02 TeV data, utilizing the ATLAS detector, with a dedicated photonuclear event trigger, at the Large Hadron Collider. The first measurement presents the unidentified-charged-hadron yields over the pseudorapidity range of $-2.5 < \eta < +2.5$ and as a function of p_{T} to characterize photonuclear collisions to constrain Monte-Carlo photonuclear models. Furthermore, we start

to address the inquiry of QGP formation in these photonuclear events by measuring the $\langle p_{\mathrm{T}} \rangle$ of charged hadrons, indicating the presence of radial flow in the system. The results are also compared to low-multiplicity 2016 p+Pb collisions at 5.02 TeV, with the multiplicity matched that of the photonuclear events.

The second measurement reports the identified-hadron yields, such as $\mathrm{K}^0_{\mathrm{S}}$, Λ, and Ξ^-, as a function of η and p_{T}, aiming to investigate the possible formation of tiny quark-gluon plasma droplets that flow hydrodynamically in these photonuclear events. The ratios of the yield of these strange particles to inclusive charged hadrons, and Λ to $\mathrm{K}^0_{\mathrm{S}}$, are compared between γ+Pb and p+Pb collisions to investigate strangeness enhancement and enhanced baryon-to-meson production, respectively.

Chapter 2 provides an overview of the physics of the QCD theory and its exploration in ultra-relativistic heavy-ion collisions, as well as the detailed QGP signatures observed in heavy-ion collisions and small systems. Chapter 3 explores the physics of photonuclear collisions. Chapter 4 offers an overview of the Large Hadron Collider and the ATLAS experiment. Chapters 5 and 6 report the measurements of unidentified-charged-hadron yields and identified-hadron yields. Chapter 7 focuses on the physics discussions of the results. Finally, Chapter 8 presents the conclusions.

Chapter 2

Ultra-Relativistic Heavy-Ion Collisions

Ultra-relativistic heavy-ion collisions are an important tool in high-energy nuclear physics and provide a unique opportunity to study the properties of matter under extreme conditions. This chapter aims to provide a broad introduction to the field of heavy-ion collisions, from the Standard Model of particle physics to the evolution of nuclear collisions.

2.1 The Standard Model

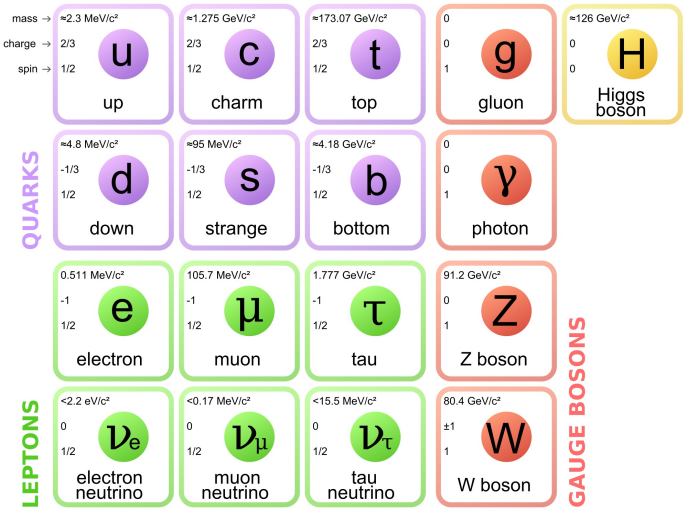

Figure 2.1: The Standard Model of particle physics describes the fundamental particles and the force-carrying particles. Reproduced from Ref. [13].

The Standard Model (SM) of particle physics is our current best theory to describe the most basic building blocks of the universe and the four fundamental forces that govern it. In 1897,

physicist J.J. Thomson discovered the electron, the first identified particle of the Standard Model. In 2012, researchers at the Large Hadron Collider made a significant discovery by confirming the existence of the Higgs boson, a crucial piece of the Standard Model of particle physics. However, several outstanding questions in particle physics, such as the nature of dark matter and the existence of supersymmetry, continue to motivate ongoing research efforts.

The basic building blocks of all physical matter are quarks and leptons, as shown in the first three columns of Figure 2.1. Combined, they are called fermions, spin 1/2 particles. The fermions interact via the force-carrying particles or exchange particles called bosons, spin 1 particles shown in the fourth column.

The Standard Model explains three fundamental interactions that govern the universe: electromagnetism and the strong and weak forces. The biggest missing piece in the standard model is the fourth fundamental force, gravity, about a factor of 10^{30} weaker than the rest. The weak force is responsible for nuclear reactions present in the Sun and other stars for billions of years, and the force carriers are W and Z bosons. Electromagnetism involves the interaction with electric and magnetic fields, and the force carrier is the photon. The strong force, stronger than the electromagnetic force by a factor of 100, is carried by gluons and keeps the atomic nuclei stable.

2.2 Quantum Chromodynamics

Quantum Chromodynamics (QCD) is the theory of the strong force, which explains the interaction of subatomic particles like quarks and gluons and how they hold together to form stable nucleons. Exciting physics phenomena emerge at short-length scales and/or high energy scales due to the complexity of the interactions. Two such important behaviors of sub-atomic particles, explained by QCD, are confinement and asymptotic freedom, which can be explained by QCD. Color-charged quarks and gluons are confined to form color-neutral hadrons. When quarks approach each other at a very small distance, they become asymptotically free and have no interaction with each other. The state of matter in which quarks and gluons are in a deconfined state is called quark-gluon plasma. This occurs when the matter's temperature is very high, and

Flavor	Electric charge	Mass	Isospin	Strangeness
u	+2/3	$\sim$ 2.16 MeV	+1/2	0
d	-1/3	$\sim$ 4.67 MeV	-1/2	0
c	+2/3	$\sim$ 1.27 MeV	0	0
s	-1/3	$\sim$ 93.4 MeV	0	-1
t	+2/3	$\sim$ 172.69 GeV	0	0
b	-1/3	$\sim$ 4.18 GeV	0	0

Table 2.1: The six flavors of quarks and their properties. Reproduced from Ref. [14].

the baryon number density is finite.

The simplest of the quantum field theories is called Quantum Electrodynamics (QED) which describes how electrically charged particles interact with each other via the exchange of photons. In QCD, particles that carry color charges, quarks and gluons, interact with each other via the exchange of gluons, which also carry a color charge. Quarks exist in six flavors: up, down, strange, charm, top, and bottom. These "flavor" degrees of freedom allow quarks to combine with each other in different combinations, resulting in the existence of a variety of composite hadrons. The properties of different flavors of quarks are shown in Table 2.1.

This section will discuss the QCD Lagrangian and its main two properties, namely, color confinement and asymptotic freedom.

2.2.1 QCD Lagrangian

QCD is a type of quantum field theory called a non-abelian gauge theory, with symmetry group SU(3). Quarks are the fermions fields ψ_{q} that carry colour quantum numbers:

$$\psi_q = \begin{bmatrix} \psi_r \\ \psi_b \\ \psi_g \end{bmatrix}, \tag{2.1}$$

where the three elements of the vector, ψ_{r}, ψ_{b} and ψ_{g} corresponds to the three different colors - red, blue and green. Each of these elements is a four-component Dirac spinor. ψ transform as $\psi \to U\psi$ where U is any unitary 3×3 matrix: $U^T U = 1$. Any unitary matrix can be written as

an exponential Hermitian matrix, $U = e^{i\omega^a T^a}$, where the T^a are the generators of the SU(3) Lie group. The label a runs over $3^2 - 1 = 8$ values, giving rise to eight gluonic gauge fields, A^a.

The dynamics of the quarks and gluons can be described by the quantum chromodynamics Lagrangian, given by:

$$L_{QCD} = \sum_q \bar{\psi}_q (i\gamma^\mu D_\mu - m_q)\psi_q - \frac{1}{4}.F^a_{\mu\nu}F^{\mu\nu}_a \tag{2.2}$$

Here, the summation over q is carried out for up (u), down (d), strange (s), charm (c), bottom (b), and top (t) quarks. The first term, $\bar{\psi}_q(i\gamma^\mu D_\mu)\psi_q$, represents the gauge covariant quark kinetic term, accounting for the kinetic energy of the quark as well as its interaction with the gauge field. In this term, D_μ is the gauge covariant derivative, given as $D_\mu = \partial_\mu - igA_\mu$, where g_s is the strong coupling constant. The second term, $-m_q\bar{\psi}_q\psi_q$, represents the quark mass term, where m is the mass of quarks of each flavor. The last term, $-\frac{1}{4}F^a_{\mu\nu}F^{\mu\nu}a$, is the gauge field kinetic term. It accounts for the kinetic energy density of the gluon field. The field strength tensor from gluon fields A^a, $F^a_{\mu\nu}$, is defined as:

$$F^a_{\mu\nu} = \partial_\mu A^a_\nu - \partial_\nu A^a_\mu - g_s f_{abc} A^b_\mu A^c_\nu. \tag{2.3}$$

Here, f_{abc} are the structure constants of the QCD gauge group SU(3).

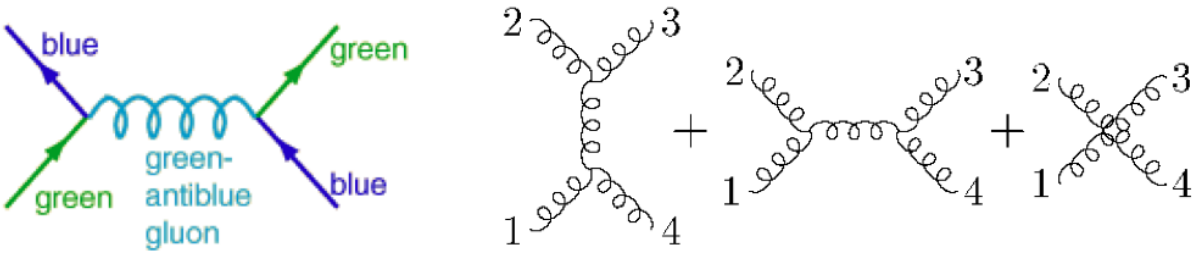

Figure 2.2: Left: Feynman diagram of a gluon exchange between two quarks, with their color charge. Right: Feynman diagrams showing self-interactions of gluons. Reproduced from Ref. [15].

Quarks and gluons are collectively referred to as partons. The quark-gluon interaction term shows that when a quark emits a gluon, it changes its color, as shown in the left side of Figure 2.2. There are also cases where a quark emits color-neutral gluons. The interactions of gluons with themselves, termed self-interactions of gluons, are shown on the right side of Figure 2.2.

2.2.2 Color Confinement

Quarks always exist in groups and cannot be isolated and observed experimentally as individual quarks. This property of individual particles is called quark confinement. This is an important feature of QCD in the low-energy regime. To understand it quantitatively, non-perturbative calculations are performed on a discrete lattice of space and time. One can visualize quark confinement as a quark and an anti-quark connected by a color flux tube, as shown in Figure 2.3. When this quark-antiquark pair is pulled apart, it becomes energetically more favorable to produce another set of a quark-antiquark pair from the color flux tube. This process will continue, hence it becomes impossible to isolate a single quark.

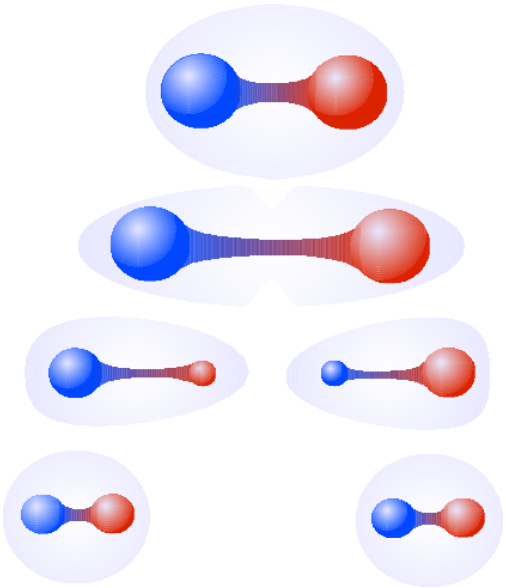

Figure 2.3: Color confinement shown by a quark and antiquark pair, represented by blue and red colors, connected by a color flux tube. Reproduced from Ref. [16].

2.2.3 Asymptotic Freedom

Asymptotic freedom is an important property arising from QCD interactions in the high-energy regime. This interaction can be expressed in terms of the QCD coupling constant, α_s, given by:

$$\alpha_s(q^2) = \frac{\alpha_0}{1 + \alpha_0 \frac{(33-2n_f)}{12\pi} \ln(\frac{-q^2}{\mu^2})}. \tag{2.4}$$

Here q is the momentum transfer, α_0 is the coupling constant for the momentum transfer μ, and n_f is the number of flavors. When quarks interact with each other at a short distance scale, the QCD coupling constant becomes small, resulting in a weak interaction between quarks. This phenomenon is known as asymptotic freedom. Perturbative calculations are applicable in small distance scales or, in other words, large energy scales. Figure 2.4 shows the range of QCD coupling constant, α_s, in different experimental measurements.

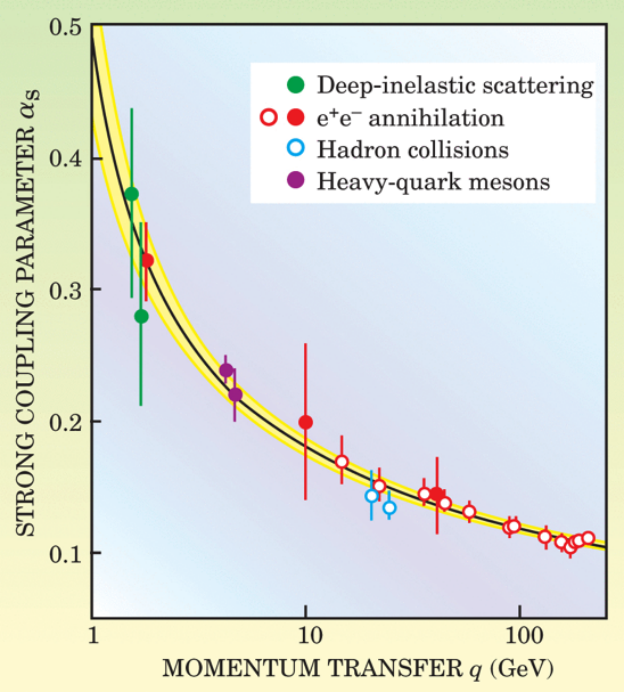

Figure 2.4: QCD coupling constant, α_s, as a function of momentum transfer, q, in different physics processes. Reproduced from Ref. [17].

2.3 Quark-Gluon Plasma

The previous section outlines the QCD theory and its properties. Extensive research to study the current quarks remains an active area of research, continuing to the present day. However, the most interesting development has been in comprehending the emergent properties of QCD matter under extreme conditions. Figure 2.5 shows the QCD phase diagram, where the temperature of the matter is shown as a function of the baryon chemical potential (μ_B), which is equivalent to the net baryon density. The region of the diagram characterized by very small baryon chemical potential and higher temperature is the focus of experimental facilities at LHC and RHIC. These experiments have achieved significant progress in understanding the emergent properties of the strongly interacting matter known as Quark-Gluon Plasma (QGP). This state is also recognized as the one that existed at the beginning of the universe in the first microseconds.

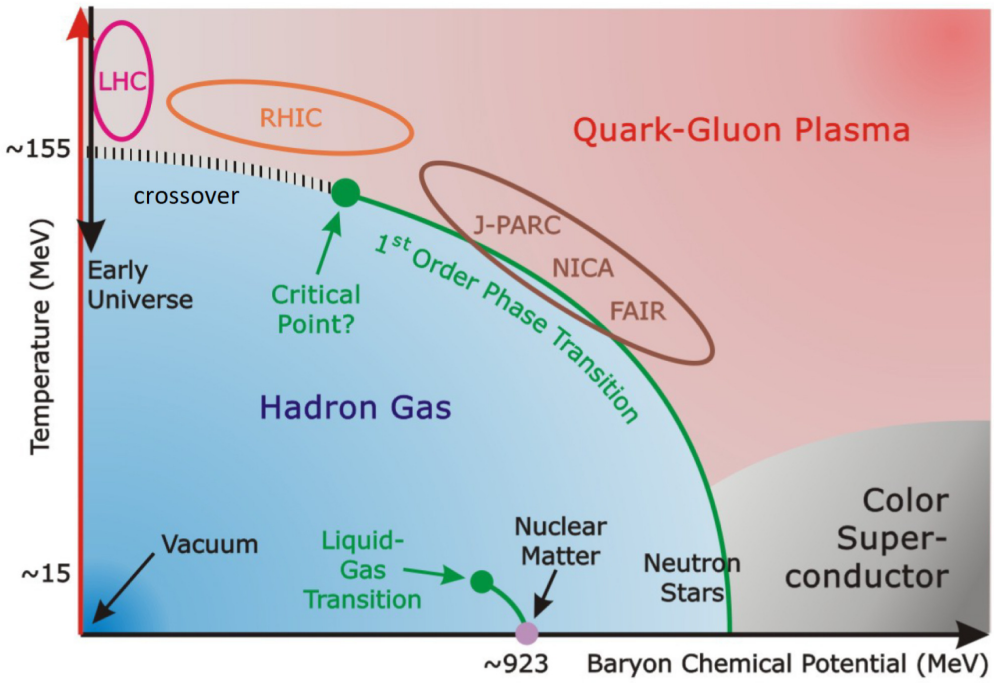

Figure 2.5: QCD phase diagram with boundaries that define various states of QCD matter. Experiments at LHC and RHIC attempt to recreate the early moments of the universe, defined by high temperature and low baryon chemical potential. Reproduced from Ref. [18].

At lower temperatures and small baryon densities, the quarks are confined inside the hadrons, forming a hadron gas. Nuclear matter, which constitutes our everyday matter, is located at 0 temperature and a μ_{B} of $\sim$ 923 MeV in the phase diagram. At finite baryon densities, QGP undergoes a broad cross-over to a hadron gas. At larger energy densities and lower temperatures, the state of matter is characterized by a superconducting phase.

The investigation into the phase diagram of QCD in the $T - \mu_{\mathrm{B}}$ plane, determining whether the transition from a hadron gas to QGP matter is a broad crossover (characterized by a smooth transition) or a real phase transition (marked by an abrupt change), is one of the most important aspects of the field. Recent advancements from first-principle lattice QCD calculations suggest that the transition at $\mu_B = 0$ is a smooth crossover [19, 20]. This section gives a brief overview of the thermodynamics of QGP matter, and the different models employed in describing the cross-over between a hadron gas to a deconfined QGP state.

2.3.1 Historical Overview

Beginning with a brief historical overview, a zoo of hadrons emerged in accelerator experiments in the late 1960s. During this period, there was a substantial effort to explain hadron production using statistical mechanics. In 1968, Rolf Hagedorn proposed that particle production in hadronic collisions follows statistical mechanics. In other words, under equilibrium, a state (hadron) with mass m_i is populated according to:

$$N_i \sim \exp\left(-\frac{m_i}{T}\right), \tag{2.5}$$

where the parameter T has the meaning of a temperature in thermal equilibrium.

The total number of hadrons can be calculated from the density of states $\rho(m)$, which represents the number of states i in a mass interval $m + dm$. The total number of hadrons is given by:

$$N(T) \sim \int_0^\infty \rho(m) \exp\left(-\frac{m}{T}\right) dm. \tag{2.6}$$

Through a quantitative analysis, Hagedorn concluded that the density of states increases exponentially with mass, along with a parameter $T_0 = 160$ MeV:

$$\rho(m) = \exp\left(+\frac{m}{T_0}\right). \tag{2.7}$$

However, this exponential dependence with mass indicated that if the temperature of the system is greater than $T_0 = 160$ MeV, the number of hadrons, given by Eq 2.6, would not be numerically possible to calculate, *i.e.*, the integral diverges. Hagedorn interpreted T_0 as the limiting temperature of the system. Beyond this limit, the additional energy doesn't increase the temperature further; instead, it leads to the production of heavier hadronic resonances with exponentially increasing density of states. The interpretation of $T_0 = 160$ MeV as the limiting temperature of a physical system was widely accepted during the era of confined quarks that cannot be separated.

A decade later, a paradigm shift occurred in QCD, with the discovery of asymptotic freedom in the theory of strong interaction by David Gross, Frank Wilczek, and David Politzer, who were also awarded the Nobel Prize for the same discovery. They formulated that quarks are confined within hadrons because the QCD coupling constant, α_s (detailed in Section 2.2.3), becomes large at a large distance. Conversely, at smaller distances, α_s becomes exceedingly small and quarks exhibit asymptotic freedom. This phenomenon is observed in deep-inelastic scattering, where quarks inside nucleons behave like free particles.

This shift challenged the notion of a limiting temperature for a physical system. Instead, it introduced the idea that when nuclear matter is heated or when density is increased, the interaction between quarks asymptotically diminishes, allowing them to move freely over large distances. In other words, a system of quasi-free quarks and gluons, known as quark-gluon plasma, is formed.

2.3.2 QGP Thermodynamics

The previously discussed notion of a limiting temperature in the context of statistical mechanics does not explain the QGP formation. This requires incorporating the dynamics of quarks and gluons within the framework of statistical mechanics. This has led to the idea that QGP

can be treated as a grand canonical ensemble, a relativistic ideal gas with fermions (quarks and antiquarks) and bosons (gluons), thus determining the thermodynamic variables using the grand-canonical partition function.

The Bose-Einstein distribution can be naturally derived from a grand canonical ensemble for a quantum system of non-interacting bosons, and the expected number of particles in an energy state i for a boson is given by:

$$N_i = \frac{g_i}{e^{(\varepsilon_i - \mu)/k_B T} - 1}, \tag{2.8}$$

where g_i is the degeneracy of energy level i, ε_i is the energy of the i^{ith} state, μ is the chemical potential, k_B is the Boltzmann constant, and T is the absolute temperature. The corresponding boson energy density is given by:

$$\varepsilon = \int N_i p d^3p = \frac{4\pi g}{(2\pi)^3} \int \frac{p^3 dp}{e^{p/T} - 1}, \tag{2.9}$$

$$\varepsilon = \frac{3g}{\pi^2} T^4 \zeta(4), \tag{2.10}$$

with the Riemann zeta function, $\zeta(4) = \frac{\pi^2}{90} \approx 1.08$, so that

$$\varepsilon = g \frac{\pi^2}{30} T^4. \tag{2.11}$$

The pressure of the ideal gas is

$$P = \frac{1}{3}\varepsilon = g \frac{\pi^2}{90} T^4. \tag{2.12}$$

Using Fermi–Dirac particle energy distribution, the expected number of particles in an energy state i for a fermion can be derived as:

$$N_i = \frac{g_i}{e^{(\varepsilon_i - \mu)/k_B T} + 1}, \tag{2.13}$$

and the corresponding pressure is

$$P = \frac{7}{8} g \frac{\pi^2}{90} T^4. \tag{2.14}$$

2.3.2.1 Bag Model of Hadrons

Phenomenological models are required to explain the QGP transition in the case of a non-perturbative approach, where the coupling constant α_s is not negligible. One such model is the

MIT bag model.

Utilizing the thermodynamic variables described in the previous section, the transition of hadron gas into a state of deconfined quark-gluon plasma can be understood. A simple description of quark confinement within the hadrons is provided by the MIT bag model [21].

In the MIT bag model, hadrons are conceptualized as bags containing confined quarks. Within the bag, quarks are treated as massless, becoming infinitely massive outside the bag. The cost of maintaining the bag is referred to as the bag pressure (B), which is the required energy per unit volume directed inward. The bag pressure is a phenomenological quantity introduced to include the non-perturbative effects of QCD. The total energy inside volume V consists of BV along with the energy associated with the kinetic motion of quarks and gluons inside the bag. The total color charge of the matter inside the bag must be colorless, in accordance with Gauss's law. The allowed bags thus include a combination of colorless qqq and $q\bar{q}$, as there are three different color degrees of freedom.

If the pressure of the quark matter inside the bag is increased, it will reach a point at which pressure directing outward, *i.e.*, the energy associated with the kinetic motion of quarks and gluons inside the bag, is greater than the pressure directing inward, *i.e.*, energy from bag pressure. From this moment onward, the bag will not be able to confine quarks inside it. This leads to the possible formation of a new phase of matter, where quarks and gluons are in a deconfined state, called Quark-Gluon Plasma. The criterion for this to happen is to achieve a pressure inside the hadron greater than the bag pressure. This can be achieved by increasing the temperature of the quark matter and/or increasing the baryon density of the quark matter. Here, I discuss the case in which Quark-Gluon Plasma is formed at high temperatures.

Let's consider a simple quark-gluon system in thermal equilibrium, where quarks and gluons are assumed to be non-interacting and massless, and there is no net baryon number. The total pressure of the system, including individual contributions from gluons, from Eq 2.12 and quarks

and antiquarks from by Eq 2.14, is given by:

$$P = g_{\text{total}} \frac{\pi^2}{90} T^4, \tag{2.15}$$

where T is the temperature of the system, and

$$g_{\text{total}} = [g_{\text{g}} + \frac{7}{8} \times (g_{\text{q}} + g_{\bar{\text{q}}})], \tag{2.16}$$

where g_{g}, g_{q} and $g_{\bar{\text{q}}}$ are the degeneracy numbers associated with gluons, quarks, and antiquarks, respectively. For gluons

$$g_{\text{g}} = 8 \times 2, \tag{2.17}$$

given there are 8 gluons, and each of them has two possible polarizations. For quarks

$$g_{\text{q}} = g_{\bar{\text{q}}} = N_{\text{c}} N_{\text{s}} N_{\text{f}}, \tag{2.18}$$

where N_{c} $(= 3)$ is the number of colors, N_{s} $(= 2)$ is the number of spins and N_{f} $(= 2^1)$ is the number of flavors. Thus, Eq 2.15 implies: the pressure of a quark-gluon system at temperature T is

$$P = 37 \frac{\pi^2}{90} T^4, \tag{2.19}$$

and the energy density of the quark-gluon system at temperature T is

$$\varepsilon = \frac{P}{3} = 37 \frac{\pi^2}{30} T^4. \tag{2.20}$$

Hence, the temperature at which the pressure inside a hadron containing confined quarks and gluons equals the bag pressure, B, is given by:

$$T_{\text{c}} = \left(\frac{90}{37\pi^2} \right)^{1/4} B^{1/4}. \tag{2.21}$$

With $B^{(1/4)}$ estimated to be 206 MeV, we obtain $T_{\text{c}} \approx 144$ MeV, and T_{c} is referred to as the critical temperature. This critical temperature marks the point at which the confined state of quarks and gluons within the hadron transitions to a deconfined phase. In other words, if the bag of hadrons is heated up to a temperature greater than $T = T_{\text{c}}$, the bag will melt, and the quark matter becomes a deconfined state of matter, known as quark-gluon plasma.

[1] Only two light flavors are considered, up and down, since the mass of the strange quarks is already ~ 100 MeV, and the other flavors are even heavier.

2.3.2.2 Lattice QCD

Our current understanding of the QGP transition in the phase diagram still remains very limited. Traditional hadronic models have been demonstrated to be insufficient to describe the transition region. At low temperatures and for finite-size systems, the coupling constant, described by Equation 2.4, is of the order 1. Thus perturbation theory falls short due to the presence of large QCD coupling. Consequently, lattice field theory was utilized, exploiting the non-perturbative nature of QCD. In this method, the field degrees of freedom are discretized on a four-dimensional space-time grid. Through the lattice approach, a detailed understanding of the QGP transition dynamics becomes feasible, rooted solely in first principles - *i.e.*, from the QCD Lagrangian [22].

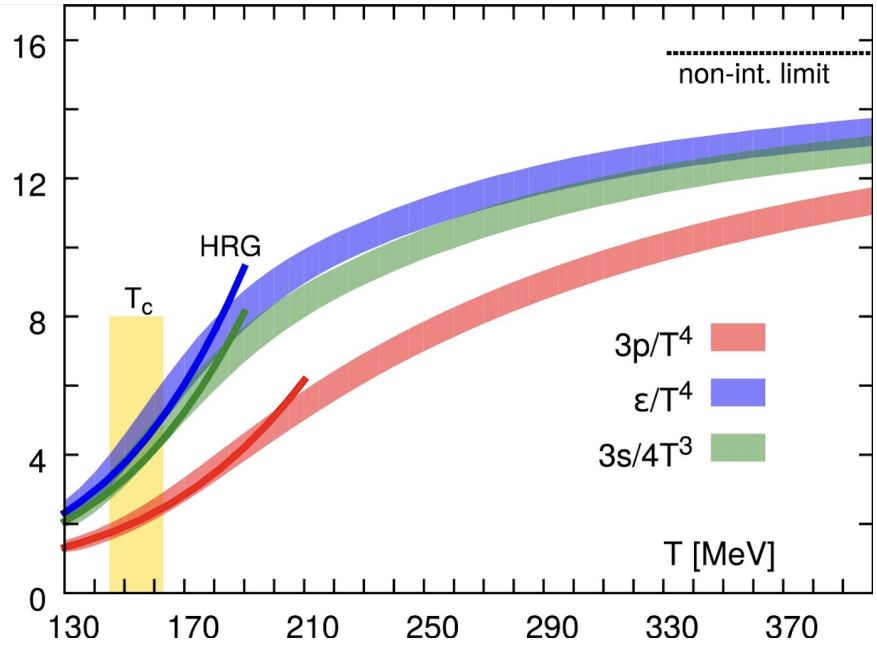

Figure 2.6: The pressure, energy, and entropy density (scaled by T^4) as functions of the temperature from lattice QCD calculation by the HotQCD Collaboration (shaded bands) as compared to hadron resonance gas (HRG) model results (solid lines). Reproduced from Ref. [23].

Figure 2.6 shows the thermodynamic variables such as pressure, energy density, and entropy density as a function of temperature from lattice calculations. The same variables are also compared with the hadron resonance gas (HRG) model at low temperatures. There is a reasonable agreement for $T < 150$ MeV. At the highest temperature $T = 400$ MeV, the thermodynamic quantities

are 15-20% below the Stefan-Boltzmann limit. The rapid rise of energy density signals the rapid increase in degrees of freedom due to the transition from hadrons to quarks and gluons, *i.e.*, deconfinement. The recently reported lattice QCD calculation suggests that $T_c = 156 \pm 1.5$ MeV, where T_c corresponds to the crossover temperature at zero chemical potential.

2.4 Heavy-Ion Collisions

An ultra-relativistic heavy-ion collision is a head-on collision of heavy ions such as Pb, Au, or Xe occurring at a velocity greater than 99% of the speed of light and at TeVs of energy levels in collider facilities like LHC and RHIC. Figure 2.7 is considered the "standard model" of heavy-ion collisions. This model includes the different stages of a typical collision: (i) Initial state, (ii) Pre-equilibrium, (iii) Hydrodynamic expansion, (iv) hadronization, and (v) hadronic transport. In this section, we will discuss the complete story of a heavy-ion collision, which has been developed utilizing the wealth of information from experimental data, and theoretical advances in the field. The story begins from the initial moment of collision at time $\tau = 0$ fm/c, progresses through the formation of a hot-dense state of matter known as QGP, leads to the expansion of the matter forming hadrons which eventually reach the detector at $\tau \leq 10^{15}$ fm/c.

2.4.1 Initial State

A dynamical description of a heavy-ion collision begins with the essential component of initial conditions. At $\tau = 0$ fm/c, two Lorentz-contracted nuclei (along the beam direction, z) interact and deposit a large amount of energy in the overlapping region. The geometry of the overlapping region is of particularly high importance while understanding the characteristics of heavy-ion collisions. This is because the area of the overlapping region directly influences the amount of energy deposited, and the energy deposited in this region is directly proportional to the number of particles contributing to the experimental observables. Moreover, the shape of the overlapping region also conveys information on the possible formation of the QGP droplet.

However, we do not have any initial state models based on first principles. The most com-

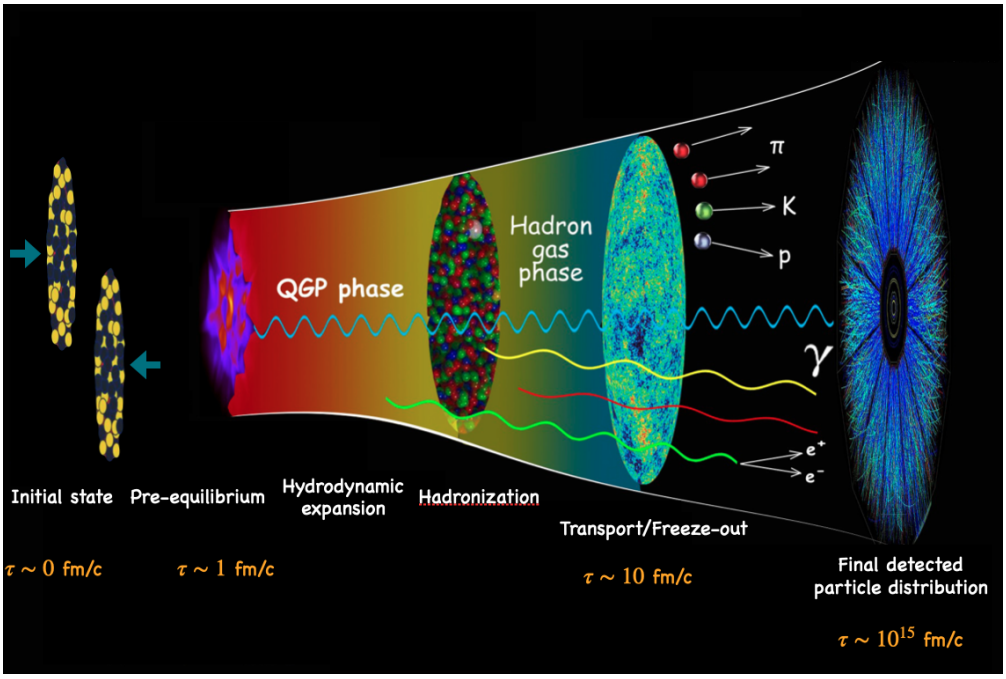

Figure 2.7: Illustration of the evolution of the fireball created in relativistic heavy-ion collisions. Adapted from Ref. [24].

monly used model for the initial state is the "Glauber model", introduced by Roy Glauber [25]. Using this model, one can calculate the cross-sections of A+A, p+A, and pp collisions utilizing individual interactions of constituent nucleons. Two important inputs to the Glauber calculations are the following:

1) Nuclear charge densities ($\rho(r)$): The nucleon density is usually parameterized by a Fermi distribution with three parameters, given by:

$$\rho(r) = \rho_0 \frac{1 + w(r/R)^2}{1 + \exp(\frac{r-R}{a})}, \tag{2.22}$$

where ρ_0 is the nucleon density in the center of the nucleus, R is the nuclear radius, a is the skin depth, and w denotes the deviations from a spherical shape.

2) Inelastic nucleon-nucleon cross section ($\sigma_{\text{inel}}^{\text{NN}}$): This provides the non-trivial beam-energy dependence to Glauber calculation.

Figure 2.8 illustrates a typical heavy-ion collision between the projectile nucleus "B" and the target nucleus "A". Impact parameter or $\vec{b}$ is the displacement between the center of the two nuclei.

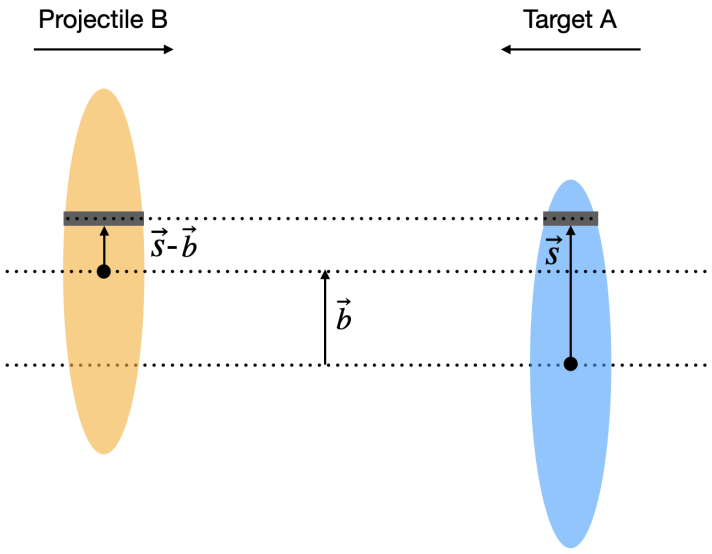

Figure 2.8: Schematic representation of the Glauber model geometry, with a transverse view. Adapted from Ref. [25].

During the collision, one flux tube located at a displacement $\vec{s}$ with respect to the center of target nucleus overlaps with another flux tube located at a displacement $\vec{s}-\vec{b}$ with respect to the center of projectile nucleus. The joint probability per unit area of nucleons located in the overlap zone of the projectile and target flux tubes within a differential area d^2s is known as the "nuclear thickness function", $\hat{T}_{AB}$ given by:

$$\hat{T}_{AB}(\vec{b}) = \int \hat{T}_A(\vec{s})\hat{T}_B(\vec{s}-\vec{b})d^2s, \tag{2.23}$$

where the probability per unit area of a given nucleon is given by $\hat{T}_A(\vec{s}) = \int \rho_A(\vec{s},z)dz$ and ρ_A is the Woods–Saxon density profile given by Equation 2.22.

Now, one can compute geometric quantities like N_{part} and N_{coll} using the nuclear thickness function $\hat{T}_{AB}$. N_{part} is defined as the number of "wounded" or participant nucleons that interact with at least one nucleon of the opposite nucleus, given by:

$$\begin{aligned} N_{part} = A \int \hat{T}_A(\vec{s})\{1-[1-\hat{T}_B(\vec{s}-\vec{b})\sigma_{NN}]^B\}d^2s \\ + B \int \hat{T}_B(\vec{s}-\vec{b})\{1-[1-\hat{T}_A(\vec{s})\sigma_{NN}]^A\}d^2s, \end{aligned} \tag{2.24}$$

where $\hat{T}_A(\vec{s})\sigma_{NN}$ is the probability of a single nucleon-nucleon interaction.

The next geometric quantity is N_{coll}, defined as the number of binary nucleon-nucleon collisions, given by:

$$N_{\text{coll}} = AB\hat{T}_{AB}(\vec{b})\sigma_{NN}. \tag{2.25}$$

In the above description, we used a continuous energy density profile. However, in reality, there are event-to-event fluctuations as well as spatial variations in energy deposition of nucleon-nucleon collision within an event. Therefore, a more realistic representation involves a "lumpy" description of the initial density profile, requiring the implementation of a Monte Carlo process with random impact parameter, $\vec{b}$, generated for each event, based on the probability distribution $dN/db \propto b$. Figure 2.9 shows a Glauber Monte Carlo simulation illustrating the collision of two gold nuclei at an impact parameter $b = 6$ fm head-on (left panel) and from a side view (right panel). The participants are shown in darker blue and red, and the spectators are in lighter colors.

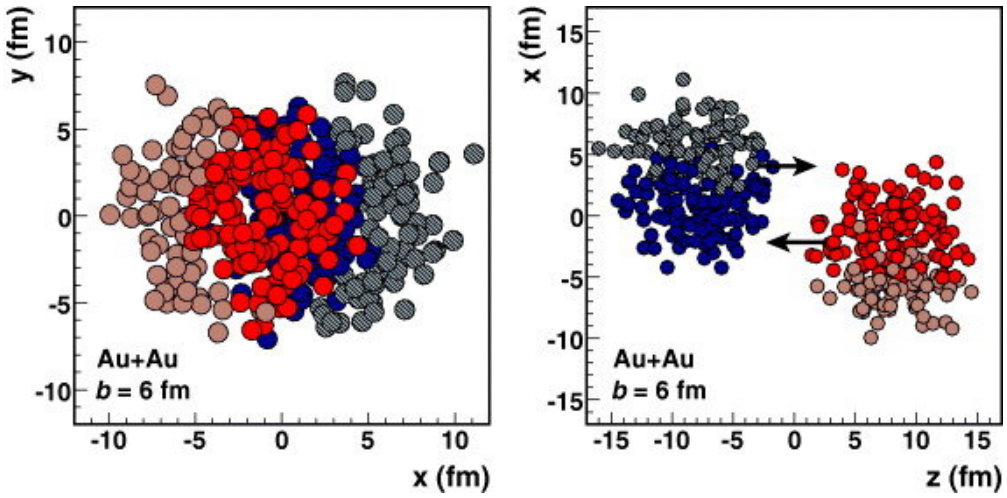

Figure 2.9: Glauber Monte Carlo calculation showing the collision of two gold nuclei at an impact parameter $b = 6$ fm head-on (left panel) and from a side view (right panel). Reproduced from Ref. [25].

Now, the most important element is establishing a connection between these geometric quantities and experimentally measurable quantities. Utilizing the energy deposits of particles produced in a collision as well as the tracking of charged particles within an event, collision events can be categorized experimentally using either centrality or multiplicity. By employing N_{part} and N_{coll}, one can simulate the production of charged particles in an event, denoted as N_{ch} or, equivalently,

multiplicity. This multiplicity can be mapped to centrality classes as shown in Figure 2.10. Each centrality class corresponds to a specific range of impact parameters, illustrated by overlapping circles, where more central events are associated with smaller impact parameters. A central event is characterized by an impact parameter closer to 0, whereas a peripheral event has larger impact parameters. A simple method to precisely determine the centrality from impact parameters in nucleus-nucleus collision can be found in Ref. [26].

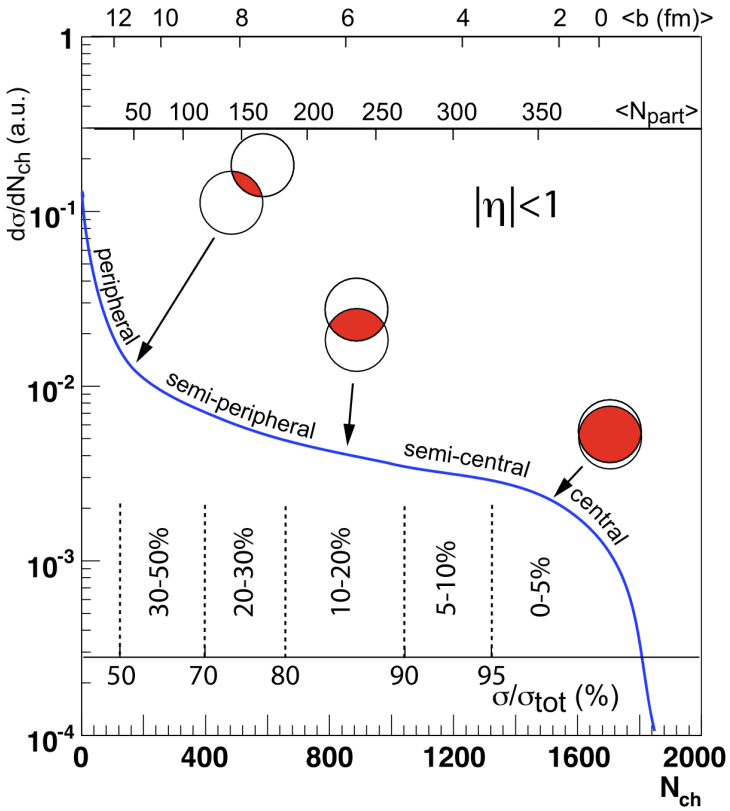

Figure 2.10: Shown is the cartoon example of the correlation of final state observable N_{ch} with Glauber quantities (b, N_{part}). Reproduced from Ref. [25].

2.4.2 Pre-equilibrium

The initial conditions described in the previous section now serve as an input for the hydrodynamic evolution of dense hot matter produced in high-energy heavy-ion collisions. Up until τ = 1 fm/c, the system remains highly hot and dense and very far away from thermal equilibrium,

referred to as the pre-equilibrium phase. Eventually, the system evolves into a state where it can be described using relativistic hydrodynamics.

2.4.3 Hydrodynamic Expansion

Landau introduced the idea of the hydrodynamic evolution of a proton-proton collision, building upon Fermi's description of an instantaneous break-up of a nucleus into a multi-particle hadronic state. Landau assumed that the two colliding protons released their energy in the volume corresponding to the Lorentz-contracted size of a proton. However, he also noticed that the substantial contraction would lead to the formation of a large longitudinal pressure gradient (along the beam direction), resulting in one-dimensional expansion governed by the laws of relativistic hydrodynamics of the perfect fluid. At some point, the transverse expansion cannot be neglected, and the hydrodynamic expansion becomes three-dimensional as long as the mean free path is smaller than the system size. As matter further expands, the mean free path is no longer smaller, and the system breaks up into final state particles.

Fluid dynamics is based on the equations for the conservation laws:

$$\partial_\mu T^{\mu\nu} = 0, \quad \text{and} \quad \partial_\mu N_i^\mu = 0 \tag{2.26}$$

of the energy-momentum tensor $T^{\mu\nu}$ and the current density N_i^μ of any conserved quantum number and an equation of state, $P = P(\varepsilon, \rho_B)$. The simplest equation of state corresponds to a relativistic ideal gas consisting of massless particles, $P = \frac{\varepsilon}{3}$.

The degrees of freedom of a relativistic fluid component are the Lorentz four-vector flow u^μ ($= dx^\mu/d\tau$), energy density ε, pressure P, and baryon energy density ρ_B, and $\mu = 0, 1, 2, 3$ denotes the Minkowski 4-space metric $g^{\mu\nu} = \text{diag}(+, -, -, -)$. The quantum number current density has the simple form $N^\mu = nu^\mu$, where n is the density measured in the local rest frame.

In simple fluid dynamics, when an ideal fluid is in local equilibrium, the energy-momentum tensor is given by:

$$T^{\mu\nu} = (\varepsilon + P)u^\mu u^\nu + Pg^{\mu\nu}. \tag{2.27}$$

For ideal hydrodynamics to be applied, the systems need to be at exact thermal equilibrium. Considering a more realistic scenario, one needs to include contributions from bulk viscosity and shear viscosity terms, which includes small deviations from the exact thermal equilibrium. This is known as "viscous hydrodynamics", and the energy-momentum tensor for a viscous hydrodynamics is given by:

$$T^{\mu\nu} = \varepsilon u^{\mu} u^{\nu} - \Delta^{\mu\nu}(p + \Pi) + \pi^{\mu\nu}, \tag{2.28}$$

where Π is the bulk pressure, $\Delta^{\mu\nu} = g^{\mu\nu} - u^{\mu}u^{\nu}$, and $\pi^{\mu\nu}$ is the shear stress tensor defined by $\pi^{\mu\nu} = \Delta^{\mu\nu}_{\alpha\beta} T^{\alpha\beta}$, where $\Delta^{\mu\nu}_{\alpha\beta} = \frac{1}{2}(\Delta^{\mu}_{\alpha}\Delta^{\nu}_{\beta} + \Delta^{\mu}_{\beta}\Delta^{\nu}_{\alpha}) - \frac{1}{3}\Delta^{\mu\nu}\Delta_{\alpha\beta}$.

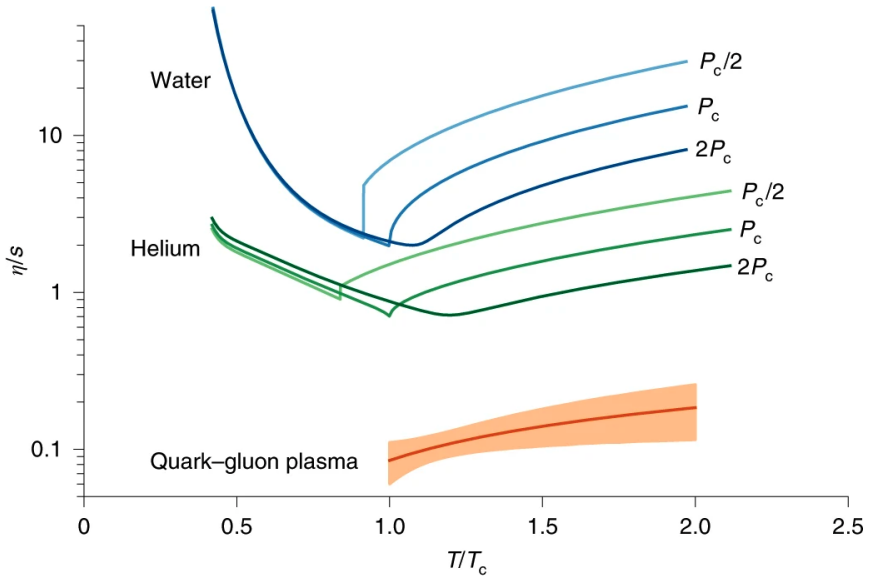

Figure 2.11: Shown is the Bayesian estimate of the specific shear viscosity of QGP compared with measurements of water and helium as a function of T/T_c, where T_c is each fluid's critical temperature. Reproduced from Ref. [27].

As input to the contributions from viscosity terms, one needs to provide transport coefficients such as shear viscosity, η, and bulk viscosity, ζ. They depend on the microscopic properties of the system, and then the fluid dynamics describes the macroscopic properties of the system. For a strongly interacting system like QGP, the ratio of shear viscosity to volume density of entropy, know as the specific shear viscosity η/s, is used to characterize how close a given fluid is to being perfect [28]. Figure 2.11 shows the Bayesian estimate of the specific shear viscosity of QGP com-

pared with measurements of water and helium. The QGP η/s is at least an order of magnitude smaller than that of most common fluids, meaning that it behaves more like a "perfect" fluid.

2.4.4 Hadronization and Hadronic Transport

When the matter formed in heavy-ion collisions becomes dilute enough, the fluid undergoes hadronization, giving rise to a myriad of particles. Chemical freeze-out is defined as the temperature at which hadron abundances are fixed and the inelastic interactions between different species of particles cease to exist. Later, the system reaches a temperature at which elastic scattering also ceases, known as the kinetic freeze-out.

For modeling purposes, immediately after hydrodynamic evolution, a 4-dimensional freeze-out surface, Σ, is defined, where all the cells on the surface share the same temperature. The freeze-out surface is used to calculate the distribution of particles with well-defined position and momenta, and this is done using the Cooper–Frye formula [29], given by:

$$E\frac{dN}{d^3p} = \frac{dN}{dydp_Td\phi_p} = \int_\Sigma f(u^\mu p_\mu)p^\mu d\Sigma_\mu, \tag{2.29}$$

where $f(u^\mu p_\mu)$ is the appropriate Fermi–Dirac or Bose–Einstein distribution for particles in thermal equilibrium, and $d\Sigma$ is the hypersurface element.

Afterward, the system consists of a hadron gas that can be described using kinetic theory. The hadron gas undergoes rescatterings, eventually leading to the particles free-streaming to the detectors.

2.5 QGP Signatures and Small Systems

In the field of heavy-ion physics, a wealth of opportunities emerged when it was established that the hot-dense matter produced in an ultra-relativistic heavy-ion collision behaved as a nearly perfect fluid. This phenomenon was first observed in Au+Au collisions by experimental facilities at RHIC [30–33]. Subsequently, similar behavior was observed in Pb+Pb collisions at LHC [34]. Abundant experimental data were produced by experimental collaborations such as ATLAS, CMS, and ALICE, continuing to make precision measurements characterizing the behavior and properties of QGP, adding an element of excitement and success to the field.

In the early years of heavy-ion collisions, small collision systems like *pp* were utilized as control measurements under the assumption that QGP is not produced in these collisions. The main idea is that small systems are made of very few particles, and thus cannot be described using statistical models, thereby cannot exhibit any fluid-like behavior. However, contradicting this hypothesis, CMS collaboration observed the presence of a tiny Quark-Gluon Plasma (QGP) droplet in ultra-central *pp* collisions at LHC [35]. This observation was argued about for a long time, whether it was due to similar features observed in Pb+Pb collisions or features present in the initial state of the collisions. Interestingly, other small systems such as d+Au [36] and p+Pb [7, 37, 38] indicated that most of the QGP signatures for hydrodynamic flow also existed in these smaller systems, marking a significant shift in focus within the field. This raised many important questions in the field. Could the QGP be formed in small systems? What is the smallest system that is necessary to create a tiny droplet of QGP? What are the mechanisms involved in the formation of QGP such that it could be formed in small systems?

Currently, active research is ongoing to explore QGP-like signals in smaller and exotic systems like photo-nuclear (γ+A) collisions, which constitutes the core of this thesis, as well as high multiplicity $e^+ + e^-$ collisions [39] and the search from a single fragmenting parton that forms a jet [40]. The section delves into various observables suggesting the presence of a QGP droplet, known as QGP signatures, with a specific focus on small systems. There are a multitude of QGP

signatures that are actively investigated in the field [41–43]. In this section, only those which are relevant to the content of the thesis will be discussed, such as collective flow, radial flow, baryon anomaly, and strangeness enhancement.

2.5.1 Collective Flow

In section 2.4.3, the concept of describing QGP as a nearly perfect fluid is motivated. In this section, we delve into a detailed discussion of its experimentally observed signature, known as the "collective flow" [2, 44, 45].

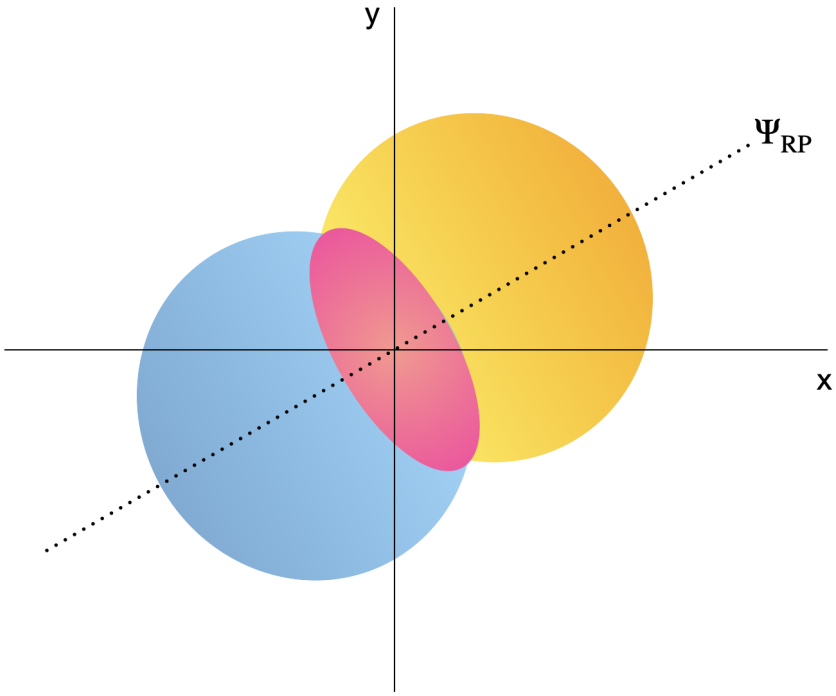

Figure 2.12: Schematic view of a semi-central Pb+Pb collision along the beam axis. The impact parameter makes an angle Ψ_{RP} with the x-axis, defining the reaction plane. The overlap region creates an almond-shaped geometry.

Figure 2.12 shows a schematic representation of a semi-central Pb+Pb collision along the beam axis (*i.e.*, the z-axis). During the collision, the direction of the impact parameter (*i.e.*, the distance between the centers of the nuclei) defines a plane known as the reaction plane. The angle that the reaction plane makes with the x-axis is referred to as the event-plane angle, Ψ_{RP}. When

two heavy ions collide, the overlap region appears to have an almond shape, purely driven by the geometry of the collision. This specific geometry creates a higher pressure gradient along the short axis (x-axis when $\Psi_{\mathrm{RP}} = 0$) than the long axis (y-axis when $\Psi_{\mathrm{RP}} = 0$). Consequently, QGP will expand hydrodynamically along the preferred direction of higher pressure gradient (*i.e.*, the short axis) in the reaction plane. The final-state particles will be emitted preferentially with respect to a certain azimuthal angle and with back-to-back symmetry, resulting in an anisotropic flow of particles, as depicted in Figure 2.13. In other words, one can say that the initial state spatial anisotropy is translated to final state momentum anisotropy through the hydrodynamic expansion of QGP This phenomenon is known as "collective flow".

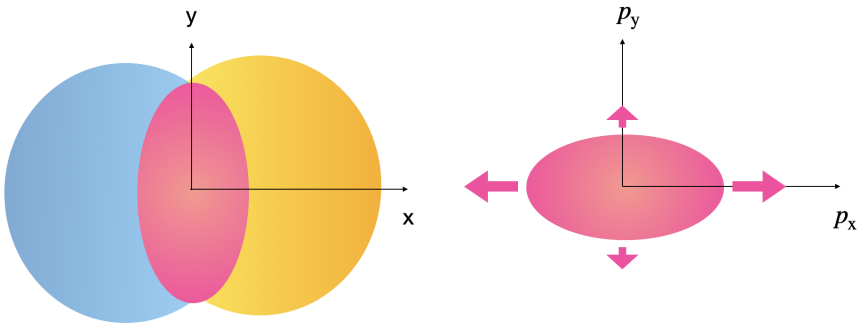

Figure 2.13: Schematic view of a semi-central Pb+Pb collision along the beam axis. The conversion of initial state spatial anisotropy (left) into final state momentum anisotropy (right) is shown. This figure assumes $\Psi_{\mathrm{RP}} = 0$.

The momentum anisotropy of emitted particles can be quantified by the Fourier coefficients of the azimuthal distribution of particles [46, 47]:

$$E\frac{d^3N}{dp^3} = \frac{1}{2\pi p_{\mathrm{T}}}\frac{d^2N}{dp_{\mathrm{T}}dy}(1 + 2\sum_{n=1}^{\infty} v_{\mathrm{n}}\cos[n(\phi - \Psi_n)]), \tag{2.30}$$

where p_{T} is the transverse momentum, y is the rapidity, ϕ is the azimuthal angle, and Ψ_n is the overall orientation of the n^{th} moment. Due to reflection symmetry with respect to the reaction plane, all the sine terms disappear. The Fourier coefficients quantify the anisotropy, and they are referred to as "flow coefficients". The first harmonic, v_1, known as the directed flow, refers to the sideward motion of participants in ultra-relativistic nuclear collisions, and it carries information

from the early stage of the collision. The elliptic flow coefficient, v_2, is the most extensively studied and dominant flow coefficient in non-central heavy-ion collisions since the final state anisotropy mainly arises from the steep pressure gradients developed due to the almond-shaped geometry of the initial state anisotropy, as described in Figure 2.13. The higher-order coefficients, $n > 2$, such as triangular flow (v_3) and quadrupolar flow (v_4), are also important due to their sensitivity to initial-state geometric fluctuations [48] and viscous effects. v_2 and v_3 are highlighted in Figure 2.14.

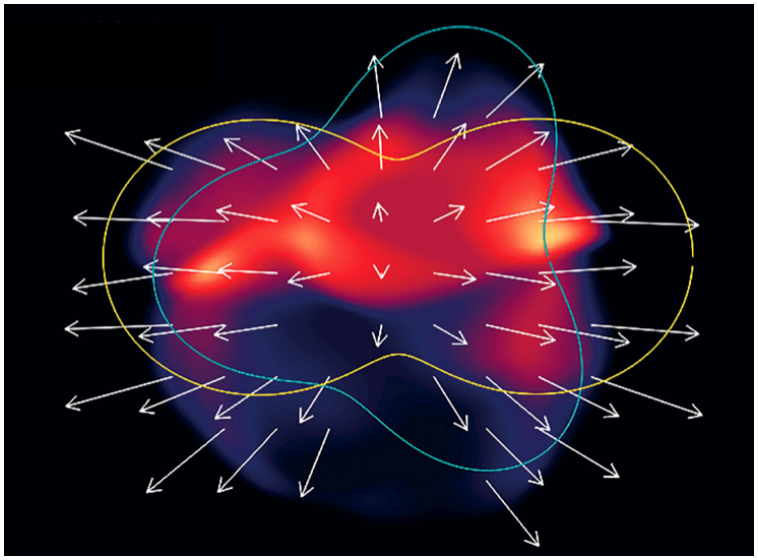

Figure 2.14: An illustration of the evolving energy density of the QGP created in a non-central collision. Pressure gradients act on the initial geometrical anisotropy to create a final velocity field (arrows), which may be decomposed into elliptic (yellow), triangular (teal), and higher-order components. Reproduced from Ref. [49].

Non-vanishing values of v_n have been measured to high precision at RHIC and LHC as a function of transverse momentum, particle species, and centrality [50]. Various experimental methods, such as two-particle correlation, scalar-product, and event-plane methods, have been established to determine the v_n values with great precision. In the two-particle correlation method, the distribution of particle pairs in relative azimuthal angle $\Delta\phi = \phi^a - \phi^b$ and pseudorapidity separation $\Delta\eta = \eta^a - \eta^b$ is measured. The labels, a and b, denote the two particles used to make a pair, referred to as "trigger" and "associated" particles, respectively. The two-particle correlation

function, $C(\Delta\eta, \Delta\phi)$, is defined as:

$$C(\Delta\eta, \Delta\phi) = \frac{S(\Delta\eta, \Delta\phi)}{B(\Delta\eta, \Delta\phi)}, \tag{2.31}$$

where

$$S(\Delta\eta, \Delta\phi) = \frac{1}{N_{\text{evt}}} \frac{dN^{\text{same}}}{d\Delta\eta d\Delta\phi}, \quad \text{and} \quad B(\Delta\eta, \Delta\phi) = \frac{1}{N_{\text{evt}}} \frac{dN^{\text{mix}}}{d\Delta\eta d\Delta\phi}, \tag{2.32}$$

where N^{same} corresponds to the number of pairs within the same event, and N^{mix} denotes the number of mixed-event pairs. Event-mixing is performed to remove the effects of detector inefficiencies in the distribution.

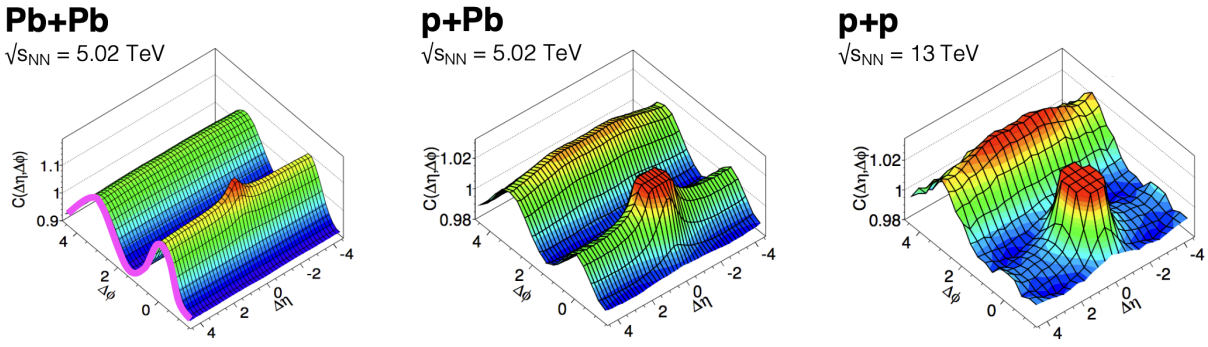

Figure 2.15: Two-particle correlation functions $C(\Delta\eta, \Delta\phi)$ from Pb+Pb (left), p+Pb (middle) and pp (right) collisions at $\sqrt{s_{\text{NN}}}$ = 5.02 TeV, 5.02 TeV, and $\sqrt{s}$ = 13 TeV respectively. Reproduced from Ref. [51].

Figure 2.15 illustrates the two-particle correlations, $C(\Delta\eta, \Delta\phi)$, measured in Pb+Pb [52], p+Pb [53] and pp [54] collisions at the LHC. Notably, long-range correlation features dominate at $\Delta\phi = 0, \pi$ extending across the entire $\Delta\eta$ direction. The elliptic modulation of the long-range correlation along the $\Delta\phi$ direction is the result of the global anisotropy within the event. However, there are several sources in these correlations, which does not emerge from a hydrodynamic description. They are referred to as non-flow contributions. This includes the long-range correlation appearing at $\Delta\phi = \pi$, referred to as the "away-side", which is mainly from dijets – pairs of collimated sprays of hadrons that have balanced transverse momenta but point at an azimuthal

angle opposite to each other ($\Delta\phi = \pi$). Also, the contribution of a "near-side" peak at $(\Delta\eta, \Delta\phi) \sim (0, 0)$ arises from various sources, including resonance decays and jet fragmentation. The symmetric double ridge, both near-side and away-side, is very obvious in Pb+Pb collisions. In *pp*, one can still tell there is a symmetric ridge there because the near-side is high, even though the away-side is buried by the large non-flow. Notably, the long-range correlation feature appearing at $|\Delta\eta| > 2$, spanning the $\Delta\eta$ direction, visible across systems of different sizes, serves as clear evidence of collective flow in heavy-ion collisions.

To determine the flow coefficients v_n from the two-particle correlation function, one can treat the same as a single-particle distribution and expand it as a Fourier series following the Equation 2.30:

$$C(\Delta\eta, \Delta\phi) = C_0(\Delta\eta)(1 + 2\sum_{n=1}^{\infty} v_{\mathrm{n,n}}(p_{\mathrm{T}}^a, p_{\mathrm{T}}^b)\cos[n\Delta\phi]), \tag{2.33}$$

where $v_{\mathrm{n,n}}$ are the Fourier coefficients of the two-particle correlation and C_0 is its average value. If the two-particle distribution is simply the product of two single-particle distributions, then it can be shown that the Fourier coefficients of the two-particle correlation factorize as:

$$v_{\mathrm{n,n}}(p_{\mathrm{T}}^a, p_{\mathrm{T}}^b) = v_{\mathrm{n}}(p_{\mathrm{T}}^a)v_{\mathrm{n}}(p_{\mathrm{T}}^b). \tag{2.34}$$

Therefore, the flow coefficients, v_n, can be evaluated from the measured $v_{n,n}$ as:

$$v_{\mathrm{n}}(p_{\mathrm{T}}^b) = \frac{v_{\mathrm{n,n}}(p_{\mathrm{T}}^a, p_{\mathrm{T}}^b)}{v_{\mathrm{n}}(p_{\mathrm{T}}^a)} = \frac{v_{\mathrm{n,n}}(p_{\mathrm{T}}^a, p_{\mathrm{T}}^b)}{\sqrt{v_{\mathrm{n,n}}(p_{\mathrm{T}}^a, p_{\mathrm{T}}^b)}}, \tag{2.35}$$

where $v_{\mathrm{n,n}}(p_{\mathrm{T}}^a, p_{\mathrm{T}}^b) = v_n^2(p_{\mathrm{T}}^a)$ is used in the denominator.

v_n can also be computed using the event-plane method. In this method, the orientation of the event plane associated with each harmonic, Ψ_n, can be calculated from particle positions ϕ_i measured in a reference detector, typically at forward rapidities, as:

$$\Psi_n = \frac{1}{n}\tan^{-1}\frac{\sum_i \sin(n\phi_i)}{\sum_i \cos(n\phi_i)}. \tag{2.36}$$

From the measured Ψ_n, flow coefficients can be simply determined as:

$$v_n = \langle\cos[n(\phi - \Psi_n)]\rangle, \tag{2.37}$$

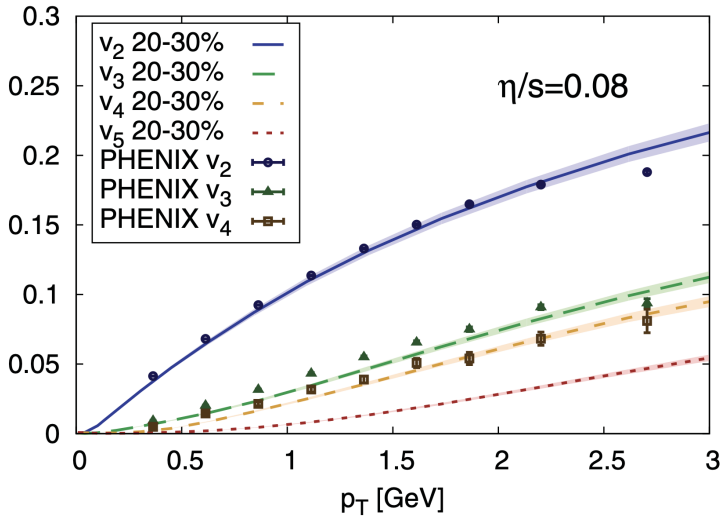

Figure 2.16: Elliptic (v_2), triangular (v_3) and quadrupolar (v_4) flow coefficients in 20-30% central collisions using experimental data from PHENIX compared to hydrodynamic calculations. Reproduced from Ref. [55].

where the angle represents an average over all the particles and all the events.

Figure 2.16 shows the first observation of flow coefficients, v_n, determined using the experimental data from PHENIX in mid-central Au+Au collisions at RHIC using the event-plane method compared to the predictions of a 3+1D hydrodynamic model [55]. Observations of v_2, v_3 and v_4, measured by different experiments such as ATLAS [53], CMS [56, 57], and ALICE [58] at LHC across systems of different sizes, Pb+Pb, p+Pb and pp, decreasing in size is presented in Figure 2.17. A comparison to a hydrodynamic model is also shown [59]. The agreement of hydrodynamic calculations with anisotropic flow measurements affirms the paradigm that the quark-gluon plasma exhibits an extremely low ratio of shear viscosity to entropy density and is, therefore, one of the most "perfect" fluids in nature [60]. Additionally, it confirms the paradigm that even these small systems exhibit flow, indicating their flow characteristics arise from final-state interactions rather than initial-state features.

Pushing the limits of system sizes, the flow observables that provided strong evidence for the presence of QGP in heavy-ion collisions have now been measured in photo-nuclear collisions by ATLAS [10]. Figure 2.18 depicts the flow coefficient, v_2, measured in photo-nuclear collisions,

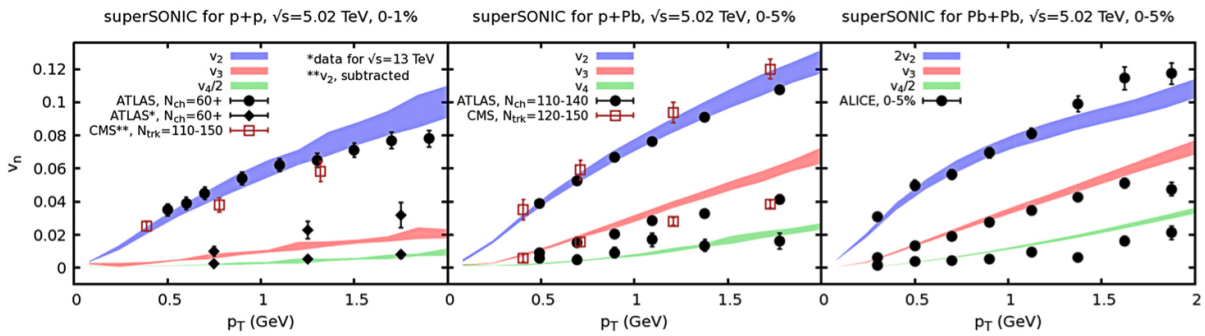

Figure 2.17: Elliptic (v_2), triangular (v_3) and quadrupolar (v_4) flow coefficients from hydrodynamic simulations (bands) compared to experimental data from ATLAS, CMS, and ALICE (symbols) for pp (left panel), p+Pb (center panel) and Pb+Pb (right panel) collisions. Reproduced from Ref. [59].

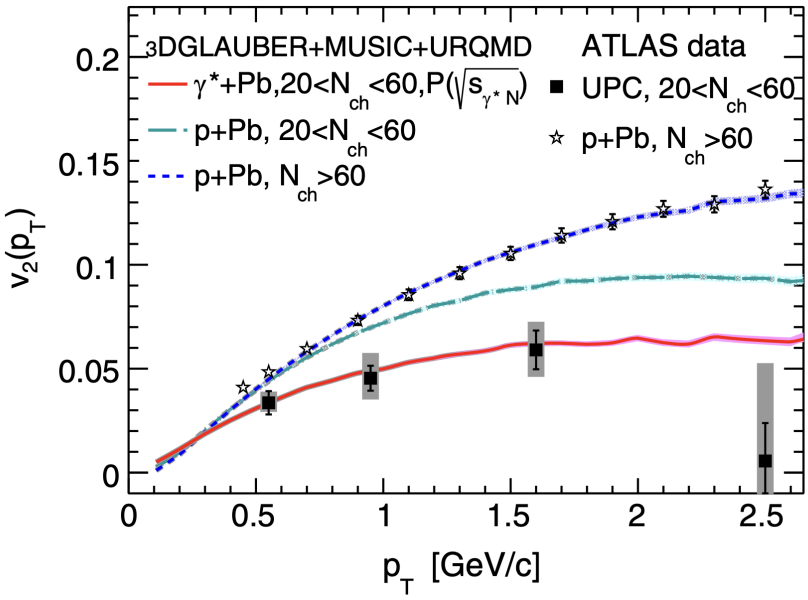

Figure 2.18: The p_{T} differential elliptic flow coefficient ($v_2(p_{\mathrm{T}})$) of charged hadrons in γ+Pb and p+Pb collision data from ATLAS collaboration compared to hydrodynamic simulations. Reproduced from Ref. [61].

indicating the persistence of collective phenomena with the strength of correlations slightly smaller than that observed in p+Pb collisions. The hydrodynamical model [61] predicts agrees well with the measured v_2 in both γ+Pb and p+Pb collisions. Figure 2.19 (left) illustrates the flow coefficients measured in high multiplicity $e^+ + e^-$ collisions [62] compared to those measured in pp collisions by CMS [57]. Previously, in $e^+ + e^-$ collisions at 91 GeV, no measurable long-range near-side

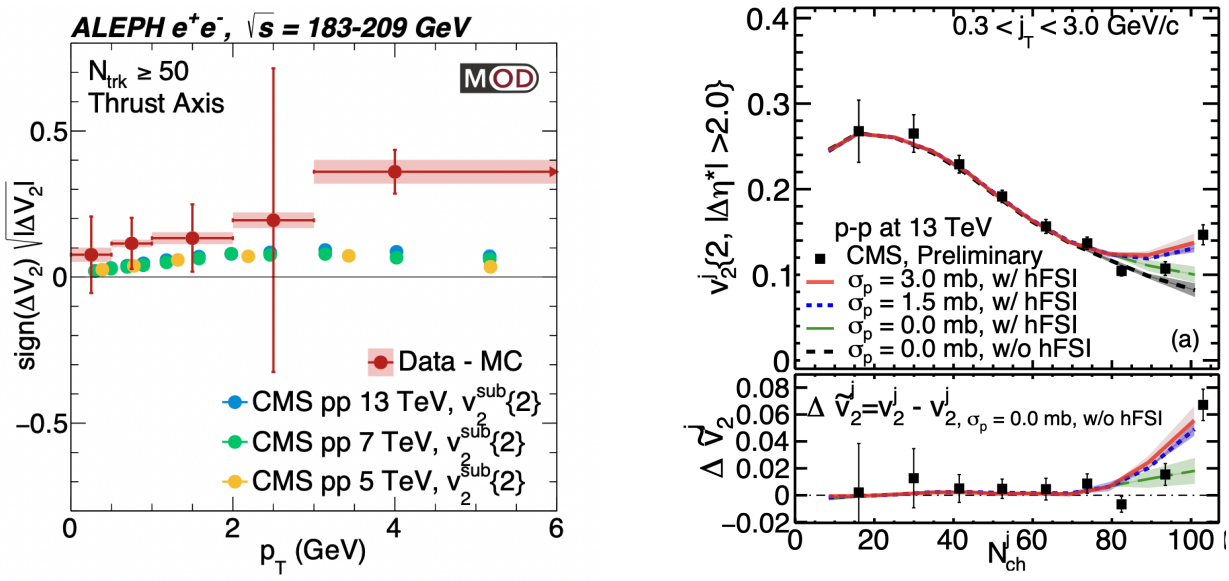

Figure 2.19: (a) The elliptic flow coefficient $\mathrm{sign}(\Delta V_2)\sqrt{\Delta V_2}$ as a function of p_{T} in high multiplicity $e^+ + e^-$ collisions from ALEPH collaboration compared to CMS pp data. Reproduced from Ref. [62]. (b) The elliptic flow coefficients $v_2^j\{2, |\Delta\eta^*| > 2\}$ as functions of charged hadron multiplicity N_{ch}^j inside jets in pp collisions at 13 TeV (top panels), and the v_2^j difference due to final-state interactions (bottom panels) from model calculations compared to CMS data. Reproduced from Ref. [63].

signals were observed [39]. However, high-multiplicity $e^+ + e^-$ collisions at 183-209 GeV claim to observe flow signals. Figure 2.19 (right) illustrates the flow coefficients measured within jets in pp collisions [40], along with model predictions with and without final-state interactions [63]. The model prediction with the final-state interactions describes the observed increasing trend of v_2 as a function of multiplicity at higher multiplicity values ($N_{\mathrm{ch}}^j > 80$).

2.5.2 Radial Flow

In the previous section, we established the mechanism of collective hydrodynamic expansion of the fluid. The radial expansion of the fluid along the transverse plane significantly affects the shape of the p_{T} distribution of the particles. As the fluid expands radially, particles in the transverse plane experience a substantial velocity boost. Consequently, the momentum boost will be larger for massive particles that gained a common velocity boost. This is evident in the p_{T} distribution of the particles, where the heavier hadrons are pushed out to higher p_{T} resulting in a comparatively

flat distribution, providing evidence for the presence of strong radial flow [64–66].

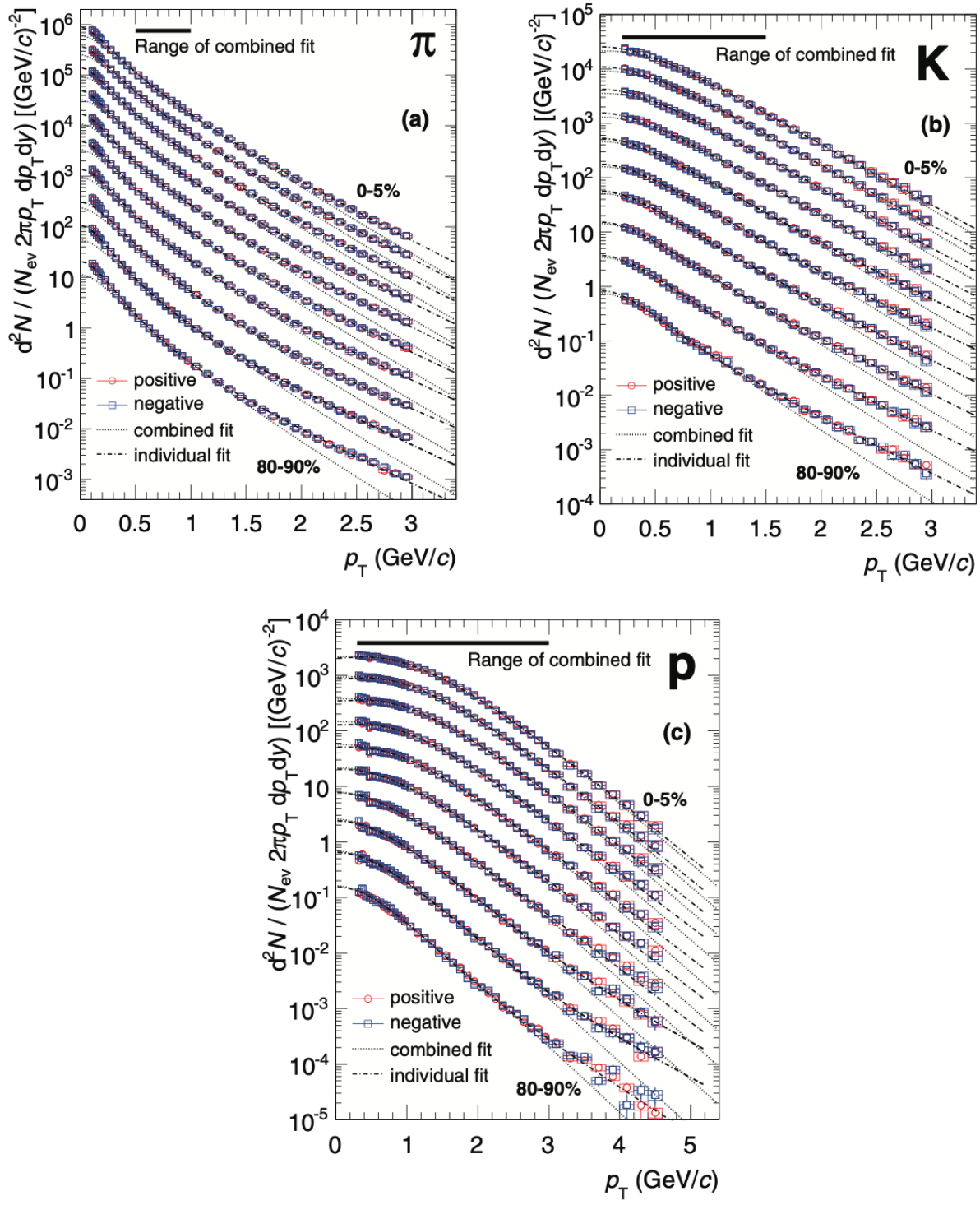

Figure 2.20: Transverse-momentum (p_{T}) distribution of (a) π, (b) K, and (c) p in Pb+Pb collisions at $\sqrt{s_{\mathrm{NN}}} = 2.76$ TeV from ALICE for different centralities. Reproduced from Ref. [67].

Figure 2.20 illustrates the p_{T} distribution of $\pi^{\pm}$, $K^{\pm}$, and $p^{\pm}$ in heavy-ion collisions at LHC [67]. The momentum distribution of particles is expected to follow an exponential distribution assuming the Boltzmann distribution:

$$\frac{1}{p_{\mathrm{T}}}\frac{dN}{dp_{\mathrm{T}}} \propto e^{-p_{\mathrm{T}}/T_{\mathrm{eff}}}, \tag{2.38}$$

where T_{eff} is the slope of the distribution in a semi-log scale. The shoulder at the low-p_{T} of the distribution indicates a deviation from thermal expectations and becomes flatter with increasing mass of the hadrons. This behavior is expected in the hydrodynamical models as a consequence of the momentum boost induced by the collective expansion. Furthermore, this flattening at low-p_{T} for protons, the most massive of the measured hadrons, is more pronounced in central collisions compared to peripheral collisions, suggesting stronger radial flow with increasing centrality.

Furthermore, one can extract kinetic freeze-out temperatures (T_{kin}) and average flow velocities ($\langle\beta\rangle$) by fitting the transverse momentum spectra of several particle species using the blast-wave function, assuming particles emitted from a boosted fireball follow a common radial expansion profile. The functional form is given by [68]:

$$\frac{1}{p_{\mathrm{T}}}\frac{dN}{dp_{\mathrm{T}}} \propto \int_0^R \mathrm{d}r \cdot r \cdot m_{\mathrm{T}} \cdot I_0\left(\frac{p_{\mathrm{T}}\sinh\rho}{T_{\mathrm{kin}}}\right) \cdot K_1\left(\frac{m_{\mathrm{T}}\cosh\rho}{T_{\mathrm{kin}}}\right), \tag{2.39}$$

where the velocity profile ρ is described by:

$$\rho = \tanh^{-1}\beta_{\mathrm{T}}(r) = \tanh(\beta_{\mathrm{s}}(r/R)^n). \tag{2.40}$$

Here, $m_{\mathrm{T}} = \sqrt{p_{\mathrm{T}}^2 + m^2}$ is the transverse mass, I_0 and K_1 are modified Bessel functions, r is the radial distance in the transverse plane, R is the transverse radius of the fireball, $\beta_{\mathrm{T}}(r)$ is the transverse expansion velocity and β_{s} is the transverse expansion velocity at the surface.

Figure 2.21 illustrates the extracted kinetic freeze-out temperatures (T_{kin}) and average flow velocities ($\langle\beta\rangle$) for different beam energies and centralities [69]. The results are similar for different collision types and energies. In the most peripheral bins, the results indicate an earlier freeze-out at a higher temperature and with less transverse flow. In central collisions, the QGP had a longer lifetime, i.e., freeze-out at a lower temperature with substantial transverse flow.

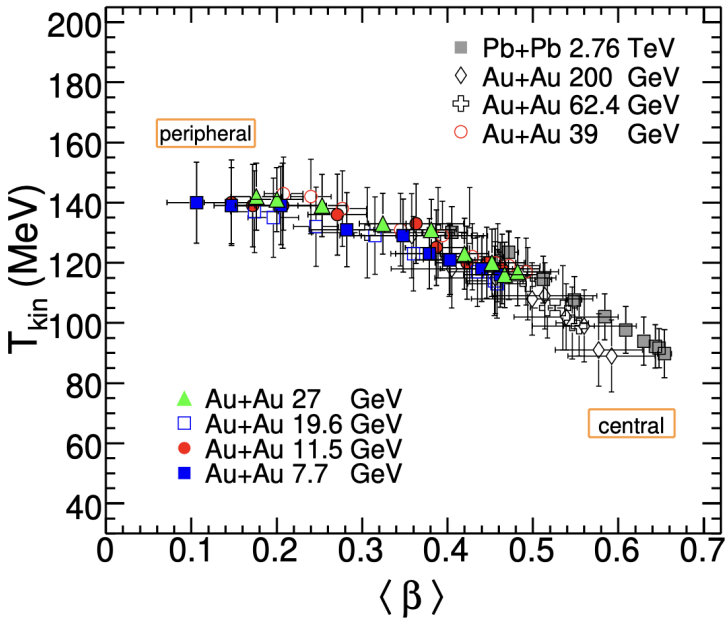

Figure 2.21: Results for kinetic freeze-out temperature and radial velocity from fits to transverse momentum spectra from the RHIC beam energy scan. Reproduced from Ref. [69].

Figure 2.22 depicts the p_{T} spectra of identified particles such as π^+, K^+, p, K^0_S, Λ, and the ϕ meson in Pb+Pb collisions at $\sqrt{s_{NN}} = 2.76$ TeV for the 0-5% and 80-90% centrality intervals [70]. The shape of the distribution is flatter for central collisions compared to peripheral collisions. Additionally, the peak of the distribution is located at a higher momentum value in central collisions compared to peripheral collisions. Furthermore, the flattening of the spectra in the low-p_{T} region is mass-dependent and is more prominent for heavier particles. This observation is in line with the expected effect of increasing radial flow with collision centrality.

The flattening of the p_{T} spectra for each particle species can be captured by calculating the mean transverse momentum, denoted as $\langle p_{\mathrm{T}} \rangle$. Figure 2.23 illustrates the mean transverse momentum, $\langle p_{\mathrm{T}} \rangle$, as a function of event multiplicity in pp collisions for all identified particles studied by the ALICE experiment [71]. The results include the $\langle p_{\mathrm{T}} \rangle$ of several identified particles, arranged in increasing order of masses: $\pi^{\pm} < K^{\pm} \sim K^0_S < p < \phi < \Lambda < \Xi^{\pm} < \Omega^{\pm}$. Notably, the

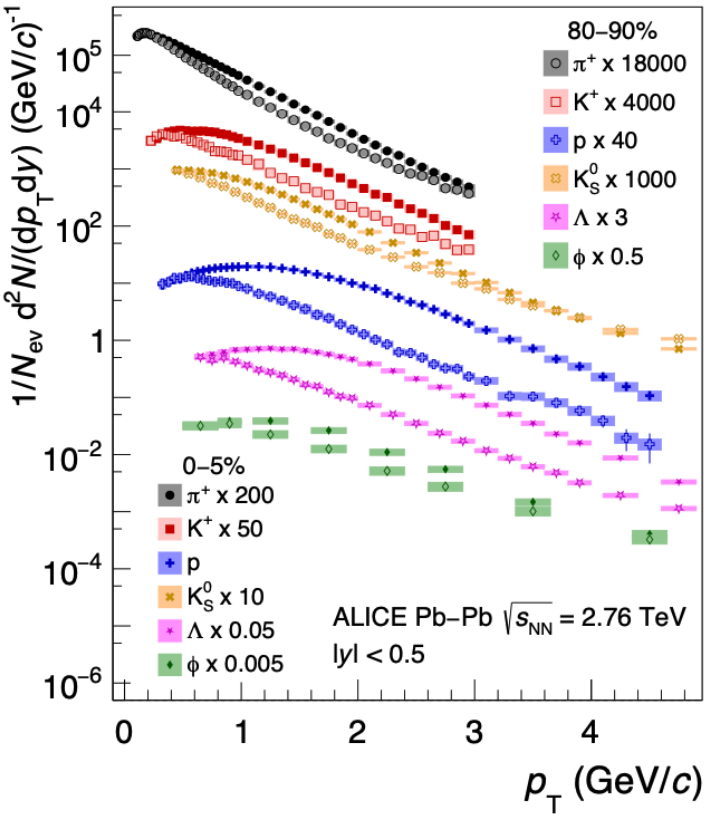

Figure 2.22: Transverse momentum distributions of $\pi^+, K^+, p, K^0_S, \Lambda$ and ϕ meson for the 0-5% and 80-90% centrality intervals in Pb+Pb collisions at $\sqrt{s_{NN}}$ = 2.76 TeV measured by ALICE collaboration. Reproduced from Ref. [70].

ordering of the $\langle p_{\mathrm{T}} \rangle$ aligns with the ordering of particle mass, i.e., particles with high masses exhibit a flatter p_{T} distribution, indicating a higher $\langle p_{\mathrm{T}} \rangle$. Specifically, $\Omega^{\pm}$, which has the highest mass, demonstrates the highest $\langle p_{\mathrm{T}} \rangle$ at all multiplicities. Furthermore, a hardening of the p_{T} spectrum for increasing multiplicity is observed, and the same effect is present for all the other particles considered.

2.5.3 Baryon Anomaly

As detailed in the previous section, the transverse momentum spectra of identified particles are sensitive to the radial flow imparted by the collective expansion of the medium. This translates into a shift of the p_{T} spectra towards the higher $\langle p_{\mathrm{T}} \rangle$ values, prominent for massive particles in

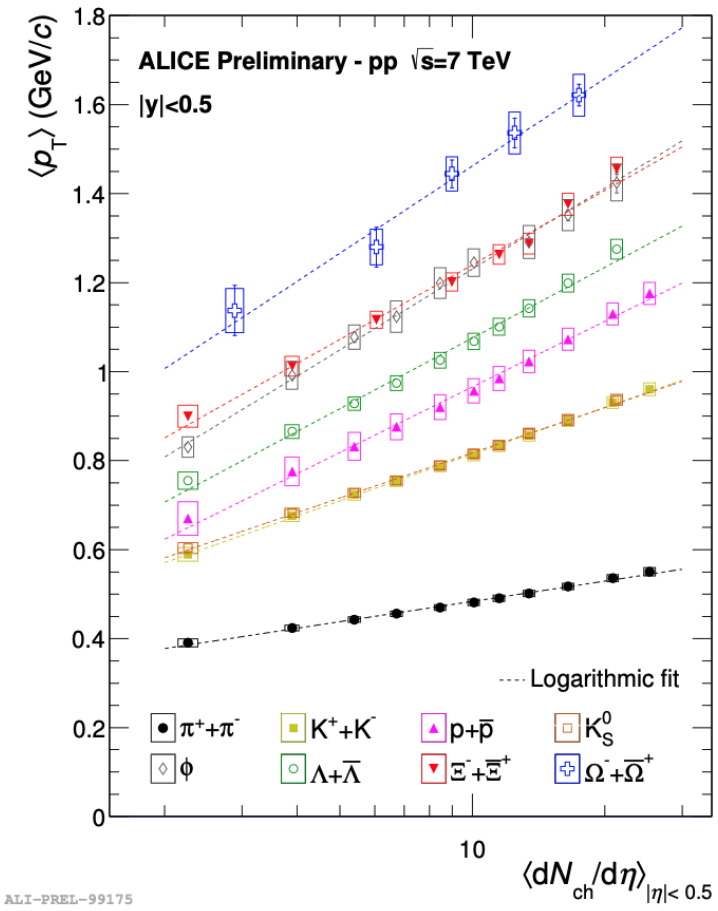

Figure 2.23: $\langle p_{\mathrm{T}} \rangle$ as a function of event multiplicity for various identified particles in pp collisions measured by ALICE collaboration. Reproduced from Ref. [71].

heavy-ion collisions. Specifically, the low-p_{T} range, up to ~ 2 GeV/c, becomes flatter for the most central collisions as observed in Figure 2.22. The effect has been observed in Pb+Pb collisions, and also in small systems like pp and p+Pb collisions. One could wonder if these observations are solely due to the radial expansion of the fluid.

To answer this question, an observable defined as the ratio of the Λ and K^0_{S} p_{T} spectra is actively used in the field. The idea behind the observable is that the momentum boost would be higher for massive hadrons in a radially expanding system, indicating an observation of enhanced baryon-to-meson ratio at intermediate p_{T}, around ~ 2 GeV/c. Figure 2.24 depicts the $(\Lambda + \bar{\Lambda})/K^0_S$ as a function of p_{T} in the highest and lowest multiplicity classes considered in pp, p+Pb, and

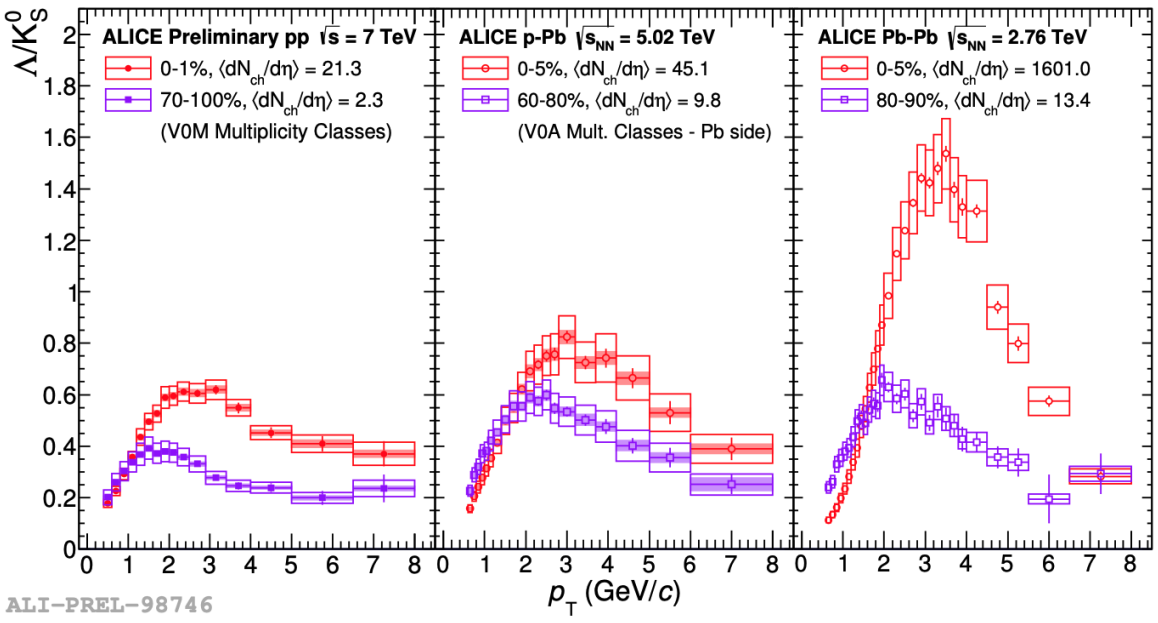

Figure 2.24: $(\Lambda+\bar{\Lambda})/K^0_S$ as a function of p_{T} in the highest and lowest multiplicity classes considered in pp (left), p+Pb (center) and Pb+Pb (right) collisions at $\sqrt{s_{NN}} = 7, 5.02, 2.76$ TeVs respectively. Reproduced from Ref. [71].

Pb+Pb collisions measured by the ALICE collaboration. The baryon-to-meson ratio enhancement is observed at intermediate p_{T} across all collision systems and various centrality ranges. The magnitude of the enhancement is prominent in heavy-ion collisions like Pb+Pb, and decreasing moving towards small systems. Furthermore, the peak of the enhancement shifts towards central collisions, in agreement with the framework of the hydrodynamic expansion of the fluid.

Furthermore, the quark coalescence model has been successful in explaining the baryon-to-meson ratio enhancement in the intermediate p_{T} [72, 73]. In a simple quark coalescence model, the three quarks (qqq) recombine to form a baryon of higher momentum than that of the individual partons, the two quarks ($q, \bar{q}$) recombine to form a meson of higher momentum than that of the individual partons, and the gluons split into quark-antiquark pairs. Therefore, the p_{T} spectra of the final state hadron shifts from lower momentum ($p_{\mathrm{T}} < 2$ GeV/c) to intermediate momentum (p_{T} $\sim$ 2–3 GeV/c), enhancing the production of baryons relative to that of mesons. In addition, there

are contributions from hard processes like fragmentation of minijet partons from higher transverse momentum ($p_{\mathrm{T}} > 3$ GeV/c) to intermediate p_{T} region, adding a very small contribution to the baryon-to-meson ratio enhancement.

2.5.4 Strangeness Enhancement

Strangeness enhancement was the first proposed observable for detecting the presence of QGP, as discussed in references [74, 75]. The production of strange hadrons in high-energy hadronic interactions provides a way to investigate the properties of QCD. Unlike up (u) and down (d) quarks, which constitute ordinary matter, strange (s) quarks are not present as valence quarks in the initial state, yet they are sufficiently light to be abundantly created during the collisions.

In the QGP, strangeness production proceeds mainly via gluons, allowing strangeness to reach equilibrium within the timescale of the formation of the hot-dense matter in a heavy-ion collision. In the early stages of high-energy collisions, strangeness is produced in hard (perturbative) $2 \rightarrow 2$ partonic scattering process by flavor creation ($gg \rightarrow s\bar{s}, q\bar{q} \rightarrow s\bar{s}$) and flavor excitation ($gs \rightarrow gs, qs \rightarrow qs$). Strangeness is also created during the subsequent partonic evolution via gluon splitting ($g \rightarrow s\bar{s}$). These processes tend to dominate the production of high transverse momentum (p_{T}) strange hadrons. At low p_{T}, non-perturbative processes dominate the production of strange hadrons.

Strangeness enhancement is expected in heavy-ion collisions for several reasons: Firstly, the dominance of the gluonic channel for producing strange quarks and the high gluon density in the QGP. In addition, the mass of the s-quark, approximately 150 MeV, is comparable to the critical temperature of the QCD phase transition. This similarity results in the thermal formation of strange particles occurring within the expected lifetime of the QGP. Consequently, an abundant strange quark density is produced, and thus the QGP matter contains u, d, and s quarks, as well as gluons.

The strangeness enhancement is quantified as the ratio of the strange particle yield (K^0_{S}, Λ, Ξ^-, Ω^-) to the pion yield since the average number of charged particles does not scale linearly

with the average number of nucleons participating in the collision. Moreover, these ratios are mostly related to the final-state charged-particle production rather than the collision system or beam energy. In the earlier days, small systems like pp and p+Pb were used as the reference for strangeness enhancement, *i.e.*, the enhancement was measured with respect to the ratio of the yields in pp, assuming the conditions to form QGP was not achieved in these. Following the observation of collectivity in small systems, strangeness enhancement was also observed in pp and p+Pb collisions by the ALICE experimental collaboration at the LHC.

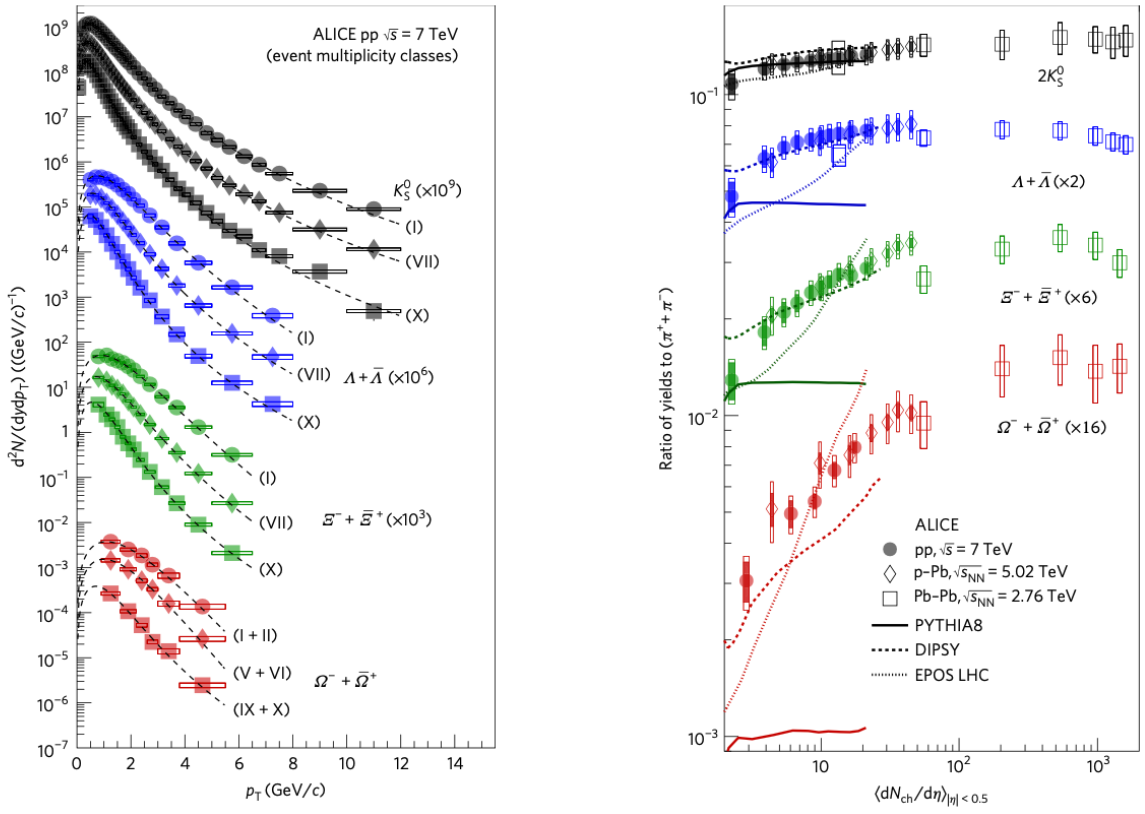

Figure 2.25: (left) p_{T} differential yields of K^0_S, $\Lambda + \bar{\Lambda}$, $\Xi^- + \bar{\Xi}^+$ and $\Omega^- + \bar{\Omega}^+$ measured by ALICE collaboration in pp collisions at $\sqrt{s_{NN}} = 7$ TeV. (right) p_{T} integrated yields ratios to pions ($\pi^+ + \pi^-$) as a function of multiplicity measured by ALICE collaboration in pp, p+Pb, and Pb+Pb collisions at $\sqrt{s_{NN}} = 7, 5.02, 2.76$ TeVs respectively. Reproduced from Ref [11].

Figure 2.25 depicts the p_{T} differential yields of K^0_S, $\Lambda + \bar{\Lambda}$, $\Xi^- + \bar{\Xi}^+$ and $\Omega^- + \bar{\Omega}^+$ and their ratios to pions ($\pi^+ + \pi^-$) measured by the ALICE collaboration [11]. The particle yield ratios to pions increase with multiplicity, and there appears a continuous transition from small systems to heavy-ion collisions. Moreover, the ratio increases steeply for particles with higher strange quark content. For example, the ratio of the triply-strange hadron, $\Omega^{\pm}$, to $\pi^{\pm}$ increases faster with multiplicity compared to other particle ratios. Thus the strangeness enhancement magnitude is proportional to the strangeness content of the hadron. It is largest for triply-strange Ω^- and progressively less evident for doubly strange Ξ^- and for particles with one strange quark (Λ, K^0_S).

Chapter 3

Photo-Nuclear Collisions

When ultra-relativistic beams of heavy-ion beams are brought together into collision, ultra-peripheral collisions (UPCs) are produced when the distance between the two nuclei is larger than the sum of the two radii of the incoming nuclei ($b > 2R$). In these collisions, nuclei interact via a long-range force, either via an electromagnetic interaction or a QCD interaction via the exchange of a colorless state. The physics of ultra-peripheral collisions has gained significant attention in the past few decades, as evidenced by the growing body of review articles listed in the references: [8, 76–79]. This thesis focuses on photo-nuclear (γ+A) collisions, a subset of ultra-peripheral collisions, where the photon emitted by one nucleus interacts with the other incoming nucleus, generally breaking it apart.

In the early days, collider facilities like the Hadron-Electron Ring Accelerator (HERA), the only electron-proton collider to date, were used to understand the structure of hadrons and the behavior of quarks and gluons inside them. Currently, we have hadronic colliders like RHIC and LHC, which collide heavy ions at hundreds of GeV of energy, producing photonuclear and other interactions at luminosities and energies beyond those accessible elsewhere.

The first section below provides an overview of the photon flux involved in these interactions. The subsequent section delves into the various processes associated with ultra-peripheral collisions, namely "one-photon" and "two-photon" processes. Finally, the QGP signatures observed and predicted in photo-nuclear collisions are discussed.

3.1 Photon Flux

The strong electromagnetic (EM) fields of the fully ionized nuclei (i.e., $Z = 82$ for Pb) can induce interactions when the nuclei have significantly large impact parameters [80]. Following the work of Fermi, where the electromagnetic field of a charged particle is treated as a virtual photon, Weizsacker and Williams modeled the electromagnetic field surrounding the ultra-relativistic heavy-ions as a flux of quasi-real, high-energy photons [81, 82]. This is known as the "Equivalent Photon Approximation" (EPA). Under the equivalent photon approximation, the nuclei can produce high-energy photons coherently from the entire nucleus, resulting in an enhancement, proportional to Z^2, to the photon spectrum over a broad energy range.

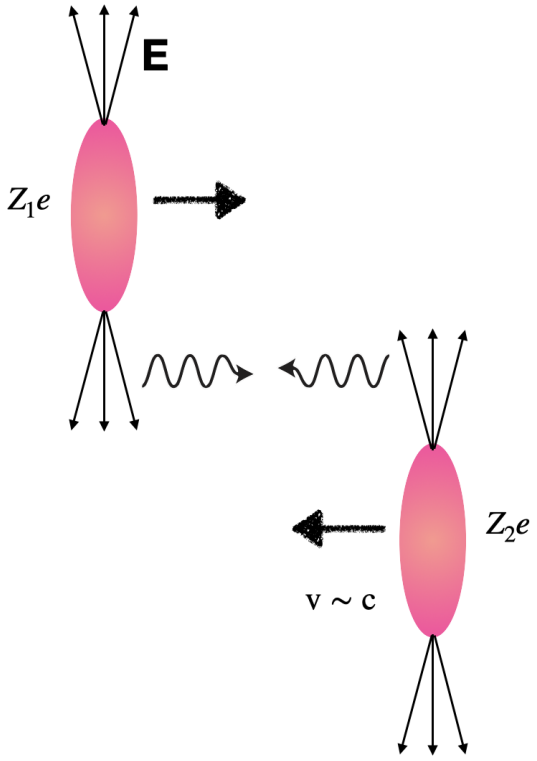

Figure 3.1: Highly energetic charged particles have Lorentz contracted electric fields. The interaction of these fields can be replaced by the interaction of real (or quasi-real) photons.

Figure 3.1 shows the electric field vectors pointing radially outward from Lorentz-contracted

Accelerator	Ions	Max. Energy (CM) per Nucleon pair	Luminosity ($cm^{-2}s^{-1}$)	Max. γp/γA Energy
CERN SPS	Pb+Pb	17 GeV	-	3.1 GeV
RHIC	Au+Au	200 GeV	2.6×10^{26}	24 GeV
RHIC	p+p	500 GeV	6×10^{30}	79 GeV
LHC	Pb+Pb	5.6 TeV	10^{27}	705 GeV
LHC	p+p	14 TeV	10^{34}	3.1 TeV

Table 3.1: A selection of ion species, maximum energy, luminosity for several accelerators, and maximum effective γA energies. The CERN SPS is a fixed target accelerator; the effective luminosity depends on the target thickness. Not mentioned here are lower-energy accelerators, where photon exchange processes have also been studied. Reproduced from Ref. [8].

nuclei in a heavy-ion collision. The maximum photon energy is given as:

$$\omega = \frac{\hbar}{\Delta t} \sim \frac{\gamma \hbar v}{b}, \tag{3.1}$$

where Δt is the interaction time, b is the impact parameter and γ is the Lorentz boost of the ion. In the case of a peripheral collision, where nuclei can barely touch, $b = 2R_{\mathrm{A}}$, where R_{A} is the nuclear radius. At the LHC in top-energy pp collisions, UPCs reach γp center of mass energies of 3 TeV, i.e., ten times higher than those available at HERA and 30 times higher than those available at fixed target experiments at accelerators like CERN SPS. Refer to Table 3.1 for a comparison of the maximum γA or γp energies achieved in various accelerators using different ion species.

The flux of equivalent (or virtual) photons per unit area is determined from the Fourier transform of the electromagnetic field:

$$N(\omega, b) = \frac{Z^2 \alpha \omega^2}{\pi^2 \gamma^2 \hbar^2 v^2} \left(K_1^2(x) + \frac{1}{\gamma^2} K_0^2(x) \right), \tag{3.2}$$

where $x = \omega b / \gamma \beta \hbar c$, $\alpha = 1/137$, and K_0 and K_1 are modified Bessel functions. The first term ($K_1^2(x)$) gives the flux of photons transversely polarized to the ion direction, and the second is the flux for longitudinally polarized photons. The longitudinal term is negligible since we are dealing with ultra-relativistic particles ($\gamma \gg 1$).

The photon flux induced by a point charge, $n(\omega)$, is obtained by integrating Equation 3.2:

$$n(\omega) = \int N(\omega, b) d^2 b. \tag{3.3}$$

In the case of photo-nuclear processes, where one photon interacts with the other nucleus, the impact parameter $b > b_{\min} = 2R_{\mathrm{A}}$. The photon flux in such collisions $n(\omega)$ is given by integrating Equation 3.2 over the range, $b > b_{\min} = 2R_{\mathrm{A}}$, yielding

$$n(\omega, b) = \frac{2Z^2\alpha}{\pi\beta^2}\left[\zeta K_0(\zeta)K_1(\zeta) - \frac{\zeta^2}{2}(K_1^2(\zeta) - K_0^2(\zeta))\right], \tag{3.4}$$

where $\zeta = \omega b_{\min}/\gamma\beta\hbar c = 2\omega R_{\mathrm{A}}/\gamma\beta\hbar c$.

Finally, the cross-section of photoproduction is given as:

$$\sigma_X = \int d\omega \frac{n(\omega)}{\omega}\sigma_X^{\gamma}(\omega), \tag{3.5}$$

where $n(\omega)$ is the photon flux described previously, and $\sigma_X^{\gamma}(\omega)$ is the photonuclear cross section at that specific photon energy. One has to be careful to remember that the total γ+A cross-section in UPCs is a convolution over the cross-section of the entire photon energy range, which has a changing flux.

3.2 Ultra-Peripheral Collisions

In the previous section, we detailed the flux of photons equivalent to the electromagnetic fields from a fast particle. This section delves into the various processes through which photons can interact with other nuclei or with photons themselves.

Ultra-peripheral collisions, in general, encompass two distinct types of interactions: 1) two-photon processes and 2) one-photon interactions. Two-photon interactions occur when high-energy photons from the electromagnetic fields of each nucleus interact with each other. One-photon interactions, or in other words, photo-nuclear processes, occur in various ways, primarily involving the fluctuation of the photon into a vector meson, which then interacts with the nucleus.

3.2.1 Two-Photon Processes

The photon-photon or "two-photon" interactions primarily include exclusive dilepton production with only two oppositely-charged leptons in the final state and light-by-light scattering, where

the two photons interact through a box diagram, and only two photons are emitted in the final state, as depicted in Figure 3.2. ATLAS has measured UPC events where the basic interactions are photon-photon collisions [83–85], including light-by-light scattering and scattering where two leptons in the final state are produced.

The cross-section for two-photon processes is

$$\sigma_X = \int d\omega_1 \omega_2 \frac{n(\omega_1)}{\omega_1} \frac{n(\omega_2)}{\omega_2} \sigma_X^{\gamma\gamma}(\omega_1, \omega_2), \tag{3.6}$$

where $\sigma_X^{\gamma\gamma}(\omega_1, \omega_2)$ is the two-photon cross section.

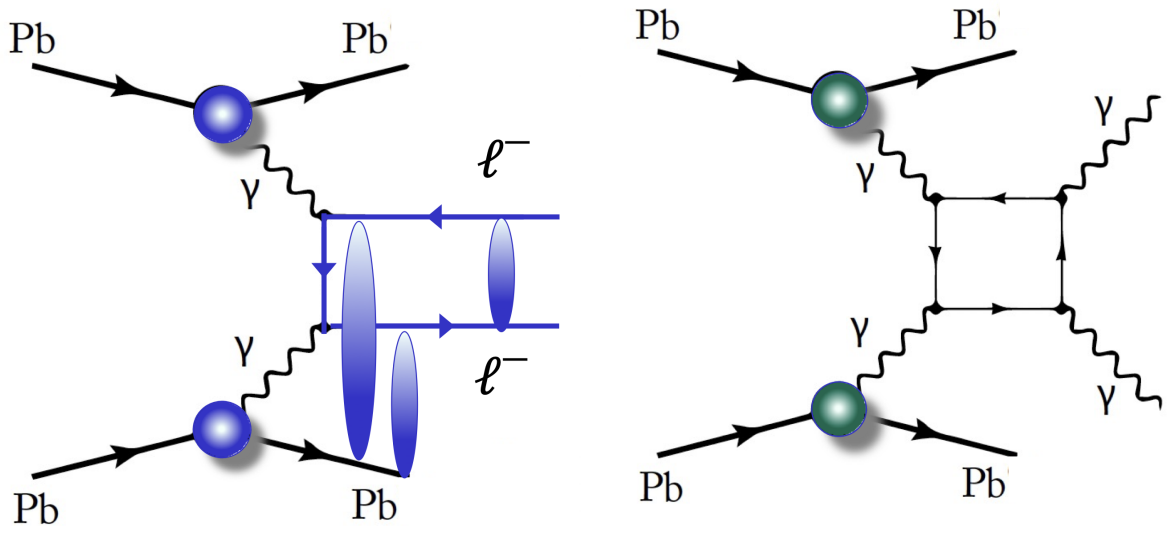

Figure 3.2: (a) Lepton-antilepton pair production in UPCs. The blobs represent possible higher-order processes. (b) Feynman diagram for light-by-light scattering in UPCs. Reproduced from Ref. [79].

Dilepton production was initially proposed to study QED processes in detail. When Fermi predicted the existence of the positron, appearing as a "hole" in the "vacuum sea" of electrons, the only way to confirm these was in UPCs with cosmic rays with large kinetic energies, E. Assuming that the energy of the produced pairs is much larger than the electron rest mass, m_e, all theoretical predictions yield a production cross section to leading order equal to $Z_1^2 Z_2 \alpha^2 \ln^3 \gamma$, where the Lorentz factor is $\gamma \simeq E/m_e$. Current experiments at the LHC measure the fundamental pair-

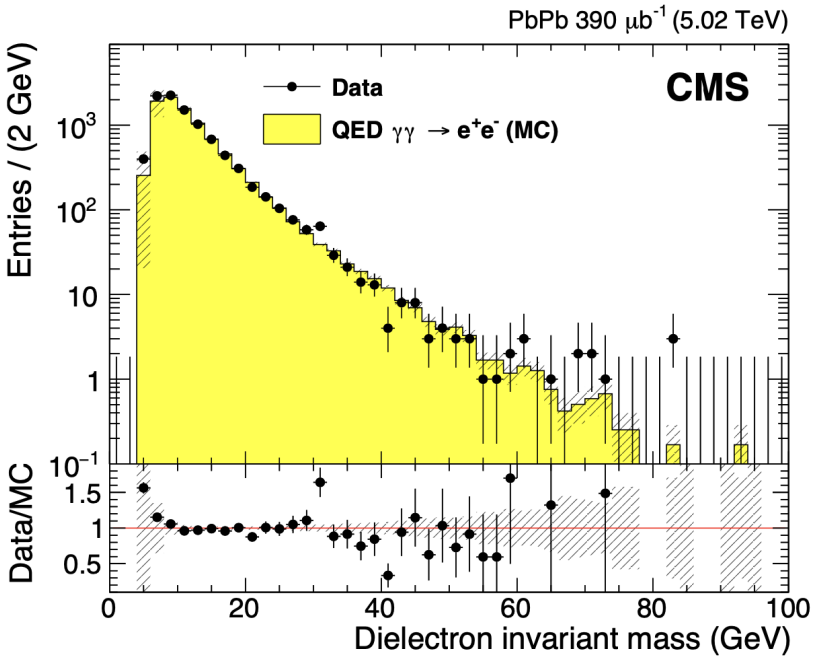

Figure 3.3: UPC production of e^+e^- pairs as observed in the CMS detector at the LHC, compared to STARLIGHT MC. Reproduced from Ref. [86].

production cross sections initially calculated in the 1930s, including $\gamma + \gamma \to e^+ + e^-$, $\gamma + \gamma \to \mu^+ + \mu^-$, $\gamma + \gamma \to \tau^+ + \tau^-$, and others. These processes are now predominantly understood theoretically [86], as depicted in Figure 3.3, where QED theoretical calculations align well with the experimental data.

Light-by-light (LbL) scattering, $\gamma + \gamma \to \gamma + \gamma$, is a fundamental QED process involving contributions from charged fermions (leptons+quarks) and $W^{\pm}$ bosons. The LbL process can be experimentally observed in UPCs, exploiting the very large fluxes of quasi-real photons emitted by the nuclei accelerated at TeV energies. The first proposal to observe this phenomenon was to detect the process $Z_1 + Z_2 \to Z_1 + Z_2 + \gamma + \gamma$ in UPCs [87]. In this process, two virtual photons scatter through a box diagram, resulting in the production of two real photons. This process was successfully observed in a 2017 experiment at the Large Hadron Collider (LHC) by the ATLAS Collaboration [84], as illustrated in Figure 3.4. Such an observation not only validates theoretical predictions but also paves the way for exploring physics beyond the Standard Model (SM). A

measured cross-section larger than that predicted by the SM model [88] could potentially indicate the presence of new particles, such as axions [89, 90].

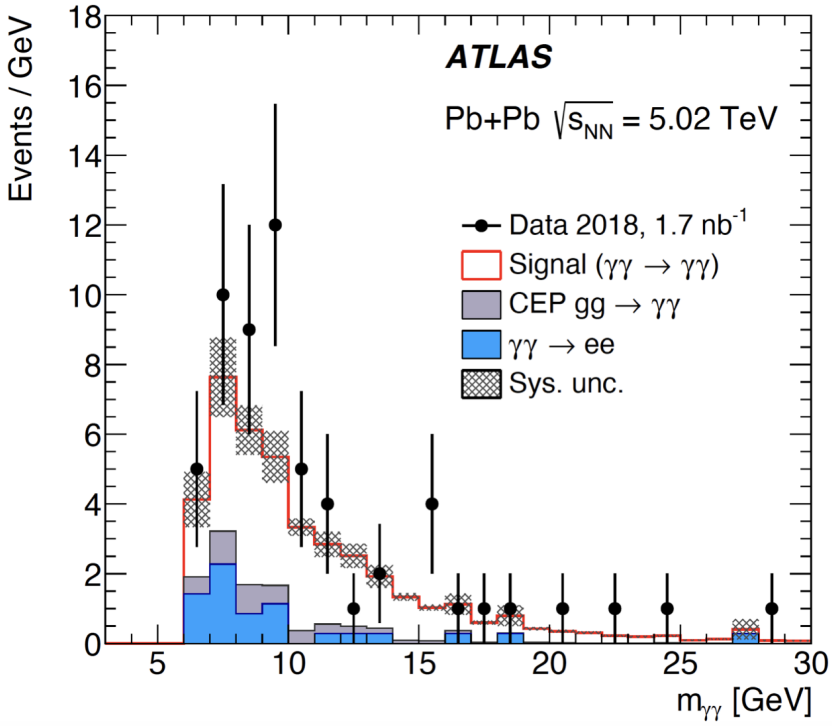

Figure 3.4: Light-by-light scattering events observed in UPCs at the ATLAS detector at the LHC. Reproduced from Ref. [84].

3.2.2 One-Photon Processes

One-photon processes are extensively studied and are the most common interactions in ultra-relativistic heavy-ion collisions. These processes can be broadly categorized into three groups: low-energy photon exchange, exclusive and diffractive vector meson production, and inclusive and non-diffractive photonuclear collisions. For information on other processes, such as heavy-quarkonium production, dijets, vector boson production, multiple interactions between single ion pairs, etc., please refer to Ref. [91–95].

The first one-photon process, the low energy photon exchange, primarily involves exciting the giant dipole resonance (GDR) in nuclei, occurring at 10-20 MeV [96, 97]. The strong electro-

magnetic fields generated by the collisions of heavy ions provide energy to the nucleus, causing the collective oscillation of all protons against all neutrons within the nucleus. Treating this oscillation theoretically as harmonic, with excitation energy $\hbar\omega$, one then has these higher excitation modes with energies $N\hbar\omega$ also occur, known as double [98], triple, and so forth, giant dipole resonances.

The second one-photon process is the exclusive and diffractive vector meson production [99, 100]. Compared to other mesons (scalar and pseudo-scalar), vector mesons can be measured with very high precision simply because they have the same quantum numbers as the photon. The exclusive particle production in photon-hadron or photon-nucleus interactions occurs when the protons or nuclei remain in their ground state or are only internally excited, dominated by the production of vector mesons:

$$A + A \rightarrow A + A + V. \tag{3.7}$$

In these reactions, a photon from the electromagnetic field of one of the projectiles interacts coherently with the nuclear field of the other (target), producing the vector meson.

Using Equation 3.5 one can calculate the total vector meson cross-section in p+p or A+A interactions, by differentiating and changing the variable ω to y, the rapidity of the produced vector meson:

$$\frac{d\sigma(A + A \rightarrow A + A + V)}{dy} = n(\omega)\sigma_{\gamma A \rightarrow V A}. \tag{3.8}$$

Here the photon energy ω is related to the final state mass M_V and rapidity y, via:

$$\omega = \frac{M_V c^2}{2} \exp(\pm y). \tag{3.9}$$

The $\pm$ sign reflects the two-fold ambiguity as to which nucleus emits the photon and which is the target.

Next, we focus on the diffractive production of vector mesons. Diffractive processes are defined by the exchange of a gluonic system, sometimes called a *pomeron*, which transfers no quantum numbers, i.e., no net color exchange, between the two interacting particles. The pomerons can cause one of the incoming particles to fragment or undergo a process of excitation and then

decay (single diffraction), or both incoming particles can fragment (double diffraction) or create pomeron-pomeron collision (central diffraction).

The significant interest in vector meson production originates from its potential for the direct determination of the gluon distribution in nucleons and nuclei. Unlike in deep-inelastic scattering, where gluons cannot be accessed directly due to their lack of electrical or weak charge, vector meson production provides a unique opportunity to probe gluon distributions.

The nuclear gluon density, $G^A(x, Q^2)$, as a first approximation, can be written as the nucleon gluon density $g(x, Q^2)$, multiplied by the number of nucleons (A) [101]:

$$G^A(x, Q^2) = Ag(x, Q^2), \tag{3.10}$$

where x is the fraction of the target momentum carried by the gluon, and Q^2 is the 4-momentum transfer squared.

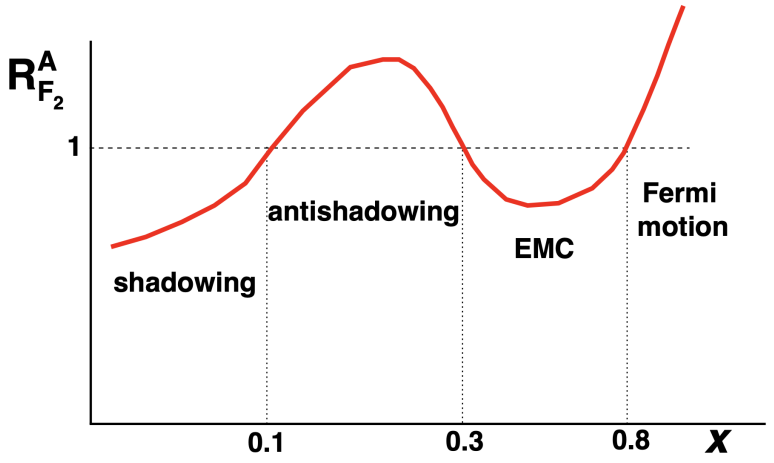

Figure 3.5: Cold nuclear medium modification function displaying numerous effects as a function of the momentum fraction x for a given fixed Q^2. Reproduced from Ref. [102].

The nuclear ratio is defined as the nuclear structure function, $F_2(x, Q^2)$, per nucleon divided by the nucleon structure function [102]:

$$R^A_{F_2}(x, Q^2) = \frac{F_2^A(x, Q^2)}{AF_2^{\text{nucleon}}(x, Q^2)}. \tag{3.11}$$

The behavior of $R_{F_2}^A(x, Q^2)$ as a function of x for a given fixed Q^2 is shown schematically in Figure 3.5. It can be divided into four regions:

- $R_{F_2}^A(x, Q^2) > 1$ for $x > 0.8$: the Fermi motion region
- $R_{F_2}^A(x, Q^2) < 1$ for $0.3 < x < 0.8$: the EMC region (EMC stands for European Muon Collaboration)
- $R_{F_2}^A(x, Q^2) > 1$ for $0.1 < x < 0.3$: the antishadowing region
- $R_{F_2}^A(x, Q^2) < 1$ for $x < 0.1$: the shadowing region

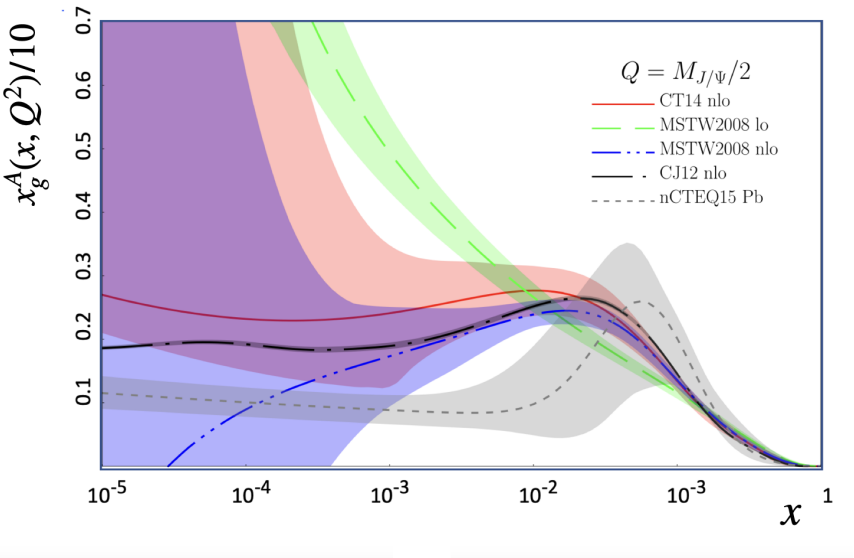

Figure 3.6: Uncertainties in theoretical compilations of gluon distribution functions. Reproduced from Ref. [79].

Depending on the value of x and Q^2, suppression (or shadowing) up to 30% and enhancement (or anti-shadowing) up to $\sim$ 10% has been observed from the results of deep inelastic scattering measurements. Figure 3.6 shows that the theoretical predictions of gluon distribution functions are largely uncertain within the nucleus, specifically at small x [79]. Exclusive vector-meson production, such as J/Ψ, at heavy-ion collisions is a powerful tool to study gluon shadowing in the region $x < 10^{-3}$.

Cross-sections have been measured for vector mesons like ρ, ω, J/Ψ, and Υ states. Figure 3.7 shows the J/Ψ cross-sections as a function of photon energy, W [103]. The LHCb data ($\sqrt{s} = 13$ TeV and $\sqrt{s} = 7$ TeV) are in good agreement with the H1 [104], ZEUS [105], and ALICE [106] results. Figure 3.7 also shows the power law fit to H1 data, and it can be seen that this is insufficient to describe the J/Ψ data at the highest energies ($W > 1$ GeV). In contrast, the data is in good agreement with the JMRT prediction, which takes account of most of the NLO QCD effects and deviates from a simple power-law shape at high W.

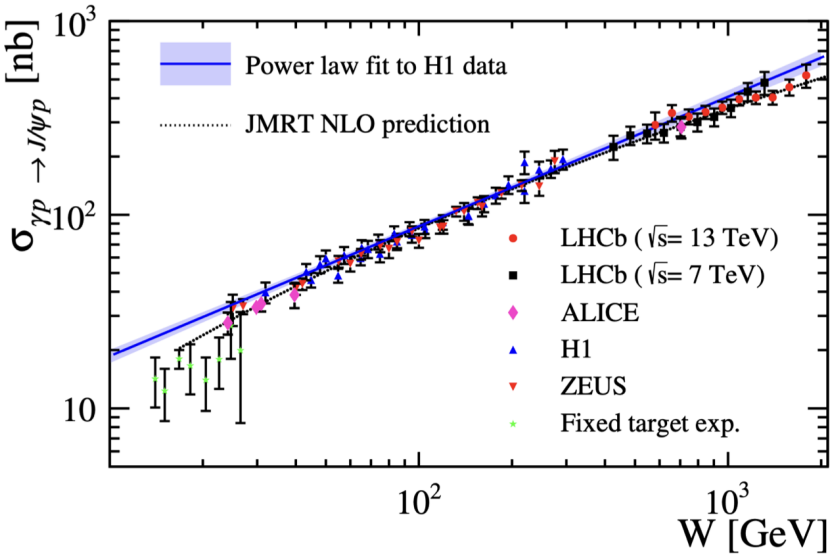

Figure 3.7: Compilation of cross sections for UPC production of J/Ψ in different nuclear facilities. Reproduced from Ref. [103].

The third single-photon process, the non-diffractive photo-nuclear collision, is the most relevant to the content of this thesis. This kind of interaction remains relatively unexplored to date. ATLAS has measured UPC photo-nuclear collisions, such as in the case of dijet production [93] and two-particle azimuthal correlations [10]. This thesis aims to delve into the characterization of non-diffractive photo-nuclear collisions, such as exploring the basic kinematic distribution of inclusive charged particles as a function of transverse momentum and pseudorapidity.

Event topologies are crucial in selecting non-diffractive photo-nuclear interactions. When a

photon undergoes non-diffractive interactions by forming QCD color strings, these strings fragment, leading to particle production across the rapidity space in the Pb-going direction. Conversely, diffractive interactions involve no exchange of colors, causing large gaps in the produced particles along the entire rapidity direction. The various types of interactions have distinct event topologies, with "rapidity gaps" serving as a significant factor in their selection [107].

Furthermore, there are contributions from non-diffractive hadronic Pb + Pb collisions, where the two nuclei interact via QCD, and their impact parameter is less than twice their radii ($b < 2R$). This background contribution is predominantly "peripheral" collisions where the impact parameter is slightly smaller than $b = 2R$. Some of these collisions can be non-diffractive, leading to particle production across the rapidity space with no rapidity gaps. However, one can get gaps just from fluctuations in the particle production, so low-multiplicity Pb+Pb collisions do show up as a background even with the rapidity gap selection. To eliminate most of these contributions, experimental collaborations use a large acceptance detector to implement the requirement of a single-sided nuclear breakup, labeled as "0nXn" or "Xn0n", where "Xn" corresponds to multiple neutrons emitted from the nuclear breakup and "0n" indicates that the nuclei stay intact without breaking up. This criterion is implemented for photo-nuclear interactions, as the non-diffractive hadronic Pb + Pb collisions result in a double-sided nuclear breakup, labeled as "XnXn".

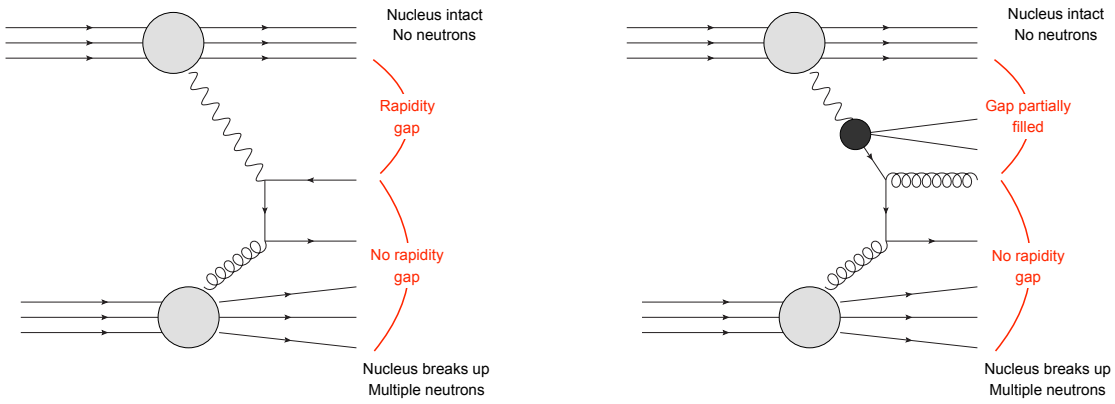

Figure 3.8: Diagrams representing different types of photo-nuclear collisions and the general features of their event topologies. Reproduced from Ref. [10].

As detailed below, the inclusive photo-nuclear collisions consist of three event classes stemming from the three possible photon states, "direct", "resolved", and "anomalous".

- Direct: The photon could act as a point-like particle and interact directly with a parton in the oncoming nucleus. There is a large rapidity gap observed in the γ-going direction. This is shown in the left diagram of Figure 3.8.

- Resolved: The photon fluctuates to a vector meson state (ρ, ω, or ϕ) and interacts hadronically with the oncoming nucleus. In the case of non-diffractive scattering, a partially filled rapidity gap is observed in the γ-going direction. This is shown in the right diagram of Figure 3.8.

- Anomalous: Photon fluctuates to a $q\bar{q}$ pair at higher virtuality, Q^2, resulting in higher-p_{T} final states. These types of interactions are very similar to the resolved case.

The photo-nuclear interactions are dominated by the contribution of resolved processes, resembling inelastic hadron-nucleon/nucleus collisions (e.g., p+Pb collisions). Moreover, there have been interesting predictions on the anisotropic flow hierarchy between γ+Pb and p+Pb collisions from a final-state-dominated theoretical framework [61]. This thesis includes a comparison of results from photo-nuclear collisions with those from p+Pb collisions.

3.3 QGP Signatures

As outlined in Section 2.5, numerous striking features of QGP, such as collective expansion, have been observed in very small collision systems, such as p+Au, d+Au, ^{3}He+Au at RHIC and pp and p+Pb collisions at the LHC. The small sizes of these collision systems push the limit of the applicability of causal relativistic viscous hydrodynamic descriptions [108, 109]. Consequently, the question arises about the presence of QGP-like signals in photo-nuclear collisions. In general, photo-nuclear collisions encounter challenges in the theoretical modeling due to their extreme asymmetry, resulting in significant violation of boost invariance [110, 111]. Resolving these challenges would

bring new exciting opportunities to study collectivity in small systems at the upcoming Electron-Ion Collider, where one has experimental control over the virtuality of the colliding photon and can use it as a dial to change the dipole size and thus the collision system size. This section details the QGP signatures found in photo-nuclear collisions, such as collective flow, and the predicted QGP signature in such collisions, such as radial flow, while outlining future directions.

3.3.1 Collective Flow

The ATLAS Collaboration has recently reported intriguing results on two-particle azimuthal correlations in photo-nuclear collisions [10]. These findings suggest the persistence of collective phenomena, with the strength of correlations comparable to those observed in proton-proton and proton-lead collisions within similar multiplicity ranges, as illustrated in Figure 3.9.

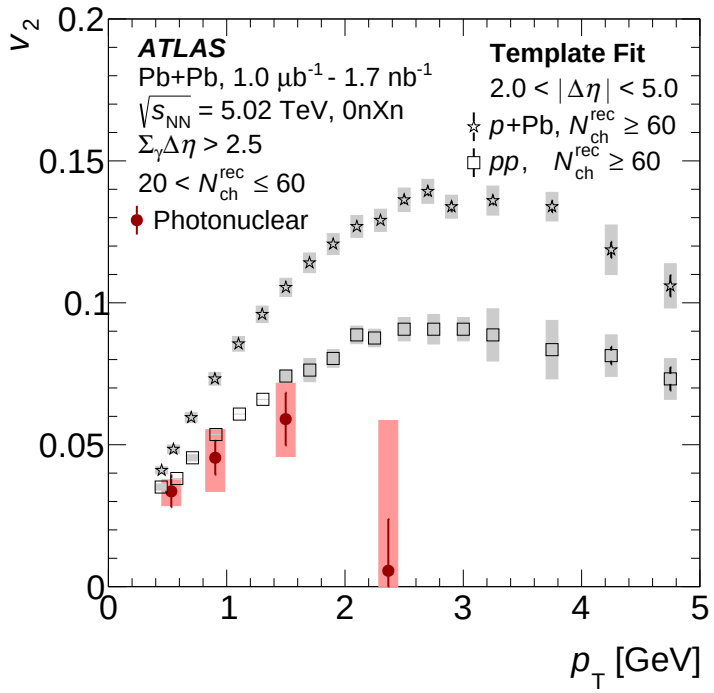

Figure 3.9: The p_T differential elliptic flow coefficient ($v_2(p_T)$) of charged hadrons in γ+Pb collisions are compared p+Pb and pp collision data from ATLAS Collaboration. Reproduced from Ref. [10].

Recently, a new implementation of the so-called "hybrid" model enables hydrodynamic calculations for both γ+Pb collisions and p+Pb collisions [61]. The hybrid model incorporates initial

conditions via an extension of Monte Carlo Glauber to three dimensions, time evolution via viscous hydrodynamics using the publicly available package MUSIC, and finally, hadronic scattering via the publicly available package URQMD [112]. This model describes collective signatures in γ+Pb collisions and provides the first quantitative prediction of the anisotropic flow, v_n, hierarchy between γ+Pb and p+Pb collisions from the final-state-dominated theoretical framework. This holds particular significance as it addresses whether γ+Pb collisions behave like inelastic hadron-nucleus collisions (p+Pb). This assumption is based on the concept that photo-nuclear collisions are dominated by "resolved interactions", where the photon fluctuates to a vector meson like ρ, ω, or ϕ. This exploration opens new avenues for understanding the dynamics of particle production in photo-nuclear collisions.

In the model, the virtual photon is treated as a vector meson, with a lifetime longer than the time of interactions in the low virtuality regime, $Q^2 \sim \Lambda^2_{QCD} - 1$ GeV^2 [113]. The photon-nucleus interaction proceeds as a vector meson-nucleus collision at an energy lower than that of the associated nucleus-nucleus collisions. Considering the fluctuating event-by-event kinematics of photon-nucleus collisions with the probability distribution of the center-of-mass collision energy [76]:

$$P(\sqrt{s_{\gamma N}}) \propto \frac{1}{s_{\gamma N}} \left(w_R^{AA} K_0(w_R^{AA} K_1(w_R^{AA})) - \frac{(w_R^{AA})^2}{2} \left[K_1^2(w_R^{AA}) - K_0^2(w_R^{AA}) \right] \right), \tag{3.12}$$

where $w_R^{AA} = 2kR_A/\gamma_L$ and $k = s_{\gamma N}/(2\sqrt{s_{NN}})$ and $\gamma_L = \sqrt{s_{NN}}/2m_N$. For the Pb nuclei, Woods–Saxon radius, $R_A = 6.62$ fm is used, and $K_0(w)$ and $K_1(w)$ are the modified Bessel functions. The energy of these collisions ranges from 0 to ~894 GeV, corresponding to the $\sqrt{s_{NN}} = 5.02$ TeV collisions at LHC. The model calculation uses a low virtuality of $Q^2 = 0.0625$ GeV^2.

Figure 3.10 represents the p_{T} differential elliptic flow coefficient $v_2(p_{\mathrm{T}})$ of charged hadrons in γ+Pb collisions from the 3D-GLAUBER + MUSIC + URQMD simulations. The results, obtained with various photon virtualities, are compared to ATLAS data. It is important to highlight the sensitivity of v_2 to the incoming photon's virtuality Q^2, or, in other words, to the vector meson size, given that Q^2 is inversely proportional to the vector meson size. The default value of $Q^2 = 0.0625$ GeV^2 corresponds to a vector meson size of 0.8 fm. In the photo-nuclear collisions at LHC, the

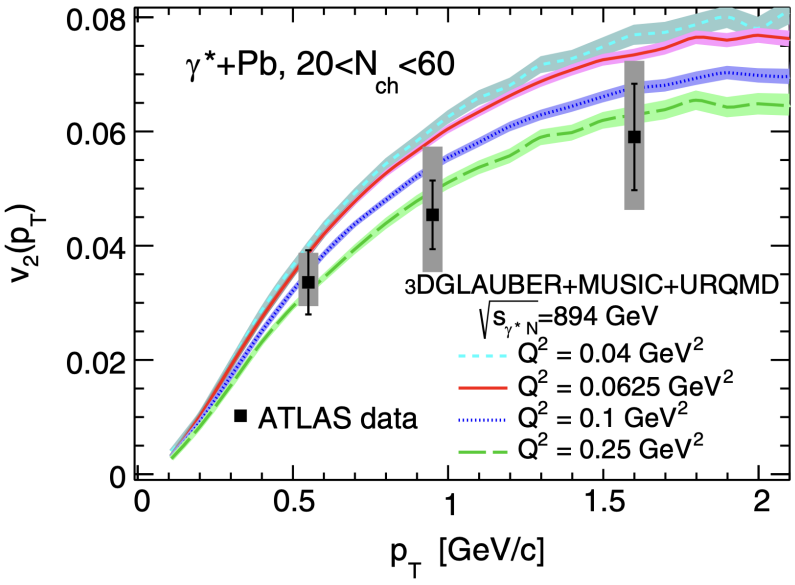

Figure 3.10: The p_{T} differential elliptic flow coefficient $v_2(p_{\mathrm{T}})$ of charged hadrons in γ+Pb collisions from the 3D-GLAUBER + MUSIC + URQMD simulations with different photon virtualities are compared to the ATLAS data. Reproduced from Ref. [61]

virtuality of the incoming photon, Q^2, fluctuates from event to event. Therefore, to understand the dependence of flow coefficients on Q^2, the p_{T} differential v_2 is examined over a range of Q^2, ranging from 0.04 GeV^2 to 0.25 GeV^2. The figure illustrates that the vector mesons with large virtuality result in a smaller value of v_2 since there is less transverse space for the geometry to fluctuate and the average ellipticities are smaller.

However, the color glass condensate (CGC) framework, which stems from initial-state interactions, provides an opposite observation, where v_2 increases with increasing Q^2, as depicted in Figure 3.11 [113, 114]. The explanation is that, as Q increases, the system size decreases, leading to a higher probability of the two particles (trigger and reference particle entering v_2 calculation) scattering within the same color domain of size $1/Q_s$, where Q_s is the saturation momentum. One then expects the v_2 to increase with increasing Q/Q_s ratio since CGC correlations predominantly occur within a color domain. Future experiments at an Electron-Ion Collider, providing direct access to the photon's virtuality, offer the opportunity to test the hydrodynamic framework predictions as well as CGC predictions by measuring elliptic anisotropies for different photon virtualities.

Furthermore, EIC can serve as a "tie-breaker" between the initial-state (CGC) and final-state (hydrodynamic) frameworks.

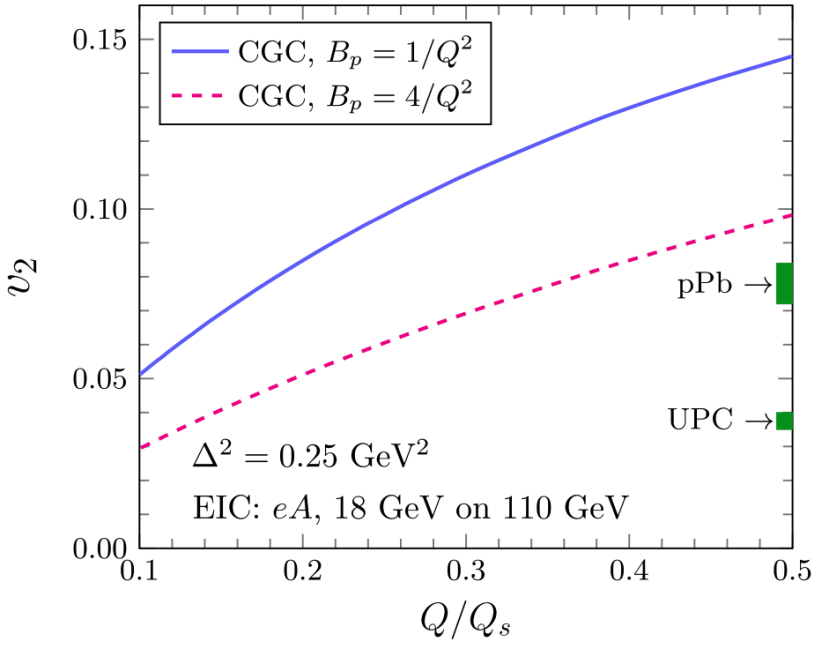

Figure 3.11: The CGC prediction for integrated v_2 in the EIC regime. Also shown are those observed in Pb+Pb UPC and p+Pb collisions at LHC. Reproduced from Ref. [113]

Figure 3.12 illustrates the multiplicity dependence of anisotropic flow coefficients v_2 and v_3 in γ+Pb collisions [10] at LHC energy compared p+Pb collisions [115] and 3D-GLAUBER + MUSIC + URQMD simulations. The lower elliptic flow in γ+Pb events is explained through the stronger longitudinal decorrelations observed in the rapidity-shifted γ+Pb events. This emphasizes that the longitudinal structure plays a more significant role in generating final state momentum anisotropies compared to the contribution of the initial state spatial anisotropy in the transverse plane. The authors of the referred paper make a specific prediction that the actual "flow" of the medium is similar in magnitude between the systems and the hierarchy of collective flow is observed only due to the longitudinal dynamics.

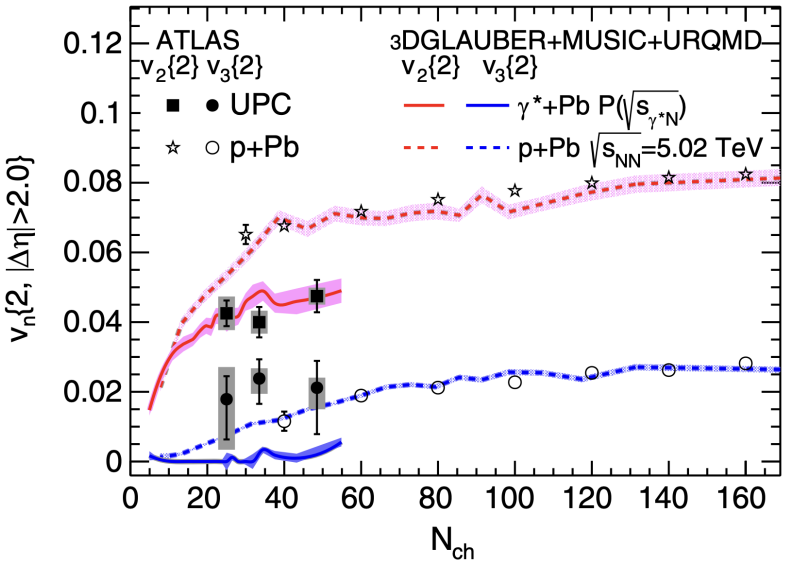

Figure 3.12: Charged hadron anisotropic flow coefficients v_2 and v_3 as functions of charged hadron multiplicity N_{ch} in p+Pb collisions (dashed lines) and γ+Pb (solid lines) collisions at LHC energy from 3D-GLAUBER + MUSIC + URQMD simulations, compared to ATLAS data. Reproduced from Ref. [61].

3.3.2 Radial Flow

Radial flow is quantified by the mean value of the transverse momenta distribution of particles, as detailed in Section 2.5.2. Following from the previous section, the authors of the hydrodynamic model propose that the actual "flow" of the medium, denoting the hydrodynamic translation of initial state spatial anisotropy in the transverse plane, remains essentially the same in γ+Pb and p+Pb collisions. In other words, radial flow, as measured via the mean p_{T} of particles, should be of similar quantity for both systems.

Figure 3.13 represents the mean transverse momenta, $\langle p_{\text{T}} \rangle$, of identified particles such as π, K, and p as functions of charged hadron multiplicity in p+Pb collisions from the ALICE collaboration [116]. This data is compared to model predictions in γ+Pb and p+Pb collisions. The model predictions suggest that the identified particles' $\langle p_{\text{T}} \rangle$ measured in γ+Pb collisions should be very similar to those in p+Pb collisions. This thesis focuses on providing experimental data for the $\langle p_{\text{T}} \rangle$ of charged hadrons, and an experimental confirmation would strongly indicate that γ+Pb

behaves like a hadron-nucleus interaction (p+Pb), experiencing strong final state effects. Additionally, this thesis provides $\langle p_{\mathrm{T}} \rangle$ values for identified particles such as K^0_{S}, Λ, and Ξ^-, as heavier particles are more sensitive to the effects of radial flow, along with other signatures of QGP such as baryon/meson enhancement [12], as detailed in Section 2.5.3 and strangeness enhancement [11], as elaborated in Section 2.5.4.

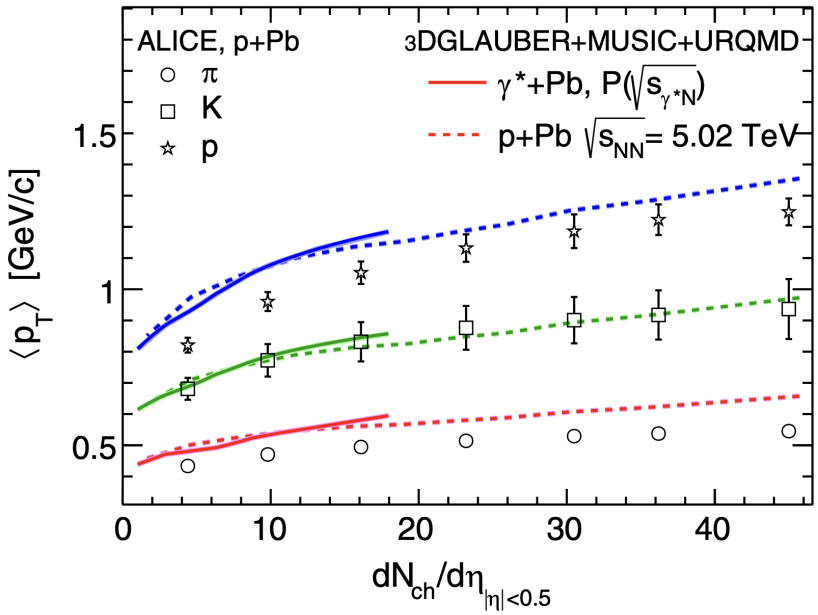

Figure 3.13: $\langle p_{\mathrm{T}} \rangle$ as a function of event multiplicity for various identified particles, $\pi^{\pm}$, $K^{\pm}$, and $p^{\pm}$, in p+Pb collisions measured by ALICE collaboration compared to hydrodynamic simulations. Reproduced from Ref. [61].

Chapter 4

The ATLAS Experiment at the Large Hadron Collider

Technological advancements are inevitable when it comes to understanding the fundamental mysteries of the universe. The Large Hadron Collider, the most powerful particle accelerator ever built, attempts to mimic the extreme conditions, i.e., temperatures and densities, that existed at the beginning of the universe by smashing hadrons together at near the speed of light. Several experiments at the collider facility have their detectors situated around the collision points, and they analyze the particles produced by these collisions. The analyses presented in this thesis utilize the data recorded by the ATLAS experiment. This chapter presents an overview of the Large Hadron Collider and the ATLAS experiment.

4.1 The Large Hadron Collider

The Large Hadron Collider (LHC) [117] consists of a 26.7 km ring of superconducting magnets with several accelerating structures that boost the energy of the particles along the way. The accelerator sits in a tunnel 100 meters underground at CERN, the European Organization for Nuclear Research, on the Franco-Swiss border near Geneva, Switzerland. This tunnel was constructed between 1984 and 1989 specifically for the Large Electron-Positron collider [118]. The LHC is built to explore the fundamental nature of particles and their interactions and to answer the open questions in particle physics and nuclear physics. The recent discovery of the Higgs boson at CERN confirmed the Brout-Englert-Higgs mechanism, which explains how fundamental particles gain mass [119, 120]. Ongoing investigations at LHC include searches for supersymmetry, dark

matter, and dark energy. LHC has been successfully probing the properties of QGP, the "fireball" of hot and dense matter created just after the Big Bang, particularly relevant to the content of this thesis.

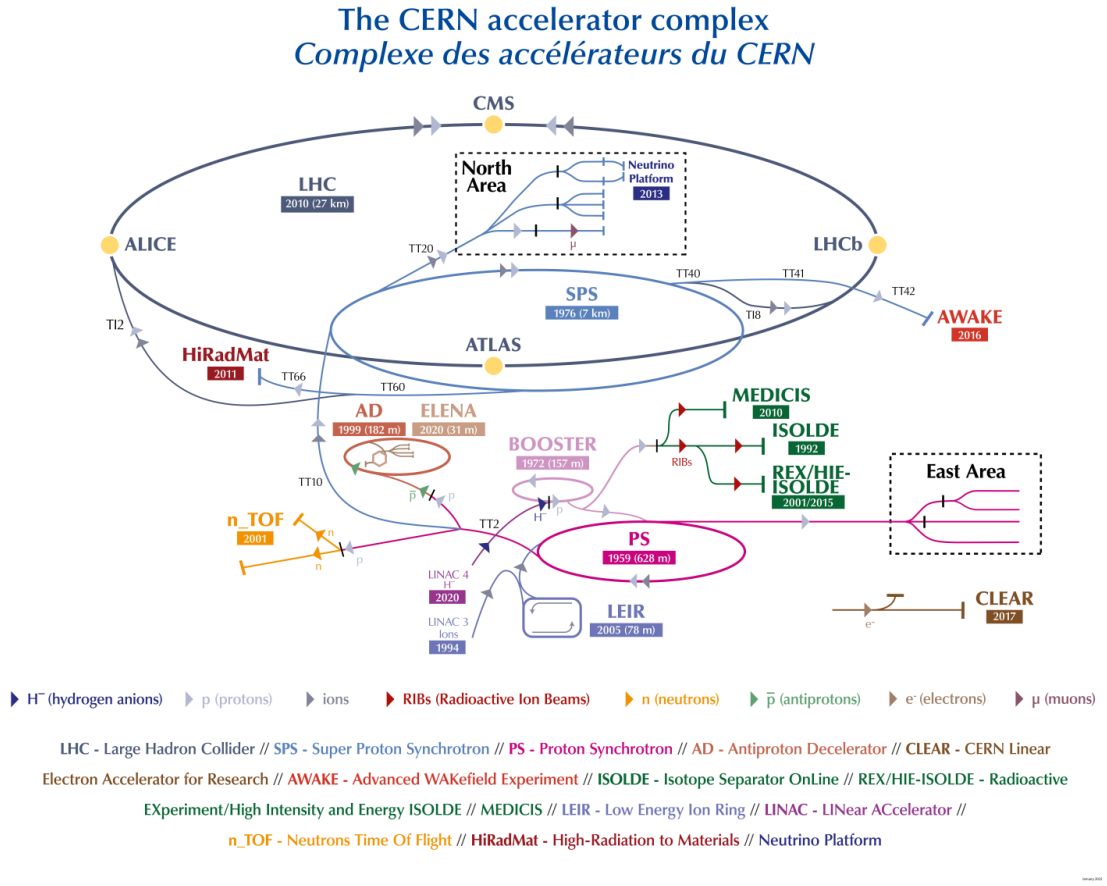

Figure 4.1: Overview of the CERN accelerator complex: Heavy-ion beams are injected to the LHC via LINAC3 → LEIR → PS → SPS → LHC sequence. Reproduced from Ref. [121].

The LHC is a part of the CERN accelerator complex, consisting of a complex succession of machines with increasing energies, as illustrated in Figure 4.1. Each machine accelerates a beam of particles to a specific energy before injecting the beam into the next machine in the chain. The next machine in the chain accelerates the beam to even higher energy, leading eventually to the LHC, the last machine in this chain, where beams reach their highest energies. The source of protons is simply a bottle of H_2, fired through a cavity, where the electrons are stripped off. In the case of heavy ions, LHC injection chains supply the ring with concentrated bunches of Pb^{+82} high-energy

ions. The protons/ions now pass through radio-frequency cavities that speed them up and force them into spatially-separated bunches.

For protons, the injection chain consists of the linear accelerator LINAC2, the Proton Synchrotron (PS), and the Super Proton Synchrotron (SPS). For ions, the chain includes LINAC3, the Low Energy Ion Ring (LEIR), the PS, and the SPS. The energy setup during Run-2 (2015–2018) is described as follows: LINAC2 first accelerates protons to 50 MeV, while LINAC3 accelerates ion beams to 4.2 MeV per nucleon. The LEIR, functioning as an ion storage and cooler unit, brings the ions to 72 MeV per nucleon. Subsequently, the ions are further accelerated to 5.9 GeV per nucleon, and protons to 28 GeV, by the PS. Then, the SPS accelerates the protons to 450 GeV and ions to 177 GeV per nucleon before being injected into the LHC ring, where they reach maximum energies: $\sqrt{s} = 13$ TeV for proton-proton collisions and $\sqrt{s} = 5.02$ TeV for Pb+Pb collisions.

Inside the LHC, two particle beams circulate in opposite directions at close to the speed of light before they are made to collide. The beams are maintained at ultrahigh vacuum inside the beam pipes. Along the beam path, 1232 dipole magnets are placed, each measuring 14.3 meters long and weighing approximately 35 tons, as illustrated in Figure 4.2. These magnets generate the necessary Lorentz force to bend the trajectories of protons or ions along the eight LHC arcs and focus the beam. The design of the dipole magnets ensures that the direction of the magnetic field in each pipe is opposite to that of the other, resulting in the generation of a Lorentz force in the same direction. This force bends the proton/ion beams traveling in opposite directions toward the center of the LHC ring, facilitating their collision.

The magnetic field required to bend a particle traveling at a velocity approaching the speed of light, given its enormous momentum and radius of the LHC ring, is approximately 8T, which is 10^5 times the strength of Earth's magnetic field. Achieving such a strong magnetic field is only possible through superconducting electromagnets. They can generate a current of approximately 11500 A, producing the required magnetic field of 8T. These superconducting electromagnets are made of Nb_3S_n, with a critical temperature of 2K or -271.3°C, colder than outer space. They are bathed in liquid helium, which cools the magnets to keep them in a superconducting state, thereby offering

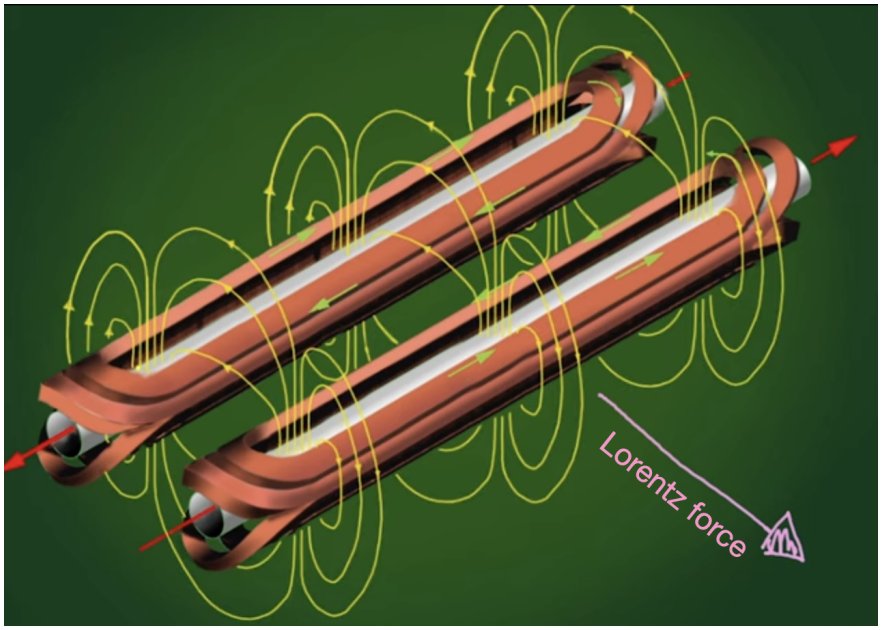

Figure 4.2: The pipes carry the proton beams in opposite directions, shown by the red arrows. The coils have currents flowing in opposite directions, shown by green arrows on top of the coils. They produce magnetic fields in opposing directions, shown by green circles surrounding the coils. Consequently, the Lorentz force produced by both pipes is in the same direction, as the pink arrow shows. Reproduced from Ref. [122].

no resistance to the passage of electric current. In addition to these dipoles are quadrupoles, a series of four magnets designed to focus the beams. Since protons/ions bear the same charge and can repel each other, quadrupoles squeeze the beams together in the transverse plane.

The primary indicator of the accelerator's performance in providing the required number of interactions is called luminosity ($\mathcal{L}$). The instantaneous luminosity is defined as the number of potential collisions per surface unit (or cross-section) over a given period of time and is defined as [123]:

$$\mathcal{L} = \frac{1}{\sigma}\frac{dN}{dt}, \tag{4.1}$$

where dN/dt is the number of events per second and σ is the cross-section. Assuming Gaussian distributions for the incoming beams, one can obtain $\mathcal{L}$ as:

$$\mathcal{L} = f N_b \frac{n_1 n_2}{4\pi\sigma_x\sigma_y}. \tag{4.2}$$

Here, n_1 and n_2 are the number of particles in the colliding bunches 1 and 2, N_b is the number of

colliding bunches, f is the frequency at which they collide and σ_x and σ_y are the beam widths in x and y. Integrated luminosity is a measure of the collected data size and is defined as the time integral of the instantaneous luminosity. The integrated luminosity of heavy-ion data is typically measured in inverse nanobarns (nb^{-1}).

There are four detector experiments located at the four interaction points (IPs) in the ring: A Toroidal LHC ApparatuS (ATLAS) at IP-1, A Large Ion Collider Experiment (ALICE) at IP-2, the Compact Muon Solenoid (CMS) at IP-5, and the Large Hadron Collider beauty (LHCb) experiment at IP-8. ATLAS and CMS are two general-purpose detectors, while the ALICE experiment is built explicitly for heavy-ion physics, and the LHCb experiment focuses on physics related to the "bottom" quark or b-quark. The main focus of the LHC physics program revolves around proton-proton collisions. However, heavy-ion collisions with Pb ions are integrated into the program during shorter running periods, typically occurring once a month each year.

Year	Systems	$\sqrt{s}/\sqrt{s_{\text{NN}}}$ (TeV)	Integrated Luminosity
Run-1			
2010	pp	7	45.0 pb^{-1}
2011	pp	7	5.25 fb^{-1}
2011	Pb+Pb	2.76	158 ub^{-1}
2012	pp	8	21.7 fb^{-1}
2013	p+Pb	5.02	29.85 nb^{-1}
Run-2			
2015	pp	5,13	27 pb^{-1}, 3.9 fb^{-1}
2015	Pb+Pb	5.02	548 ub^{-1}
2016	pp	13	35.6 fb^{-1}
2016	p+Pb	5.02,8.16	179.8 nb^{-1}
2017	pp	5,13	272 pb^{-1}, 46.9 fb^{-1}
2017	Xe+Xe	5.44	3 μb^{-1}
2018	pp	13	60.6 fb^{-1}
2018	Pb+Pb	5.02	1.76 nb^{-1}
Run-3			
2022	pp	13.6	35.7 fb^{-1}
2023	pp	13.6	29.9 fb^{-1}
2023	Pb+Pb	5.36	1.75 nb^{-1}

Table 4.1: A summary of ATLAS data-taking statistics, displaying the year, collision systems, collision energy, and the total recorded luminosity.

The first run of LHC happened from 2009 to 2013, during which LHC collided two opposite particle beams of protons up to collision energy of $\sqrt{s} = 8$ TeV and two opposite particle beams of Pb nuclei at $\sqrt{s_{\mathrm{NN}}} = 2.76$ TeV. The second run happened from 2015 to 2018 after a two-year break, with the successful upgrade of collision energy up to $\sqrt{s} = 13$ TeV for proton-proton collision. The work presented in this thesis utilizes the 5.02 TeV Pb+Pb data collected by the ATLAS experiment during Run 2 of the LHC in 2018, with an integrated luminosity of 1.76 nb^{-1}. The third run began in 2022 with a new maximum collision energy of $\sqrt{s} = 13.6$ TeV for proton-proton collisions. In 2023, LHC performed its Pb+Pb collision at $\sqrt{s_{\mathrm{NN}}} = 5.36$ TeV. A summary of the data collected by the ATLAS experiment is depicted in Table 4.1. A short period of O + O and p+O collisions will be included in Run 3, for the first time in LHC collisions, with the goal of exploring the emergence of QGP-like effects in small colliding systems.

4.2 The ATLAS Experiment

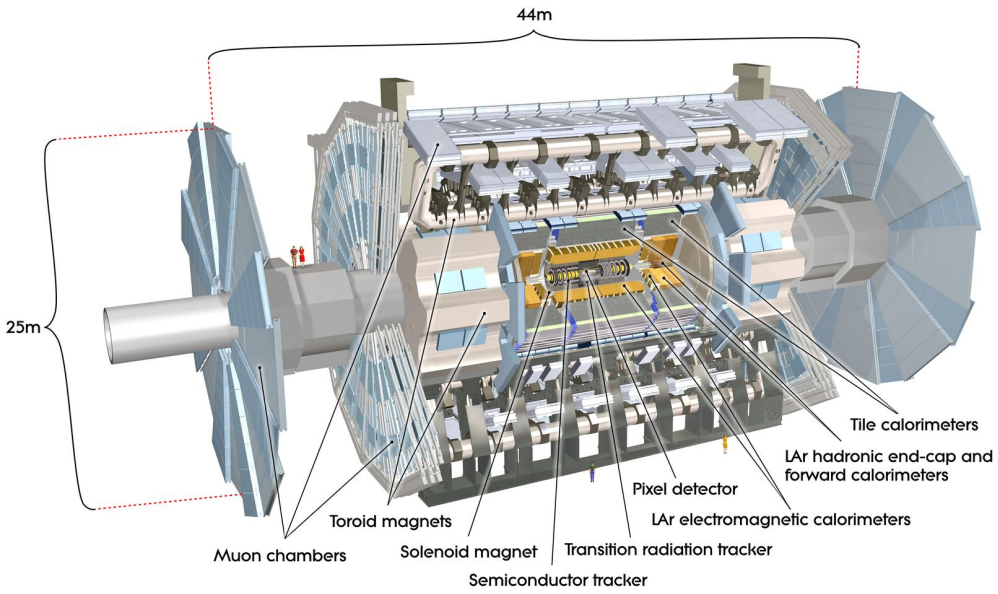

Figure 4.3: A rendering of the ATLAS detector. Reproduced from Ref. [124].

The ATLAS experiment [124] is a multipurpose detector designed for high luminosity data-

taking at LHC, located at the interaction point, IP1. The detector consists of several specialized subsystems in a cylindrical format, including a barrel and endcap, to provide the most complete coverage in detection of particles. It has a diameter of 25 meters and a length of 44 meters, as depicted in Figure 4.3. This thesis utilizes the inner detector to identify the tracks left by the charged particles. The hadronic calorimeter and the Zero-Degree Calorimeter are used for event selection purposes.

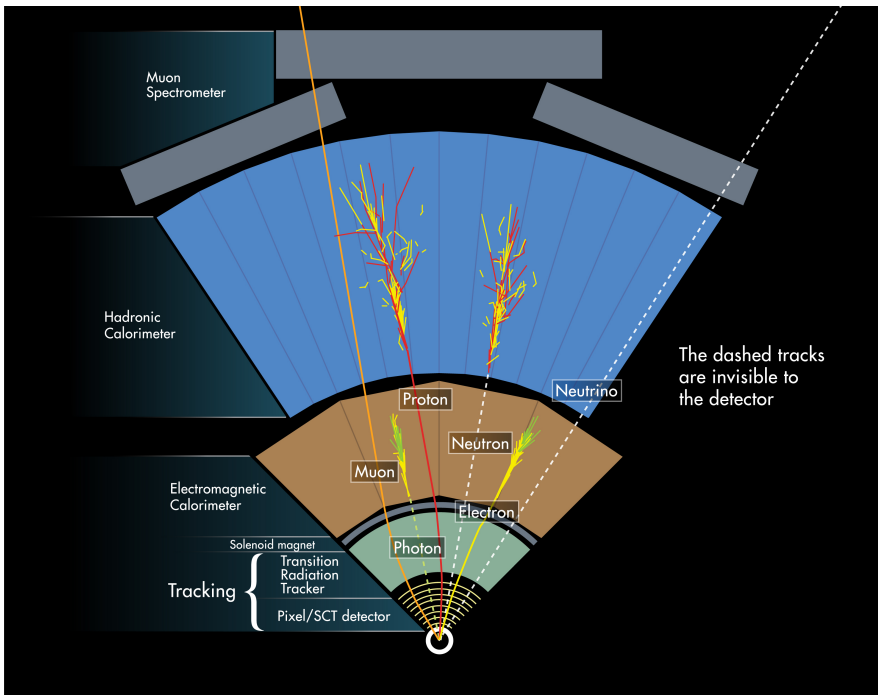

Figure 4.4: How ATLAS detects particles: diagram of particle paths in the detector. Reproduced from Ref. [125].

The inner detector, situated closest to the interaction point, serves as the initial detection point in the ATLAS experiment. The detector measures the direction, momentum, and charge of electrically charged particles produced in each collision by bending the particle in a magnetic field. Lightweight, low-Z materials are utilized to measure the particle's position precisely. Then, multiple calorimeters are used to detect particles through total absorption. This process is destructive for almost all particles except muons and neutrinos. Electromagnetic calorimeters use high-Z material to catch electrons and photons. The hadronic calorimeter interacts mainly via

the strong interaction, although there are many microscopic processes that are electromagnetic in nature (*e.g.*:ionization). Therefore, high-A materials (iron, copper) are used. Finally, the muon spectrometer outside the detector core and its strong electromagnets track the muons with high momentum resolution. Figure 4.4 illustrates how different types of particles interact with the different subdetectors. Multilevel trigger systems reduce the data-taking rate while maintaining maximum efficiency for the targeted physics process. This section details the subsystems of the ATLAS detector.

The standard coordinate system in high-energy physics is represented as $(p_{\mathrm{T}}, \eta, \phi)$, where p_{T} is the transverse momentum, η is the pseudorapidity, and ϕ is the azimuthal angle of the particle, and is detailed below:

The IP defines the origin of the coordinate system, while the beam direction defines the z-axis, and the x–y plane is transverse to the beam direction. The positive x-axis is defined as pointing from the interaction point to the center of the LHC ring, and the positive y-axis is defined as pointing upwards. The side-A of the detector is defined as that with positive z, and side-C is that with negative z. The azimuthal angle ϕ is measured around the beam axis, and the polar angle θ is the angle from the beam axis. The pseudorapidity is defined as $\eta = -\ln\tan(\theta/2)$, while rapidity is defined as $y = (1/2)\ln\left[(E + p_{\mathrm{z}})/(E - p_{\mathrm{z}})\right]$. For massless particles, pseudorapidity is equivalent to their rapidity along the z-axis. Rapidity is used for massive particles and jets. The transverse momentum p_{T} and the transverse energy E_{T} are defined in the x–y plane. The ATLAS detector is nominally forward-backward symmetric with respect to the IP, with large acceptance in pseudorapidity and full azimuthal angle coverage.

4.2.1 The Inner Detector

The ATLAS Inner Detector (ID) lies the closest to the interaction point, consists of three sub-detectors: the Pixel detector, which includes the Insertable B-Layer (IBL), the Semiconductor Tracker (SCT), and the Transition Radiation Tracker (TRT), all embedded in a superconducting solenoid, which produces a 2 T axial magnetic field. The position of these sub-detectors in the

barrel and endcap are shown in Table 4.2. Figure 4.5 shows a schematic representation of the barrel and endcap region. The ID has been designed to reconstruct the trajectories of the charged particles within a pseudorapidity range of $|\eta| < 2.5$.

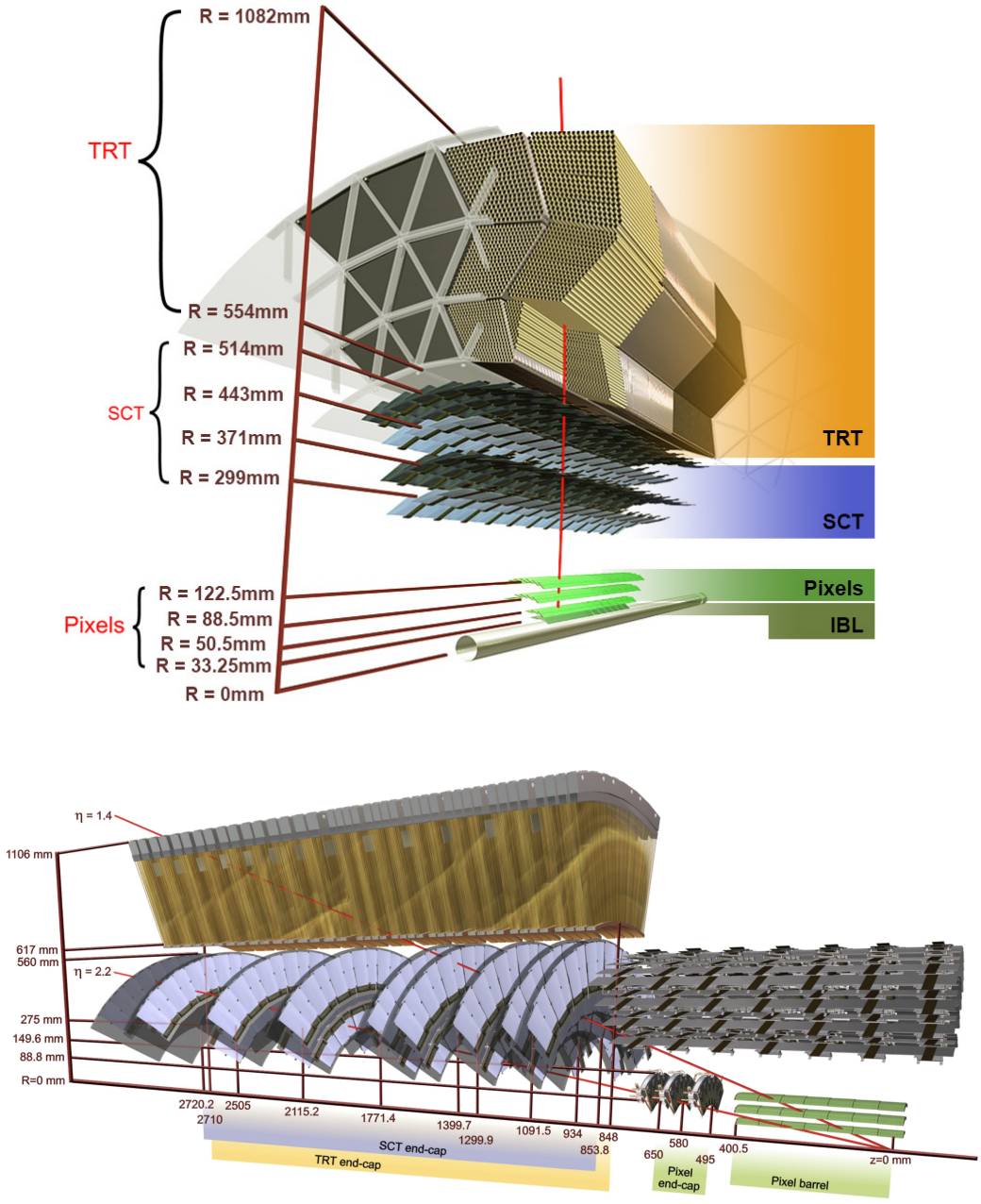

Figure 4.5: Drawing showing the sensors and structural elements traversed by a charged track of 10 GeV p_{T} in the barrel inner detector ($\eta = 0.3$) (top) and by two charged tracks of 10 GeV p_{T} in the endcap inner detector ($\eta = 1.4$ and 2.2) (bottom). Reproduced from Ref. [124].

Item		**Radial extension (mm)**	**Length (mm)**
Overall ID envelope		$0 < R < 1150$	$0 < \|z\| < 3512$
Beam-pipe		$29 < R < 36$	
Pixel	Overall envelope	$45.5 < R < 242$	$0 < \|z\| < 3092$
3 cylindrical layers	Sensitive barrel	$50.5 < R < 122.5$	$0 < \|z\| < 400.5$
2×3 disks	Sensitive endcap	$88.8 < R < 149.6$	$495 < \|z\| < 650$
SCT	Overall envelope	$255 < R < 549$ (barrel)	$0 < \|z\| < 805$
		$251 < R < 610$ (endcap)	$810 < \|z\| < 2797$
4 cylindrical layers	Sensitive barrel	$299 < R < 514$	$0 < \|z\| < 749$
2×9 disks	Sensitive endcap	$275 < R < 560$	$839 < \|z\| < 2735$
TRT	Overall envelope	$554 < R < 1082$ (barrel)	$0 < \|z\| < 780$
		$617 < R < 1106$ (endcap)	$827 < \|z\| < 2744$
73 straw planes	Sensitive barrel	$563 < R < 1066$	$0 < \|z\| < 712$
160 straw planes	Sensitive endcap	$644 < R < 1004$	$848 < \|z\| < 2710$

Table 4.2: Main parameters of the inner-detector system. Reproduced from Ref. [124].

The Pixel Detector is the first detection point in the ATLAS experiment, located just 3.3 cm from the LHC beam line. It comprises four layers of silicon pixels, each pixel smaller than a grain of sand. The Pixel Detector is incredibly compact, with over 92 million pixels and almost 2000 detector elements. The pixel size in R-$\phi \times z$ is 50×400 μm^2 for the external layers and 50×250 μm^2 for the innermost layer. The IBL [126] has been operating as a part of the silicon pixel detector since 2015. Outside the pixel detector is the SCT which detects and reconstructs the tracks of charged particles produced during collisions. It comprises over 4000 modules of 6 million "micro-strips" of silicon sensors. Its layout is optimized so that each particle crosses at least four silicon layers.

The Pixel Detector and the SCT are semiconductor charged-particle trackers, generally reverse-bias PN junctions. As charged particles from the collision pass through the silicon, they cause small ionization currents from the ejection of electrons from the silicon atoms. These currents are measured with a precision of almost 10 μm to determine the origin and momentum of the particle. Knowing which pixels have been touched lets us deduce the particle's trajectory. The charged particle tracks are measured with a precision of up to 25 μm.

The third and final layer of the Inner Detector is the Transition Radiation Tracker (TRT). Unlike its neighboring sub-detectors, the TRT comprises 300,000 thin-walled drift tubes (or "straws"). Each straw is just 4 mm in diameter, with 30 μm gold-plated tungsten wire in its center. The straws are filled with a gas mixture. As charged particles cross through the straws, they ionize the gas to create a detectable electric signal. This is used to reconstruct the tracks and, owing to the so-called transition radiation, provides information on the particle type that flew into the detector since different particles create different currents. The TRT has 350,000 readout channels and a precision of 0.17 mm. The magnetic field around these inner detectors curves the particle paths, enabling us to calculate the particle's momentum.

Signals from adjacent channels in the Pixel and SCT subdetector are combined into clusters, interpreted as deposits left by individual traversing particles [127]. These clusters create three-dimensional measurements referred to as "space-points". They represent the point where the

charged particle traversed the active material of the ID. In the pixel detector, each cluster equates to one space-point, while in the SCT, clusters from both sides of a strip layer must be combined to obtain a three-dimensional measurement. Track seeds are formed from sets of three space points. Several criteria are placed on the seeds to maximize their purity, which results in a good-quality track. A combinatorial Kalman filter [128] is used to build track candidates from the chosen seeds by incorporating additional space-points from the remaining layers of the pixel and SCT detectors, which are compatible with the preliminary trajectory. A track score is applied to these track candidates, calculated based on how many clusters were used, how many holes were found, and the fit χ^2.

After calculating the track scores, the ambiguity solver deals with clusters assigned to multiple track candidates. Clusters can be shared by no more than two tracks, giving preference to tracks processed first in the ambiguity solver. Also, a track can have no more than two shared clusters. A cluster is removed from a track candidate if it causes either the candidate or an accepted track not to meet the shared-cluster criterion. The track candidate is then scored again and returned to the ordered list of remaining candidates. The ambiguity solver rejects track candidates if they fail to meet basic quality criteria defining a certain "working point". The `HILoose` working point, utilized in the analysis of charged hadron production, contains the following track quality cuts:

- $p_{\mathrm{T}} > 100$ MeV
- $|\eta_{\mathrm{trk}}| < 2.5$
- Number of pixel hits: $\mathrm{N_{Pix}} \geq 1$
- Number of SCT hits: $\mathrm{N_{SCT}} \geq 2, 4, 6$ for $p_{\mathrm{T}} < 300$ MeV, < 400 MeV, > 400 MeV respectively
- $\mathrm{N_{IBL}} + \mathrm{N_{B-Layer}} > 0$, if both IBL hit and B-layer hit are expected. B-layer refers to the second layer of the Pixel Detector, surrounding the IBL.
- $\mathrm{N_{IBL}} + \mathrm{N_{B-Layer}} \geq 0$, if either IBL hit or B-layer hit is not expected

- d_0 wrt. primary vertex less than 1.5 mm
- $z_0 \sin\theta$ wrt. primary vertex less than 1.5 mm

where d_0 is the transverse impact parameter with respect to the beam axis, and z_0 is the longitudinal distance of the closest approach, respectively.

The procedure of primary vertex reconstruction is detailed below [129] briefly:

- A set of tracks satisfying the track selection criteria is defined.
- A seed position for the first vertex is selected.
- The tracks and the seed estimate the best vertex position with a fit. The fit is an iterative procedure, and in each iteration, less compatible tracks are down-weighted, and the vertex position is recomputed.
- After the vertex position is determined, tracks incompatible with the vertex are removed from it and allowed to be used to determine another vertex.
- The procedure is repeated with the remaining tracks in the event.

4.2.2 The Calorimeter System

The ATLAS Calorimeter System, as illustrated in Figure 4.6, consists of several sampling detectors with full ϕ-symmetry and coverage around the beam axis, spanning pseudorapidity range $|\eta| < 4.9$. The calorimeter is designed to absorb most particles from a collision, forcing them to deposit all their energy and stop within the detector. ATLAS calorimeters consist of layers of an "absorbing" high-density material that stops incoming particles interleaved with layers of an "active" medium that measures their energy. The electromagnetic calorimeter, a liquid argon calorimeter, measures the energy of photons and leptons as they interact with matter. The hadronic calorimeter system, which consists of both liquid argon calorimeters and the tile hadronic calorimeter, samples the energy of hadrons as they interact with atomic nuclei. Calorimeters can stop most known particles except neutrinos and moderate-p_{T} muons.

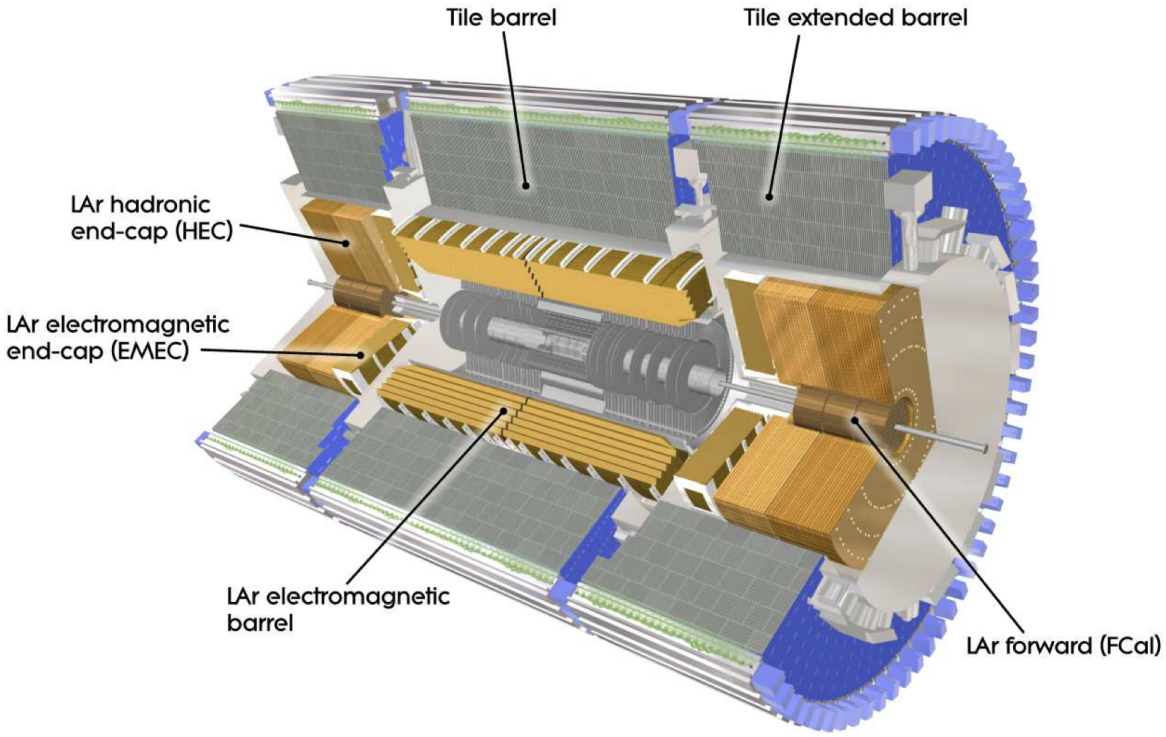

Figure 4.6: A rendering of the ATLAS calorimeter system. Reproduced from Ref. [124].

Outside the Inner Detector is the Liquid Argon (LAr) Calorimeter, which consists of the electromagnetic barrel calorimeter (EMBC), an electromagnetic endcap calorimeter (EMEC), a hadronic endcap calorimeter (HEC), and a forward calorimeter (FCal) to cover the region closest to the beam. The electromagnetic calorimeter spans the pseudorapidity region $|\eta| < 3.2$, the HEC covers the range $1.5 < |\eta| < 3.2$ and the FCal covers the range $3.1 < |\eta| < 4.9$.

The LAr Calorimeter has a characteristic accordion structure with a honeycomb pattern to ensure no particle escapes without interaction. The calorimeter is made of layers of metals, such as tungsten, copper, and lead, that absorb incoming particles, converting them into a "shower" of new, lower-energy particles. When an electron hits the electromagnetic calorimeters (EMBC and EMEC), an electromagnetic shower of electrons and photons is created. Electrons create photons through bremsstrahlung, and photons create electrons through pair production (there are other interactions, but these are the two main ones). Inside the hadronic calorimeters (HEC and FCal),

energy loss through bremmstrahlang radiation is strongly suppressed by the large (relative to the $e^{\pm}$) hadron mass. Typically, the high-energy hadrons undergo inelastic collisions with nuclei in the material, producing a hadronic shower of many light hadrons (mostly pions). These processes continue until the calorimeter material absorbs the total energy of the hadron. Between the layers is a liquid argon at -180°C, serving as the active medium. The particles produced ionize the liquid argon filled in between the layers, producing an electric current. The energy deposited by the original particle that hit the detector is determined by measuring the detected electric current.

The Tile Calorimeter surrounds the LAr calorimeter and measures the energy of hadronic particles. Its barrel covers the region $|\eta| < 1.0$, and its two extended barrels cover the range $0.8 < |\eta| < 1.7$. It is made of layers of steel as the absorber and scintillating tiles used as the active material. Ionizing particles crossing the tiles induce the production of ultraviolet scintillation light in the base material (polystyrene). The light produced in the scintillating material is collected at the edges of each tile using two wavelength-shifting fibers into photomultiplier tubes. The Tile Calorimeter comprises approximately 420,000 plastic scintillator tiles working together. It is the heaviest part of the ATLAS experiment, weighing almost 2900 tonnes.

The Calorimeter system is used in the analyses presented in this thesis to reconstruct the basic event topology, such as the presence of rapidity gaps, as detailed in Section 3.2. A cluster of topologically connected calorimeter cell signals, known as topoclusters, are used to provide the energy deposited by the hadron [130]. The topocluster algorithm reconstructs a three-dimensional "energy blob", which represents a full or partial energy deposited by a single particle, or merging of several particles, or a combination of merged full and partial showers. The primary observable defining the cluster formation is the cell signal significance, ζ_{cell}, given as:

$$\zeta_{\text{cell}} = \frac{E_{\text{cell}}}{\sigma_{\text{noise,cell}}}, \tag{4.3}$$

where the E_{cell} is the energy of the calorimeter cell, and $\sigma_{\text{noise,cell}}$ is the average noise in this cell. By imposing several threshold criteria on the signal significance, topoclusters are reconstructed, efficiently removing insignificant signals induced by noise.

4.2.3 The Zero Degree Calorimeter

The Zero-Degree Calorimeter (ZDC) [131] plays a crucial role in identifying UPC events in heavy-ion collisions. In these collisions, there is a significant probability that at least one neutron will be detached from the nuclei and continue to travel forward with the beam momentum. These neutrons can be detected by symmetrically placing two calorimeters relative to the interaction point farther along the beam direction. UPCs can thus be identified by triggering only the ZDCs since there is almost no activity in the central rapidities. The ZDC, as illustrated in Figure 4.7, is used to detect forward neutrons with an acceptance of $|\eta| > 8.3$. It is positioned at $z = \pm 140$ m from the interaction point and located in a Target Absorber Neutral (TAN) absorber to protect the cryogenic magnets beyond the pipe transition region from the radiation damage due to the neutral particle flux.

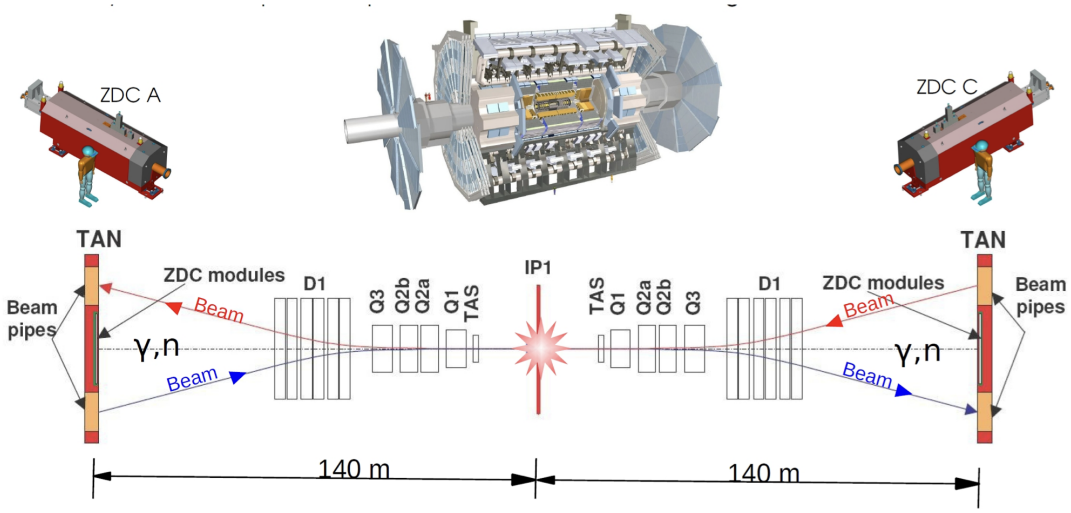

Figure 4.7: The ATLAS interaction point and the location of ZDCs. Reproduced from Ref. [132].

The ZDC is a sampling calorimeter utilizing tungsten plates as absorber material and quartz rods interspersed in the absorber as active media. As the neutrons pass through the tungsten plates, a shower of highly energetic charged particles is produced. These quartz rods collect the Cherenkov light produced by the energetic charged particles, which is then detected by the photomultipliers and transmitted to 120 electronic channels. The tungsten plates and quartz rods are arranged

to segment the calorimeters into four longitudinal modules. The first module, situated close to the interaction point, acts as an electromagnetic calorimeter, while the remaining three act as a hadronic calorimeter. Figure 4.8 illustrates the electromagnetic and hadronic modules. These modules have 1.5 mm quartz rods oriented perpendicular to the beam direction, and the light from these fibers is detected by photomultiplier tubes, which are used to measure energy deposited in the module. The 1 mm quartz rods running parallel to the beam direction are grouped to form calorimeter cells, used for the position information of the incident particles. Each ZDC module provides energy and trigger information using a dedicated set of quartz rods grouped together and connected to a photomultiplier tube.

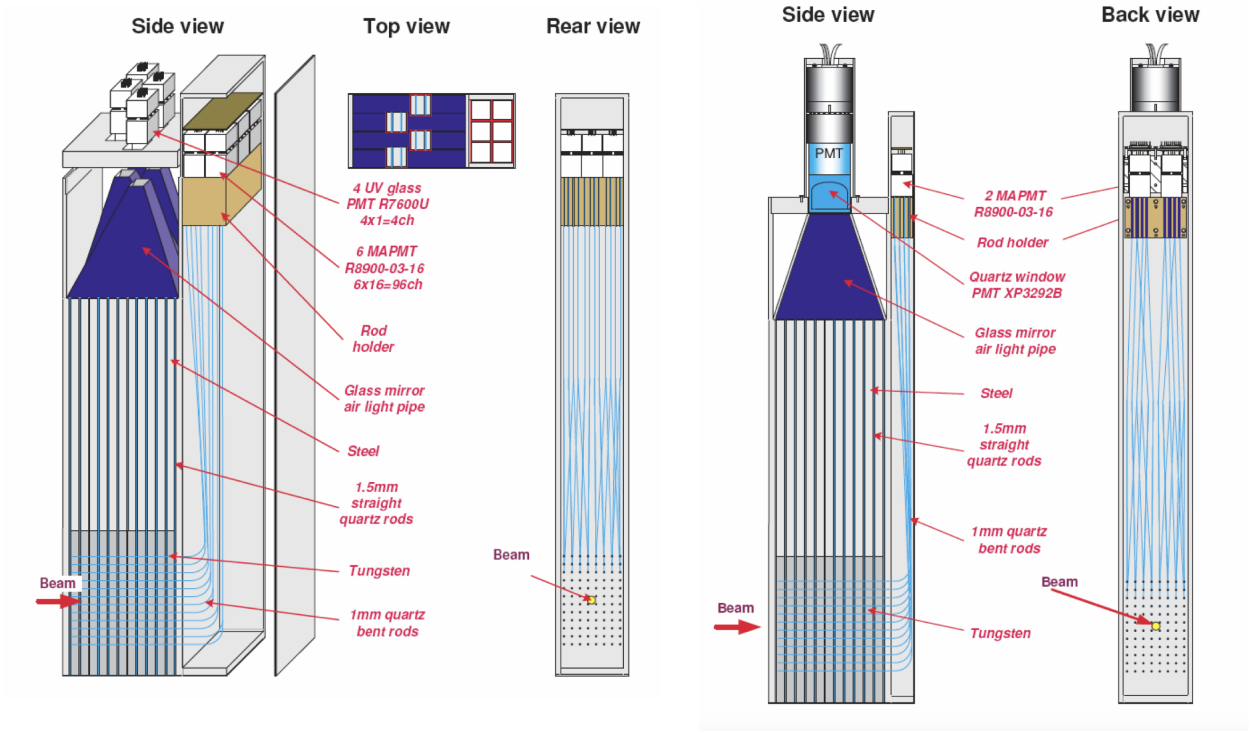

Figure 4.8: (left) The side, top, and rear views of the electromagnetic ZDC module. (right) The side and back views of the hadronic ZDC module. Reproduced from Ref. [124].

4.2.4 The Trigger and Data Acquisition

The trigger system [133] is an essential component of any collider experiment, given its main job is to decide whether or not to keep an event from a given bunch-crossing interaction for later study. The setup as it existed in Run-2 is described here. Since the start of Run 2, the ATLAS detector has a two-level trigger system. The first level trigger, the Level-1 (L1) trigger, is implemented in hardware and uses a subset of the detector information to reduce the rate of accepted events from an input rate of up to 100 kHz. This is followed by a software-based trigger, the high-level trigger (HLT), which consists of a Level-2 (L2) trigger and an event filter. This reduces the rate of recorded events to an average rate of $\sim$ 200Hz written out for physics analysis.

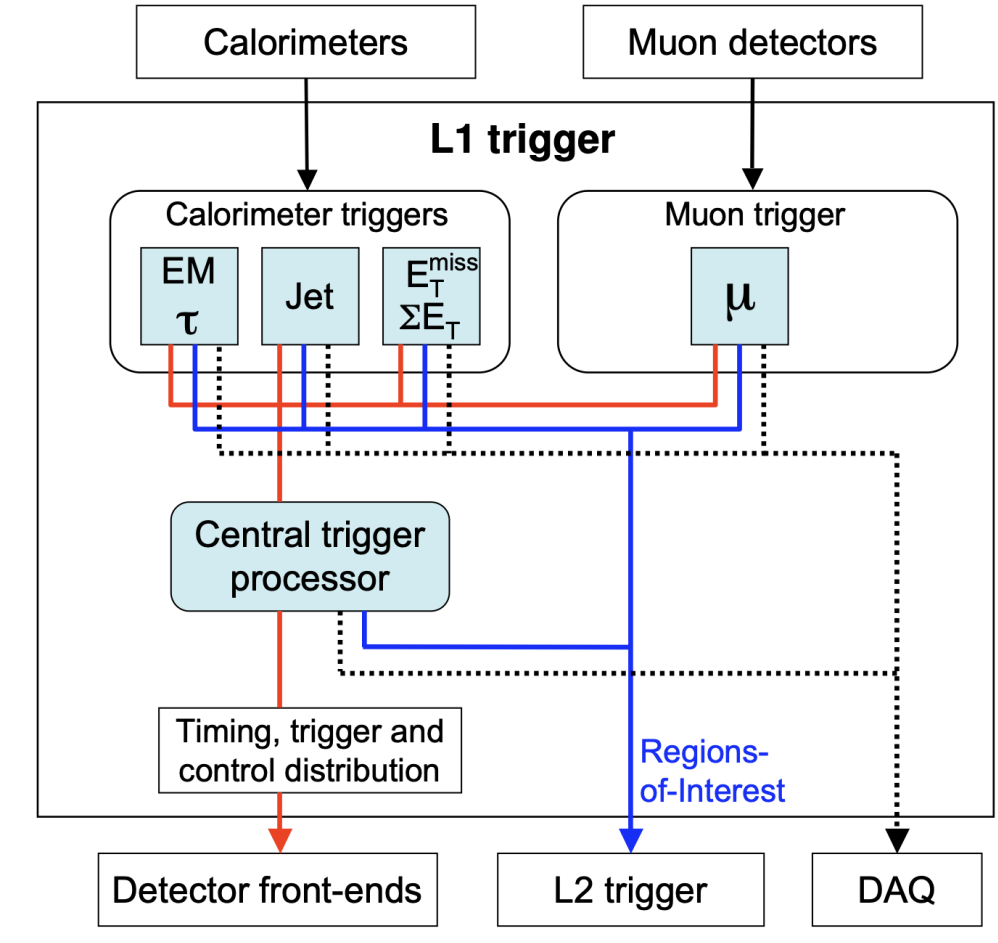

Figure 4.9: Block diagram of the L1 trigger. Reproduced from Ref. [124].

The L1 trigger initiates the initial event selection based on the information from the calorimeters and muon detectors, as illustrated in Figure 4.9. The L1 Calorimeter (L1Calo) trigger identifies high E_{T} objects such as electrons and photons, jets, and τ-leptons decaying into hadrons, as well as events with large transverse energy, utilizing information from all the calorimeters. The L1 muon trigger is based on signals in the muon detector. This initial trigger stage is crucial, as it reduces the event rate to a maximum of 100 kHz, with decisions transmitted to the front-end electronics within 2.5 μs after the associated bunch-crossing.

Following the L1 trigger, the L2 trigger is activated based on the identified Regions-of-Interest (RoI). These RoIs represent regions in the detector, i.e., the geographical coordinates in η and ϕ, where the L1 trigger has identified possible trigger objects within the event. The L2 trigger utilizes RoI information on coordinates, energy, and type of signatures to limit the amount of data transferred from the detector readout. The L2 trigger reduces the event rate to below 3.5 kHz, with an average event processing time of approximately 40 ms.

Following the L2 trigger, the event filter employs offline analysis techniques on fully reconstructed events to further select events, reducing to a rate of approximately 200 Hz, with an average event processing time of order four seconds. The selected events are recorded for subsequent offline analysis.

The data acquisition system (DAQ) [134] receives and buffers the event data from the detector-specific readout electronics at the L1 trigger rate. The data transmission is performed over point-to-point Readout Links (ROLs). Upon receiving requests from the trigger, typically for data corresponding to Regions-of-Interest (RoIs), the DAQ transmits the necessary data to the L2 trigger. The requests are for events that satisfy the L2 selection criteria. Following this, the event-building processes are initiated. Subsequently, the DAQ transfers the assembled events to the event filter. Events selected by the event filter are then directed to permanent event storage.

During the 2018 HI run, the LHC provided Pb+Pb collisions with center-of-mass energies of $\sqrt{s_{\mathrm{NN}}} = 5.02$ TeV. The instantaneous luminosity peaked at $6.2 \times 10^{27}\mathrm{cm}^{-2}\mathrm{s}^{-1}$, resulting in a collision rate of 48 kHz for hadronic interactions and approximately 1.5 MHz for events with single Pb electromagnetic dissociation. The number of events recorded by the primary triggers (L1 and HLT) is depicted in Figure 4.10, where triggers are categorized into eight groups. Each L1 and HLT trigger is typically associated with a prescale, denoted as p_{L1} and p_{HLT}, respectively. These prescales determine that only $1/p_{\mathrm{L1}}$ events is accepted by the L1 trigger for HLT processing, and subsequently, only $1/p_{\mathrm{HLT}}$ events is accepted by the HLT trigger.

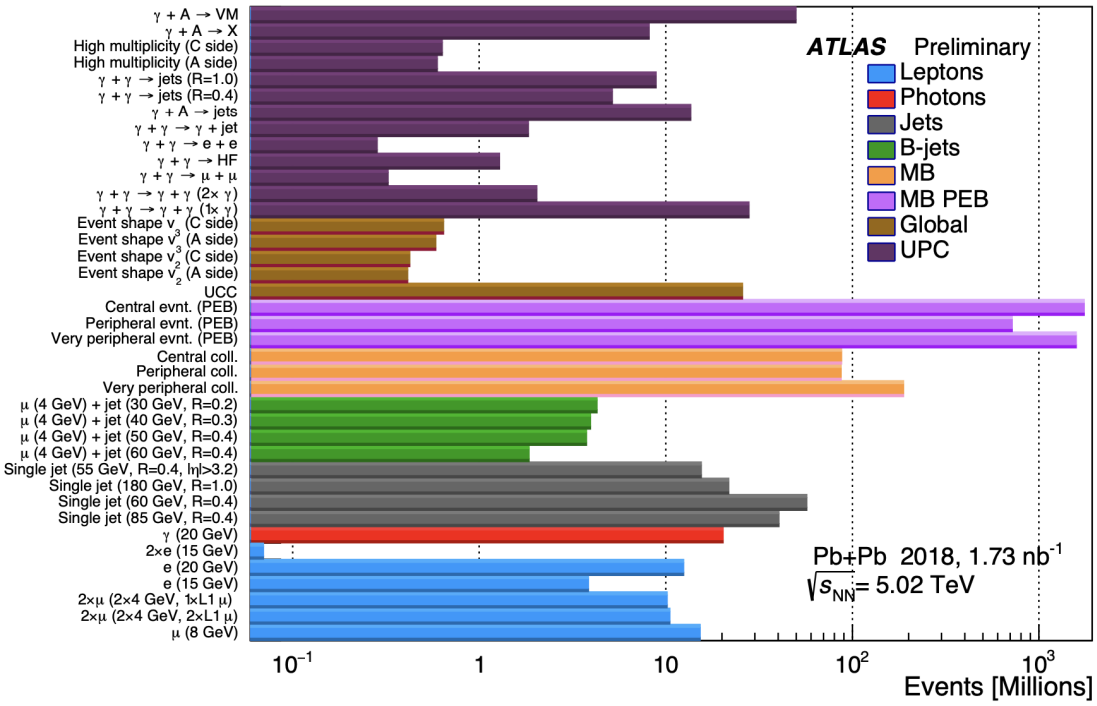

Figure 4.10: Number of events collected by primary HI triggers during the 2018 HI data-taking period. Triggers are grouped into eight categories. Reproduced from Ref. [133].

Chapter 5

Measurement of Charged Hadron Production

As detailed in Chapter 2, when ultra-relativistic beams of lead nuclei are brought into collision, the typical processes studied are those for which the nuclei have an impact parameter less than twice their radius ($b < 2R_A$). Such Pb+Pb collisions are understood to create a tiny droplet of QGP and produce a large number of particles that exhibit collective expansion. This behavior is also observed in small collision systems such as p+Au, d+Au, ^{3}He+Au at RHIC and pp and p+Pb collisions at the LHC, as detailed in Section 2.5. A natural question arises as to whether these signatures are observed in even smaller collision systems. As detailed in Chapter 3, photo-nuclear (γ+Pb) collisions are one such exotic small system where the strong electromagnetic (EM) fields of the fully ionized nuclei give rise to a flux of quasi-real, high-energy photons, effectively breaking apart the incoming nuclei.

As discussed in Section 3.3, ATLAS has previously published two-particle azimuthal correlations observed in γ+Pb collisions [10]. These results indicate significant non-zero elliptic and triangular flow coefficients *i.e.*, v_2 and v_3, respectively. These coefficients have been interpreted in terms of a hydrodynamically flowing medium [61], and alternatively in terms of scattering diagrams in the color glass condensate framework [113]. The hydrodynamic simulations put forth a specific prediction that the "flow" is essentially the same in γ+Pb and p+Pb collisions and that other measurements such as radial flow, determined by the mean transverse momentum, $\langle p_{\mathrm{T}} \rangle$, of charged and identified particles, should be the same for both systems. This interpretation raises questions about whether one can observe indications of radial hydrodynamic flow [2] or other signals of collectivity

in these photo-nuclear collisions.

Hence, the analysis presented here is motivated by two central physics questions: (1) Can the underlying physics processes in photo-nuclear events be well modeled? and (2) Is there strong evidence for the formation of small quark-gluon plasma droplets that flow hydrodynamically in these UPC events? Detailed comparisons of these measurements with the Monte Carlo model DPMJET-III [135, 136] enables key constraints on the physics processes. Detailed comparisons between UPC and p+Pb data enable tests of the hydrodynamics model predictions [61], whether γ+Pb collisions behave like a hadron-nucleus interaction (p+Pb), experiencing strong final-state effects.

This chapter presents a measurement of unidentified-charged-hadron yields in photo-nuclear collisions with the ATLAS detector. The inclusive yields of charged hadrons are presented as a function of pseudorapidity (η) and p_{T}, while the $\langle\eta\rangle$ and $\langle p_{\mathrm{T}}\rangle$ are reported as a function of collision multiplicity $N_{\mathrm{ch}}^{\mathrm{rec}}$. Additionally, the chapter provides comparisons to the Monte Carlo model DPMJET-III and p+Pb collision data.

The analysis utilizes the identical 2018 Pb+Pb 5.02 TeV dataset and event selection cuts as the photo-nuclear flow analysis [137]. The same analysis procedure is also applied to low-multiplicity 2016 p+Pb collisions at 5.02 TeV, with $N_{\mathrm{ch}}^{\mathrm{rec}}$ selected to match that of the photo-nuclear events. Primary charged hadrons are utilized and defined as those with a mean lifetime $\tau > 300$ ps (3×10^{-10} s), either directly produced in γ+Pb and p+Pb interactions or from subsequent decays of directly produced particles with $\tau < 30$ ps. Inner detector tracks are utilized to reconstruct charged hadrons, which are corrected for reconstruction inefficiencies and the contribution of backgrounds such as fakes and secondary tracks. Finally, the inclusive yields of primary charged hadrons are determined as a function of η over the pseudorapidity range $-2.5 < \eta < +2.5$ and as a function of p_{T}, and relevant observables are computed.

5.1 Datasets

In this section, the Pb+Pb UPC and p+Pb data and Monte Carlo samples are detailed.

5.1.1 Pb+Pb UPC

The Pb+Pb UPC dataset in this analysis is the 2018 Pb+Pb $\sqrt{s_{NN}} = 5.02$ TeV dataset recorded by ATLAS at the LHC with 733 bunches with a separation of 75 and 150 ns. The full data set corresponds to an integrated luminosity of 1.7 nb^{-1}, with a total uncertainty of 4.1%. The data were collected over 45 runs including 7 runs with the toroid off. The average interaction per bunch crossing corresponds to the range $\mu = 0.001$ - 0.005.

Events used in this analysis were recorded using several different triggers to sample high-multiplicity photo-nuclear collisions. These triggers are crucial as these collisions have a very steeply falling multiplicity spectrum. The primary triggers are as follows:

- `HLT_mb_sptrk_L1ZDC_XOR_VTE200`
- `HLT_mb_sp50_trk15_hmt_hi_upc_FgapC5_L1MBTS_1_ZDC_A_VZDC_C_VTE200`
- `HLT_mb_sp50_trk15_hmt_hi_upc_FgapA5_L1MBTS_1_ZDC_C_VZDC_A_VTE200`
- `HLT_mb_sp50_trk15_hmt_hi_upc_FgapC5_L1_ZDC_A_VZDC_C_VTE200`
- `HLT_mb_sp50_trk15_hmt_hi_upc_FgapA5_L1_ZDC_C_VZDC_A_VTE200`
- `HLT_mb_sp400_trk25_hmt_hi_upc_FgapC5_L1TE4_ZDC_A_VZDC_C_VTE200`
- `HLT_mb_sp400_trk25_hmt_hi_upc_FgapA5_L1TE4_ZDC_C_VZDC_A_VTE200`
- `HLT_mb_sp400_trk25_hmt_hi_upc_FgapC5_L1TE3.0ETA49_ZDC_A_VZDC_C_VTE200`
- `HLT_mb_sp400_trk25_hmt_hi_upc_FgapA5_L1TE3.0ETA49_ZDC_C_VZDC_A_VTE200`
- `HLT_mb_sp700_trk35_hmt_hi_upc_FgapC5_L1TE5_ZDC_A_VZDC_C_VTE200`

- HLT_mb_sp700_trk35_hmt_hi_upc_FgapA5_L1TE5_ZDC_C_VZDC_A_VTE200
- HLT_mb_sp700_trk35_hmt_hi_upc_FgapC5_L1TE7.0ETA49_ZDC_A_VZDC_C_VTE200
- HLT_mb_sp700_trk35_hmt_hi_upc_FgapA5_L1TE7.0ETA49_ZDC_C_VZDC_A_VTE200
- HLT_mb_sp_L1VTE50
- HLT_noalg_L1ZDC_XOR

A set of supporting triggers were also used and are listed as follows:

- HLT_mb_sp50_trk15_hmt_hi_upc_FgapC10_L1MBTS_1_ZDC_A_VZDC_C_VTE200
- HLT_mb_sp50_trk15_hmt_hi_upc_FgapA10_L1MBTS_1_ZDC_C_VZDC_A_VTE200
- HLT_mb_sp50_trk15_hmt_hi_upc_FgapC10_L1_ZDC_A_VZDC_C_VTE200
- HLT_mb_sp50_trk15_hmt_hi_upc_FgapA10_L1_ZDC_C_VZDC_A_VTE200
- HLT_mb_sp400_trk25_hmt_hi_upc_FgapC10_L1TE4_ZDC_A_VZDC_C_VTE200
- HLT_mb_sp400_trk25_hmt_hi_upc_FgapA10_L1TE4_ZDC_C_VZDC_A_VTE200
- HLT_mb_sp400_trk25_hmt_hi_upc_FgapC10_L1TE3.0ETA49_ZDC_A_VZDC_C_VTE200
- HLT_mb_sp400_trk25_hmt_hi_upc_FgapA10_L1TE3.0ETA49_ZDC_C_VZDC_A_VTE200
- HLT_mb_sp700_trk35_hmt_hi_upc_FgapC10_L1TE5_ZDC_A_VZDC_C_VTE200
- HLT_mb_sp700_trk35_hmt_hi_upc_FgapA10_L1TE5_ZDC_C_VZDC_A_VTE200
- HLT_mb_sp700_trk35_hmt_hi_upc_FgapC10_L1TE7.0ETA49_ZDC_A_VZDC_C_VTE200
- HLT_mb_sp700_trk35_hmt_hi_upc_FgapA10_L1TE7.0ETA49_ZDC_C_VZDC_A_VTE200

The nomenclature used in these trigger names is detailed in Table 5.1.

Name	Possible values	Condition
`trk`X	X=15, 25, 35	Minimum number of HLT tracks
`sp`X	X = 50, 400,700	Minimum number of space points in the tracker to enter track counting trigger
`Fgap`XY	X = A or C side Y = 5, 10	Maximum energy in GeV (Y) in FCAL of side (X) A or C
`MBTS_1`		1 hit in the MBTS
`TE`X	X = 3, 5	Minimum total energy in GeV in the calorimeter at level 1 precision
`VTE`X	X = 200	Maximum total energy in GeV in the calorimeter at level 1 precision
`ZDC_`X	X = A or C	Minimum total energy in either A or C side ZDC that is associated with at least one neutron. The complement is labeled with a V prefix.

Table 5.1: Trigger object names, specific settings, and a short descriptor are listed for the triggers used in this γA analysis.

The goal of these triggers is to maximize the recorded data sample of asymmetric, high-multiplicity collisions of interest. The asymmetry selection is achieved by a combination of ZDC and Fgap requirements. First the ZDC_XOR, ZDC_A_VZDC_C, and ZDC_C_VZDC_A are used to suppress the contribution of non-diffractive and double-diffractive collisions associated with either break-up of both colliding Pb nuclei (and thus a probable signal in both ZDCs of at least one neutron) or with no break-up of any colliding Pb nuclei (and thus no signal in either ZDC). A large rate of non-diffractive Pb+Pb collisions with low event activity can pass the XOR requirement and thus the Fgap requirement is also imposed. This trigger requirement further suppresses the contribution of non-diffractive Pb+Pb collisions and in turn, enhances the recorded fraction of photo-nuclear collisions. The Fgap trigger selection has a two-condition requirement, where a maximum selection is made on the total energy sum of L1 trigger towers (Y) and then a maximum on the cell level sum in the associated FCAL. The first requirement is a very low resolution (generally a lower bound) on the amount of energy in the associated FCAL but uses strictly L1 information and thus provides faster rejection speed to reduce the load on the HLT system during data taking. The cell-level sum has a higher degree of precision and is thus used to reject peripheral Pb+Pb collisions. The Fgap requirement is only in place for triggers utilizing the high-multiplicity trigger. This is because, at low multiplicity, the total rate of photo-nuclear collisions dominates over other backgrounds, such as peripheral Pb+Pb collisions.

The dataset was collected by ATLAS over 45 runs that are listed in Table 5.2 along with information about the per-run integrated luminosity and event counts selected by a few candidate triggers. The data used for this analysis was obtained from the physics_UPC stream which was reconstructed using version 21.0.90 of ATHENA with do_HIP mode. The production tag used for the reconstruction was 1032_m2055 or f1028_m2055 depending on the run number. The conditions tag used in the reconstruction was CONDBR2-BLKPA-2018-12 and the geometry version was ATLAS-R2-2016-01-00-01. In do_HIP mode, the tracking is configured in low-p_{T} mode with a minimum p_{T} of 100 MeV. The calorimeter reconstruction was configured in low-μ mode.

Run number	# of LBs	$L_{\text{int}}^{\text{Live}}$ [μb^{-1}]	MinBias [μb^{-1}]	`trk15` [μb^{-1}]	`trk25` [μb^{-1}]	`trk35` [μb^{-1}]
365502	228	0.984	0.00020	0.529	0.900	0.900
365512	160	0.910	0.00014	0.535	0.910	0.910
365573	255	7.775	0.00003	1.879	7.775	7.775
365602	295	9.800	0.00020	2.289	9.800	9.800
365627	341	24.947	0.00025	3.224	24.947	24.947
365678	177	16.306	0.00018	1.192	16.306	16.306
365681	400	24.748	0.00027	3.275	24.748	24.748
365709	432	35.418	0.00028	3.248	35.418	35.418
365752	477	36.821	0.00029	3.417	36.821	36.821
365834	230	5.597	0.00010	1.684	5.597	5.597
365914	360	6.518	0.00011	2.756	6.518	6.518
365932	446	41.773	0.00033	3.438	41.773	41.773
366011	451	43.923	0.00035	3.511	43.923	43.923
366029	421	42.853	0.00043	3.281	42.853	42.853
366092	445	45.454	0.03640	3.554	45.454	45.454
366142	442	41.904	0.03358	3.514	41.904	41.904
366268	666	54.336	0.04354	5.303	54.336	54.336
366337	631	44.176	0.03540	4.540	44.176	44.176
366383	30	0.156	0.00013	0.050	0.156	0.156
366413	417	40.830	0.03270	3.317	40.830	40.830
366476	434	42.264	0.03387	3.455	42.264	42.264
366526	9	1.039	0.00057	0.021	1.039	1.039
366528	298	33.219	0.03550	2.351	33.219	33.219
366627	394	36.819	0.03953	3.129	36.819	36.819
366691	520	55.475	0.04550	4.301	55.475	55.475
366754	478	61.869	0.04170	3.874	61.869	61.869
366805	604	73.150	0.04970	4.892	73.150	73.150
366860	490	65.380	0.04435	4.044	65.380	65.380
366878	480	64.341	0.04380	3.941	64.341	64.341
366919	600	73.955	0.04563	4.709	73.955	73.955
366931	359	58.064	0.03620	2.914	58.064	58.064
366994	34	9.598	0.00327	0.192	4.962	9.598
367023	536	64.878	0.04168	4.242	61.115	64.878
367099	490	66.272	0.04140	3.868	61.159	66.272
367134	507	72.666	0.04374	4.085	65.040	72.666
367165	30	8.728	0.00327	0.156	3.959	8.728
367170	796	47.723	0.03820	5.375	47.180	47.711
367233	476	54.999	0.03654	3.798	53.095	54.999
367273	461	52.711	0.03543	3.625	51.682	52.711
367318	509	64.042	0.03799	3.981	56.647	64.042
367321	491	65.513	0.03800	3.877	57.672	65.513
367363	45	13.132	0.00448	0.286	7.588	13.132
367364	517	66.466	0.03866	4.057	58.485	66.466
367365	257	40.380	0.02490	1.988	37.501	40.380
367384	76	7.626	0.00500	0.350	7.225	7.626

Table 5.2: Run number, number of good lumiBlocks (LBs), recorded-integrated luminosity for each run, and effective-integrated luminosities for different triggers.

5.1.2 p+Pb

For the p+Pb data analysis, a single run (312796) from 2016 p+Pb $\sqrt{s_{NN}} = 5.02$ TeV data taking is used. This particular run has a large minimum bias trigger bandwidth and low interaction rate $\mu = 3.147 \times 10^{-4}$. The beams during this run were oriented such that the protons (beam 1) were traveling from the A-side to the C-side (positive η to negative η) and the lead ions (beam 2) were traveling in the reverse direction. The trigger `HLT_mb_sptrk_L1MBTS_1`, which requires a hit in the `MBTS` at Level-1 and the `sptrk` algorithm to fire at the `HLT` level, is used. In the comparison between photo-nuclear and p+Pb collisions, the statistical uncertainties are essentially entirely from the photo-nuclear data sample and hence restricting the p+Pb analysis to a single, high-statistics run is not a limitation on the analysis.

5.1.3 Monte Carlo Samples

In this section, several Monte Carlo samples utilized in this analysis are detailed.

5.1.3.1 DPMJET-III + STARLIGHT Minimum Bias γ + A Collisions

The Monte Carlo sample used in the Pb+Pb UPC analysis is the DPMJET-III + STARLIGHT minimum bias γA collision sample. Events were generated with different minimum requirements on $N_{\mathrm{ch}}^{\mathrm{rec}}$ to provide good statistical coverage over the $N_{\mathrm{ch}}^{\mathrm{rec}}$ range accessed in data. First, the distribution of photon flux for ^{208}Pb beams at the LHC was calculated using STARLIGHT [138]. The flux distribution was passed to a multipurpose generator based on the Dual Parton Model (DPM) and referred to as DPMJET-III [135, 136], which simulates direct and resolved photon–lead (γ+Pb) interactions at the generator level.

The DPM model is a diagrammatic way of describing particle production in hadron-hadron collisions [15]. Two major concepts underlie the dual-parton model. The first is the dual resonance model [139]. This model states that there are two alternative (or "dual") descriptions of hadron-hadron interactions – the t-channel diagram where particles can be exchanged as a form of interaction and the s-channel diagram where the two incoming particles fluctuate into an inter-

mediate state as a type of interaction. The second is the Veneziano scattering amplitude, which allows for a convergent calculation of the scattering amplitude for an exchange of a large set of particles. These two concepts enable calculations in soft hadron physics through the *pomeron*. The pomeron is a particle with vacuum quantum numbers analogous to a closed string and can be exchanged between hadrons as a form of interaction. Thus, through the dual resonance model, there are intermediate states in elastic hadron-hadron collision with a large number of pomerons. These diagrams can be "cut" to calculate the amplitude of the inelastic process of hadrons interacting to form a large number of primarily meson final states. The DPMJET-III Monte Carlo simulator combines the dual parton model with pQCD, as well as other features, to attempt a full description of hadron-hadron, hadron-photon, and photon-photon collisions [136].

The full set of particles is then run through a full GEANT4 simulation of the ATLAS detector. Thirteen million γ+Pb events were simulated in this way.

Both photon kinematics were simulated independently: `photPosEta` (photon traveling in positive z direction) and `photNegEta` (photon traveling in the negative z direction). The final-state particles were recorded in HepMC format and served as input to the full ATLAS detector simulation using GEANT4. Finally, the simulated $\gamma + \mathrm{A}$ events are reconstructed in the same pp mode and the final Analysis Object Data (AODs) are listed below:

`mc16_5TeV.860044.Starlight_DPMJet_gammaA_photNegEta.recon.AOD.e8077_s4050_r14685`

`mc16_5TeV.860045.Starlight_DPMJet_gammaA_photPosEta.recon.AOD.e8077_s4050_r14685`

`mc16_5TeV.860046.Starlight_DPMJet_gammaA_trk2_photNegEta.recon.AOD`
`.e8077_s4050_r14685`

`mc16_5TeV.860047.Starlight_DPMJet_gammaA_trk2_photPosEta.recon.AOD`
`.e8077_s4050_r14685`

`mc16_5TeV.860048.Starlight_DPMJet_gammaA_trk10_photNegEta.recon.AOD`
`.e8077_s4050_r14685`

`mc16_5TeV.860049.Starlight_DPMJet_gammaA_trk10_photPosEta.recon.AOD`
`.e8077_s4050_r14685`

mc16_5TeV.860050.Starlight_DPMJet_gammaA_trk25_photNegEta.recon.AOD
.e8077_s4050_r14685
mc16_5TeV.860051.Starlight_DPMJet_gammaA_trk25_photPosEta.recon.AOD
.e8077_s4050_r14685

5.1.3.2 PYTHIA Minimum Bias $\gamma + p$ Collisions

A sample of 12 million $\gamma+p$ was generated using PYTHIA (tagged as Pythia8_i--00-14-12 which is available in ATHENA since 19.2.5.32.3,MCProd) with NCTEQ PDFs with A14 tune. The simulation is configured for $\gamma+p$ collisions with the photons produced via bremsstrahlung from a muon beam. All photon-parton interactions are turned "on" to include both direct and resolved photo-nuclear interactions.

The sample (listed below) was generated to ensure optimal coverage over the $N_{\mathrm{ch}}^{\mathrm{rec}}$ range in this analysis. This was achieved by a filtering process of the PYTHIA final state charged particles in the sample. More specifically charged particles of $p_{\mathrm{T}} > 400$ MeV and $|\eta|$ were counted and if this number was less than 20 the event was rejected.

The response of the ATLAS detector is simulated using GEANT4. The simulated PYTHIA $\gamma+p$ events are reconstructed in the same do_HIP mode as in the data sets used in this analysis but without any trigger simulation.

mc16_5TeV.420194.Pythia8EvtGen_A14_NNPDF23LO_mup_PhotonFlux_ntrk20.recon.AOD
.e7566_s3428_r11334

5.1.3.3 HIJING p+Pb Collisions

The Monte Carlo sample used in p+Pb analysis is the HIJING p+Pb collision sample. The HIJING model is detailed in Ref. [140]. The HIJING model combines perturbative-QCD inspired models for multiple jet production with low p_{T} multi-string phenomenology. The model thus extends PYTHIA-type Monte Carlo to include modeling of both high-energy pp collisions, as well as p+A and A+A collisions. Monte Carlo Glauber geometry [25] is included for multiple collisions in

p+A and A+A collisions. The model also includes multiple mini-jet production, nuclear shadowing of parton distribution functions, and a schematic mechanism of jet interactions in dense matter. The phenomenological parameters are adjusted to reproduce essential features of pp multi-particle production data for a wide energy range ($\sqrt{s_{NN}}$ = 5 GeV to 2 TeV). For the sample used here the so-called "jet quenching" feature is turned off.

A sample of five million p+Pb HIJING events is generated. The sample name is listed below.

`mc16_5TeV.420118.Hijing_pPb_Flow_5TeV.recon.AOD.e7285_s3699_r12713`

5.1.3.4 HIJING Pb+Pb Collisions

A sample of 1M peripheral HIJING [141] Pb+Pb collision events at $\sqrt{s_{NN}}$ = 5.02 TeV with impact parameter cut of $10 < b < 20$ fm was utilized for background modeling. The flow modulation in Φ is introduced to the final-state particles at the truth level by implementing the flow-burner module (`FlowAfterburner-00-02-00`):

`mc16_5TeV.420001.Hijing_PbPb_5p02TeV_Peripheral_Flow_JJFV6.recon.AOD`
`.e4858_a890_s3136_r11321`

The response of the ATLAS detector is simulated using GEANT4 [142]. The simulated HIJING events are reconstructed in the same `do_HIP` mode as in the data sets used in this analysis but without any trigger simulation. This sample is used to study the track reconstruction efficiency and background peripheral Pb+Pb event characteristics.

5.2 Event Selection

In this Section, we detail the event selection criteria for UPC and p+Pb events. We focus on the criteria for UPC events first and then p+Pb events while noting the common details for both.

5.2.1 UPC Event Selection

The event selection criteria are matched to those used in the ATLAS UPC two-particle correlation analysis [137]. In the ATLAS UPC two particle-correlation analysis, reconstructed

tracks were selected with $p_{\mathrm{T}} > 400$ MeV and the `MinBias` working point. In the current analysis, reconstructed tracks that enter the charged-hadron yields are selected with $p_{\mathrm{T}} > 100$ MeV and with the `HILoose` working point, which is identical to that of `MinBias` working point above $p_{\mathrm{T}} = 400$ MeV.

In the following subsections event-level definitions such as $N_{\mathrm{ch}}^{\mathrm{rec}}$, $\sum_{\gamma} \Delta\eta^{\mathrm{rec}}$, and ZDC criteria are explained and their selection for this analysis is detailed.

5.2.1.1 Multiplicity Definition

In each selected event, the number of reconstructed tracks passing the `HILoose` working point and $p_{\mathrm{T}} > 400$ MeV is referred to as the charged-particle multiplicity ($N_{\mathrm{ch}}^{\mathrm{rec}}$). This standard ATLAS event class definition utilizes reconstructed tracks that are not corrected for track acceptance and efficiency, see for example Refs. [115, 143–145]. Monte Carlo studies indicate that selections on $N_{\mathrm{ch}}^{\mathrm{rec}}$ correspond to equivalent selections on truth-level charged particles also with $p_{\mathrm{T}} > 0.4$ GeV and $|\eta| < 2.5$, but with $N_{\mathrm{ch}}^{\mathrm{truth}} \approx 1.2 \times N_{\mathrm{ch}}^{\mathrm{rec}}$.

There is one important event selection difference from [10] in that the measurement of charged-particle yields is auto-correlated with the event classification $N_{\mathrm{ch}}^{\mathrm{rec}}$, that is, a single track can enter both the yield and $N_{\mathrm{ch}}^{\mathrm{rec}}$. This auto-correlation bias between the particles included in the event-class definition and those included in the yield calculation results in a bias, which can be visibly seen as a kink feature in the charged-hadron yield at $p_{\mathrm{T}} = 400$ MeV. To address this issue, we utilize a modified definition of event-class multiplicity.

We perform an azimuthal separation of (i) the particles included in the event-class definition and (ii) those included in the yield calculation. The yield is defined over the fraction (ε_{ϕ}) of azimuthal space, while the event-class multiplicity is defined within the other fraction (1-ε_{ϕ}) of azimuthal space. In the limit as $\varepsilon_{\phi} \to 0$, one recovers the standard event-class multiplicity. The default is to set $\varepsilon_{\phi} = 0.01$ such that 99% of the azimuthal space is used for $N_{\mathrm{ch}}^{\mathrm{rec}}$ and only 1% for the yield. In the limit, as ε_{ϕ} goes to zero, the $N_{\mathrm{ch}}^{\mathrm{rec}}$ definition is identical to the standard definition. Note that we do not correct this modified $N_{\mathrm{ch}}^{\mathrm{rec}}$ by a multiplicative factor of $1/0.99 = 1.01$ since

the $N_{\mathrm{ch}}^{\mathrm{rec}}$ values must be integer. This small difference is covered by the systematic uncertainty determined by the variation done with $\varepsilon_{\phi} = 0.02$ as detailed in Section 5.5.3.

The above procedure is well defined; however, it would result in a loss of 99% of the charged-hadron statistics and thus limit the yield measurements. Thus, we perform 100 (50) pseudo-experiments per event for $\varepsilon_{\phi} = 0.01$ (0.02), where in each case we select a different region in azimuthal space for the yield. Each pseudo-experiment is then treated as a separate event, *i.e.*, with its only $N_{\mathrm{ch}}^{\mathrm{rec}}$ and yield. Thus, the full statistical precision is regained. Closure tests with Monte Carlo indicate that this method effectively removes the auto-correlation bias.

The $N_{\mathrm{ch}}^{\mathrm{rec}}$ distribution in Pb+Pb UPC collisions is shown in Figure 5.1, corresponding to minimum bias events with the additional $\sum_{\gamma} \Delta\eta^{\mathrm{rec}}$ requirement. The $N_{\mathrm{ch}}^{\mathrm{rec}}$ range [25,60] utilized in this analysis is highlighted. This range is chosen since UPC events with $N_{\mathrm{ch}}^{\mathrm{rec}} < 25$ suffer from a rather uncertain mixture of photo-nuclear and background processes. The upper bound is chosen as $N_{\mathrm{ch}}^{\mathrm{rec}} = 60$ considering the statistical limitations in the higher multiplicity region.

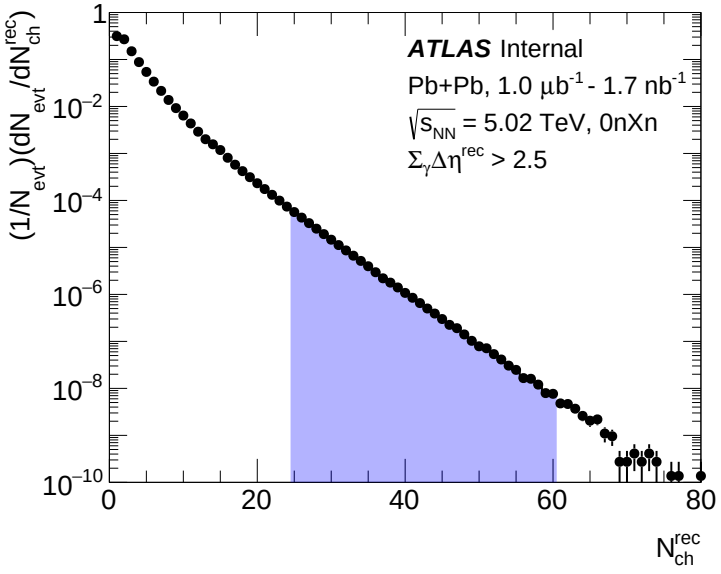

Figure 5.1: Shown is the multiplicity distribution ($N_{\mathrm{ch}}^{\mathrm{rec}}$) from Pb+Pb UPC collisions. The $N_{\mathrm{ch}}^{\mathrm{rec}}$ range [25,60] utilized in this analysis is highlighted.

5.2.1.2 Photo-Nuclear Gap and Coordinate Definitions

The photon- vs Pb-going direction is determined in the data sample by the ZDC trigger, which has exclusive OR logic. The photon-going direction has a ZDC trigger signal consistent with no incident neutrons. This also sets the customary coordinates for $\gamma + \mathrm{A}$ collisions with the photon-going direction defined as positive rapidity.

Pseudorapidity gap selections [107] are made to distinguish between different physics processes such as photo-nuclear collisions, rapidity-asymmetric peripheral Pb+Pb collisions, and $\gamma + \gamma \to X$ processes. For $\gamma + \mathrm{A}$ collisions, a gap in particle production in the photon-going direction should be present. Such a gap requirement can effectively remove most of the Pb+Pb background. To that end, the $\sum_\gamma \Delta\eta^{\mathrm{rec}}$ variable is calculated using both tracks and topoclusters. The topoclusters are required to have $p_{\mathrm{T}} > 200$ MeV, pass the hot-spot rejection, and pass an additional significance cut used in Ref. [107]. The tracks must pass the `HILoose` working point and have $p_{\mathrm{T}} > 400$ MeV. These two sets of objects are combined and ordered in η, giving an ordered list η_i. The list is used to calculate $\sum_\gamma \Delta\eta^{\mathrm{rec}}$. Considering one half of the detector ($\eta > 0$), all gaps of $|\Delta\eta| > 0.5$ are summed, where the location $\eta = 0$ is considered to have a default particle as detailed in the equation:

$$\sum_{\gamma} \Delta\eta^{\mathrm{rec}} = \sum_{i=N}^{p} (\eta_i - \eta_{i-1})\Theta(\eta_i - \eta_{i-1} - 0.5), \tag{5.1}$$

where Θ is the Heaviside step function, N is the number of particles in the one half of the detector and p is the imaginary particle at $\eta = 0$. The so-called "photon sum-of-gap" variable ($\sum_\gamma \Delta\eta^{\mathrm{rec}}$) is the sum of all rapidity gaps that are greater than 0.5 on the photon-going side of the detector. The $\sum_\gamma \Delta\eta^{\mathrm{rec}}$ distribution in Pb+Pb UPC collisions and DPMJET-III for comparison are shown in Figure 5.2. We note that the DPMJET-III results have fewer events at large $\sum_\gamma \Delta\eta^{\mathrm{rec}}$ values. The data has a significant contribution at small $\sum_\gamma \Delta\eta^{\mathrm{rec}}$ not present in DPMJET-III, likely dominated by non-UPC interactions, e.g., hadronic peripheral Pb+Pb collisions, that are a background to this measurement modeled using HIJING Pb+Pb, also shown in Figure 5.2. Hence, the region $\sum_\gamma \Delta\eta^{\mathrm{rec}} > 2.5$ is utilized in this analysis following the procedure in Ref. [137].

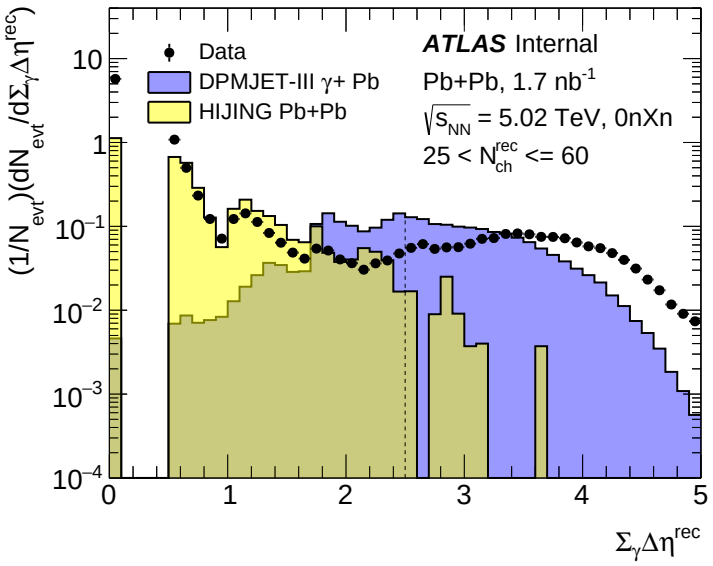

Figure 5.2: Shown are the $\sum_\gamma \Delta\eta^{\text{rec}}$ distribution from Pb+Pb UPC collisions, as well as from the Monte Carlo DPMJET-III and HIJING for comparison. The Monte Carlo results are scaled to match the data integral in the region $\sum_\gamma \Delta\eta^{\text{rec}} > 2.5$.

5.2.1.3 UPC Event Selection Criteria

The set of minimal requirements in Pb+Pb UPC events enforced at the AOD to the Tree-level processing is now detailed. The events must:

- pass the Good Run List (GRL), which ensures the high quality of data received from the sub-detectors of ATLAS:

  The Pb+Pb UPC GRL used is `data18_hi.periodAllYear_DetStatus-v104-pro22-08_Unknown_PHYS_HeavyIonP_All_Good_ignore_TOROIDSTATUS.xml`.

- have at least 1 but fewer than 400 tracks in the InDetTrackParticles container
- have one reconstructed vertex
- $|z_{\text{vtx}}^{\text{pri}}| < 100$ mm

These requirements, except the GRL requirement, were also imposed on the MC samples used in this analysis.

In addition to this, we apply specific event classification criteria for photo-nuclear events which are the same event selection cuts detailed in Ref [137]. These cuts select photo-nuclear collisions while rejecting physics backgrounds, such as peripheral Pb+Pb events or $\gamma + \gamma \rightarrow$ (charged particles) and non-physics backgrounds with systematic detector effects (such as pileup).

- ZDC_A_VZDC_C or ZDC_C_VZDC_A trigger bits required.
- Offline ZDC energy > 1 TeV on the side with positive ZDC signal (ZDC trigger).
- Offline ZDC energy < 1 TeV on the side with no ZDC signal (VZDC trigger).
- $\sum_{\gamma} \Delta\eta^{\mathrm{rec}} > 2.5$ with photon direction set by VZDC trigger.
- out-of-time pileup: $\mathrm{FCAL_A}$ and $\mathrm{FCAL_C}$ $\sum \mathrm{E_T} > -10$ GeV as well as the number of significantly negative calorimeter energy sum rings less than 15.

5.2.1.4 Residual Backgrounds in the Event Sample

The UPC Pb+Pb event selection is identical to that in Ref. [10], with full details provided in ATLAS Analysis Note [146]. Thus, the issue of residual backgrounds in the event sample is identical to the previous analysis – see the discussion starting in Section 4.2.1 [146]. We briefly summarize those findings here.

There are two different pileup effects considered: out-of-time pileup (effects from collisions in previous bunch crossings) and in-time pileup (effects from multiple collisions in the same bunch crossing). With specific selection cuts detailed above, the remaining effects from these contributions are negligible and require no further accounting.

Beam splash events have been studied as a possible contamination in ZDC_XOR triggered events [93]. These are events where beam particles collide with the beam pipe or collimators or protons from the imperfect vacuum upstream of the interaction region. These events can leave energy deposits in some sub-detectors and have an asymmetric distribution due to the fixed-target nature of the collisions. These events are effectively removed by requiring exactly one reconstructed

vertex. With specific selection cuts detailed above, the remaining effects from these contributions are negligible and require no further accounting.

Finally, there is the important potential contribution of Pb+Pb peripheral inelastic collisions contaminating the UPC Pb+Pb sample despite the 0nXn ZDC requirement and photon sum-of-gaps selection. This background is detailed in Section 4.4 of ATLAS Analysis Note [146].

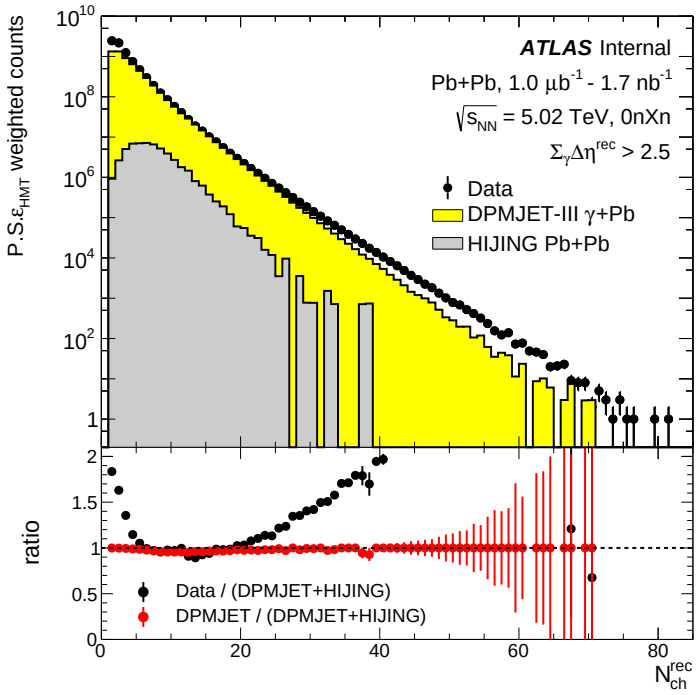

Figure 5.3: Shown in the top panel are the signal (DPMJET-III) and background (HIJING) utilized in the two-component fit, along with Pb+Pb UPC data as a function of $N_{\mathrm{ch}}^{\mathrm{rec}}$. The bottom panel shows the ratio of data to the two-component fit in black markers and the ratio of DPMJET-III to the two-component fit, referred to as purity, in red markers.

Figure 5.3 shows the signal and background utilized in the two-component fit, along with Pb+Pb UPC data as a function of $N_{\mathrm{ch}}^{\mathrm{rec}}$ in the region $\sum_{\gamma} \Delta\eta^{\mathrm{rec}} > 2.5$. The fit is performed using DPMJET-III as the signal and HIJING as the background. The lower panel shows the ratio of DPMJET-III to the two-component fit in red markers, essentially the purity of γA events as a function of $N_{\mathrm{ch}}^{\mathrm{rec}}$. This procedure indicates an estimated purity of 95% at approximately $N_{\mathrm{ch}}^{\mathrm{rec}} = 10$, while higher multiplicity bins, $N_{\mathrm{ch}}^{\mathrm{rec}} > 25$, indicate a significantly higher purity of 98%. This purity estimation is re-binned and shown in Figure 5.4 as the DPMJET-III +HIJING $N_{\mathrm{ch}}^{\mathrm{rec}}$ derived result.

The details of the other two procedures, namely, DPMJET-III +HIJING $\sum_\gamma \Delta\eta^{\rm rec}$ derived result and PYTHIA +HIJING $\sum_\gamma \Delta\eta^{\rm rec}$ derived result are included in Appendix A.6.

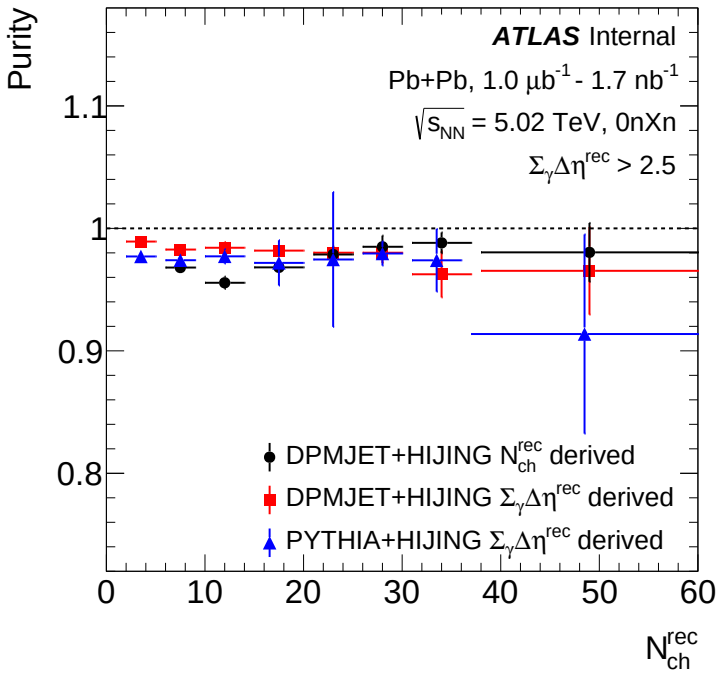

Figure 5.4: Three estimates for the purity of UPC Pb+Pb selected events utilizing the Monte Carlo DPMJET-III or PYTHIA for the UPC case and HIJING for the Pb+Pb peripheral collision case. Shown is the extracted purity (UPC / (UPC + background)) as a function of $N_{\rm ch}^{\rm rec}$.

Figure 5.4 shows the results from three methods to estimate purity. Each method involves doing a two-component fit (one component for UPC signal events and one component for background events) to a particular data observable. For the black (red) points, the signal component is modeled by DPMJET-III, and the background, *i.e.*, peripheral Pb+Pb hadronic collisions, is modeled by HIJING, and the two-component fit applied to the data distribution for $N_{\rm ch}^{\rm rec}$ ($\sum_\gamma \Delta\eta^{\rm rec}$). For the blue points, the signal component is modeled by PYTHIA and the background again by HIJING and the two-component fit is applied to the data distribution for $\sum_\gamma \Delta\eta^{\rm rec}$. None of the two-component fits gives a perfect description of the data, particularly at low $N_{\rm ch}^{\rm rec}$ as shown in Figure 5.3. The purity estimates derived using the two-component fit to the data distribution in various multiplicity bins indicate a greater than 95% purity for the entire multiplicity range.

To gauge the possible impact of contamination, we utilize the estimate from Figure 5.4, namely the purity estimate using DPMJET-III + HIJING and two-component fitting the $N_{\mathrm{ch}}^{\mathrm{rec}}$ data distribution.

UPC events with lower multiplicity also suffer from a rather uncertain mixture of photo-nuclear and other processes. Hence this analysis will only consider the region $N_{\mathrm{ch}}^{\mathrm{rec}} > 25$.

Even for the region with $N_{\mathrm{ch}}^{\mathrm{rec}} > 25$, there is still a small potential contamination. To investigate the impact of this potential contamination of the UPC Pb+Pb sample, we assume for a given $N_{\mathrm{ch}}^{\mathrm{rec}}$ selection, the measured particle yield ($\mathrm{UPC}_{\mathrm{measured}}$) is a combination of "true" UPC Pb+Pb events ($\mathrm{UPC}_{\mathrm{true}}$) and a contamination contribution ($\mathrm{UPC}_{\mathrm{contamination}}$). One can then estimate the "true" UPC yield using the following equation:

$$\mathrm{UPC}_{\mathrm{measured}} = \mathrm{purity} \times \mathrm{UPC}_{\mathrm{true}} + (1 - \mathrm{purity}) \times \mathrm{UPC}_{\mathrm{contamination}}. \tag{5.2}$$

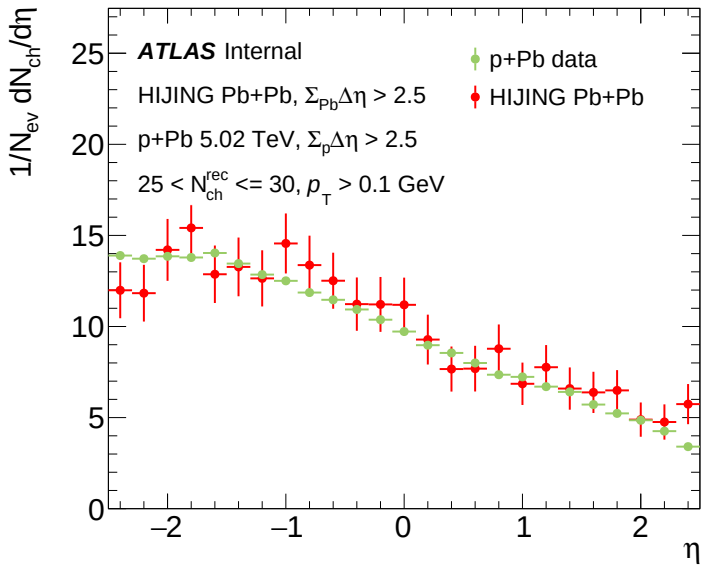

Figure 5.5: Shown is the $\mathrm{d}N_{\mathrm{ch}}/\mathrm{d}\eta$ distribution in p+Pb collisions with $\sum_{\gamma} \Delta\eta^{\mathrm{rec}} > 2.5$ applied in the proton-going direction in green markers. Additionally, shown is the HIJING Pb+Pb with $\sum_{\gamma} \Delta\eta^{\mathrm{rec}} > 2.5$ applied in the Pb-going direction with the largest gap in black markers. Both plots correspond to the $N_{\mathrm{ch}}^{\mathrm{rec}}$ selection 25-30 and $p_{\mathrm{T}} > 0.1$ GeV.

If we assume that the contamination is dominated by inelastic, hadronic peripheral Pb+Pb

events that pass the sum-of-gaps requirements, we can utilize p+Pb collision data as a proxy for the $\mathrm{UPC}_{\mathrm{contamination}}$. It is notable that for the entire $N_{\mathrm{ch}}^{\mathrm{rec}}$ range used in this analysis, the p+Pb $\mathrm{d}N_{\mathrm{ch}}/\mathrm{d}\eta$ is nearly symmetric in η and hence provides a good proxy for the kinematics in peripheral Pb+Pb collisions, but with a reduced UPC contribution since both beams do not have electric charge +82e. In p+Pb, most UPC events will have photon emitted by the Pb nucleus since the photon emission probability is substantially higher for nuclei with higher Z. To further reduce the UPC contribution, we eliminate events with lower ZDC energies in the Pb-going side, $\mathrm{E}^{\mathrm{ZDC,Pb}} < 1$ TeV. This energy cutoff is somewhat arbitrary but is far enough below the single neutron peak at 2.51 TeV that these events can safely be categorized as having no neutrons. Note that this selection has no impact on events with $N_{\mathrm{ch}}^{\mathrm{rec}} > 25$. In this procedure, p+Pb data events with the $\sum_{\gamma} \Delta\eta^{\mathrm{rec}} > 2.5$ selection in the proton-going direction are utilized. Figure 5.5 demonstrates that the p+Pb with sum-of-gap cut applied can serve as an effective proxy for the peripheral Pb+Pb collisions since it shows very good agreement with the Monte Carlo model, HIJING, which simulates peripheral Pb+Pb collisions.

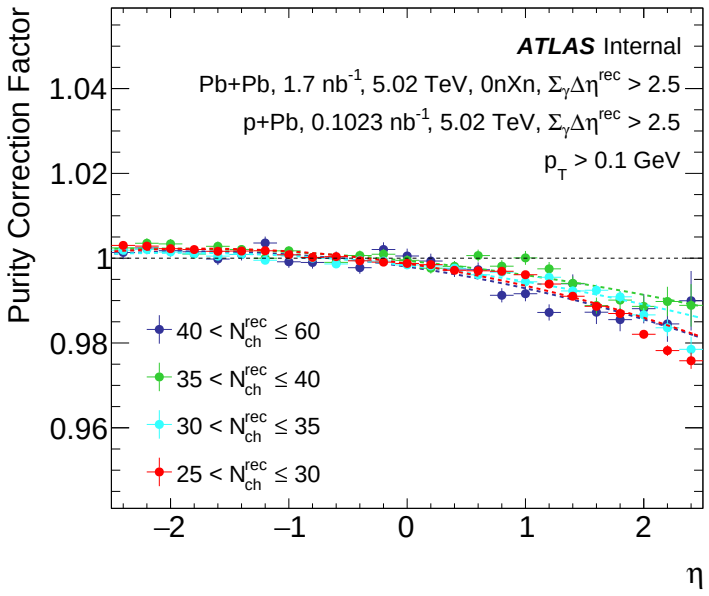

Figure 5.6: Shown are the ratio $\mathrm{UPC}_{\mathrm{true}}/\mathrm{UPC}_{\mathrm{measured}}$ for the $\mathrm{d}N_{\mathrm{ch}}/\mathrm{d}\eta$ observable as a function of η in each $N_{\mathrm{ch}}^{\mathrm{rec}}$ selection $N_{\mathrm{ch}}^{\mathrm{rec}} > 25$.

The purity correction factor, PCF, is defined as:

$$\mathrm{PCF} = \frac{\mathrm{UPC_{true}}}{\mathrm{UPC_{measured}}}, \tag{5.3}$$

and is calculated for both $\mathrm{d}N_{\mathrm{ch}}/\mathrm{d}\eta$ as a function of η and $\mathrm{d}N^2_{\mathrm{ch}}/\mathrm{d}p_{\mathrm{T}}\mathrm{d}\eta$ as a function of p_{T}. Figure 5.6 shows the purity correction factor, PCF, as a function of η in each $N^{\mathrm{rec}}_{\mathrm{ch}}$ selection. The influence of contamination is largest ($< 4\%$) at positive η as the true UPC Pb+Pb particle yields are expected to be very asymmetric as compared with the contamination particle yields.

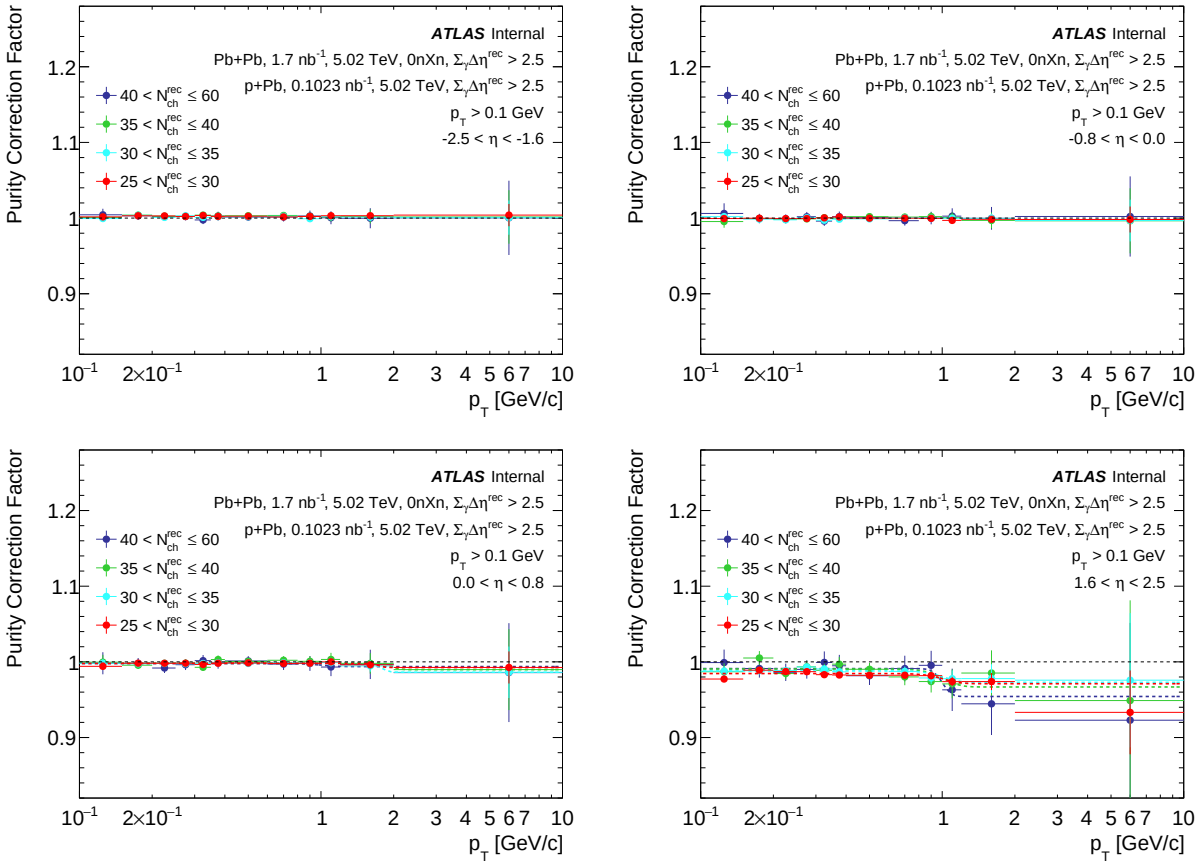

Figure 5.7: Shown are the ratio $\mathrm{UPC_{true}}/\mathrm{UPC_{measured}}$ for the $\mathrm{d}N^2_{\mathrm{ch}}/\mathrm{d}p_{\mathrm{T}}\mathrm{d}\eta$ observable as a function of p_{T} in η slices: [-2.5,-1.6] (top left panel), [-0.8,0.0] (top right panel), [0.0,0.8] (bottom left panel) and [1.6,2.5] (bottom right panel) for $N^{\mathrm{rec}}_{\mathrm{ch}} > 25$.

Figure 5.7 shows the purity correction factor, PCF, as a function of p_{T} in each η slice, for different $N^{\mathrm{rec}}_{\mathrm{ch}}$ selections. The potential contamination of UPC events at high p_{T} regions is important to estimate since hadronic backgrounds can be significant in these regions. For $N^{\mathrm{rec}}_{\mathrm{ch}} > 25$, the PCF

is approximately 95% for $p_{\mathrm{T}} > 2$ GeV even at most forward rapidity bin η:[1.6,2.5], and consistent with unity within statistical uncertainties elsewhere.

Under the assumption that the purity is correctly determined and that the p+Pb collision data is a good proxy for the contamination, the experimental data can be corrected by PCF as a function of η and p_{T}. The experimental results are corrected using the purity estimate from the DPMJET-III + HIJING $N_{\mathrm{ch}}^{\mathrm{rec}}$ derived result and then results are varied by applying a 100% systematic uncertainty on the purity estimate. For $N_{\mathrm{ch}}^{\mathrm{rec}} > 25$, the resulting correction is on the order of $<$ 1-3% and hence with a 1-3% systematic uncertainty.

5.2.2 p+Pb Event Selection

In this section, the p+Pb multiplicity definition and event selection criteria are detailed.

5.2.2.1 Multiplicity Definition

In each selected event, the number of reconstructed tracks passing the `HILoose` working point and $p_{\mathrm{T}} > 400$ MeV is referred to as the charged-particle multiplicity ($N_{\mathrm{ch}}^{\mathrm{rec}}$).

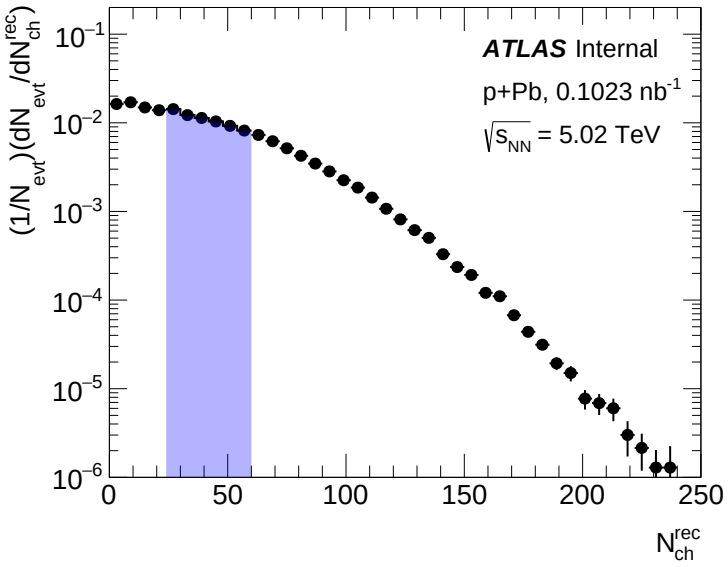

Figure 5.8: Shown is the multiplicity distribution ($N_{\mathrm{ch}}^{\mathrm{rec}}$) from p+Pb collisions corresponding to minimum bias events.

The multiplicity distribution p+Pb collisions is shown in Figure 5.8, corresponding to minimum bias events. The $N_{\text{ch}}^{\text{rec}}$ range [25,60] utilized in this analysis is highlighted, and matches that selected for the UPC Pb+Pb analysis. For later comparison of Pb+Pb UPC and p+Pb collisions, the p+Pb events are re-weighted within the shown range to match the Pb+Pb UPC $N_{\text{ch}}^{\text{rec}}$ distribution.

We highlight that the modified event selection method for Pb+Pb UPC events as detailed in Section 5.2.1.1, is not applied in the p+Pb case as it has negligible impact due to the much less steeply falling multiplicity distribution.

5.2.2.2 p+Pb Event Selection Criteria

In this subsection, the p+Pb event selection criteria are detailed. The events must:

- pass the Good Run List (GRL), which ensures the high quality of data received from the sub-detectors of ATLAS:
  The p+Pb GRL used is `data16_hip5TeV.periodAllYear_DetStatus-v105-pro22-13_Unknown_PHYS_HeavyIonP_All_Good.xml`
- have at least 1 but fewer than 400 tracks in the InDetTrackParticles container
- have one reconstructed vertex
- $|z_{\text{vtx}}^{\text{pri}}| < 100$ mm

These requirements, except the GRL requirement, were also imposed on the MC samples used in this analysis.

5.3 Track Selection

The primary reconstructed object used in the analysis of charged-hadron yields is the inner detector track.

5.3.1 Track Quality Selection

The `HILoose` working point was chosen for a high-purity selection and to most closely resemble the quality cuts imposed by the high-multiplicity trigger (HMT) component of the trigger chain. The `HILoose` working point contains the following quality cuts:

- $p_{\mathrm{T}} > 100$ MeV
- $|\eta_{\mathrm{trk}}| < 2.5$
- $\mathrm{N_{Pix}} \geq 1$
- $\mathrm{N_{SCT}} \geq 2, 4, 6$ for $p_{\mathrm{T}} < 300$ MeV, < 400 MeV, > 400 MeV respectively.
- $\mathrm{N_{IBL}} + \mathrm{N_{B-Layer}} > 0$, if both IBL hit and B-layer hit are expected
- $\mathrm{N_{IBL}} + \mathrm{N_{B-Layer}} \geq 0$, if either IBL hit or B-layer hit is not expected
- $\mathrm{d_0}$ wrt. primary vertex less than 1.5 mm
- $\mathrm{z_0} \sin\theta$ wrt. primary vertex less than 1.5 mm

The tracks entering the yield calculation in this analysis use the `HILoose` working point and $p_{\mathrm{T}} > 100$ MeV.

5.3.2 Tracking Performance

To check the performance of the chosen track selection, the distributions of the number of tracks as a function of the number of hits in the BL, IBL, SCT layer, and Pixel layer are compared between data and MC, as shown in Figure 5.9 and Figure 5.10. Figure 5.11 shows the number of

tracks as a function of d_0 and $z_0 \sin\theta$. For these results, the event and other track selections are applied (except the cut on the variable which is shown in each distribution).

The differences in data and MC for BL hits and IBL hits come from differences in the disabled modules between simulation and data. The differences in d_0 and $z_0 \sin\theta$ distribution between data and MC are within 20% in the outer region, *i.e.*, large values of d_0 and $z_0 \sin\theta$. We note that variations in these track quality selections are utilized for estimating systematic uncertainties.

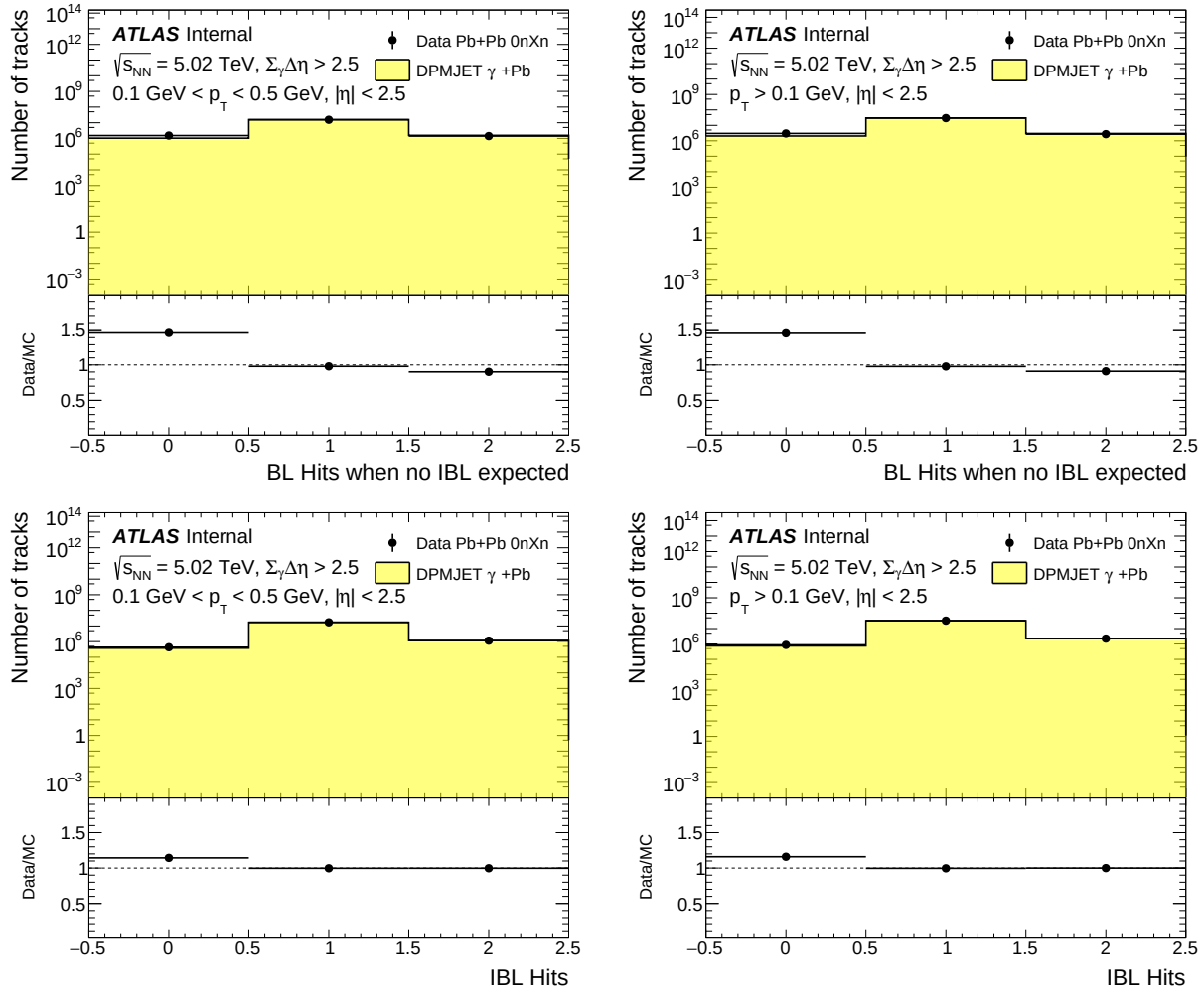

Figure 5.9: Shown is the number of tracks with different numbers of BL hits (top) and the number of tracks with different numbers of IBL hits (bottom). On the left-hand side, these are for tracks with $100 < p_{\mathrm{T}} < 500$ MeV, and on the right side for the full phase-space with $p_{\mathrm{T}} > 100$ MeV. The MC distribution is normalized to match the same area as that of the data distribution.

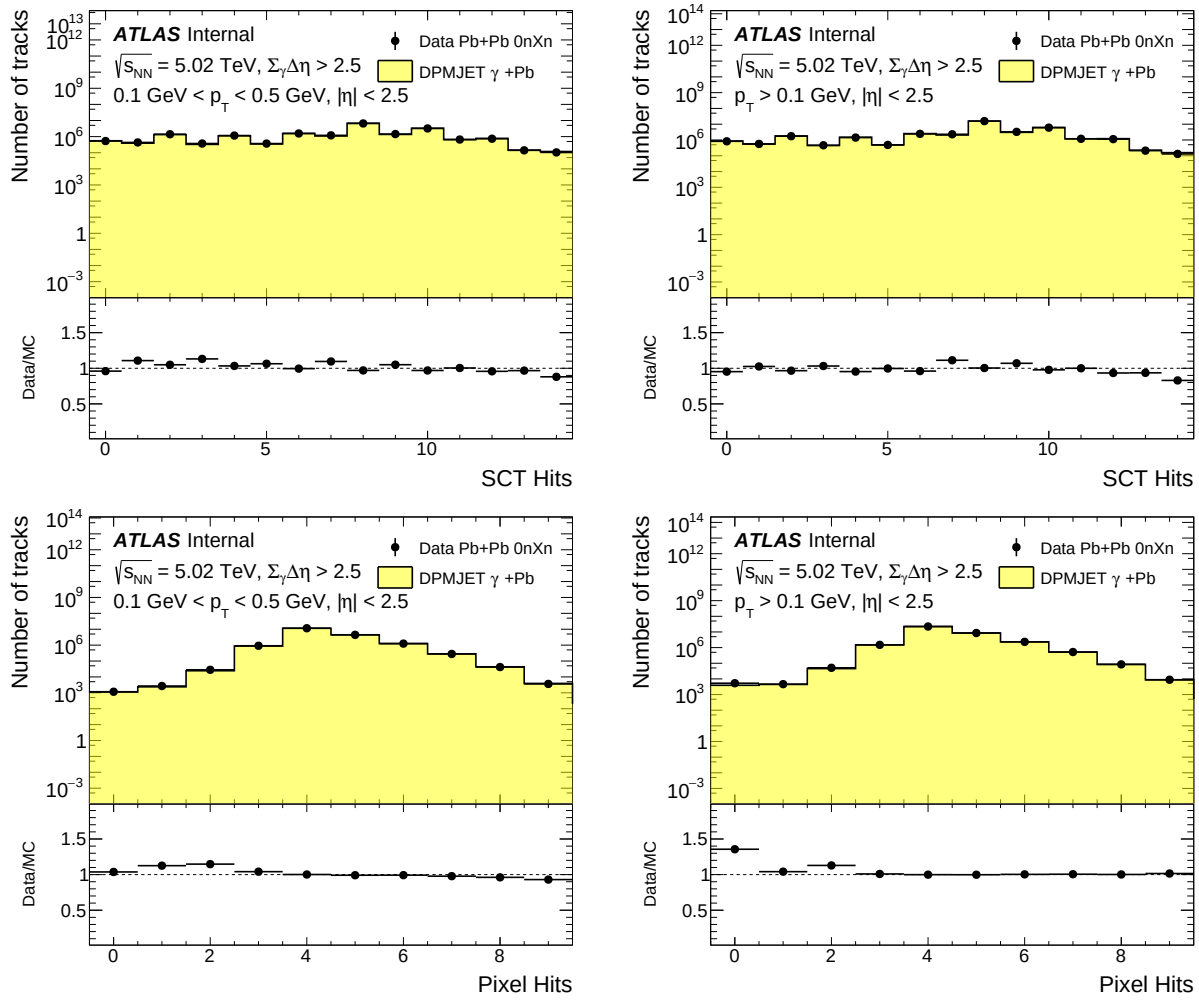

Figure 5.10: Shown is the number of tracks with different numbers of SCT hits (top) and the number of tracks with different numbers of Pixel layer hits (bottom). On the left-hand side, these are for tracks with $100 < p_{\mathrm{T}} < 500$ MeV, and on the right side for the full phase-space with $p_{\mathrm{T}} > 100$ MeV. The MC distribution is normalized to match the same area as that of the data distribution.

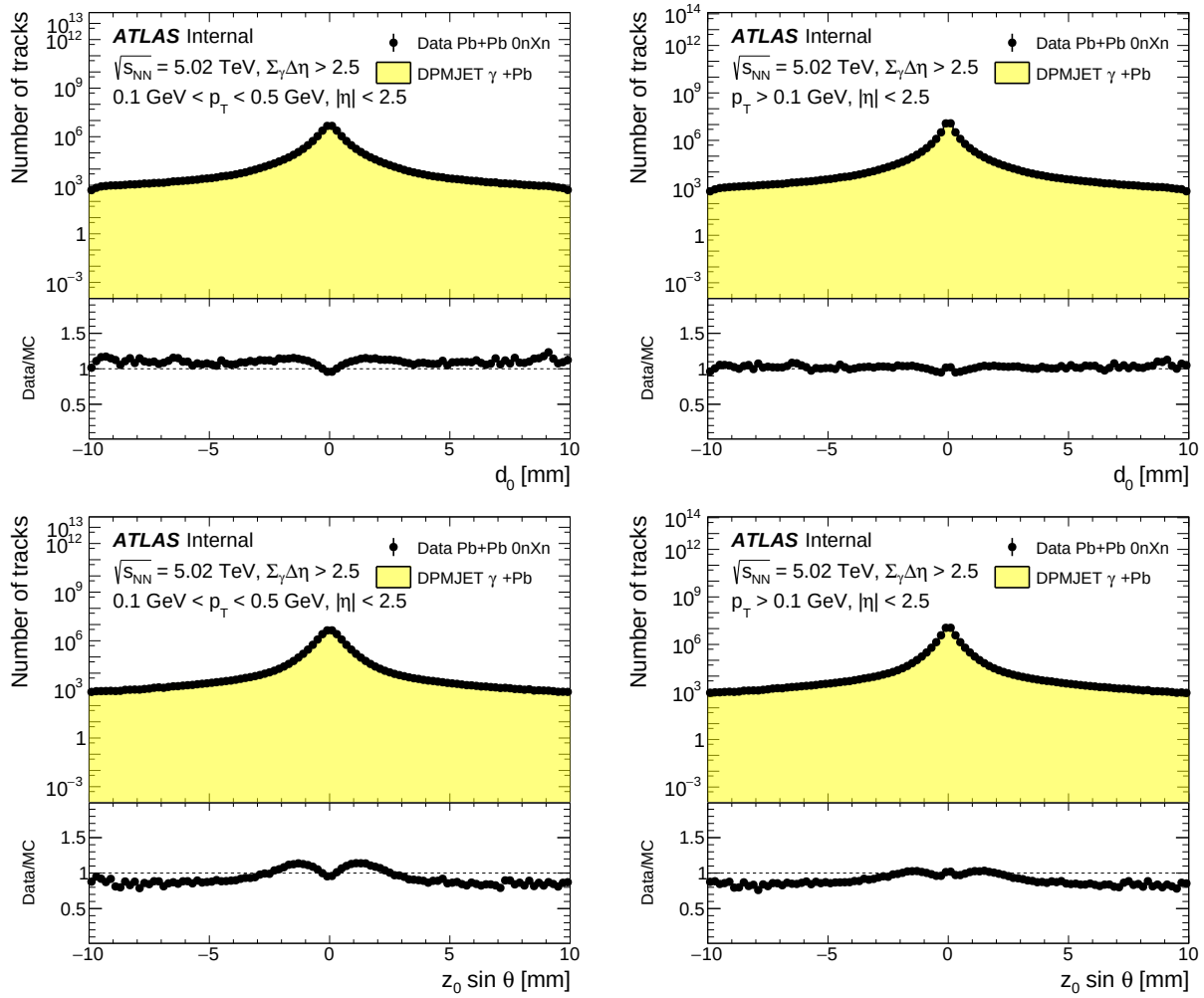

Figure 5.11: Shown are the number of tracks as a function of d_0 (top) and $z_0 \sin\theta$ (bottom). On the left-hand side, these are for tracks with $100 < p_{\mathrm{T}} < 500$ MeV, and on the right side for the full phase-space with $p_{\mathrm{T}} > 100$ MeV. The MC distribution is normalized to match the same area as that of the data distribution.

5.3.3 Track Definitions

Following are the common tracking definitions used for charged particles reconstructed in simulated events:

- The truth-matching probability is the probability that a reconstructed track corresponds to any truth track. It is defined by the expected number vs. observed number of hits between a given truth track (Ref.[147]) given by:

$$P = \frac{10 \times \mathrm{N}_{\mathrm{pixel}}^{\mathrm{common}} + 5 \times \mathrm{N}_{\mathrm{SCT}}^{\mathrm{common}} + 1 \times \mathrm{N}_{\mathrm{TRT}}^{\mathrm{common}}}{10 \times \mathrm{N}_{\mathrm{pixel}}^{\mathrm{track}} + 5 \times \mathrm{N}_{\mathrm{SCT}}^{\mathrm{track}} + 1 \times \mathrm{N}_{\mathrm{TRT}}^{\mathrm{track}}}. \tag{5.4}$$

- A track is considered truth-matched if the truth-matching probability is above 0.5.
- A track is fake if it is not truth-matched.
- A track is secondary if it is truth-matched but originates in the G4 simulation (e.g. electrons produced in an electromagnetic shower). Particles with truth bar-code $\notin (10000, 200000)$ are secondary in DPMJET-III γA.
- A track is primary if it is neither fake nor secondary.

We highlight that varying the truth-matching probability is one of the considered sources of systematic uncertainty - see Section 5.5.9. We also note that the MC has been run keeping track of truth particles down to 20 MeV.

5.3.4 Track Reconstruction Efficiency

There is a non-zero probability that a given charged particle will or will not be observed in the analysis due to detector effects, quality selection, etc. This leads to some particles being missed or left out by the reconstruction procedure. The reconstruction efficiency is defined as the ratio of the number of truth particles whose associated reconstructed track has a truth-matched particle $N_{\mathrm{truth}}^{\mathrm{matched}}$ to the total number of truth particles N_{truth}, as a function of both p_{T} and η:

$$\varepsilon(p_{\mathrm{T}}, \eta) = \frac{N_{\mathrm{truth}}^{\mathrm{matched}}(p_{\mathrm{T}}, \eta)}{N_{\mathrm{truth}}(p_{\mathrm{T}}, \eta)}. \tag{5.5}$$

To compensate for these missed particles, the reconstruction efficiency is applied as weight factor $= 1/\varepsilon(p_{\mathrm{T}}, \eta)$ for the tracks entering the charged-hadron yield as a function of p_{T} and η.

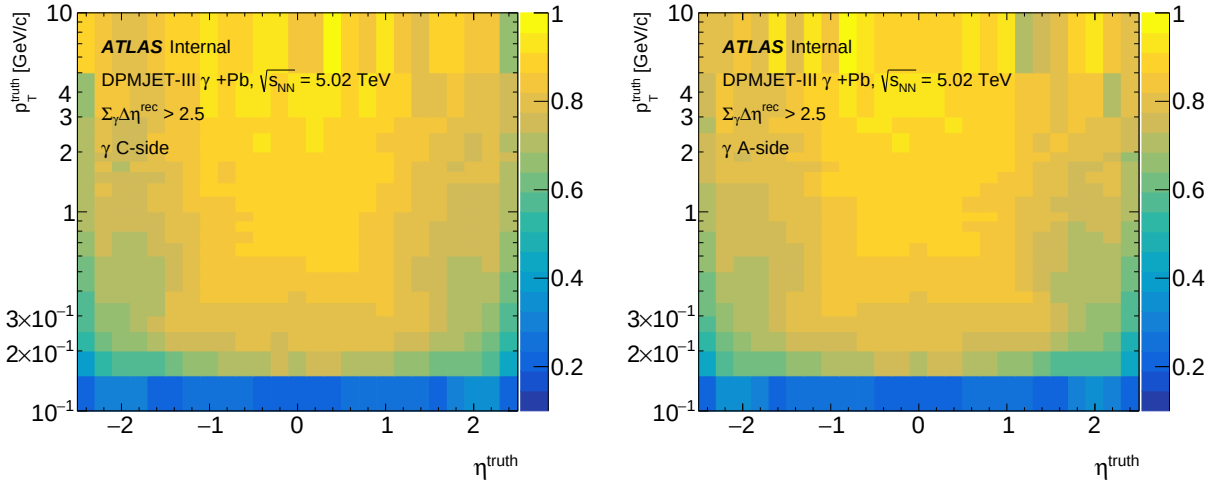

Figure 5.12: Single track efficiency map for the HILoose working point as a function of p_{T} and η in Pb+Pb UPC for photon C-side (left) and photon A-side (right).

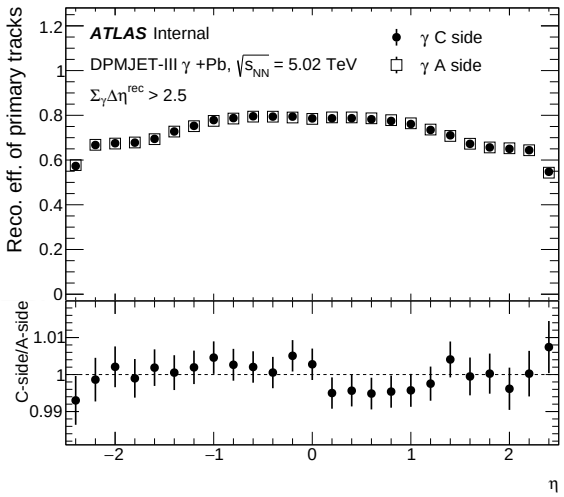

Figure 5.13: Track reconstruction efficiency as a function of η comparing photon-going direction as C-side vs A-side.

In Pb+Pb UPC collisions, to account for photon-going directions towards the C-side and A-side of the detector separately, the track reconstruction efficiency is applied separately to events where the photon is going in the C-side versus the A-side. Figure 5.12 shows the track reconstruction

efficiency for primary tracks for photons going in the C-side and A-side separately. A comparison of the track reconstruction efficiency between the cases for photons going in the C-side and A-side is shown in Figure 5.13, where $\eta < 0$ and $\eta > 0$ is treated as the Pb-going side and photon-going side respectively. There is only $< 1\%$ difference between the track reconstruction efficiency between photons going in the C-side vs A-side.

The track reconstruction efficiency for primary tracks in p+Pb is shown in Figure 5.14. This efficiency was measured with the HIJING sample as detailed in Section 5.1.3.

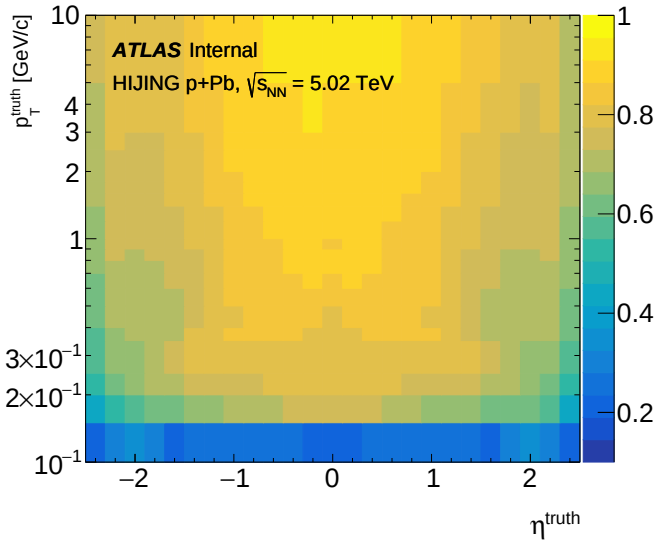

Figure 5.14: Single track efficiency map for primary tracks as a function of p_{T} and η in p+Pb.

In principle, there could be some interference/interaction between the sum-of-gaps UPC event selection cut and the track reconstruction efficiency, *i.e.*, where it is less likely to reconstruct a track and hence have a larger $\sum_{\gamma} \Delta\eta^{\mathrm{rec}}$. To test for this effect, Figure 5.15 shows the track reconstruction efficiency as a function of η in DPMJET-III with and without implementing the $\sum_{\gamma} \Delta\eta^{\mathrm{rec}}$ cut. The ratio panel shows that the sum of gaps does not change the track reconstruction efficiency in the photon-going direction significantly. No additional uncertainties are considered for this issue.

In the analysis, the track reconstruction efficiency as a function of p_{T} is fitted using a polynomial function of 5^{th} order in $\log(p_{\mathrm{T}})$ at low p_{T} ($p_{\mathrm{T}} < 1$ GeV) and a polynomial function of 1^{st} order in $\log(p_{\mathrm{T}})$ at high p_{T} ($p_{\mathrm{T}} > 1$ GeV) in each of the 25 η bins spanning from -2.5 to 2.5 as shown

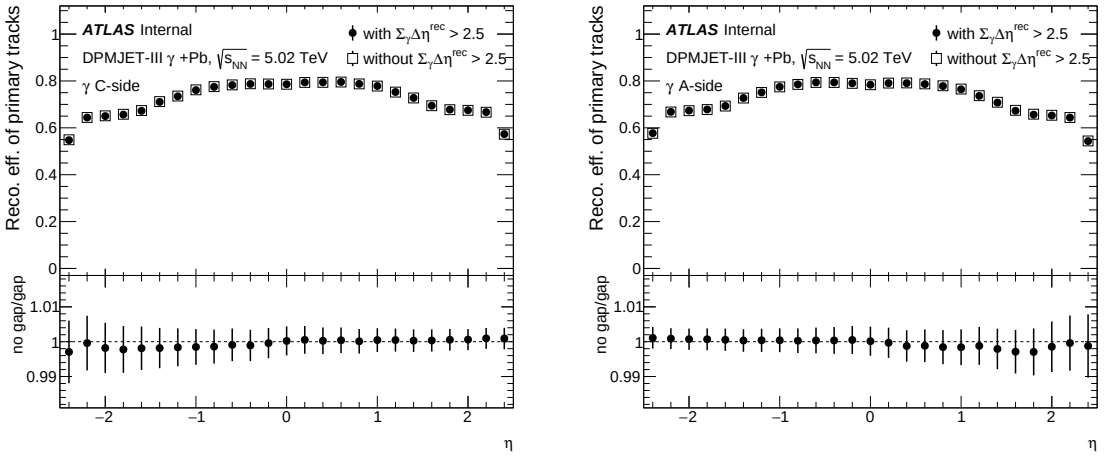

Figure 5.15: Track reconstruction efficiency as a function of η with and without the implementation of sum-of-gaps cut in DPMJET-III for photon C-side (left) and photon A-side (right).

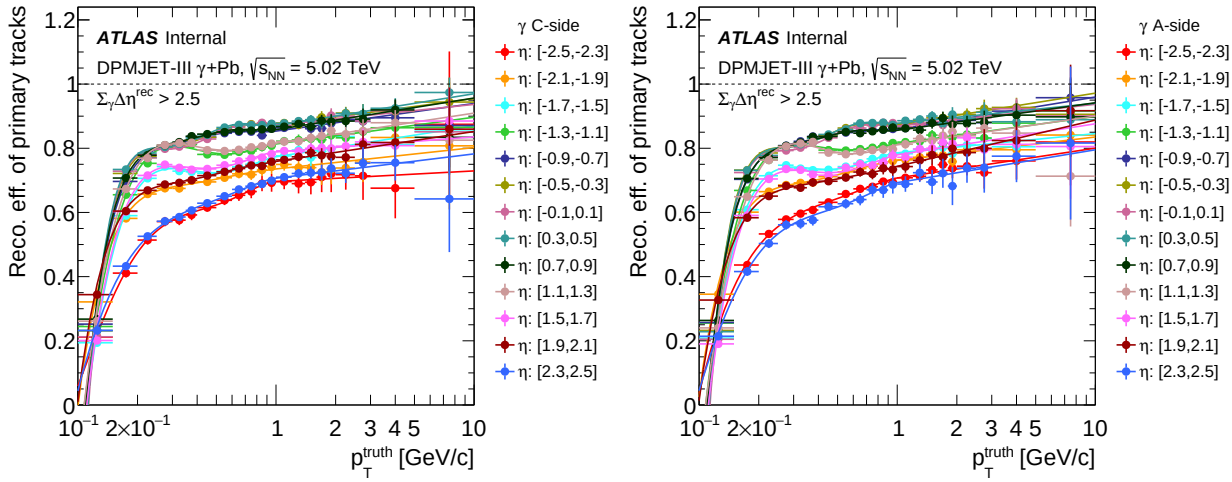

Figure 5.16: Shown is the track reconstruction efficiencies as a function of $p_{\mathrm{T}}^{\mathrm{truth}}$, fitted using a polynomial function of 5^{th} order in $\log(p_{\mathrm{T}})$ at low p_{T} ($p_{\mathrm{T}} < 1$ GeV) and a polynomial function of 1^{st} order in $\log(p_{\mathrm{T}})$ at high p_{T} ($p_{\mathrm{T}} > 1$ GeV) in selected η slices in DPMJET-III for photon C-side (left) and photon A-side (right).

in Figure 5.16 and Figure 5.17 in DPMJET-III and HIJING respectively. The two fit functions are made continuous at the intersection $p_{\mathrm{T}} = 1$ GeV. A zoomed-in version of the reconstruction efficiency in DPMJET-III is shown in Figure 5.18. The uncertainty on the fit values is accounted for and discussed in Sec 5.5.13. The fit functions are used for the actual track-by-track efficiency correction to remove statistical fluctuations, particularly at high p_{T}.

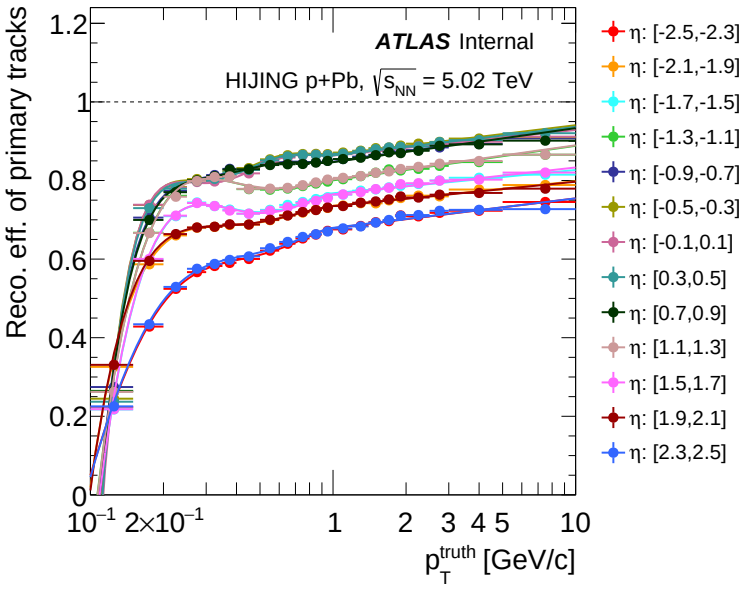

Figure 5.17: Shown are the track reconstruction efficiencies as a function of $p_{\mathrm{T}}^{\mathrm{truth}}$, fitted using a polynomial function of 5^{th} order in $\log(p_{\mathrm{T}})$ at low p_{T} ($p_{\mathrm{T}} < 1$ GeV) and a polynomial function of 1^{st} order in $\log(p_{\mathrm{T}})$ at high p_{T} ($p_{\mathrm{T}} > 1$ GeV) in selected η slices in HIJING.

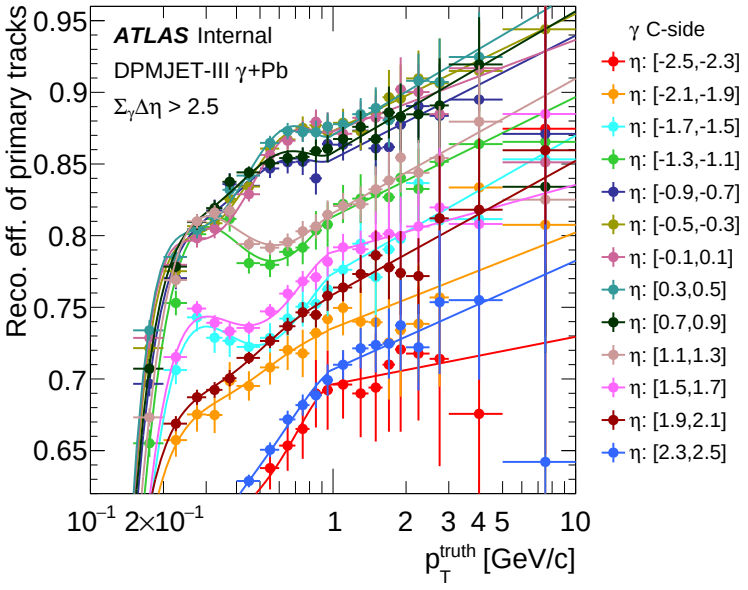

Figure 5.18: Shown is the zoomed-in track reconstruction efficiencies as a function of $p_{\mathrm{T}}^{\mathrm{truth}}$, fitted using a polynomial function of 5^{th} order in $\log(p_{\mathrm{T}})$ at low p_{T} ($p_{\mathrm{T}} < 1$ GeV) and a polynomial function of 1^{st} order in $\log(p_{\mathrm{T}})$ at high p_{T} ($p_{\mathrm{T}} > 1$ GeV) in selected η slices in DPMJET-III for photon C-side.

Figure 5.19 shows track reconstruction efficiency for different particle types as a function of $p_{\mathrm{T}}^{\mathrm{truth}}$. The left panel is for UPC Pb+Pb collisions using DPMJET-III and the right panel is for p+Pb collisions using HIJING. Notably, there is a dependence on the charged particle type, e.g., π, K, p, and thus a systematic uncertainty related to the lack of knowledge of these particle ratios is applied - see Section 5.5.5. Lastly, there is a contribution from muons to primary tracks, though they are a very small fraction in total.

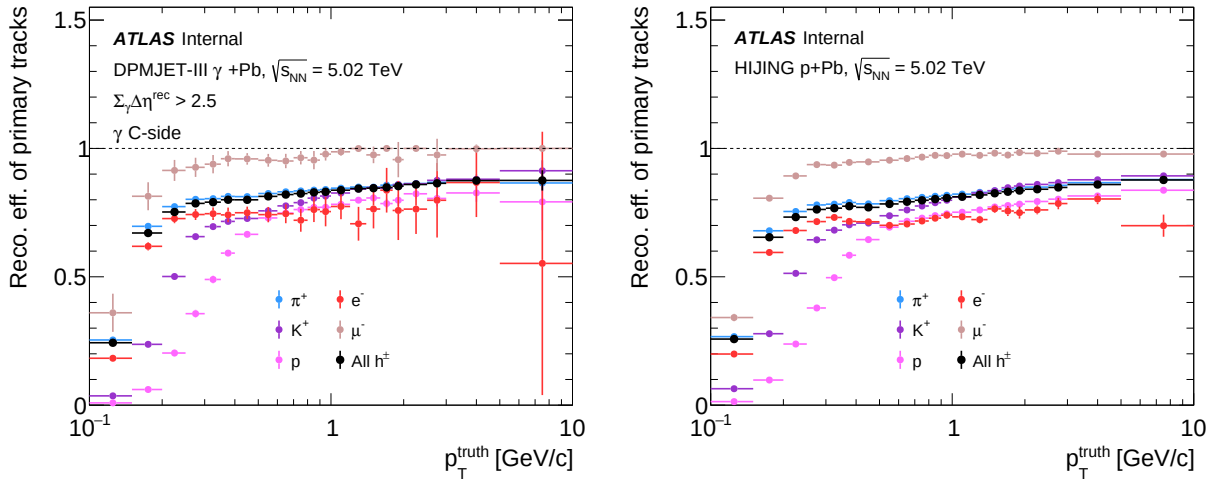

Figure 5.19: Track reconstruction efficiency is plotted for different particle types as a function of $p_{\mathrm{T}}^{\mathrm{truth}}$ in DPMJET-III (left) and HIJING (right). Note that the anti-particle of each selection is also included.

Notably, the track reconstruction efficiency is dependent on the material distribution in the detector since hadrons can have a high probability of interaction with the material of the inner detector. Two principal sources of uncertainty are considered for the track reconstruction efficiency - material uncertainties and the physics model used in the simulation. The systematic effect of such uncertainties is assessed by comparing the efficiency in samples with materials varied by a certain percentage - see Section 5.5.8.

5.3.5 Track Bin Migration

The track reconstruction efficiency is calculated using the same p_{T} threshold and η cut for the reconstructed tracks and the truth particles ($p_{\mathrm{T}} > 100$ MeV and $|\eta| < 2.5$). Thus, the current procedure does not account for the possibility of particles being reconstructed in a different bin or truth particles originating from outside of this kinematic range. This can result in a loss of efficiency, particularly at the boundaries of the acceptance region. When the bin migration effects are large, other analyses account for this via unfolding - see for example Ref. [148].

To quantify this effect, we compare two different definitions of track reconstruction efficiency, with and without allowing bin migration. In definition 1, we use Equation 5.5. In definition 2, the track reconstruction efficiency is defined as the following ratio. The numerator is the number of reconstructed tracks in a particular (p_{T}, η) bin based on the reconstructed momentum (still requiring a truth-matched particle, but not necessarily in that bin), $N_{\mathrm{rec}}^{\mathrm{matched}}$. The denominator is the total number of truth particles in a particular (p_{T}, η) bin based on the truth momentum, N_{truth}. This ratio is

$$\varepsilon_2(p_{\mathrm{T}}, \eta) = \frac{N_{\mathrm{reco}}^{\mathrm{matched}}(p_{\mathrm{T}}, \eta)}{N_{\mathrm{truth}}(p_{\mathrm{T}}, \eta)}. \tag{5.6}$$

This formulation accounts for bin migration and the possibility of truth particles outside the kinematic range to be reconstructed inside the kinematic range. Figure 5.20 shows the ratio between efficiencies calculated via the two definitions as a function of η (left panel) and p_{T} (right panel). The effect of bin migration is approximately less than 1% at all η and p_{T} within statistical uncertainties, and maybe 1.5% at high η region and $p_{\mathrm{T}} < 0.2$ GeV. The difference between the two definitions of track reconstruction efficiency is used to assign a systematic uncertainty accounting for the effects of bin migration - see Section 5.5.10.

Unfolding is a way to model bin migration between truth particles and the associated reconstructed tracks, but it comes with additional uncertainties. If the resolution blurring is small, a simple uncertainty estimation using MC calculation is preferred. As a cross-check on the bin-migration effects, an unfolding test is performed on the p_{T} distribution in different η slices. Results

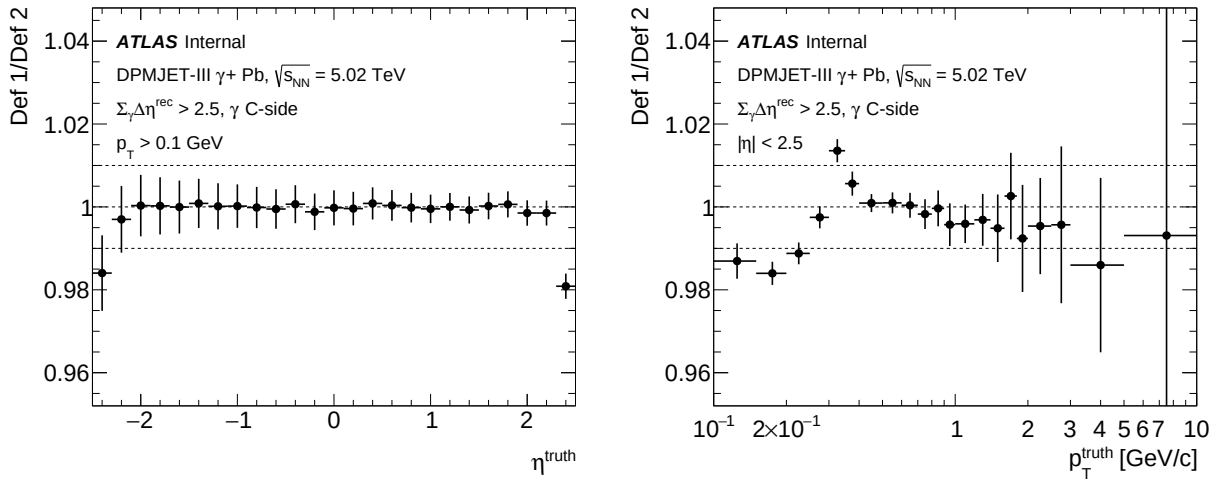

Figure 5.20: The ratio of track reconstruction efficiency definition 1 to 2 is plotted as a function of η^{truth}(left) and $p_{\text{T}}^{\text{truth}}$(right) in DPMJET-III.

shown in Appendix A.5 indicate that the bin-migration effects from the unfolding procedure are $< 1\%$ at all p_{T} and all η. Hence, for this analysis, we do not use unfolding but rather the procedure detailed above.

5.3.6 Fakes and Secondary Rates

Only tracks originating from the collision (*i.e.*, primaries) are of interest in this analysis. Primary particles are defined as charged particles with a mean lifetime $\tau > 300$ ps (3×10^{-10} s), either directly produced in pp interactions or from subsequent decays of directly produced particles with $\tau < 30$ ps. This definition is consistent with previous ATLAS publications – see for example Ref. [149]. To be explicit, this definition thus excludes charged strange baryons that have a very small probability to transverse the tracker before decaying (for example the Ξ^- with $\tau = 1.6 \times 10^{-10}$ s and Ω^- with $\tau = 0.8 \times 10^{-10}$ s). However, it includes charged hadrons resulting from the decay of Δ resonances and ρ mesons for example that have lifetimes shorter than 30 ps. That means the rates of fakes and secondaries must be accounted for. Fakes are background tracks that do not have a truth match. The largest sources of secondary tracks are from hadronic interactions of particles with the detector material and the decay products of particles with strange quark content,

mostly K^0 and Λ^0 decays. Additionally, photon conversions, specifically below 500 MeV, also contribute significantly to the production of secondary tracks. To correct for these contributions, tracks are weighted on a track-by-track basis by the probability that a track is primary. This probability, termed as "primary fraction", is estimated as a function of reconstructed kinematics in simulated events by taking the ratio of the number of primary tracks to the number of reconstructed tracks:

$$f_{\text{primary}}(p_{\text{T}}, \eta) = \frac{N_{\text{ch}}^{\text{primary}}(p_{\text{T}}, \eta)}{N_{\text{ch}}^{\text{rec}}(p_{\text{T}}, \eta)}. \tag{5.7}$$

In the analysis, the primary fraction of tracks as a function of p_{T} is fitted using a polynomial function of 6^{th} order in $\log(p_{\text{T}})$ at low p_{T} ($p_{\text{T}} < 1$ GeV) and with a linear function $y =$ constant at high p_{T} ($p_{\text{T}} > 1$ GeV) in each of the 25 η bins spanning from -2.5 to 2.5 as shown in Figure 5.21.

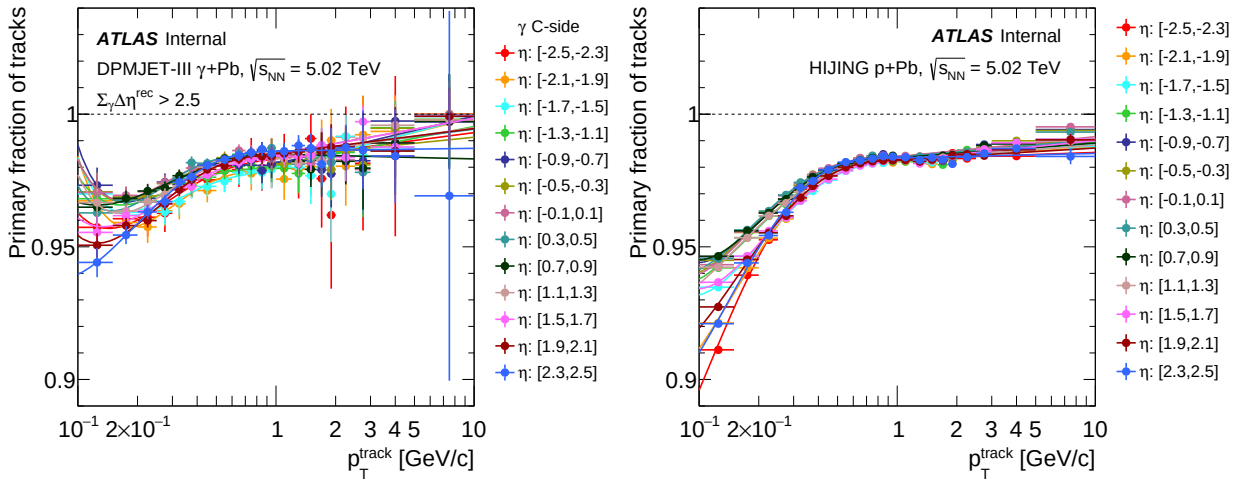

Figure 5.21: Shown are the fractions of primary tracks compared to all tracks as a function of p_{T} from DPMJET-III Pb+Pb UPC (left) and HIJING p+Pb (right).

Figure 5.22 shows the contribution of fake tracks and secondary tracks in DPMJET-III separately over the entire pseudorapidity range $|\eta| < 2.5$. Thus, the fake contribution dominates at low p_{T} while the secondaries dominate at high p_{T}. The fractions are typically less than 1-2%, except at the lowest p_{T}.

The systematic uncertainty associated with this correction is detailed in Section 5.5.7.

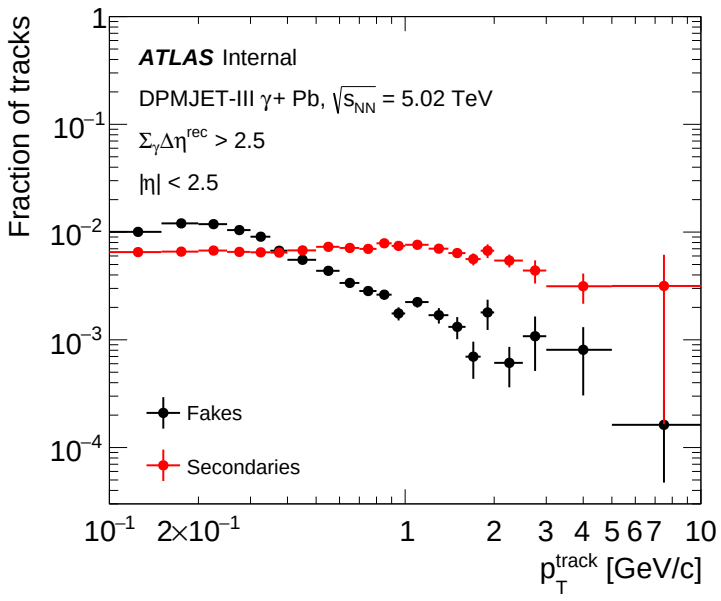

Figure 5.22: Shown are the fractions of fake tracks and secondary tracks as a function of p_{T} from DPMJET-III Pb+Pb UPC.

5.3.7 Extrapolation to $p_{\mathrm{T}} = 0$ GeV

For the $\mathrm{d}N_{\mathrm{ch}}/\mathrm{d}\eta$ results, the final values reflect the yields integrated over the entire p_{T} range. Hence there is an extrapolation of the yield for $p_{\mathrm{T}} < 0.1$ GeV where there is no measurement. Three variations are considered to gauge the sensitivity to this extrapolation. Two variations come from fitting the fully corrected yields as a function of p_{T} in exclusive bins in η using the Modified Hagedorn and Tsallis fit functions. The third method, and the default, utilizes DPMJET-III (HIJING) Monte Carlo for the photonuclear (p+Pb) case to correct for the missing low p_{T} measurements as part of the acceptance correction. Hence this third method assumes the p_{T} dependence in the Monte Carlo is correct in this low p_{T} region.

The charged-hadron yields as a function of p_{T} are fit using the Modified Hagedorn and Tsallis statistics functions shown in Equations 5.8 and 5.9, respectively. The Modified Hagedorn function is often used to describe both the "soft" particle production at low p_{T} and at higher p_{T} where hard

scattering processes dominate [150]. A modified Hagedorn function is shown as:

$$\frac{1}{N}\frac{\mathrm{d}N}{\mathrm{d}p_{\mathrm{T}}} = A_1 \frac{p_{\mathrm{T}}^2}{\sqrt{p_{\mathrm{T}}^2 + m_0^2}} \left(1 + \frac{p_{\mathrm{T}}}{p_1}\right)^{-n_1}, \tag{5.8}$$

where m_0 is the rest mass of considered particle, p_1 and n_1 are the free parameters, and A_1 is the normalization constant. Here we set m_0 to the pion mass. The Tsallis distribution [151, 152] describes near-thermal systems in terms of Tsallis parameter T and the parameter q, which measures the degree of non-thermalization and is shown as:

$$\frac{1}{N}\frac{\mathrm{d}N}{\mathrm{d}p_{\mathrm{T}}} = C p_{\mathrm{T}} \sqrt{p_{\mathrm{T}}^2 + m_0^2} \left(1 + \frac{q-1}{T}\sqrt{p_{\mathrm{T}}^2 + m_0^2}\right)^{-\frac{q}{q-1}}, \tag{5.9}$$

where C is the normalization constant. The fitting is performed in the p_{T} region 0-2 GeV to better constrain the fit in the low p_{T} region. At this time, the fits are simply used to vary the extrapolation of the p_{T} yields down to $p_{\mathrm{T}} = 0$, and no physics interpretation of the parameters is made.

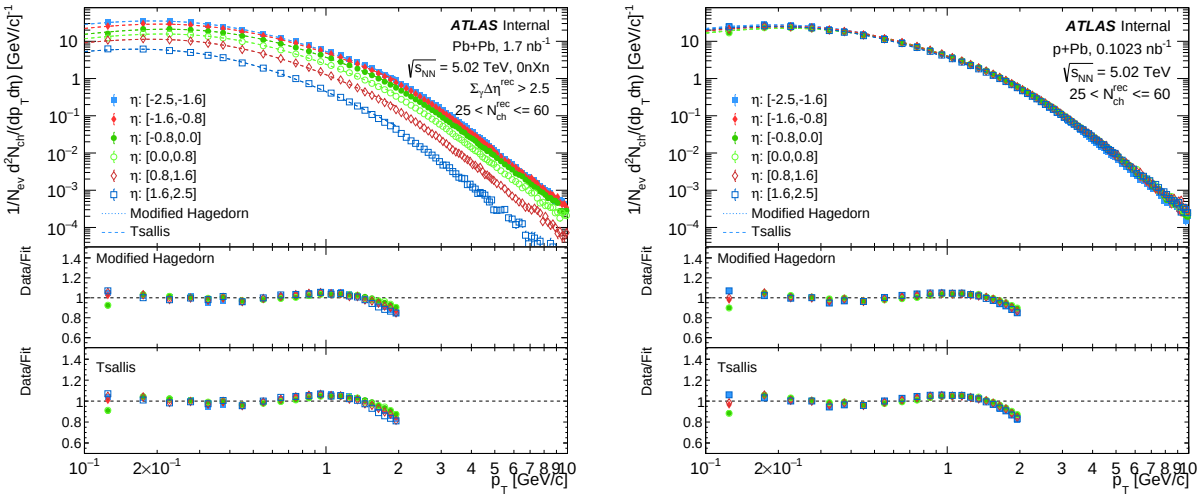

Figure 5.23: Shown are the charged-hadron yields as a function of p_{T} in six η selections and fit results to the Modified Hagedorn and Tsallis functions. The left panel is for Pb+Pb UPC and the right panel is for p+Pb collisions. The middle panel shows the ratio of the data to the Modified Hagedorn fit. The bottom panel shows the ratio of the data to the Tsallis fit.

Figure 5.23 shows the charged-hadron yield in Pb+Pb UPC (left) and p+Pb (right) as a function of p_{T} in six η selections with fit results for the Modified Hagedorn and Tsallis functions. The lower panels show the ratio of data to the Modified Hagedorn fit and the Tsallis fit. The fits

show reasonable agreement with the experimental data over many orders of magnitude and show similar features in both Pb+Pb UPC and p+Pb. Additionally, Figure 5.24 presents the same data in η selections -2.5 to -1.6 and 1.6 to 2.5 on a linear p_{T} scale and includes a comparison to the DPMJET-III truth p_{T} distribution.

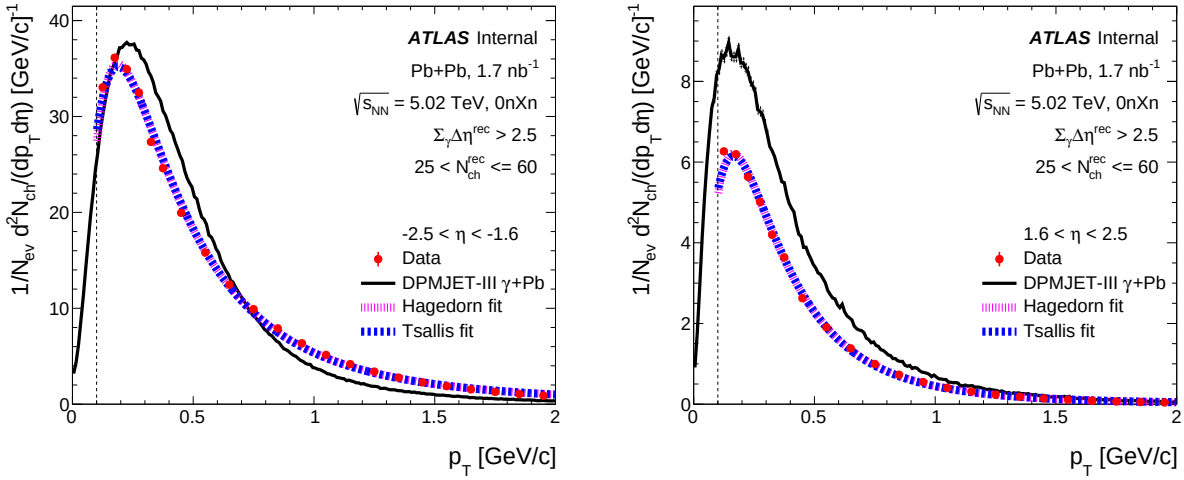

Figure 5.24: Shown are the charged-hadron yields as a function of p_{T} for two η selections in Pb+Pb UPC data, plotted on a linear p_{T} scale. The left panel shows the backward η selection (-2.5 to -1.6), while the right panel shows the forward η selection (1.6 to 2.5). The figure includes fit results to the Modified Hagedorn and Tsallis functions and also compares the data to the DPMJET-III truth p_{T} distribution. The vertical line shows the lowest range of measurement, $p_{\mathrm{T}} = 0.1$ GeV.

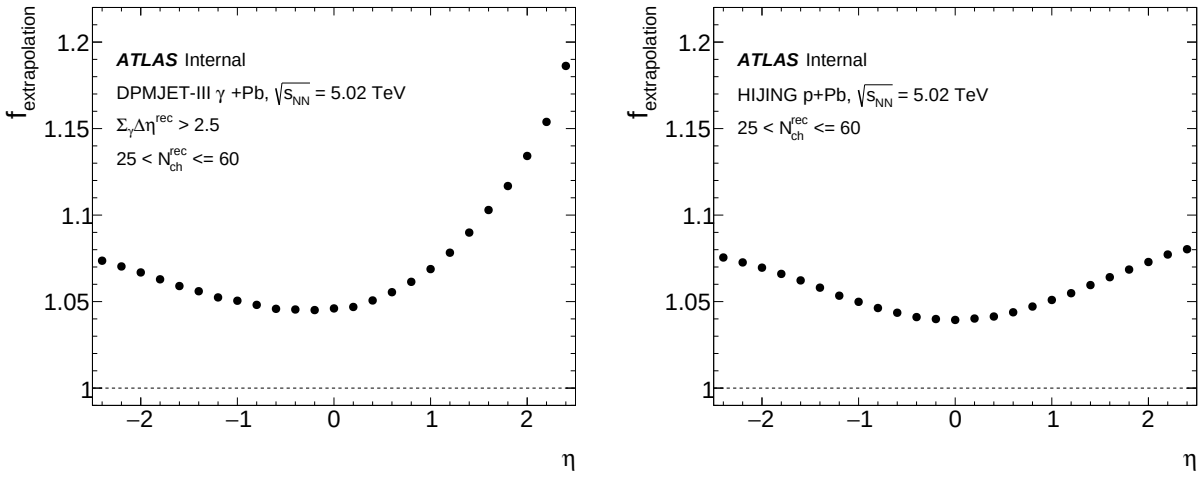

Figure 5.25: Shown are the extrapolation factors in Pb+Pb UPC (left) and p+Pb (right) as a function of η.

The charged-hadron yield in η is corrected by a factor for extrapolation to $p_{\mathrm{T}} = 0$ GeV, $f_{\mathrm{extrapolation}}$, shown in Figure 5.25, which is calculated using the equation:

$$f_{\mathrm{extrapolation}} = \frac{\int_0^2 Y(\eta, p_{\mathrm{T}})\mathrm{d}p_{\mathrm{T}}}{\int_{0.1}^2 Y(\eta, p_{\mathrm{T}})\mathrm{d}p_{\mathrm{T}}}, \tag{5.10}$$

where $Y(\eta, p_{\mathrm{T}})$ represents the charged-hadron yield described in Equation 5.12. The numerator of the equation integrates the yield in the p_{T} range of 0-2 GeV, while the denominator integrates the yield in the p_{T} range of 0.1-2 GeV. The factor is scaled to account for the yield in the p_{T} range of 2-10 GeV. In the nominal case, the integral of the yield is evaluated using DPMJET-III (HIJING) in Pb+Pb UPC (p+Pb). To evaluate the systematic uncertainty of this extrapolation factor, the factor is recalculated using two variations: The modified Hagedorn fit and the Tsallis fit. Figure 5.38 shows the fully corrected charged-hadron yield in η, denoted as $\mathrm{d}N_{\mathrm{ch}}/\mathrm{d}\eta$, with the nominal result and the variations in the top panel. The bottom panel shows the ratio of the fit extrapolations to the nominal result. The differences are utilized to assign a systematic uncertainty as detailed in Section 5.5.11.

5.4 Correction Factors

In this Section, the final measurement observables of the charged-hadron analysis are explained. The following observables are presented in this analysis.

- Charged-hadron yields as a function of η:

$$Y(\eta) = \frac{1}{N_{\mathrm{ev}}}\frac{\mathrm{d}N_{\mathrm{ch}}}{\mathrm{d}\eta} \tag{5.11}$$

- Charged-hadron yields as a function of p_{T} in different η slices:

$$Y(\eta, p_{\mathrm{T}}) = \frac{1}{N_{\mathrm{ev}}}\frac{\mathrm{d}N^2_{\mathrm{ch}}}{\mathrm{d}p_{\mathrm{T}}\mathrm{d}\eta} \tag{5.12}$$

- $\langle\eta\rangle$ as a function of $N_{\mathrm{ch}}^{\mathrm{rec}}$
- $\langle p_{\mathrm{T}}\rangle$ as a function of $N_{\mathrm{ch}}^{\mathrm{rec}}$

Here p_{T} is the transverse momentum, η is the pseudorapidity, $N_{\mathrm{ch}}^{\mathrm{rec}}$ is the number of charged particles in an event, N_{ev} is the number of selected events in the event class, $\langle p_{\mathrm{T}} \rangle$ is the average p_{T} for a given number of charged particles and $\langle \eta \rangle$ is the average η for a given number of charged particles.

The correction factors are the following:

- In data, weights (w_{evt}) are applied event-by-event to correct for inefficiencies due to trigger selection:

$$w_{\mathrm{evt}} = f_{\mathrm{trigprescales}} \times \frac{1}{\varepsilon_{\mathrm{trigeff}}(N_{\mathrm{ch}}^{\mathrm{rec}}, \sum_{\gamma} \Delta\eta^{\mathrm{rec}})}, \tag{5.13}$$

  where $f_{\mathrm{trigprescales}}$ is the relevant trigger prescale and $\varepsilon_{\mathrm{trigeff}}(\mathrm{N}_{\mathrm{ch}}^{\mathrm{rec}}, \sum_{\gamma} \Delta\eta^{\mathrm{rec}})$ is the trigger efficiency.

- The reconstructed tracks are corrected with weight factor (w_{trk}):

$$w_{\mathrm{trk}}(\eta, p_{\mathrm{T}}) = \frac{f_{\mathrm{primary}}(\eta, p_{\mathrm{T}})}{\varepsilon_{\mathrm{reco}}(\eta, p_{\mathrm{T}})}, \tag{5.14}$$

  where $f_{\mathrm{primary}}(\eta, p_{\mathrm{T}})$ is the primary fraction of tracks, given by Equation 5.7 and $\varepsilon_{\mathrm{reco}}(\eta, p_{\mathrm{T}})$ is the track reconstruction efficiency of primary tracks, given by Equation 5.5.

- The $N_{\mathrm{ch}}^{\mathrm{rec}}$-dependent purity correction factor, PCF, is applied to the charged-hadron yield as a function of η and p_{T}, given by Equation 5.3.

- In the cases where yields are integrated over all p_{T}, the $p_{\mathrm{T}} = 0$ GeV extrapolation factor, $f_{\mathrm{extrapolation}}(\eta)$, is applied to the charged hadrons yield $\mathrm{Y}(\eta)$, given by Equation 5.10.

Among the correction factors mentioned above, the PCF is exclusively applied to Pb+Pb UPC events. All the other correction factors are applied to both Pb+Pb UPC and p+Pb.

5.5 Systematic Uncertainties

In this section, various analysis checks and quantifications of systematic uncertainties on the extracted charged-hadron yields are detailed. Major sources of systematic uncertainties are listed here along with the relevant subsection where they are detailed.

(1) Photon A-side versus C-side (UPC Pb+Pb only) - Section 5.5.1

(2) Purity sensitivity (UPC Pb+Pb only) - Section 5.5.2

(3) $N_{\mathrm{ch}}^{\mathrm{rec}}$ definition (UPC Pb+Pb only) - Section 5.5.3

(4) Z-vertex dependence - Section 5.5.4

(5) Charged-particle composition check (π, K, p) - Section 5.5.5

(6) Track selection - Section 5.5.6

(7) Fake and secondary tracks - Section 5.5.7

(8) Detector material/physics model uncertainty - Section 5.5.8

(9) Track-to-particle matching probability - Section 5.5.9

(10) Track bin migration - Section 5.5.10

(11) Extrapolation to $p_{\mathrm{T}} = 0$ GeV ($\mathrm{d}N_{\mathrm{ch}}/\mathrm{d}\eta$ only) - Section 5.5.11

(12) Truth-level $\sum_{\gamma} \Delta\eta$ definition (UPC Pb+Pb only) - Section 5.5.12

(13) Uncertainty on fitting track reconstruction efficiency - Section 5.5.13

We highlight that to avoid double counting of statistical uncertainties, in all relevant cases, we divide the data sample randomly into two subsets. Then the nominal and systematic variation analysis are applied to separate subsets, such that they are statistically independent. Then one can determine if there is an additional systematic effect that needs to be accounted for, or rather

the variation is simply consistent with statistical fluctuations. This method follows the procedure used in the ATLAS UPC analysis [146]. We note that the systematic uncertainty estimation as a function of η is included in Appendix A.7.

All uncertainty contributions are tabulated and added in quadrature for the full systematic uncertainty.

5.5.1 Photon A-side versus C-side Check

In Pb+Pb UPC collisions, the photon can be emitted from either Pb nucleus. Thus, the photon-going direction can lead to low track activity on either the A- or C-side and accordingly a ZDC neutron signal on the C-side or A-side, respectively. Thus, for Pb+Pb UPC collisions, comparing results with the photon-going direction on the A- or C-side checks for potential unaccounted-for differences in the detector acceptance, gap selection, and ZDC selection. Figure 5.26 shows the charged-hadron yield as a function of p_{T} in six η selections from A- and C-side independently. The lower panel shows the ratio of the two with statistical uncertainties, noting that the two samples are completely statistically independent. The ratios are fit to a function, $y = \text{error function}(p_{\mathrm{T}})$. The systematic uncertainties are assigned based on the fit values. There is $< 4\%$ uncertainty in the p_{T} region 0.1-0.15 GeV, $< 1\%$ uncertainty elsewhere.

This uncertainty only applies to the Pb+Pb UPC case and is not relevant for p+Pb where only one run with one orientation of the beams is used.

5.5.2 Purity Sensitivity

In Pb+Pb UPC collisions, there is a potential contribution of Pb+Pb peripheral inelastic collisions contaminating the UPC Pb+Pb sample despite the `0nXn` ZDC requirement and photon sum-of-gaps selection. To account for this contribution, the experimental results are corrected in the following way as detailed in Section 5.2.1.4. The data is corrected with the PCF, as a function of η and p_{T}, which employs the purity values shown in black markers in Figure 5.4 and the p+Pb yield as a proxy for the contamination. A systematic uncertainty is assigned to this correction

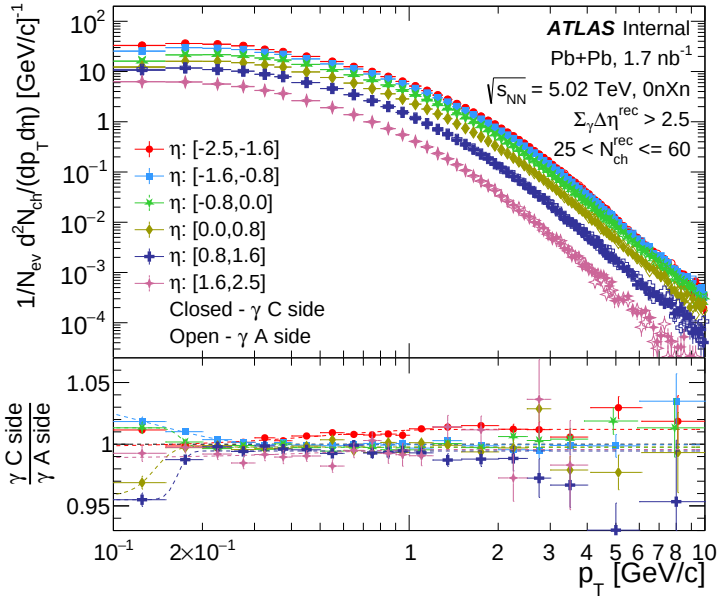

Figure 5.26: Shown are the charged-hadron yields as a function of p_{T} in six η selections from the photon-going A-side and C-side separately. The lower panel shows the ratio of the two with fits.

factor. The purity value assigned to the nominal results is varied by 100% of the difference between unity and purity, up and down, and the correction factors are re-evaluated.

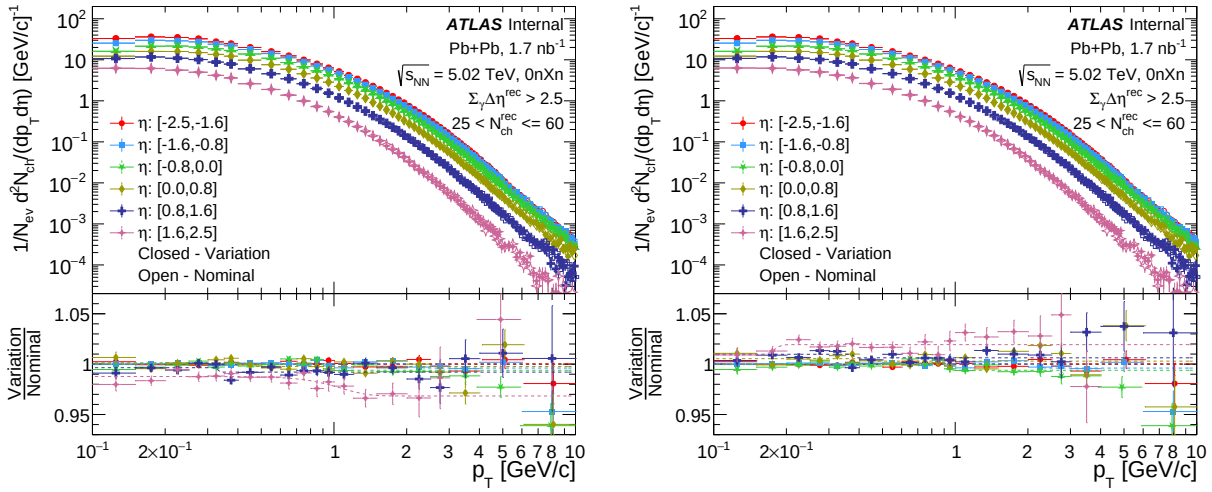

Figure 5.27: Shown are the charged-hadron yields as a function of p_{T} in six η selections in Pb+Pb UPC, with the lower bound (left) and upper bound (right) of two purity variations. The lower panel shows the ratio of the two with fits.

Figure 5.27 shows the charged-hadron yields as a function of p_{T} in six η selections for Pb+Pb

UPC, with two variations of purity (lower and upper bounds) displayed. The lower panel shows the ratio of the two with statistical uncertainties, noting that the two samples are completely statistically independent. The ratios are fit to a constant level, *i.e.*, linear function $y =$ constant. The systematic uncertainties are assigned based on the fit values. There is a 2% uncertainty in the most forward rapidity bin η:[1.6,2.5], and $< 1\%$ elsewhere.

5.5.3 $N_{\mathrm{ch}}^{\mathrm{rec}}$ Definition

There is an auto-correlation bias between the particles included in the event-class definition and those included in the yield definition. To remove this auto-correlation bias, we perform an azimuthal separation of the particles entering both definitions as detailed in Section 5.2.1.1. The value of $\varepsilon = 0.01$ corresponds to the nominal definition, while the value of $\varepsilon = 0.02$ corresponds to the varied definition.

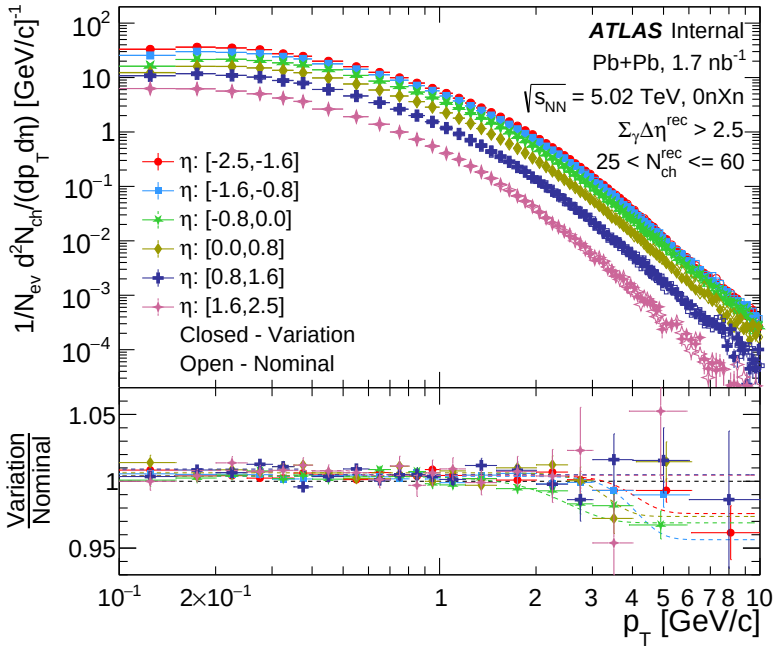

Figure 5.28: Shown are the charged-hadron yields as a function of p_{T} in six η selections with $N_{\mathrm{ch}}^{\mathrm{rec}}$ defined using $\varepsilon = 0.02$ as the variation and $N_{\mathrm{ch}}^{\mathrm{rec}}$ defined using $\varepsilon = 0.01$ as the nominal case in Pb+Pb UPC. The lower panel shows the ratio of the two with fits.

Figure 5.28 shows the charged-hadron yields as a function of p_{T} in six η selections with $N_{\mathrm{ch}}^{\mathrm{rec}}$

defined using $\varepsilon = 0.02$ as the variation and $N_{\mathrm{ch}}^{\mathrm{rec}}$ defined using $\varepsilon = 0.01$ as the nominal case in Pb+Pb UPC. The lower panel shows the ratio of the two with statistical uncertainties, noting that the two samples are completely statistically independent. The ratios are fit to a function $y =$ error function(p_{T}). The systematic uncertainties are assigned based on the fit values. There is $< 5\%$ uncertainty in the p_{T} region > 5 GeV, $< 1\%$ elsewhere.

This uncertainty only applies to the Pb+Pb UPC case and is negligible in the p+Pb case since the $N_{\mathrm{ch}}^{\mathrm{rec}}$ distribution is not steeply falling in the region of $N_{\mathrm{ch}}^{\mathrm{rec}} = 25$-60.

5.5.4 Z-Vertex Dependence

The acceptance and efficiency of the detector have a modest dependence on the Z-vertex of the collision. The analysis is re-done in two exclusive Z-vertex ranges ($z_{\mathrm{vtx}} \leq 0$ mm and $z_{\mathrm{vtx}} > 0$ mm), noting that the nominal analysis is for $z_{\mathrm{vtx}} \leq 100$ mm.

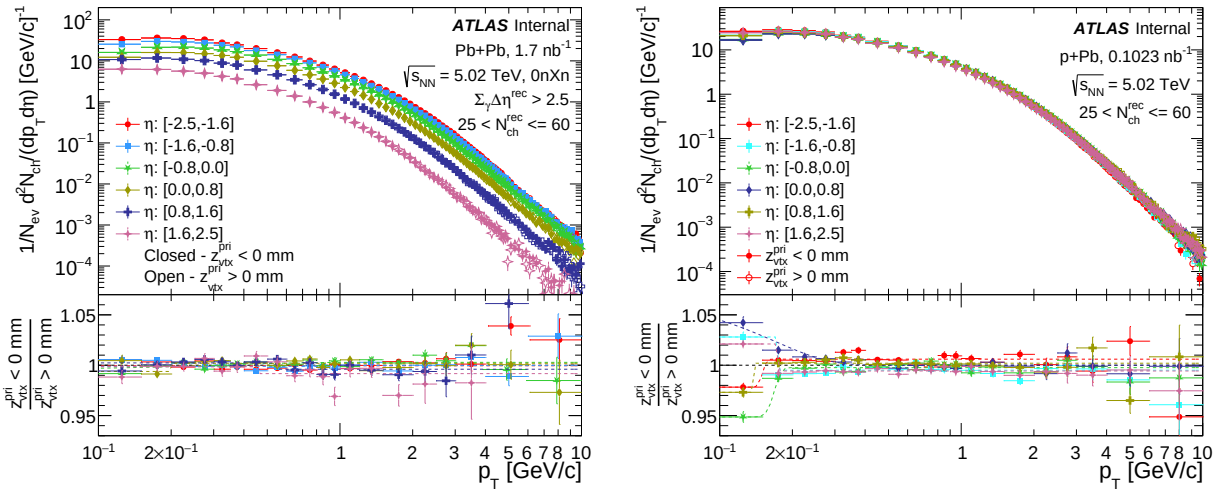

Figure 5.29: Shown are the charged-hadron yields as a function of p_{T} in six η selections from Z-vertex selections of $z_{\mathrm{vtx}} \leq 0$ mm and $z_{\mathrm{vtx}} > 0$ mm. The left panel is for Pb+Pb UPC and the right panel is for p+Pb collisions. The lower panel shows the ratio of the two with fits.

Figure 5.29 shows the charged-hadron yield as a function of p_{T} in six η selections from the two Z-vertex selections independently. The lower panel shows the ratio of the two with statistical uncertainties, noting that the two samples are completely statistically independent. The ratios are fit to a function, $y =$ error function(p_{T}). The systematic uncertainties are assigned based on the fit values. In Pb+Pb UPC, the uncertainty is $< 1\%$, and in p+Pb the uncertainty is $< 5\%$ in the p_{T} region 0.1-0.15 GeV, $< 1\%$ elsewhere.

5.5.5 Charged Particle Composition Check (π, K, p)

The acceptance and efficiency depend not only on the p_{T} of the particle but also on the particle type, e.g., π, K, p. Figure 5.19, discussed previously, shows that the acceptance is higher for π than other hadrons, particularly at low p_{T} where the different particles have very different velocities. Thus, the acceptance and efficiency applied to the charged hadrons depend on whether the DPMJET-III and HIJING Monte Carlo have the correct ratio of different hadrons in Pb+Pb UPC and p+Pb collisions, respectively. The yield of π, K, p in UPC Pb+Pb collisions is currently unmeasured, and thus the relative yield of K/π and separately the relative yield of p/π are varied by 25% and the acceptance and efficiency recalculated.

Figure 5.30 shows the charged-hadron yields as a function of p_{T} in six η selections with the two 25% re-weightings and the default result. The lower panel shows the ratios relative to the default with statistical uncertainties. The ratios are fit to a constant level, *i.e.*, linear function $y =$ constant. The systematic uncertainties are assigned based on the fit values. The uncertainty is $< 1\%$ at all p_{T}.

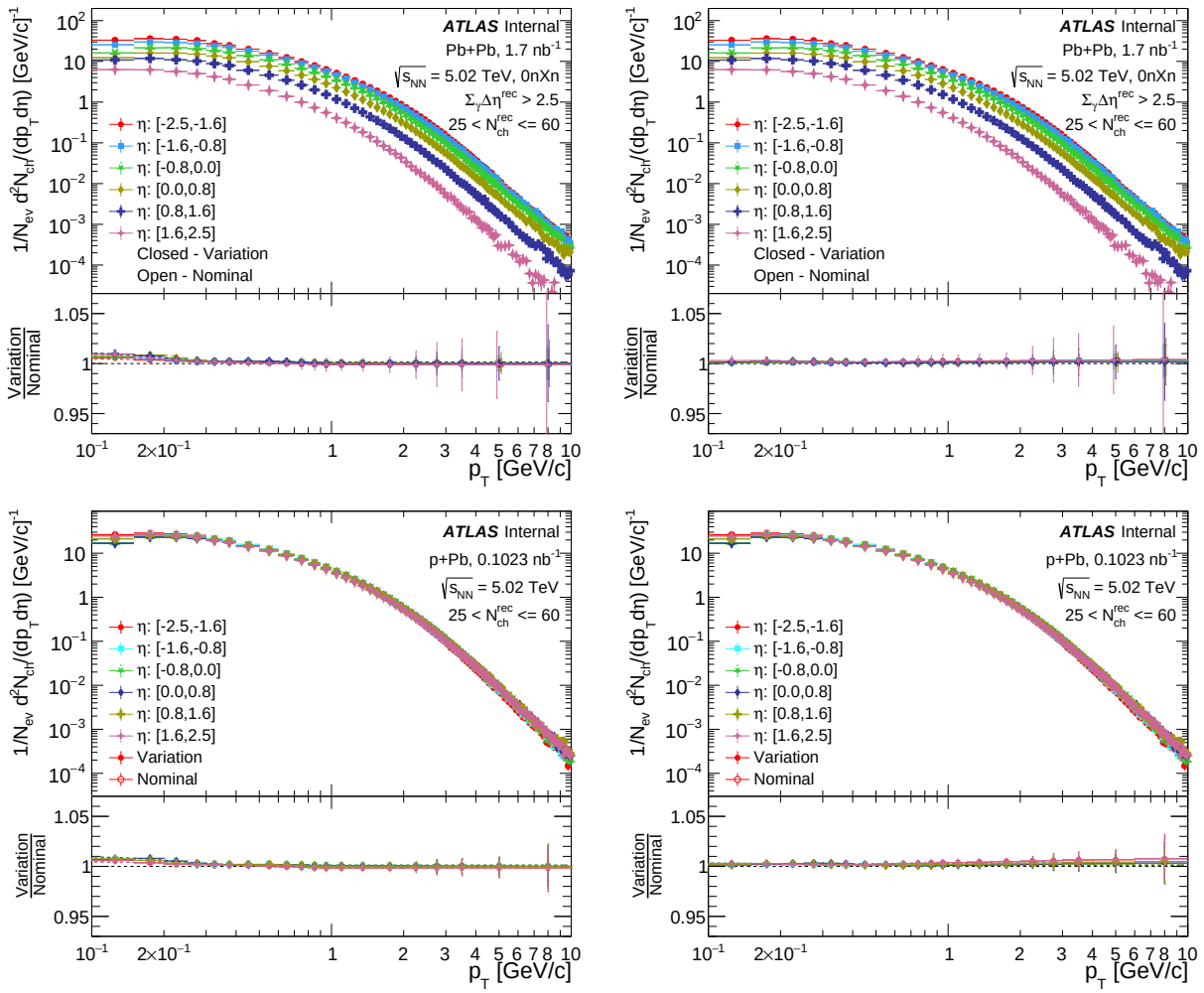

Figure 5.30: Shown is the charged-hadron yields in Pb+Pb UPC (upper set) and p+Pb (lower set) as a function of p_{T} in six η selections with particle composition checks. Here variation shows the case where the relative yield of K/π is varied by 25% (left) and the case where the relative yield of p/π by 25% (right). The lower panels show the ratio of the two with fits. Note that the vertical line statistical uncertainties on the ratios are overestimates since the variation and nominal Monte Carlo samples are highly correlated.

5.5.6 Track Selection

Although the detector conditions used in the MC are described as precisely as reasonably possible, there are still small differences between MC and data in the number of detector hits counted. A systematic uncertainty is assigned to account for this difference, by removing a certain hit requirement in the `HILoose` track quality selections.

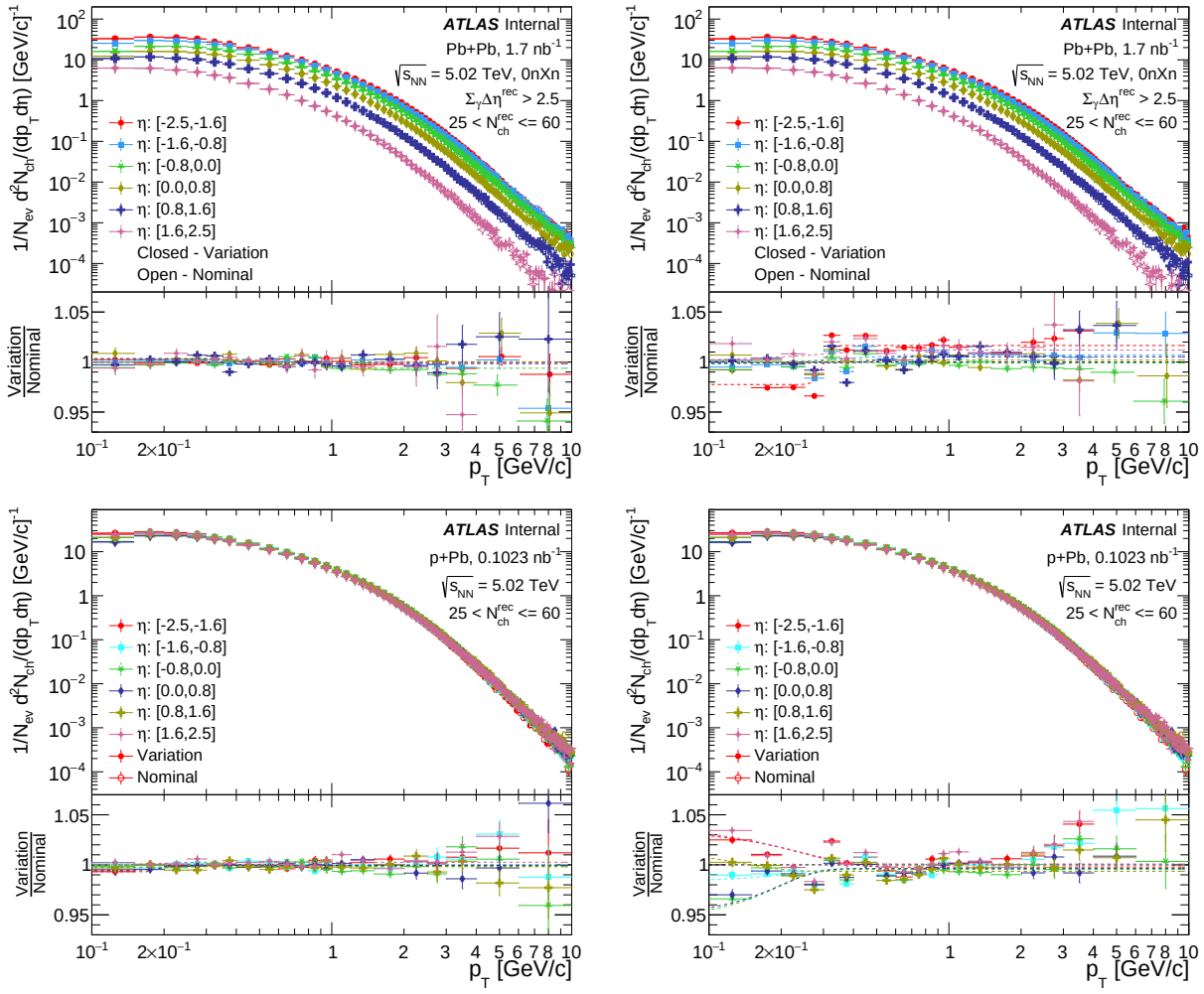

Figure 5.31: Shown are the charged-hadron yields as a function of p_{T} in six η selections with variation of track selection requirement. Here variation shows the case where the pixel hit requirement is removed (left) and the case where the SCT hit requirement is removed (right). The lower panel shows the ratio of the two with fits.

Figure 5.31 shows the charged-hadron yield as a function of p_{T} in six η selections with the nominal case with all hit requirement of the `HILoose` track quality and the varied case where the pixel hit requirements and SCT hit requirements are removed separately. The lower panel shows the ratio of the two with statistical uncertainties, noting that the two samples are statistically independent. The ratios are fit to a function, $y =$ error function(p_{T}). The systematic uncertainties are assigned based on the fit values.

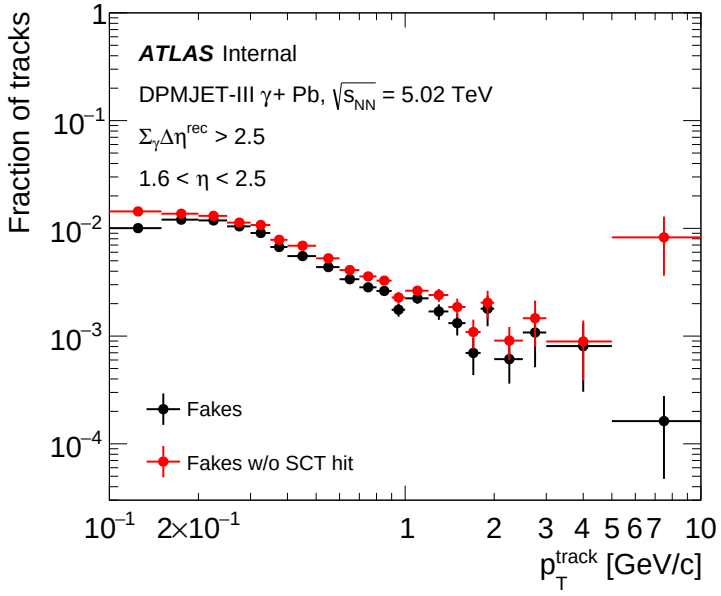

Figure 5.32: Shown are the fractions of fake tracks as a function of p_{T}, with and without the SCT hit requirement in the track quality definition, from DPMJET-III Pb+Pb UPC.

In the case of the variation where the pixel hit requirement is removed, the uncertainty is $< 1\%$. In the case of the variation where the SCT hit requirement is removed, the uncertainty is $< 3\%$ in the p_{T} region 0.1-0.4 GeV and $< 1\%$ in the p_{T} region 0.4-4 GeV. In the high p_{T} region 4-10 GeV, large differences are observed at high p_{T} in both Pb+Pb UPC and p+Pb (5-7%), and this is a result of a larger fraction of poorly measured tracks entering the measurement sample when loosening the cuts. Figure 5.32 from DPMJET-III shows that this feature is visible in the forward η region 1.6-2.5. When the SCT hits requirement is removed from the track quality definition, there is a factor > 10 increase in the number of fake tracks in the highest p_{T} bin. Any

small difference between data and MC in this bin will be overestimated. Therefore, to assess the systematic uncertainty in high p_{T} region 4-10 GeV, the fit results at $p_{\mathrm{T}} = 2$ GeV is simply linearly extrapolated to higher p_{T} region.

5.5.7 Fake and Secondary Tracks

The charged-hadron yields are specifically for primary tracks, as previously defined. The contribution of fake and secondary tracks is eliminated by applying a corrected factor, f_{primary} on a track-by-track basis, as detailed in Section 5.3.6. The uncertainty on the fakes and secondary contribution is assumed to be $\pm 50\%$ of the rate. Since these uncertainties are meant to represent approximately one standard deviation level, considering higher 100% variations would be an overestimate, e.g., there is no scenario where there would be zero fakes and zero secondaries. In particular, there is a level of double counting in this contribution, as changes to the default `HILoose` requirements detailed above will also be sensitive to potential changes in non-primary contributions.

Figure 5.33 shows the charged-hadron yield as a function of p_{T} in six η selections with the nominal case and the varied case where the fakes and secondary contribution is varied 50% of the rate up and down. The lower panel shows the ratio of the two with statistical uncertainties. The ratios are fit to a function, $y =$ error function(p_{T}). The systematic uncertainties are assigned based on the fit values. The uncertainty is 2-3% in the lowest p_{T} region 0.1-0.2 GeV, then decreasing to 1% above $p_{\mathrm{T}} = 0.4$ GeV.

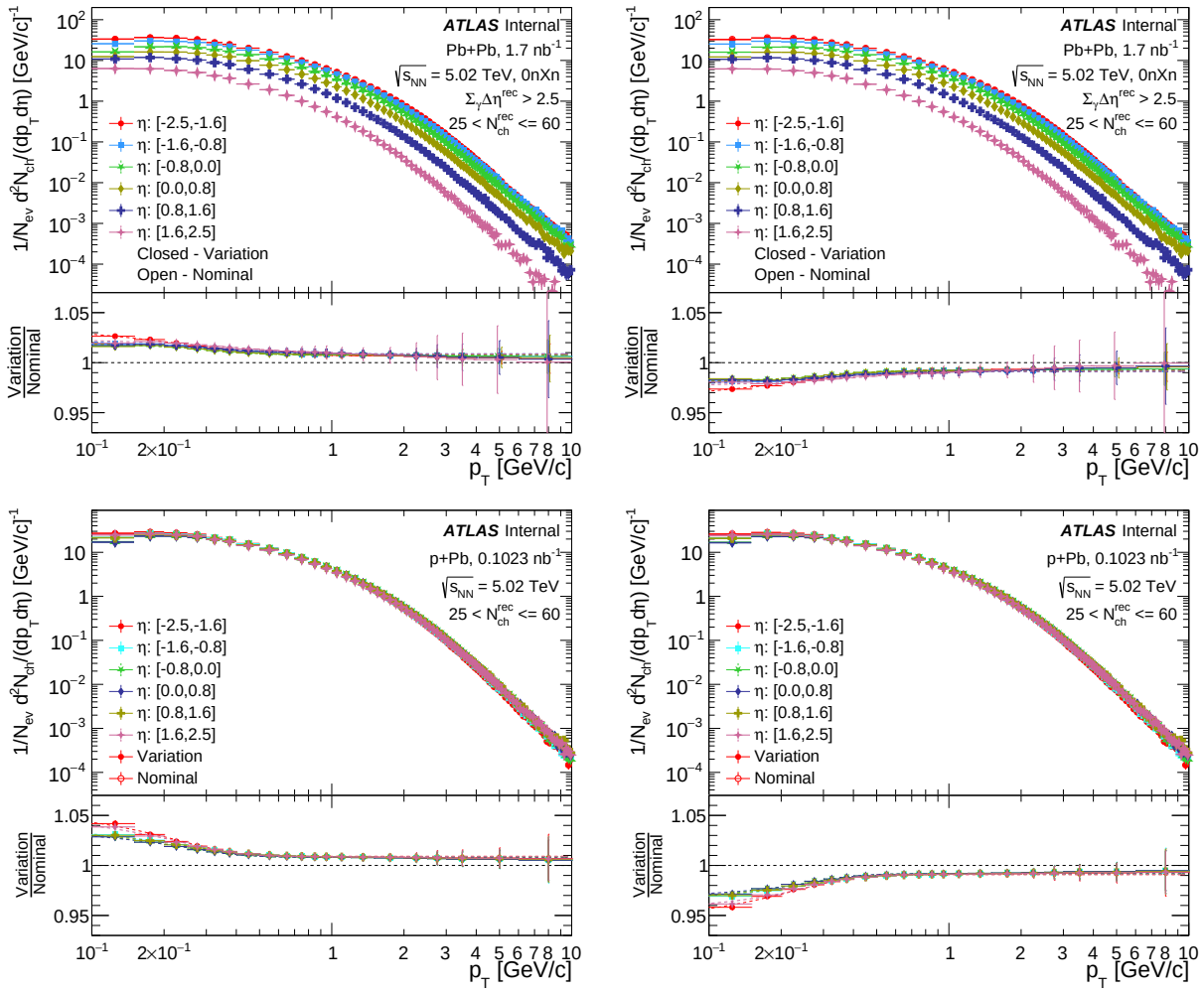

Figure 5.33: Shown is the charged-hadron yields in Pb+Pb UPC (upper set) and p+Pb (lower set) as a function of p_{T} in six η selections with fakes and secondary correction fraction varied up (left) and down (right) by 50% of the rate. The lower panels show the ratio of the two with fits. Note that the vertical line statistical uncertainties on the ratios are overestimates since the variation and nominal Monte Carlo samples are highly correlated.

5.5.8 Detector Material/Physics Model Uncertainty

Because hadrons have a significant probability for hadronic interactions with the material of the inner detector, the track reconstruction efficiency calculation is heavily dependent on the material distribution in the detector modeled in MC. For evaluating the systematic uncertainties of the track reconstruction efficiency, alternative MC samples are produced, which differ in the ATLAS geometry or physics list used in the ATLAS GEANT4 simulation. The following tracking CP recommendations are used:

- Alternative GEANT-4 geometry with +5% Overall ID material: ATLAS-R2-2016-01-00-02
- Alternative GEANT-4 geometry with +10% IBL material: ATLAS-R2-2016-01-00-03
- Alternative GEANT-4 geometry with +25% PP0 material: ATLAS-R2-2016-01-00-18
- Alternative GEANT-4 physics model: QGSP_BIC

For each of the variations, an alternative signal MC sample is produced and the track reconstruction is recalculated as a function of track p_{T} and η using the sample. The differences between the default and these material variation acceptance and efficiency results are used to determine these systematic uncertainty contributions. Figure 5.34 and 5.35 shows the charged-hadron yield as a function of p_{T} in six η selections with the nominal case and the four variations mentioned above in Pb+Pb UPC and p+Pb, respectively. The lower panel shows the ratio of the two with statistical uncertainties. The ratios are fit to a function, $y =$ error function(p_{T}). The systematic uncertainties are assigned based on the fit values. The uncertainty on the material variations is $< 5\%$ in the lowest p_{T} region 0.1-0.2 GeV, then decreasing to $< 3\%$ above 0.2 GeV.

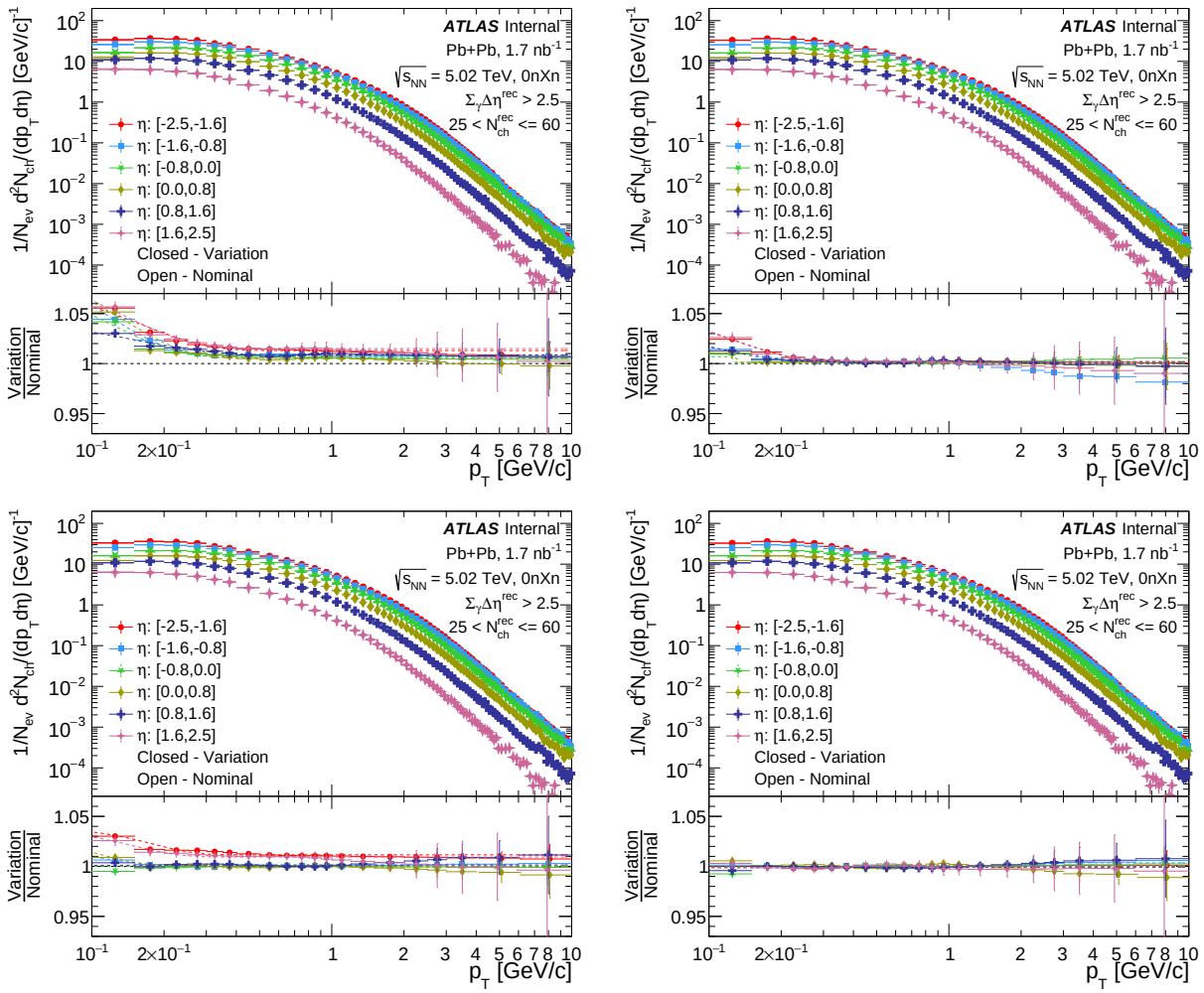

Figure 5.34: Shown is the charged-hadron yields in Pb+Pb UPC as a function of p_{T} in six η selections with material/physics model variation of reconstruction efficiency: +5% Overall ID material (top left), +10% IBL material (top right), +25% PP0 material (bottom left) and physics model (bottom right). The lower panel shows the ratio of the two with fits. Note that the vertical line statistical uncertainties on the ratios are overestimates since the variation and nominal Monte Carlo samples are highly correlated.

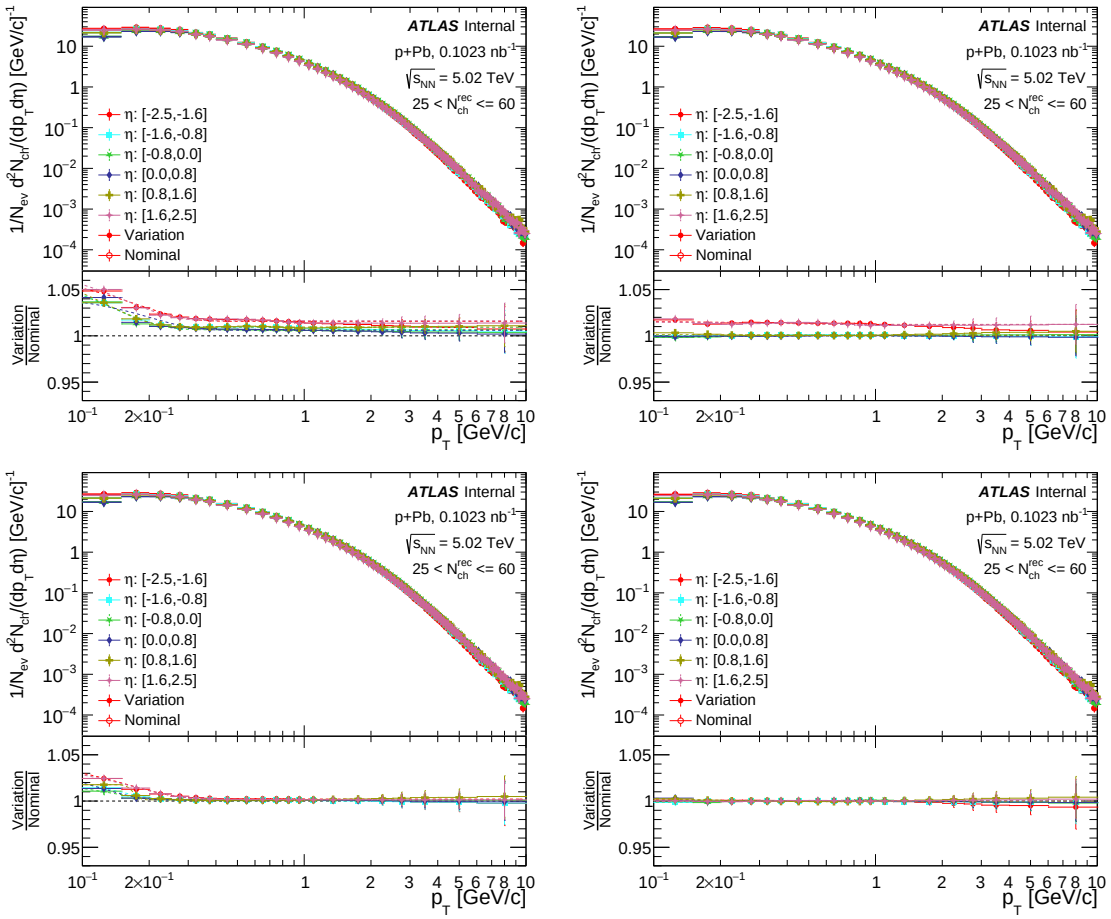

Figure 5.35: Shown is the charged-hadron yields in p+Pb collisions as a function of p_{T} in six η selections with material/physics model variation of reconstruction efficiency: +5% Overall ID material (top left), +10% IBL material (top right), +25% PP0 material (bottom left) and physics model (bottom right). The lower panel shows the ratio of the two with fits. Note that the vertical line statistical uncertainties on the ratios are overestimates since the variation and nominal Monte Carlo samples are highly correlated.

5.5.9 Track-to-Particle Matching Probability

The efficiency corrections used in the analysis rely on matching the reconstructed tracks to the generated particles. To account for ambiguities in the matching procedure, the matching probability, defined in Ref. [153], is varied to assess the systematic uncertainty. The nominal cut of track-to-particle matching probability > 0.5 is varied to probability > 0.3. When this cut is varied, the definition of primary tracks changes. Consequently, all corrections are slightly different because a different set of tracks is used.

Figure 5.36 shows the charged-hadron yields in Pb+Pb UPC (left) and p+Pb (right) as a function of p_{T} in six η selections with track to particle matching probability varied to 0.3 from the nominal value 0.5. The lower panel shows the ratio of the two with statistical uncertainties. The ratios are fit to a constant level, *i.e.*, linear function $y =$ constant. The systematic uncertainties are assigned based on the fit values. The uncertainty is $< 1\%$ at all p_{T}.

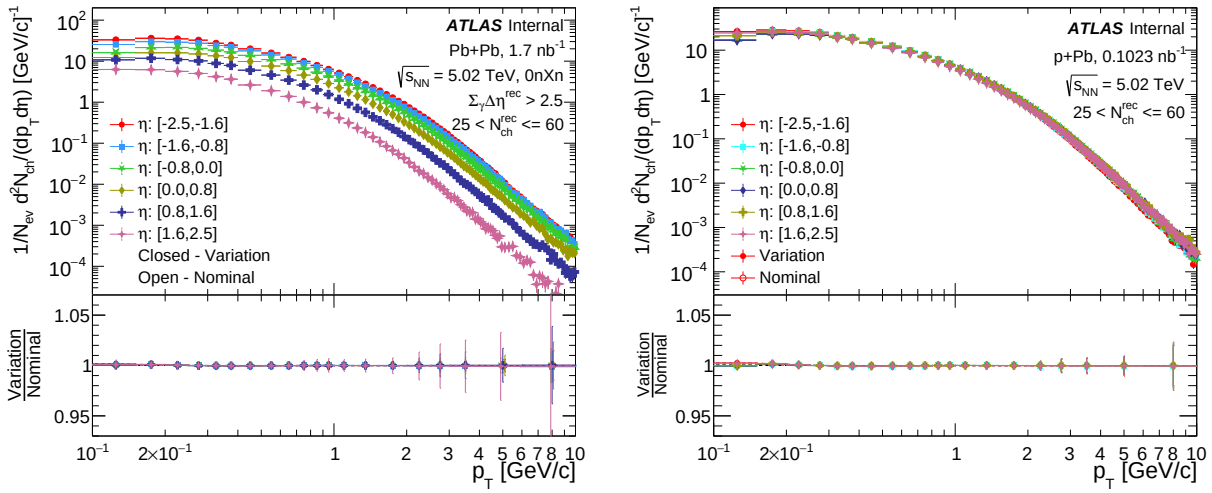

Figure 5.36: Shown are the charged-hadron yields as a function of p_{T} in six η selections with track to particle matching probability varied to 0.3 from the nominal value 0.5 in Pb+Pb UPC (left) and p+Pb (right). The lower panel shows the ratio of the two with fits. Note that the vertical line statistical uncertainties on the ratios are overestimates since the variation and nominal Monte Carlo samples are highly correlated.

5.5.10 Track Bin Migration

The definition of track reconstruction efficiency detailed in Section 5.3.4 does not account for the possibility of particles being reconstructed in a different bin or particles originating from outside of the kinematic range: $p_{\mathrm{T}} > 100$ MeV and $|\eta| < 2.5$. To quantify this effect, we compare two different definitions of track reconstruction efficiency, one with and one without allowing bin migration. In the nominal case, we use the track reconstruction efficiency defined as in Equation 5.5 where bin migration is not allowed. For the case of the variation, we apply an uncertainty equal to 100% of the differences between the two definitions, as shown in Figure 5.20.

Figure 5.37 shows the charged-hadron yields as a function of p_{T} in six η selections in Pb+Pb UPC and p+Pb with track reconstruction efficiency corrected using 100% of the differences between the two definitions for track reconstruction efficiency, one with and one without allowing bin migration. The lower panel shows the ratio of the two with statistical uncertainties. The ratios are fit to a function $y =$ error function(p_{T}). The systematic uncertainties are assigned based on the fit values.

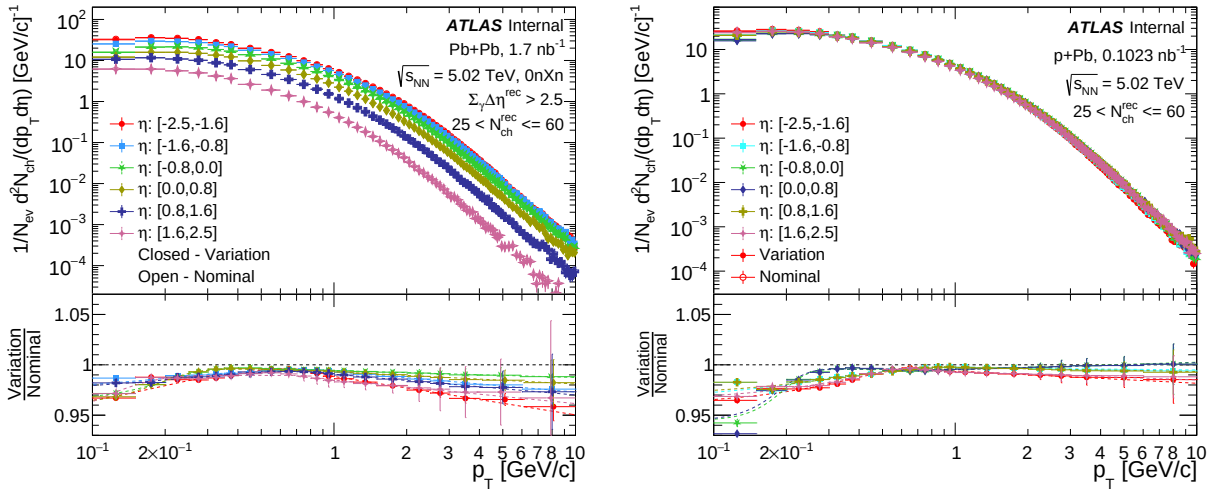

Figure 5.37: Shown are the charged-hadron yields as a function of p_{T} in six η selections in Pb+Pb UPC (left) and p+Pb (right) with track reconstruction efficiency varied by 100% of the differences between the two definitions. The lower panels show the ratio of the two with fits. Note that the vertical line statistical uncertainties on the ratios are overestimates since the variation and nominal Monte Carlo samples are highly correlated.

5.5.11 Extrapolation to $p_{\mathrm{T}} = 0$ GeV

For the $\mathrm{d}N_{\mathrm{ch}}/\mathrm{d}\eta$ results, the final values reflect the yields integrated over the entire p_{T} range. Hence there is an extrapolation of the yield for $p_{\mathrm{T}} < 0.1$ GeV where there is no measurement. Three variations are considered to gauge the sensitivity to this extrapolation. Two variations come from fitting the fully corrected yields as a function of p_{T} in exclusive bins in η using the Modified Hagedorn and Tsallis fit functions. The third method, and the default, is utilizing DPMJET-III (HIJING) Monte Carlo for the photonuclear (p+Pb) case to correct for the missing low p_{T} measurements as part of the acceptance correction. Hence this third method assumes the p_{T} dependence in the Monte Carlo is correct in this low p_{T} region. The procedure is discussed in detail in Section 5.3.7.

Figure 5.38 shows the fully corrected charged-hadron yield in η, denoted as $\mathrm{d}N_{\mathrm{ch}}/\mathrm{d}\eta$, with the nominal result and the variations in the top panel. The bottom panel shows the ratio of the fit extrapolations to the nominal result. The differences are in the range of 2-3%, which are utilized to assign a systematic uncertainty.

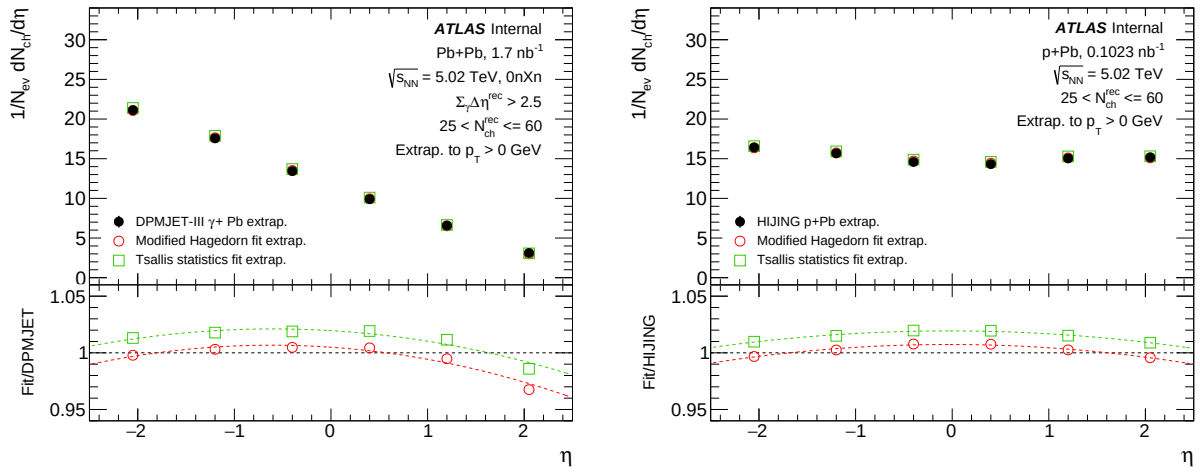

Figure 5.38: Shown are the yields in Pb+Pb UPC (left) and p+Pb (right) as a function of η. The filled markers are the fully corrected data utilizing the DPMJET-III Monte Carlo in the case of Pb+Pb UPC and HIJING in the case of p+Pb. The open points are the fully corrected data utilizing the Modified Hagedorn and Tsallis fits for the extrapolation down to $p_{\mathrm{T}} = 0$ GeV. The lower panel shows the ratio of the data corrected with Monte Carlo to the fits.

5.5.12 Truth-Level $\sum_\gamma \Delta\eta$ Definition (UPC Pb+Pb Only)

This uncertainty estimation is motivated by the following question. If a theorist wants to calculate the yield for our event categories, what are the definitions/cuts for the truth-level event selection quantities they might need? In the case of nominal yield, we use reconstructed tracks and clusters to calculate the $\sum_\gamma \Delta\eta$. In this section, we reevaluate the yield by employing truth-level particles with appropriate selection cuts. Subsequently, we assess the ratio of the recalculated yield to that of nominal yield.

Mis-modeling in DPMJET-III impacts the calculation of $\sum_\gamma \Delta\eta$, and thus cannot be used for the estimation. This is discussed in detail in Section A.4.1. Therefore, in consultation with experts, we use PYTHIA $\gamma + p$ to estimate this particular systematic uncertainty. The PYTHIA model is detailed in Section 5.1.3.2

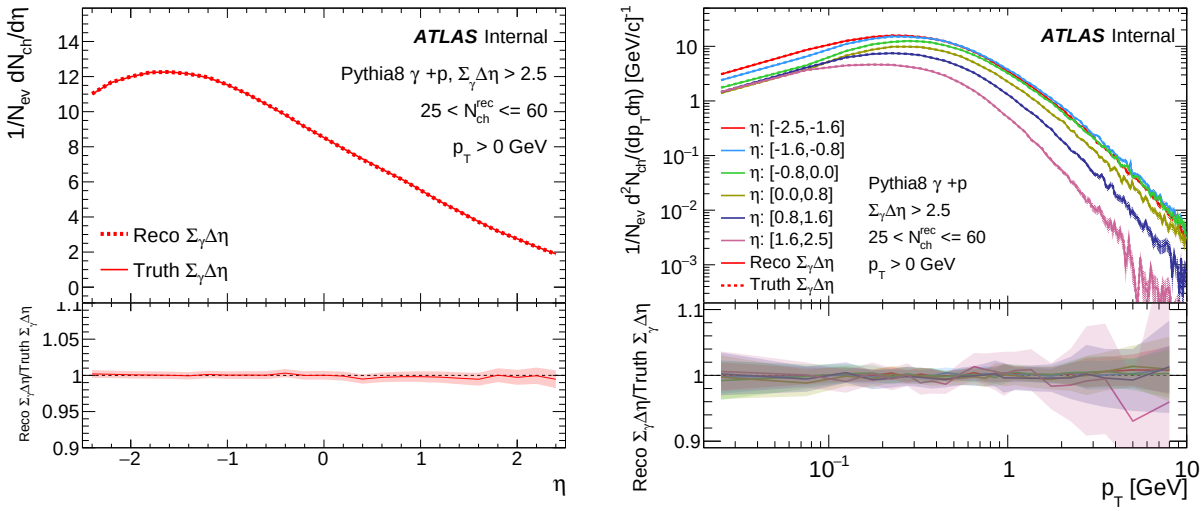

Figure 5.39: Shown are the charged-hadron yield as a function of η in PYTHIA, utilizing $\sum_\gamma \Delta\eta$ defined using reconstructed tracks, shown as a dotted line, and truth particles, shown as a solid line. The bottom panel shows the ratio of the two distributions.

Figure 5.39 compares the charged-hadron yield as a function of η in PYTHIA, using separate $\sum_\gamma \Delta\eta$ definitions based on reconstructed tracks and truth particles. We note that the $\sum_\gamma \Delta\eta^{\text{rec}}$ defined at the reconstructed level utilizes tracks with $p_{\text{T}} > 0.4$ GeV, $|\eta| < 2.5$ and clusters with $p_{\text{T}} > 0.2$ GeV, $|\eta| < 4.9$, while for the truth-level $\sum_\gamma \Delta\eta^{\text{truth}}$ definition, particles with $p_{\text{T}} > 0.45$

GeV, $|\eta| < 4.9$ are utilized to achieve better agreement with the reconstructed level gap definition. Remarkably, PYTHIA exhibits excellent agreement in $\mathrm{d}N_{\mathrm{ch}}/\mathrm{d}\eta$ between truth and reconstructed level $\sum_{\gamma} \Delta\eta$ definitions.

However, in the most forward rapidity region η:[1.6,2.5], and in the highest p_{T} region above 2 GeV, there is an observed difference of $< 5\%$ between the two distributions. This difference is fitted using a log polynomial of 2^{nd} order and the fit values are assigned as a systematic uncertainty.

5.5.13 Uncertainty on Fitting Track Reconstruction Efficiency

The track reconstruction efficiency, defined in Equation 5.5, as a function of p_{T} is fitted using a polynomial function of 5^{th} order in $\log(p_{\mathrm{T}})$ at low p_{T} ($p_{\mathrm{T}} < 1$ GeV) and a polynomial function of 1^{st} order in $\log(p_{\mathrm{T}})$ at high p_{T} ($p_{\mathrm{T}} > 1$ GeV) in each of the 25 η bins spanning from -2.5 to 2.5 as shown in Figure 5.16 and Figure 5.17 in DPMJET-III and HIJING respectively. The two fit functions are made continuous at the intersection $p_{\mathrm{T}} = 1$ GeV. A zoomed-in version of the reconstruction efficiency in DPMJET-III is shown in Figure 5.18. The uncertainty on the fit values is accounted for in this analysis.

Figure 5.40 shows the uncertainties on the fit functions utilized in track reconstruction efficiencies as a function of $p_{\mathrm{T}}^{\mathrm{truth}}$ (left) and η^{truth} (right), in DPMJET-III (top) and HIJING (bottom). The fit uncertainties as a function of p_{T} are fitted using a polynomial function of 1^{st} order in $\log(p_{\mathrm{T}})$ and fit uncertainties as a function of η is fitted using a constant function, and are shown in the figure as dotted lines.

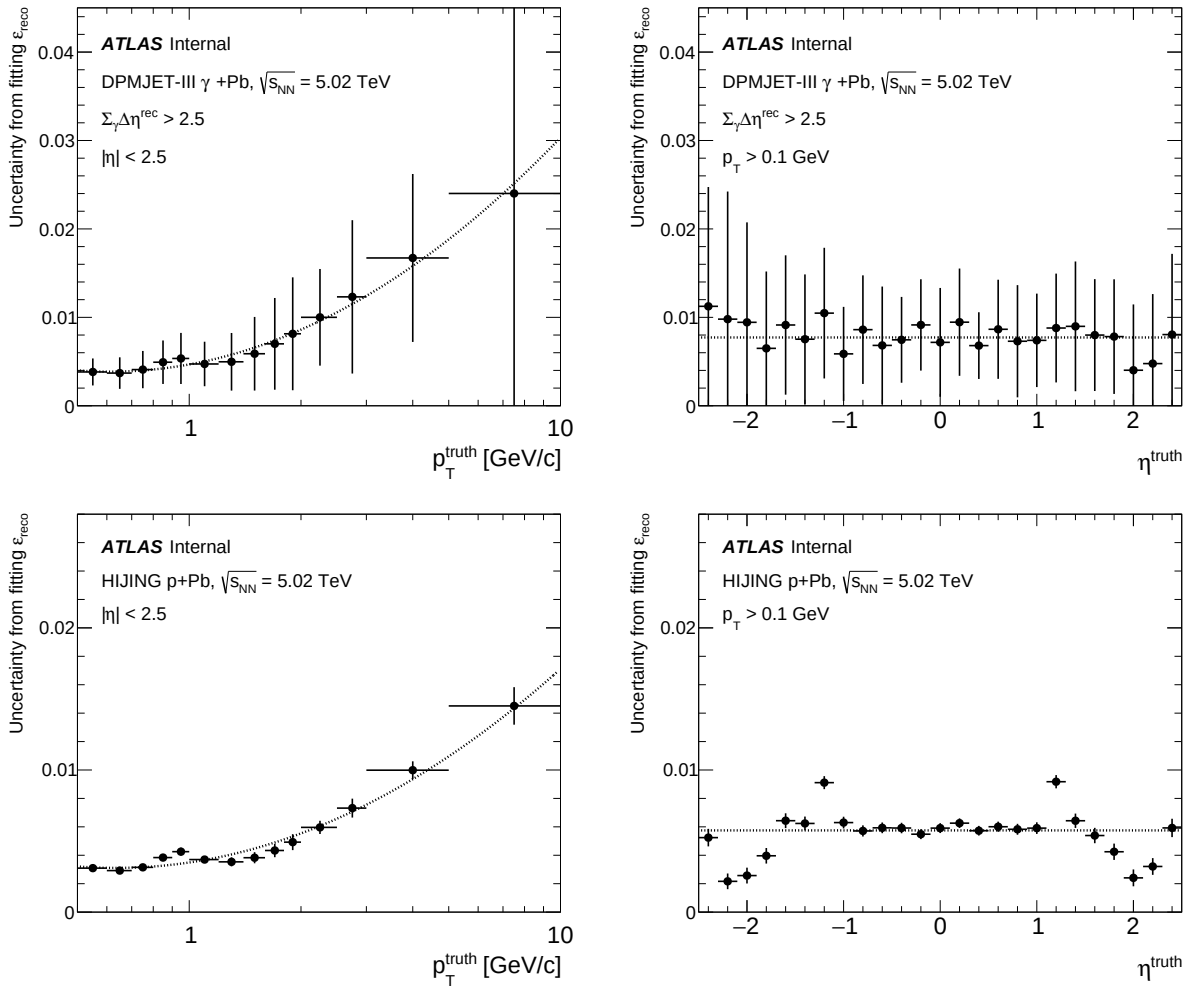

Figure 5.40: Shown are the uncertainties on the fit functions utilized in track reconstruction efficiencies as a function of $p_{\mathrm{T}}^{\mathrm{truth}}$ (left) and η^{truth} (right), in DPMJET-III (top) and HIJING (bottom).

5.5.14 Systematic Uncertainty Summary

Figures 5.41 and 5.42 show the fractional systematic uncertainties on the charged-hadron yields in Pb+Pb UPC (upper) and p+Pb (lower) as a function of p_{T} and η, respectively, based on the detailed systematic uncertainties mentioned above. All systematic uncertainties are added in quadrature, and the upper and lower error bands are symmetrized by taking the maximum value, which is also displayed in the figures.

In the p_{T} region above 0.4 GeV, the systematic uncertainty remains nearly constant and is below 5% and 3% in Pb+Pb UPC and p+Pb, respectively, with many of these uncertainties being comparable to each other. The dominant source of uncertainties in Pb+Pb UPC in the most forward rapidity bin is from event purity, track bin migration, and truth gap definition - all of these subdominant to each other. The dominant source of uncertainty in Pb+Pb UPC in the most backward rapidity bin is from track bin migration. In p+Pb, the main sources of uncertainty are material variations and track bin migration in the p_{T} region above 0.4 GeV.

In the p_{T} region below 0.4 GeV, particularly below 0.2 GeV, the systematic uncertainty increases to approximately 8-10% with the dominant sources of uncertainties being material variations of the order 4-5% in both p+Pb and Pb+Pb UPC.

The two dominant sources of systematic uncertainty in mid-rapidity region $|\eta| < 1.5$ in both Pb+Pb UPC and p+Pb are extrapolation to $p_{\mathrm{T}} = 0$ GeV and fakes/secondaries, both under 2%. In the forward/backward rapidity region $|\eta| > 1.5$, the dominant sources of uncertainties are material variations, under 4%.

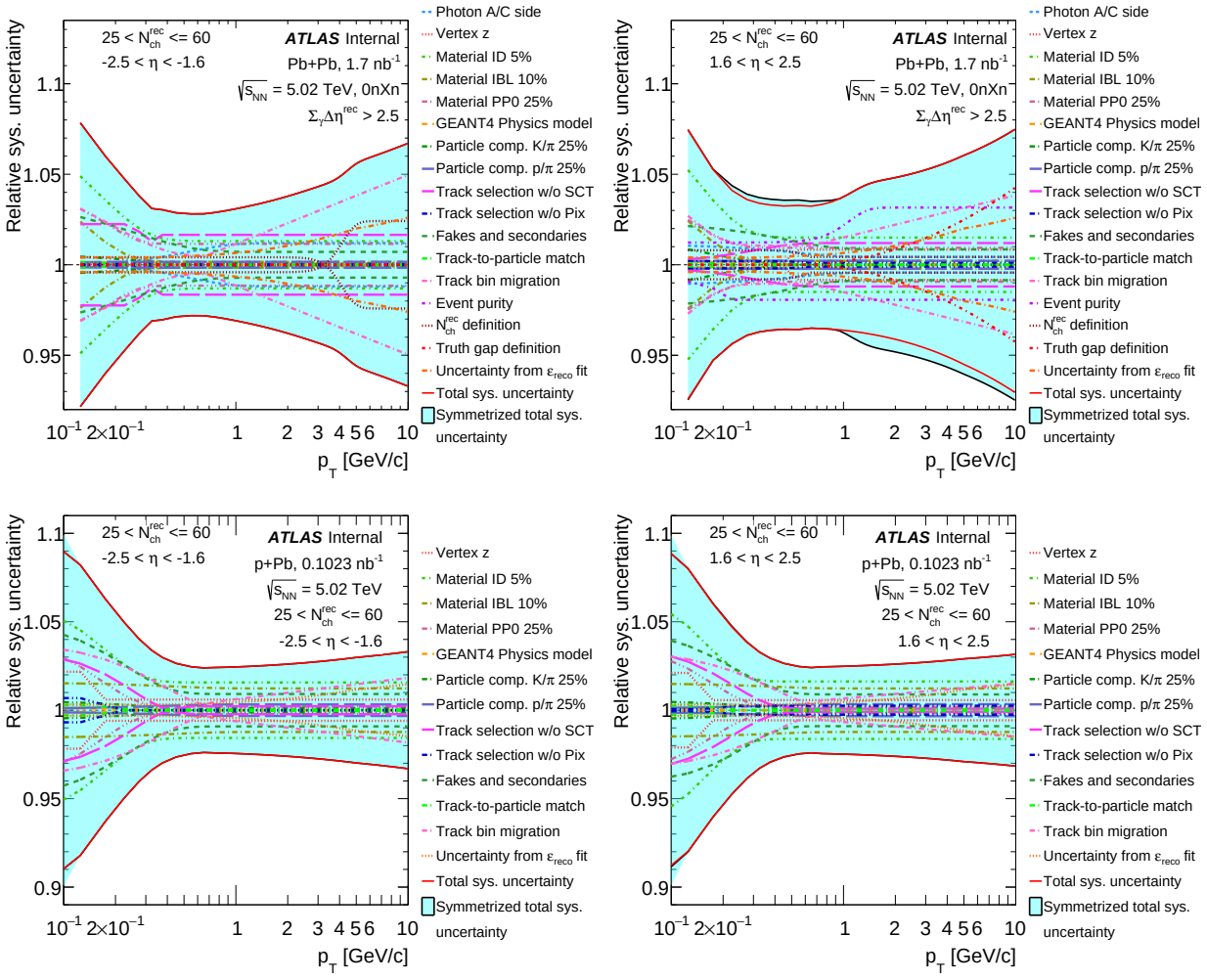

Figure 5.41: Shown are the systematic uncertainties as a function of p_{T} in Pb+Pb UPC (top row) and p+Pb collisions (bottom row) in η slices: [-2.5,-1.6] (left column) and [1.6,2.5] (right column).

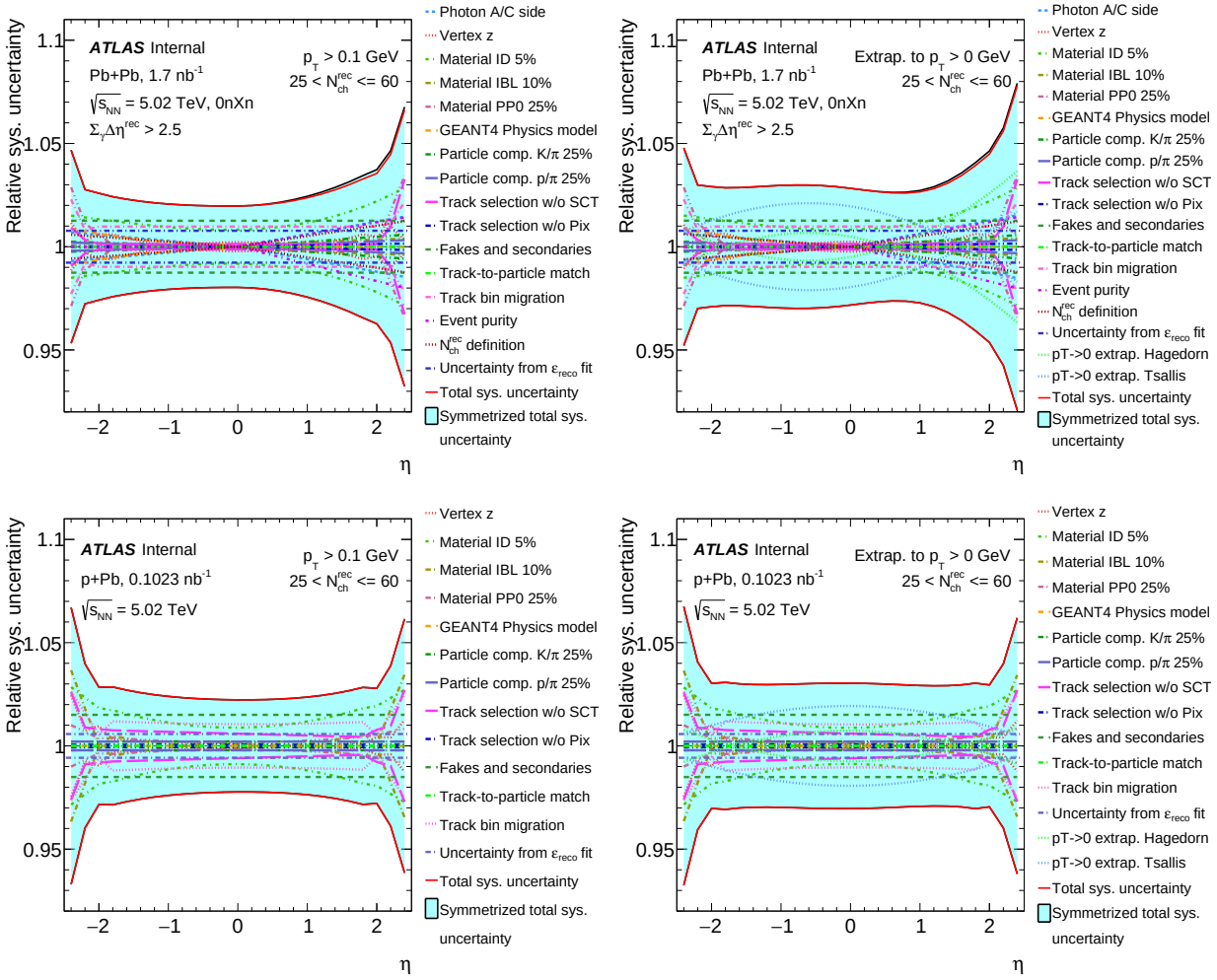

Figure 5.42: Shown are the systematic uncertainties as a function of η in Pb+Pb UPC (top row) and p+Pb collisions (bottom row) for $p_{\mathrm{T}} > 0.1$ GeV (left column) and $p_{\mathrm{T}} > 0$ GeV (right column).

5.6 Results

This section presents the final physics results including all uncertainties elaborated previously. Detailed physics discussions are included in Chapter 7.

The charged-hadron yields are presented in 5.02 TeV Pb+Pb UPC and p+Pb collisions both (i) as a function of p_{T} in six exclusive intervals of η and (ii) integrated over all p_{T} as a function of η. The yields are first shown for the $N_{\mathrm{ch}}^{\mathrm{rec}}$ selection, $25 < N_{\mathrm{ch}}^{\mathrm{rec}} \leq 60$, where the p+Pb events are re-weighted to have effectively the same $N_{\mathrm{ch}}^{\mathrm{rec}}$ distribution as the Pb+Pb UPC events. Additionally, the distribution in p+Pb is re-weighted to have the same integral of $\mathrm{d}N_{\mathrm{ch}}/\mathrm{d}\eta$ in Pb+Pb UPC over the η range, -2.5 to 2.5. Negative η corresponds to the Pb-going direction, and positive η corresponds to the photon-going and proton-going directions in Pb+Pb UPC and p+Pb, respectively.

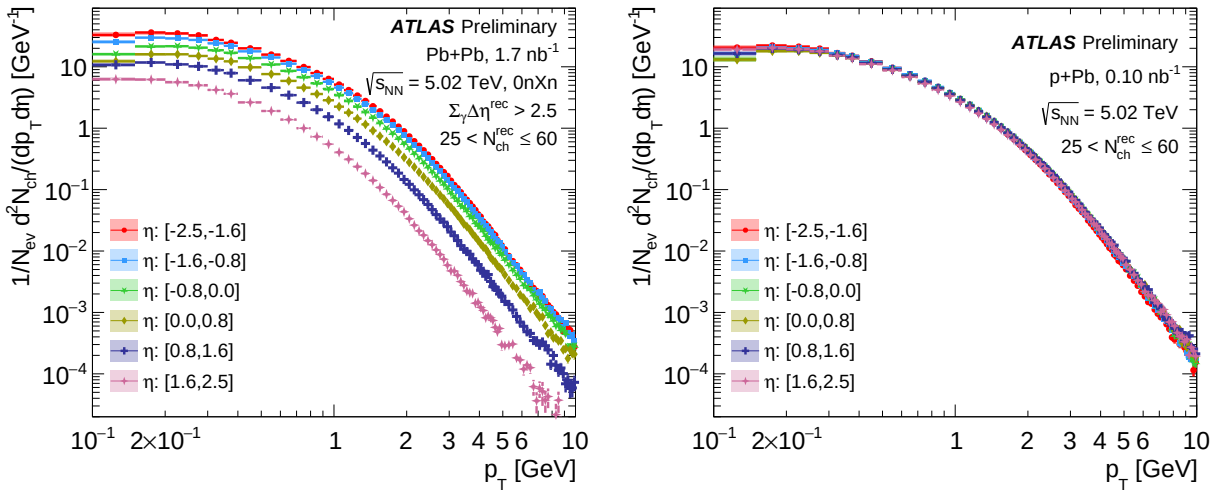

Figure 5.43: Shown are the charged-hadron yields as a function of p_{T} in six η selections. The left panel is for UPC Pb+Pb collisions and the right panel is for p+Pb collisions. Statistical uncertainties are shown as vertical lines and systematic uncertainties are shown as open boxes. For most data points, the systematic uncertainties are smaller than the markers.

Figure 5.43 shows the charged-hadron yields as a function of p_{T} in six η selections: [-2.5,-1.6], [-1.6,-0.8], [-0.8,0.0], [0,0.8], [0.8,1.6], [1.6,2.5]. The left panel shows Pb+Pb UPC results and the right panel shows p+Pb results. Positive η corresponds to the photon-going and proton-going directions, respectively. The yields are shown on a log-log scale. Statistical uncertainties are shown

as vertical lines and systematic uncertainties are shown as vertical boxes.

Figure 5.44 shows the ratio of charged-hadron yields between Pb+Pb UPC and p+Pb events for the six η selections. At forward pseudorapidity, the p_{T} distribution falls much more steeply in Pb+Pb UPC events. In contrast, the shape of the p_{T} distribution is quite comparable between Pb+Pb UPC and p+Pb at backward rapidity.

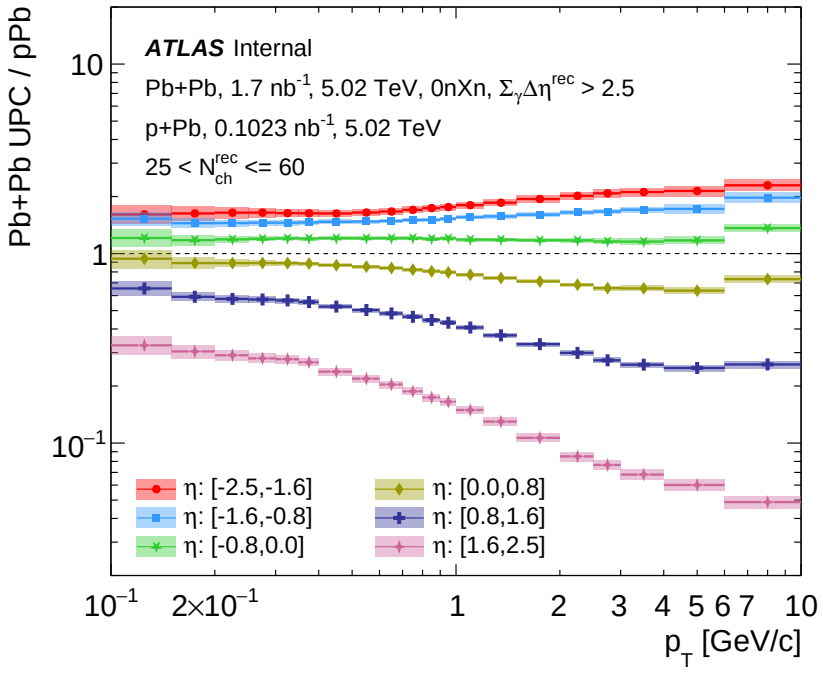

Figure 5.44: Shown are the ratios of charged-hadron yields in Pb+Pb UPC to p+Pb collisions as a function of p_{T} in six η intervals. Statistical uncertainties are shown as vertical lines and systematic uncertainties are shown as open boxes.

Figure 5.45 shows the charged-hadron yields as a function of η. The top panels show Pb+Pb UPC results and the bottom panels show p+Pb results. Two cases are included: (i) results integrated over the measured p_{T} range, *i.e.*, $p_{\mathrm{T}} > 0.1$ GeV (left panels) and (ii) results extrapolated to include the yield over all p_{T}, *i.e.*, $p_{\mathrm{T}} > 0$ (right panels). The yields are thus slightly higher in the $p_{\mathrm{T}} > 0$ case and include an additional uncertainty for the extrapolation as detailed in Section 5.5.11. Positive η corresponds to the photon-going and proton-going directions, respectively. Statistical uncertainties are shown as vertical lines and systematic uncertainties are shown as vertical boxes.

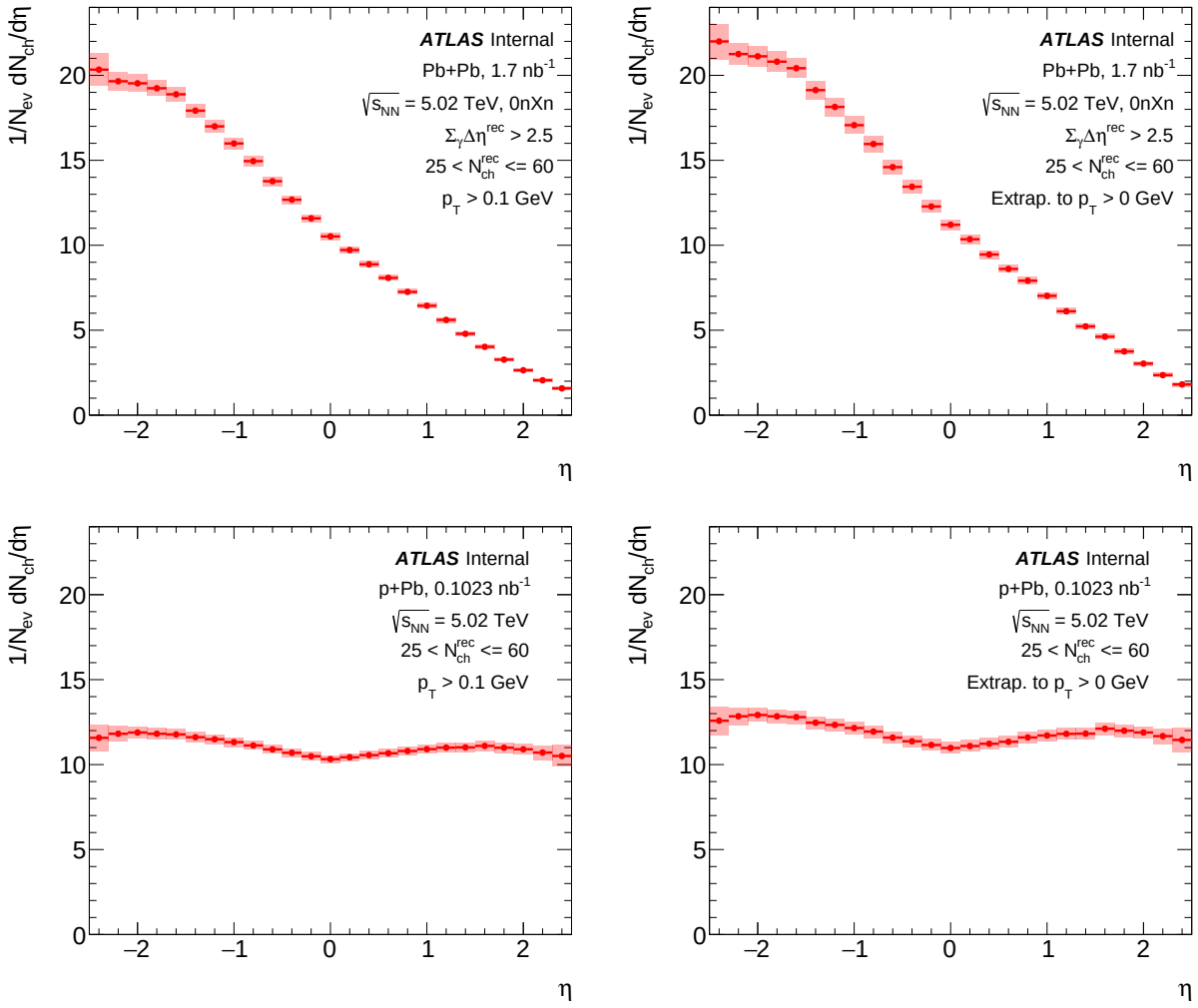

Figure 5.45: Shown are the charged-hadron yields as a function of η. The top panels are for Pb+Pb UPC and the bottom panels are for p+Pb collisions. The left panels correspond to yields integrated for $p_{\mathrm{T}} > 0.1$ GeV and the right panels for $p_{\mathrm{T}} > 0$ GeV. The statistical uncertainties are shown as vertical lines and systematic uncertainties are shown as open boxes.

Figure 5.46 shows the charged-hadron yields between Pb+Pb UPC and p+Pb events as a function of η. At forward pseudorapidity, the p_{T} distribution falls much more steeply in Pb+Pb UPC events. In contrast, the p+Pb distribution is nearly symmetric.

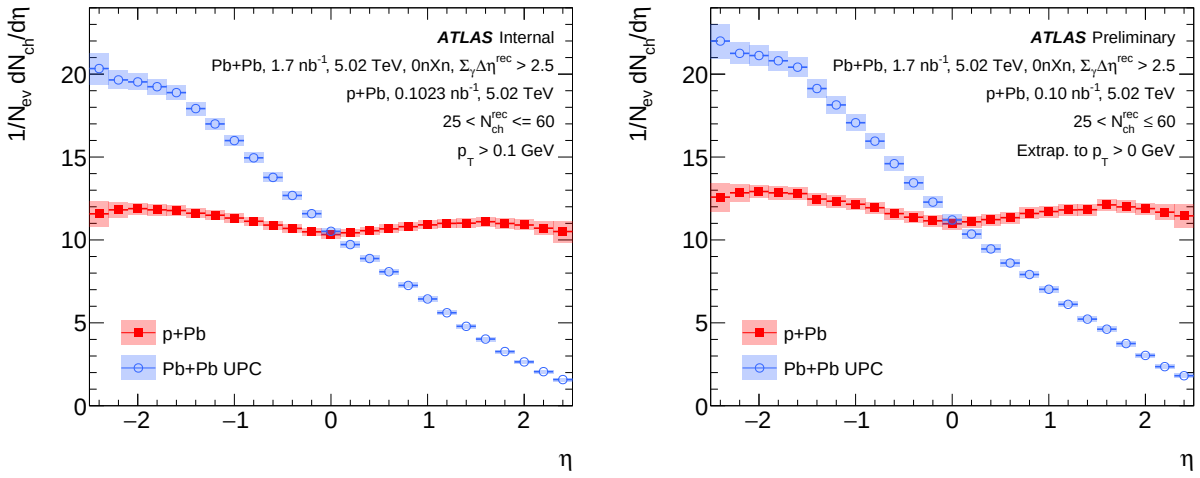

Figure 5.46: Shown are the charged-hadron yields in Pb+Pb UPC and p+Pb collisions as a function of η. The left panels correspond to yields integrated for $p_{\mathrm{T}} > 0.1$ GeV and the right panels for $p_{\mathrm{T}} > 0$ GeV. Statistical uncertainties are shown as vertical lines and systematic uncertainties are shown as open boxes.

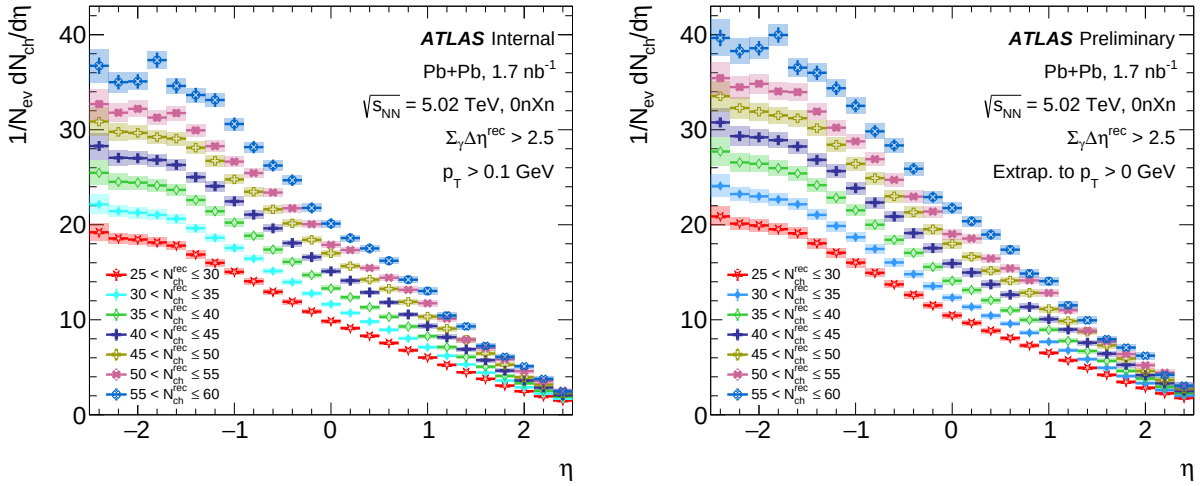

Figure 5.47: Shown are the charged-hadron yields as a function of η in different $N_{\mathrm{ch}}^{\mathrm{rec}}$ bins in Pb+Pb UPC collisions. The left panel shows the result for $p_{\mathrm{T}} > 0.1$ GeV and the right panel shows the extrapolated result, $p_{\mathrm{T}} > 0$ GeV. Vertical lines are statistical uncertainties and open boxes are systematic uncertainties.

To examine charged hadron production more differentially in Pb+Pb UPC, the experimental data is split into several $\Delta N_{\mathrm{ch}}^{\mathrm{rec}} = 5$ wide categories. Figure 5.47 shows $\mathrm{d}N_{\mathrm{ch}}/\mathrm{d}\eta$ for seven categories in $N_{\mathrm{ch}}^{\mathrm{rec}}$ for $p_{\mathrm{T}} > 0.1$ GeV (left) and $p_{\mathrm{T}} > 0$ (right). The overall rapidity shift (within the region of the measurement $-2.5 < \eta < +2.5$) is quantified for each $N_{\mathrm{ch}}^{\mathrm{rec}}$ selection in data. Figure 5.48 shows $\langle\eta\rangle$ as a function of $N_{\mathrm{ch}}^{\mathrm{rec}}$ utilizing the yields again for $p_{\mathrm{T}} > 0.1$ GeV (left) and $p_{\mathrm{T}} > 0$ (right).

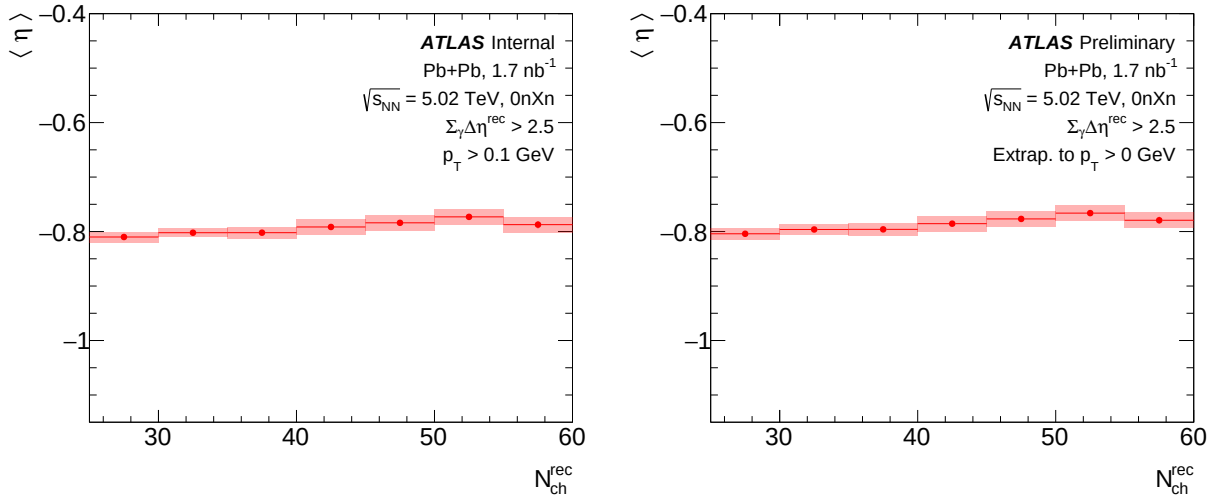

Figure 5.48: Shown are the calculated $\langle\eta\rangle$ values within the window $-2.5 < \eta < +2.5$ of charged-hadron yields as a function of $N_{\mathrm{ch}}^{\mathrm{rec}}$ in Pb+Pb UPC collisions. The left panel shows the result for $p_{\mathrm{T}} > 0.1$ GeV and the right panel shows the extrapolated result, $p_{\mathrm{T}} > 0$ GeV.

One can also examine the p_{T} distributions in these finer $N_{\mathrm{ch}}^{\mathrm{rec}}$ selections. Figure 5.49 shows $\langle p_{\mathrm{T}}\rangle$ for the range $p_{\mathrm{T}} > 0.1$ GeV in the top panels and $\langle p_{\mathrm{T}}\rangle$ for $p_{\mathrm{T}} > 0$ GeV in the bottom panels as a function of $N_{\mathrm{ch}}^{\mathrm{rec}}$ in two η selections of interest, [-1.6,-0.8] and [0.8,1.6], in Pb+Pb UPC collisions in p+Pb collisions. At negative pseudorapidity, $\langle p_{\mathrm{T}}\rangle$ between the two collision systems agrees very well. On the photon-going side ($\eta > 0$), there is a constant difference in the $\langle p_{\mathrm{T}}\rangle$ between the two collision systems. This observation is consistent with the difference in the shape of the p_{T} distributions between Pb+Pb UPC and p+Pb in the η selections of interest.

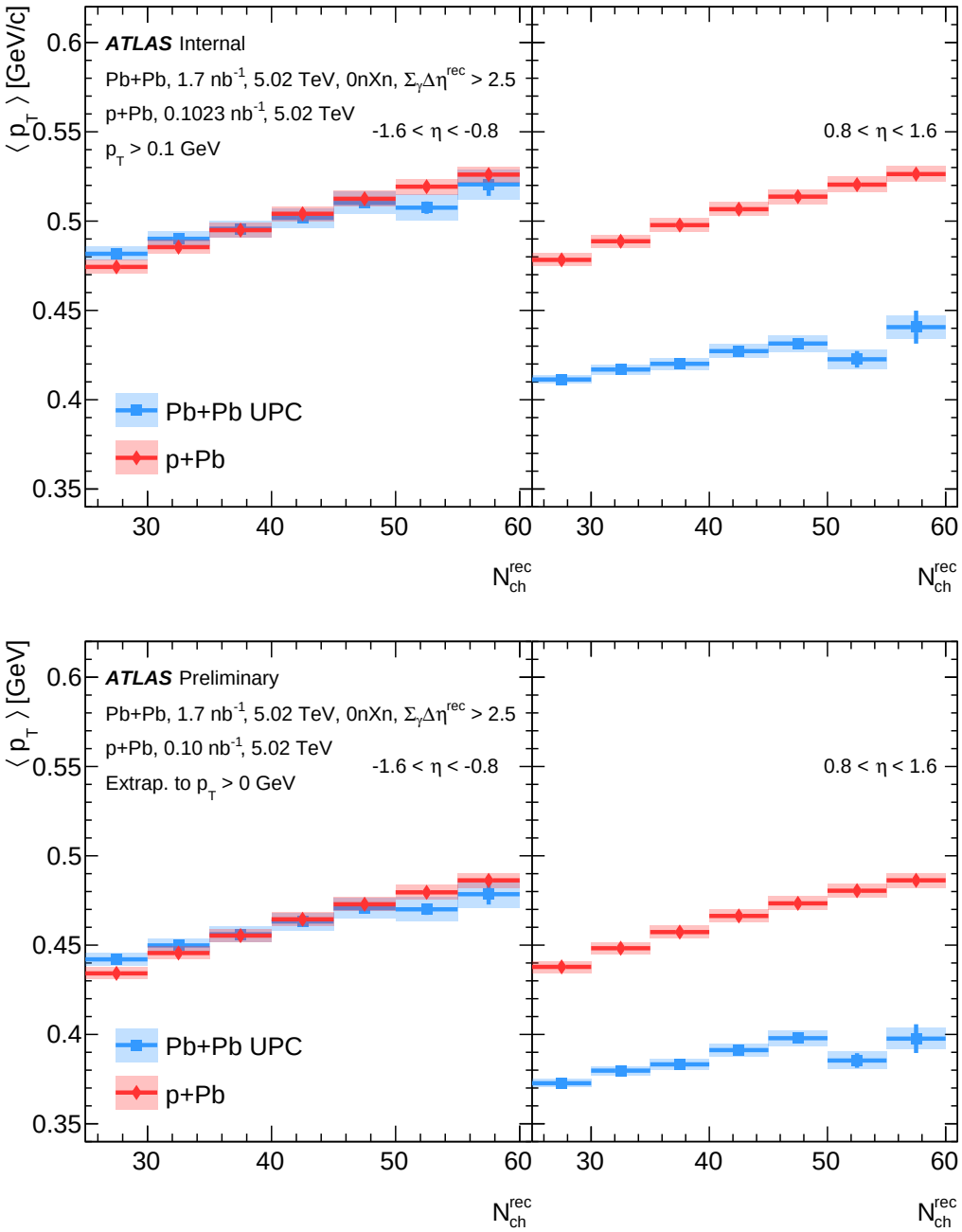

Figure 5.49: Shown are the $\langle p_{\mathrm{T}} \rangle$ of charged-hadron yields as a function of $N_{\mathrm{ch}}^{\mathrm{rec}}$ in Pb+Pb UPC collisions and p+Pb collisions in two different η slices, [-1.6,-0.8] (left) and [0.8,1.6] (right). The top panel shows the result for $p_{\mathrm{T}} > 0.1$ GeV and the bottom panel shows the extrapolated result, $p_{\mathrm{T}} > 0$ GeV.

Chapter 6

Measurement of Identified Particle Production

As discussed in Chapter 3, photo-nuclear collisions provide a valuable platform for investigating whether a small system can produce the presence of a tiny QGP droplet. ATLAS [10] has already identified evidence of the collective expansion of the QGP medium through measuring two-particle azimuthal correlations, v_2 and v_3, in these collisions. This discovery motivates a detailed measurement of identified particle production to explore additional QGP signatures, including radial flow [2], baryon/meson enhancement [12], and strangeness enhancement [11].

The analysis of charged hadrons begins to address whether there is radial flow as quantified by the p_{T} distributions of charged hadrons [154], as detailed in Chapter 5. In this Chapter, measurements of the inclusive yields of specific, identified hadrons such as K^0_{S}, Λ, and Ξ^- are used to provide significant additional information to address the question regarding quark-gluon plasma formation in detail. Radial flow, characterized by the mean value of p_{T} distributions, denoted as $\langle p_{\mathrm{T}} \rangle$, is more discerned in heavier-mass particles such as K^0_{S}, Λ, and Ξ^-. These particles, containing one or more strange quarks, allow one to answer questions related to strangeness production via the ratio of strange hadrons to charged hadrons, which is predicted to be enhanced in the QGP medium. The ratio of the yield of baryon (Λ or Ξ^-) to meson (K^0_{S}) as a function of p_{T} probes the degree of baryon/meson enhancement present in these collisions. The comparisons of photon-nuclear collisions with p+Pb collisions enable the testing of specific predictions from the hydrodynamic model framework [61], such as that radial flow should be the same for both systems.

This chapter provides a measurement of identified-hadron (K^0_S, Λ, and Ξ^-) yields in photo-nuclear collisions with the ATLAS detector. The yields of these identified hadrons are presented as a function of rapidity (y) and p_T, while the $\langle p_T \rangle$ is reported as a function of collision multiplicity N^{rec}_{ch}. Additionally, the chapter presents the ratio of baryons (Λ and Ξ^-) to mesons (K^0_S) as a function of p_T in y bins, and the ratio of strange hadrons (K^0_S, Λ, and Ξ^-) to charged hadrons as a function of multiplicity N^{rec}_{ch} in y bins. Finally, photon-nuclear results are compared with p+Pb collisions.

As in Chapter 5, this part of the measurement utilizes the identical 2018 Pb+Pb 5.02 TeV dataset and event selection cuts as the photo-nuclear flow analysis [137], and the same analysis procedure is also applied to low-multiplicity 2016 p+Pb collisions at 5.02 TeV, with N^{rec}_{ch}, selected to match that of the photo-nuclear events. Here, K^0_S, Λ, and Ξ^- hadrons are reconstructed in their two-body decay or through a three-body final state where the decay chain has proceeded through one of the two-body decays. Commonly known as the V^0 method, the V-shaped decay track of a neutral hadron is reconstructed, and a common secondary vertex is found. Invariant mass distributions of the reconstructed V^0 particles are obtained through a set of optimized selection cuts. The signal counts are extracted in each y-p_T selection by fitting the invariant mass distributions. Subsequently, the signal counts are corrected for reconstruction and selection inefficiencies. Finally, the yields of these particles are determined as a function of p_T in several y bins, and relevant observables are computed.

6.1 Data and Event Selection

The datasets utilized in this analysis, such Pb+Pb UPC data, p+Pb data, and Monte Carlo samples, are identical to those employed in the charged-hadron analysis outlined in Section 5.1. In this section, we detail the event selection criteria for UPC and p+Pb events. We focus on the criteria for UPC events first and then p+Pb events while noting the common details for both.

6.1.1 UPC Event Selection

The event selection criteria are matched to those used in the ATLAS UPC two-particle correlation analysis [137]. In the ATLAS UPC two particle-correlation analysis, reconstructed tracks were selected with $p_{\mathrm{T}} > 400$ MeV and the `MinBias` working point. In the current analysis, reconstructed tracks that enter the charged-hadron yields are selected with $p_{\mathrm{T}} > 100$ MeV and with the `HILoose` working point, which is identical to that of `MinBias` working point above $p_{\mathrm{T}} = 400$ MeV.

In the following subsections, event-level definitions such as $N_{\mathrm{ch}}^{\mathrm{rec}}$, $\sum_{\gamma} \Delta\eta^{\mathrm{rec}}$, and ZDC criteria are explained, and their selection for this analysis is detailed.

6.1.1.1 Multiplicity Definition

In each selected event, the number of reconstructed tracks passing the `HILoose` working point and $p_{\mathrm{T}} > 400$ MeV is referred to as the charged-particle multiplicity ($N_{\mathrm{ch}}^{\mathrm{rec}}$).

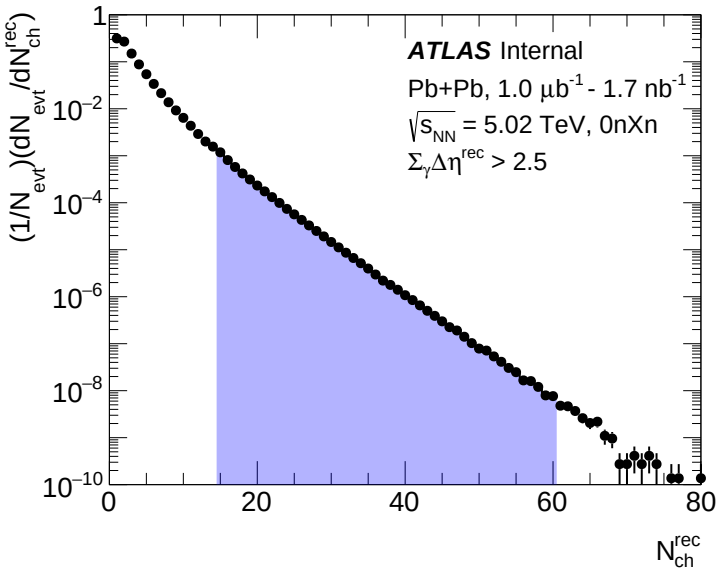

Figure 6.1: Shown is the multiplicity distribution ($N_{\mathrm{ch}}^{\mathrm{rec}}$) from Pb+Pb UPC collisions. The $N_{\mathrm{ch}}^{\mathrm{rec}}$ range [15,60] utilized in this analysis is highlighted.

The $N_{\mathrm{ch}}^{\mathrm{rec}}$ distribution in Pb+Pb UPC collisions is shown in Figure 6.1, corresponding to

minimum bias events with the additional $\sum_{\gamma} \Delta\eta^{\mathrm{rec}}$ requirement (as detailed below). The $N_{\mathrm{ch}}^{\mathrm{rec}}$ range [15,60] utilized in this analysis is color highlighted. This range is chosen since UPC events with $N_{\mathrm{ch}}^{\mathrm{rec}} < 15$ suffer from a rather uncertain mixture of photo-nuclear and background processes. The upper bound is chosen as $N_{\mathrm{ch}}^{\mathrm{rec}} = 60$ considering the statistical limitations in the higher multiplicity region. $N_{\mathrm{ch}}^{\mathrm{rec}}$ differential results are presented in the range $N_{\mathrm{ch}}^{\mathrm{rec}}$: [15,60] and $N_{\mathrm{ch}}^{\mathrm{rec}}$ integrated results are presented in the range $N_{\mathrm{ch}}^{\mathrm{rec}}$: [25,60]. The integrated result range was selected to maintain high statistics while not being dominated by the lowest multiplicity events where collective effects are expected to be small.

In the analysis of charged hadrons [154], a slightly modified definition was used for event multiplicity $N_{\mathrm{ch}}^{\mathrm{rec}}$, due to the auto-correlation bias present between particles included in the event-class definition and those included in the yield calculation. Here, reconstructed tracks utilized for the V^0's have large transverse flight distances (L_{xy} extending out to 500 mm), while the reconstructed tracks utilized for $N_{\mathrm{ch}}^{\mathrm{rec}}$ are required to come from the primary vertex ($\mathrm{d}_0 < 1.5$ mm). Thus, there is minimal overlap between the yield and event category in each event, thus eliminating the need for the above-modified method here.

6.1.1.2 Photo-Nuclear Gap and Coordinate Definitions

The photon- vs Pb-going direction is determined in the data sample by the ZDC trigger, which has exclusive OR logic. The photon-going direction requires a ZDC trigger signal consistent with no incident neutrons. This also sets the customary coordinates for $\gamma + \mathrm{A}$ collisions with the photon-going direction defined as positive rapidity. The pseudorapidity gap selection utilized in this analysis is the same as that used in the charged-hadron analysis, requiring $\sum_{\gamma} \Delta\eta^{\mathrm{rec}} > 2.5$, as elaborated in Section 5.2.1.2.

6.1.1.3 UPC Event Selection Criteria

The UPC event selection criteria utilized in this analysis are the same as those used in the charged-hadron analysis, as detailed in Section 5.2.1.3.

6.1.1.4 Residual Backgrounds in the Event Sample

The treatment of residual backgrounds in the UPC sample is the same as that used in the charged-hadron analysis, as detailed in Section 6.1.1.4. There is an important contribution of Pb+Pb peripheral inelastic collisions contaminating the UPC Pb+Pb sample despite the 0nXn ZDC requirement and photon sum-of-gaps selection. To investigate the impact of this potential contamination of the UPC Pb+Pb sample, we assume for a given $N_{\mathrm{ch}}^{\mathrm{rec}}$ selection, the measured particle yield ($\mathrm{UPC}_{\mathrm{measured}}$) is a combination of "true" UPC Pb+Pb events ($\mathrm{UPC}_{\mathrm{true}}$) and a contamination contribution ($\mathrm{UPC}_{\mathrm{contamination}}$). A purity correction factor (PCF), defined as the ratio of $\mathrm{UPC}_{\mathrm{true}}$ to $\mathrm{UPC}_{\mathrm{measured}}$ is calculated for the $\mathrm{d}N_{\mathrm{ch}}/\mathrm{d}\eta$ observable as a function of η and the $\mathrm{d}N_{\mathrm{ch}}^2/\mathrm{d}p_{\mathrm{T}}\mathrm{d}\eta$ observable as a function of p_{T}, η. Given the $N_{\mathrm{ch}}^{\mathrm{rec}}$ range utilized in this analysis extends to a minimum of $N_{\mathrm{ch}}^{\mathrm{rec}} = 15$, the calculation of PCF is extended down to $N_{\mathrm{ch}}^{\mathrm{rec}} = 15$.

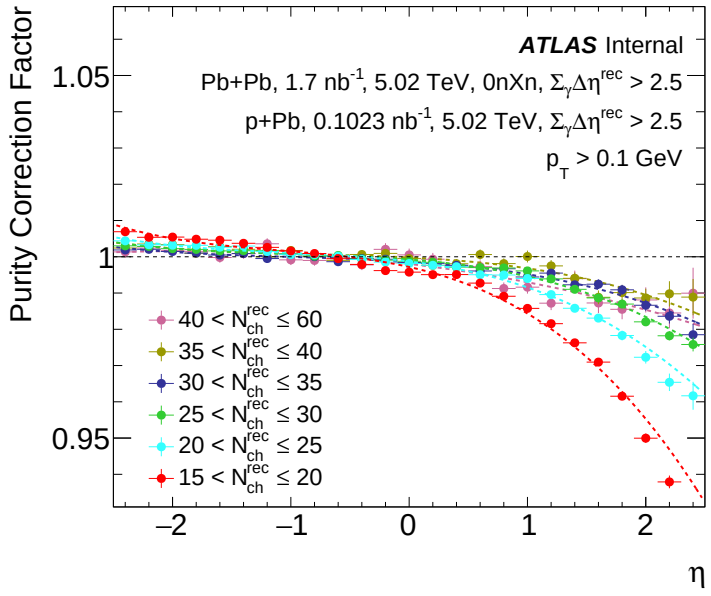

Figure 6.2: Shown are the ratio $\mathrm{UPC}_{\mathrm{true}}/\mathrm{UPC}_{\mathrm{measured}}$ for the $\mathrm{d}N_{\mathrm{ch}}/\mathrm{d}\eta$ observable as a function of η in each $N_{\mathrm{ch}}^{\mathrm{rec}}$ selection $N_{\mathrm{ch}}^{\mathrm{rec}} > 15$.

Figure 6.2 shows the purity correction factor, PCF, calculated for the $\mathrm{d}N_{\mathrm{ch}}/\mathrm{d}\eta$ observable, as a function of η in each $N_{\mathrm{ch}}^{\mathrm{rec}}$ selection. The influence of contamination is largest ($< 6\%$) at positive η for the lowest $N_{\mathrm{ch}}^{\mathrm{rec}}$ selection, $N_{\mathrm{ch}}^{\mathrm{rec}} = 15$-20, as the true UPC Pb+Pb particle yields are expected

to be very asymmetric as compared with the contamination particle yields.

Figure 6.3 shows the purity correction factor, PCF, calculated for the $\mathrm{d}N^2_{\mathrm{ch}}/\mathrm{d}p_{\mathrm{T}}\mathrm{d}\eta$ observable, as a function of p_{T} in each η slice, for different $N^{\mathrm{rec}}_{\mathrm{ch}}$ selections. The potential contamination of UPC events at high p_{T} regions is important to estimate since hadronic backgrounds can be significant in these regions. For $N^{\mathrm{rec}}_{\mathrm{ch}} > 15$, the PCF is approximately 95% for $p_{\mathrm{T}} > 2$ GeV even at most forward rapidity bin η: [1.6,2.5], and consistent with unity within statistical uncertainties elsewhere.

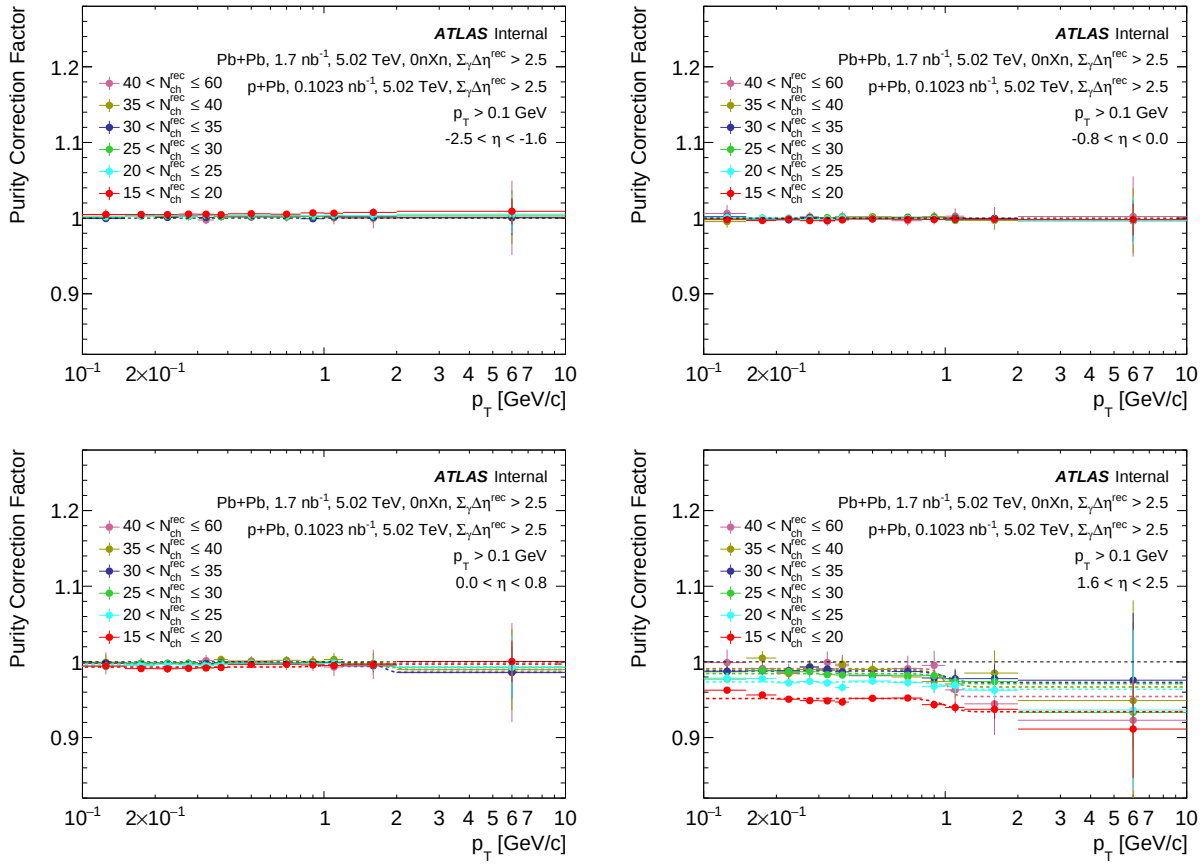

Figure 6.3: Shown are the ratio $\mathrm{UPC}_{\mathrm{true}}/\mathrm{UPC}_{\mathrm{measured}}$ for the $\mathrm{d}N^2_{\mathrm{ch}}/\mathrm{d}p_{\mathrm{T}}\mathrm{d}\eta$ observable as a function of p_{T} in η slices: [-2.5,-1.6] (top left panel), [-0.8,0.0] (top right panel), [0.0,0.8] (bottom left panel) and [1.6,2.5] (bottom right panel) for $N^{\mathrm{rec}}_{\mathrm{ch}} > 15$.

Under the assumption that the purity is correctly determined and that the p+Pb collision data is a good proxy for the contamination, the experimental data can be corrected by PCF as a function of η and p_{T}. The experimental results are corrected using the purity estimate from the

DPMJET-III + HIJING $N_{\mathrm{ch}}^{\mathrm{rec}}$ derived result, and then the results are varied by applying a 100% systematic uncertainty on the purity estimate. For $N_{\mathrm{ch}}^{\mathrm{rec}}$ selection $25-60$, the resulting correction is order $<$ 1-3% and hence with a 1-3% systematic uncertainty.

6.1.2 p+Pb Event Selection

In this Section, the p+Pb multiplicity definition and event selection criteria are detailed.

6.1.2.1 Multiplicity Definition

In each selected event, the number of reconstructed tracks passing the `HILoose` working point and $p_{\mathrm{T}} > 400$ MeV is referred to as the charged-particle multiplicity ($N_{\mathrm{ch}}^{\mathrm{rec}}$).

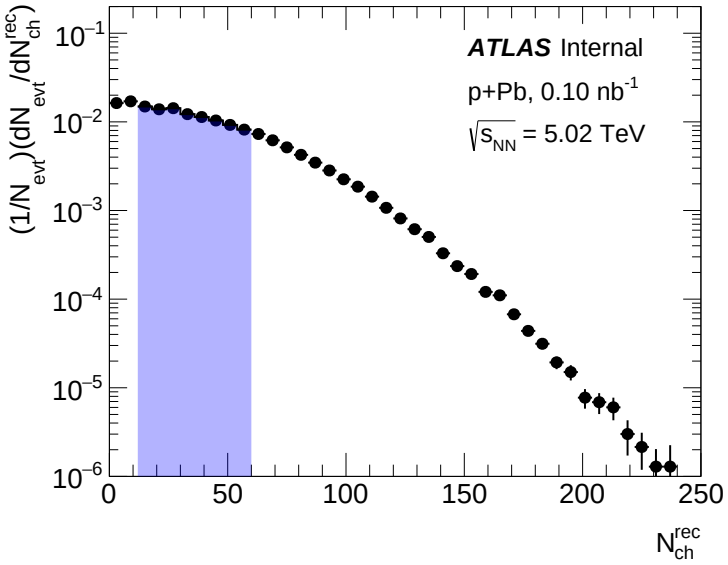

Figure 6.4: Shown is the multiplicity distribution ($N_{\mathrm{ch}}^{\mathrm{rec}}$) from p+Pb collisions corresponding to minimum bias events.

The multiplicity distribution p+Pb collisions is shown in Figure 6.4, corresponding to minimum bias events. The $N_{\mathrm{ch}}^{\mathrm{rec}}$ range [25,60] utilized in this analysis is highlighted, and matches that selected for the UPC Pb+Pb analysis. For later comparison of Pb+Pb UPC and p+Pb collisions, the p+Pb events are re-weighted within the shown range to match the Pb+Pb UPC $N_{\mathrm{ch}}^{\mathrm{rec}}$ distribution. $N_{\mathrm{ch}}^{\mathrm{rec}}$ differential results are presented in the range $N_{\mathrm{ch}}^{\mathrm{rec}}$: [15,60] and $N_{\mathrm{ch}}^{\mathrm{rec}}$ integrated results

are presented in the range $N_{\mathrm{ch}}^{\mathrm{rec}}$: [25,60].

6.1.2.2 p+Pb Event Selection Criteria

The p+Pb event selection criteria utilized in this analysis are the same as those used in the charged-hadron analysis, as detailed in Section 5.2.2.2.

6.2 V^0 Reconstruction and Selection

The inner detector track is the primary reconstructed object used in the analysis of V^0 yields.

We do not utilize anti-particles (i.e., $\bar{\Lambda}$, Ξ^+) in this analysis. We do not have statistical precision on the ratio of anti-particles to particles in Pb+Pb UPC data. Also, an additional uncertainty estimation will be required associated with the annihilation of the particles. The GEANT4 nuclear-interaction cross-section for antiprotons is overestimated by other experiments, resulting in a ratio of anti-particles to particles larger than unity over most of the p_{T} and rapidity range [155].

6.2.1 V^0 Reconstruction Procedure

The K_{S}^0 candidates were required to satisfy the following criteria.

- Oppositely charged track pairs with $p_{\mathrm{T}} > 100$ MeV are fit to a common secondary vertex using a Kalman filter. The reconstructed V^0 is required to have $p_{\mathrm{T}} > 0$ MeV, i.e., the K_{S}^0 can be reconstructed down to zero p_{T}.

- The invariant mass of the K_{S}^0 is calculated by assigning the known pion mass to both tracks and the candidate is kept if within the mass window [397.611, 597.611] MeV/c^2. The Particle Data Group (PDG) reports the mass value of K_{S}^0 as 497.611 MeV/c^2. The mass window boundaries are set with a $\pm$100 MeV/c^2 difference from the PDG mass value.

- The χ^2 of the two-track vertex fit is required to be less than 15 (with 1 degree of freedom).

- The cosine of the pointing angle in the transverse plane ($\cos\theta$) between the K^0_S momentum vector and the K^0_S flight direction, defined as the line connecting the reconstructed primary vertex to the decay direction, is required to be greater than 0.999 (equivalent to an angle of 2.56°)

- An optimization procedure is performed on the variables $\left|\frac{L_{xy}}{\sigma_{L_{xy}}}\right|$ and $\left|\frac{P_T}{\sigma_{P_T}}\right|$ using the TMVA package provided by the ROOT framework. L_{xy} is the distance from the reconstructed primary vertex to the reconstructed secondary vertex (decay vertex of the V^0 candidate) in the transverse plane, $\sigma_{L_{xy}}$ is the error associated with reconstructing the same, p_T is the reconstructed momentum of the V^0 candidate and σ_{p_T} is the error associated with reconstructing the same.

The Λ candidates were required to satisfy the following criteria.

- Oppositely charged track pairs with $p_T > 100$ MeV are fit to a common secondary vertex using the Kalman filter. The reconstructed V^0 is required to have $p_T > 400$ MeV.

- The invariant mass of the Λ is calculated by assigning proton mass to the positive track and pion mass to negative track and are kept if it is within the mass window [1015.683, 1215.683] MeV/c^2. The Particle Data Group (PDG) reports the mass value of Λ as 1115.683 MeV/c^2. The mass window boundaries are set with a $\pm$100 MeV/c^2 difference from the PDG mass value.

- The χ^2 of the two-track vertex fit is required to be less than 15 (with 1 degree of freedom).

- The cosine of the pointing angle ($\cos\theta$) is required to be greater than 0.999 (equivalent to an angle of 2.56°).

- An optimization procedure is performed on the variables $\left|\frac{L_{xy}}{\sigma_{L_{xy}}}\right|$ and $\left|\frac{P_T}{\sigma_{P_T}}\right|$ using the TMVA package provided by the ROOT framework.

The Ξ^- candidates were required to satisfy the following criteria.

- Cascade vertex fitter code available in Athena is utilized. The reconstructed Ξ^- is required to have $p_{\mathrm{T}} > 500$ MeV.

- The invariant mass of Ξ^- is calculated by assigning pion mass to negative track and the Λ reconstruction proceeds as before, and is kept if it is within the mass window [1221.71, 1421.71] MeV/c^2. The Particle Data Group (PDG) reports the mass value of Ξ^- as 1321.71 MeV/c^2. The mass window boundaries are set with a 100 MeV/c^2 difference from the PDG mass value.

- The χ^2 of the two-track vertex fit for reconstructing both Λ and Ξ^- is required to be less than 15 (with 1 degree of freedom).

- The cosine of the pointing angle ($\cos\theta$) associated with Ξ^- vertex is required to be greater than 0.998 (equivalent to an angle of 3.62°).

- The cosine of the pointing angle associated with Λ vertex is required to be greater than 0.99999 (equivalent to an angle of 0.26°).

- An optimization procedure is performed on the variable $\left|\frac{L_{\mathrm{xy}}}{\sigma_{L_{\mathrm{xy}}}}\right|$ associated with vertex fit for reconstructing Λ and Ξ^- using the TMVA package.

The Ω^- signal in data was also studied, as will be described below, but ultimately not included in the final results due to the low statistics. The invariant mass distribution of the Ω^- candidates is presented.

- Cascade vertex fitter code available in Athena is utilized. The reconstructed Ω^- is required to have $p_{\mathrm{T}} > 1000$ MeV.

- The invariant mass of Ω^- is calculated by assigning K^- mass to negative track and the Λ reconstruction proceeds as before, and is kept if it is within the mass window [1572.45, 1772.45] MeV/c^2. The Particle Data Group (PDG) reports the mass value of Ω^- as 1672.45 MeV/c^2. The mass window boundaries are set with a 100 MeV/c^2 difference from the PDG mass value.

- The χ^2 of the two-track vertex fit for reconstructing both Λ and Ω^- is required to be less than 15 (with 1 degree of freedom).

- The cosine of the pointing angle ($\cos\theta$) associated with Ω^- vertex is required to be greater than 0.999 (equivalent to an angle of 2.56°).

- The cosine of the pointing angle associated with Λ vertex is required to be greater than 0.99999 (equivalent to an angle of 0.26°).

- $\left|\frac{L_{xy}}{\sigma_{L_{xy}}}\right|$ associated with the Ω^- vertex and the Λ vertex is required to be greater than 6.0.

We do not use TRT-only tracks and no track quality selection has been applied on the tracks entering the V^0 reconstruction. In principle, background tracks or poorly reconstructed tracks should be accounted for via the signal and background fit applied to extract the hadron yield. In Pb+Pb UPC collisions, to account for photon-going directions towards the C-side and A-side of the detector separately, the V^0 reconstruction procedure is applied separately to events where the photon is going in the C-side versus the A-side, except for Ξ^- and Ω^- due to statistical limitations.

6.2.2 Track Definitions

Following are the tracking definitions used for the V^0 reconstruction in simulated events:

- The truth-matching probability is the probability that a reconstructed track corresponds to any truth track. It is defined by the expected number vs. observed number of hits between a given truth track (Ref.[147]) given by:

$$P = \frac{10 \times \mathrm{N}_{\mathrm{pixel}}^{\mathrm{common}} + 5 \times \mathrm{N}_{\mathrm{SCT}}^{\mathrm{common}} + 1 \times \mathrm{N}_{\mathrm{TRT}}^{\mathrm{common}}}{10 \times \mathrm{N}_{\mathrm{pixel}}^{\mathrm{track}} + 5 \times \mathrm{N}_{\mathrm{SCT}}^{\mathrm{track}} + 1 \times \mathrm{N}_{\mathrm{TRT}}^{\mathrm{track}}}. \tag{6.1}$$

- Matching the two tracks of a V^0 candidate to their truth particles is achieved by imposing the following conditions:

  * Each of the two decay tracks of a V^0 candidate is matched to a corresponding truth particle, and the truth-matching probability exceeds 0.7.

  - The two truth particles share a common parent (K^0_S or Λ). The common parent has two daughters and a PDG ID of 310 (3122) in the case of K^0_S (Λ).
  - The two truth particles share a common parent (Λ), while Λ and a third truth particle share a common parent (Ξ^- or Ω^-). The common parent has two daughters and a PDG ID of 3312 (3334) in the case of Ξ^- (Ω^-).

- A track is secondary if it is truth-matched but originates in the G4 simulation (e.g. electrons produced in an electromagnetic shower). Particles with truth bar-code $\notin (10000, 200000)$ are secondary in DPMJET-III γA.

6.2.3 V^0 Reconstruction Efficiency

There is a non-zero probability that a given particle will or will not be observed in the analysis due to detector effects, quality selection, etc. This leads to some particles being missed or left out by the reconstruction procedure. The reconstruction efficiency is defined as the ratio of the number of truth particles whose associated reconstructed V^0s have truth-matched particles $N^{\text{matched}}_{\text{truth}}$ to the total number of truth particles N_{truth}, as a function of both p_{T} and y:

$$\varepsilon_{\text{reco}}(p_{\text{T}}, y) = \frac{N^{\text{matched}}_{\text{truth}}(p_{\text{T}}, y)}{N_{\text{truth}}(p_{\text{T}}, y)}. \tag{6.2}$$

Truth-matched K^0_S, Λ and Ξ^- particles are required to have their masses fall within the specified ranges: [475,520] MeV for K^0_S, [1107,1127] MeV for Λ, and [1107,1127] MeV for Ξ^-. Additionally, they follow the pre-selection cuts for χ^2 and $\cos\theta$ defined in Section 6.2.1.

Both truth and truth-matched particles are required to be non-secondary, i.e., particles with truth barcodes falling outside the range (10000,200000) are excluded. An additional correction procedure is necessary to account for the contribution of secondary particles on the yield, along with the associated uncertainty estimation.

To compensate for the missed particles, the reconstruction efficiency is applied as a correction factor $= 1/\varepsilon(p_{\text{T}}, y)$ for the counts entering the V^0 yield as a function of p_{T} and y. In Pb+Pb UPC collisions, to account for photon-going directions towards the C-side and A-side of the detector

separately, the V^0 reconstruction efficiency is applied separately to events where the photon is going in the C-side versus the A-side for K^0_S and Λ.

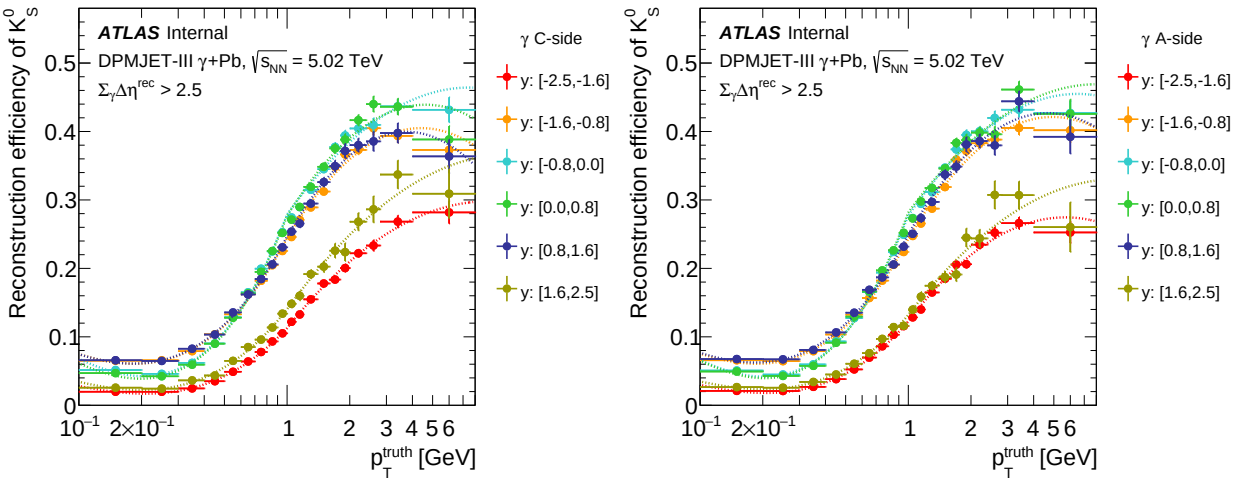

Figure 6.5: K^0_S reconstruction efficiencies as a function of p_T^{truth}, fitted using a polynomial function of 3rd order in log(p_T) at low p_T ($p_T < 1$ GeV) and a polynomial function of 2nd order in log(p_T) at high p_T ($p_T > 1$ GeV) in y bins in DPMJET-III for photon C-side (left) and A-side (right).

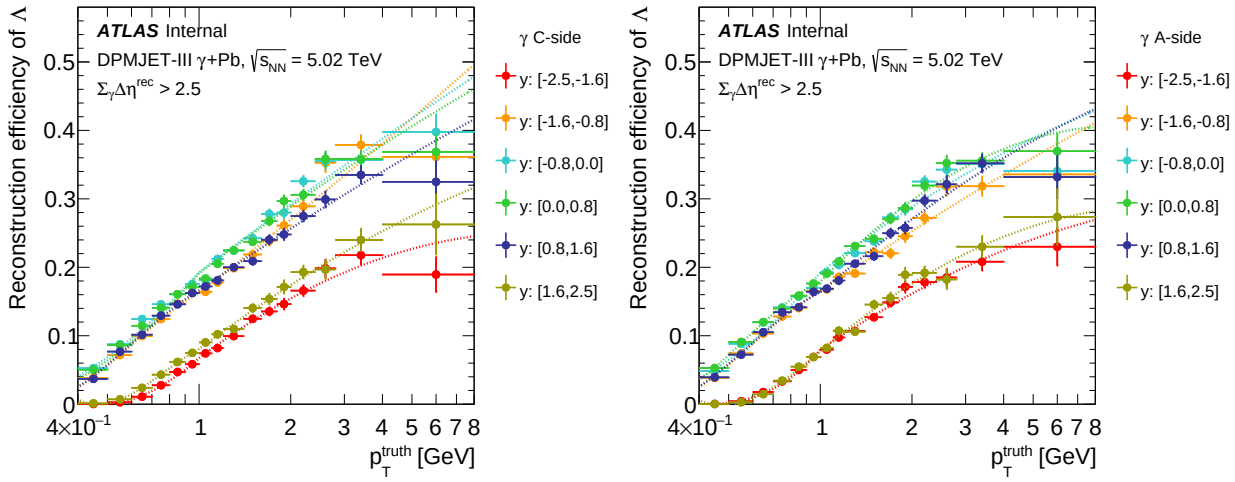

Figure 6.6: Λ reconstruction efficiencies as a function of p_T^{truth}, fitted using a polynomial function of 3rd order in log(p_T) at low p_T ($p_T < 1$ GeV) and a polynomial function of 2nd order in log(p_T) at high p_T ($p_T > 1$ GeV) in y bins in DPMJET-III for photon C-side (left) and A-side (right).

Figures 6.5 and 6.6 show the V^0 reconstruction efficiency as a function of p_T^{truth} in each of the 6 y bins spanning from -2.5 to 2.5 in UPC DPMJET-III for K^0_S and Λ respectively. Figure 6.7

shows the same in p+Pb HIJING. These reconstruction efficiencies as a function of $p_{\mathrm{T}}^{\mathrm{truth}}$ are fitted using a polynomial function of 3$^{\mathrm{rd}}$-order in $\log(p_{\mathrm{T}})$ at low p_{T} ($p_{\mathrm{T}} < 1$ GeV) and a polynomial function of 2$^{\mathrm{nd}}$-order in $\log(p_{\mathrm{T}})$ at high p_{T} ($p_{\mathrm{T}} > 1$ GeV) in each of the 6 y bins. These fit functions are used for the efficiency correction to remove statistical fluctuations, particularly at high p_{T}.

At higher p_{T}, the efficiency tends to decrease, particularly for K_{S}^{0}. This trend is visible in the p+Pb HIJING sample where statistical limitations are not a factor. This decreased efficiency at the highest p_{T} bin is due to the reduced acceptance for higher p_{T} particles where they decay outside the inner tracking layers. The statistical uncertainties on the fit values are considered systematic uncertainties to account for any significant deviation of the fit function from the data points.

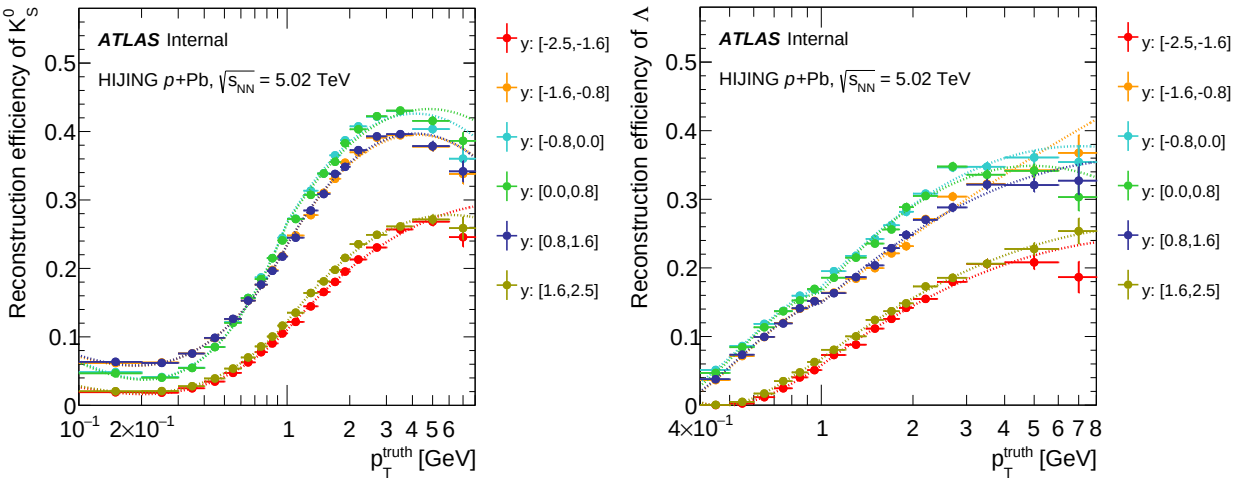

Figure 6.7: K_{S}^{0} (left) and Λ (right) reconstruction efficiencies as a function of $p_{\mathrm{T}}^{\mathrm{truth}}$, fitted using a polynomial function of 3$^{\mathrm{rd}}$ order in $\log(p_{\mathrm{T}})$ at low p_{T} ($p_{\mathrm{T}} < 1$ GeV) and a polynomial function of 2$^{\mathrm{nd}}$ order in $\log(p_{\mathrm{T}})$ at high p_{T} ($p_{\mathrm{T}} < 1$ GeV) in y bins in HIJING.

Figure 6.8 shows the V^{0} reconstruction efficiency of Ξ^{-} as a function of $p_{\mathrm{T}}^{\mathrm{truth}}$ in each of the 6 y bins spanning from -2.5 to 2.5 in DPMJET-III and HIJING. The specific values are directly propagated into the final results without undergoing any fitting process. The statistical uncertainties on these corrections are propagated as systematic uncertainties.

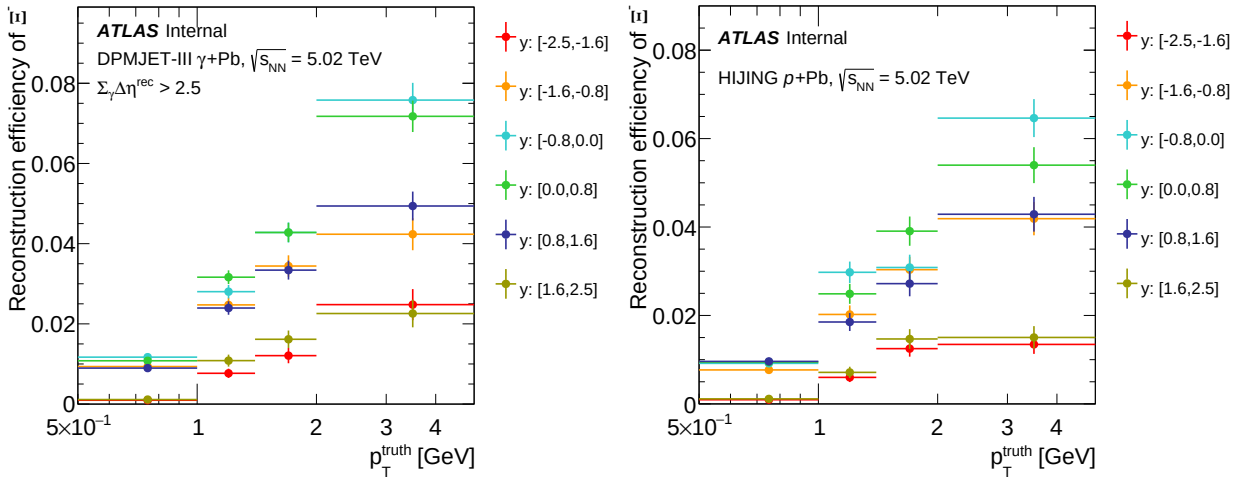

Figure 6.8: Ξ^- reconstruction efficiencies as a function of $p_{\mathrm{T}}^{\mathrm{truth}}$ in y bins in DPMJET-III (left) and in HIJING (right).

6.2.4 V^0 Signal Optimization

Particle identification in Pb+Pb UPC and p+Pb events is performed using a machine learning technique, using the Toolkit for Multivariate Analysis (TMVA) package from the ROOT framework [156]. The simplest and most common classifier for selecting signal events from a sample of signal and background events is the application of an ensemble of rectangular cuts on discriminating variables.

In this analysis, the variables that are optimized using TMVA are $\left|\frac{L_{\mathrm{xy}}}{\sigma_{L_{\mathrm{xy}}}}\right|$ and $\left|\frac{P_{\mathrm{T}}}{\sigma_{P_{\mathrm{T}}}}\right|$, where L_{xy} is the distance from the reconstructed primary vertex to the reconstructed secondary vertex (decay vertex of the V^0 candidate) in the transverse plane, $\sigma_{L_{\mathrm{xy}}}$ is the error associated with reconstructing the same, p_{T} is the reconstructed momentum of the V^0 candidate and $\sigma_{p_{\mathrm{T}}}$ is the error associated with reconstructing the same. In Pb+Pb UPC collisions, the TMVA procedure is applied separately to events where the photon is going in the C-side versus the A-side, except for Ξ^- due to statistical limitations.

The signal (S) and background (B) inputs to the TMVA machinery for observables $\left|\frac{L_{\mathrm{xy}}}{\sigma_{L_{\mathrm{xy}}}}\right|$ and $\left|\frac{P_{\mathrm{T}}}{\sigma_{P_{\mathrm{T}}}}\right|$ are provided for various p_{T} bins and y bins. Signal inputs are from MC and background inputs are from the side-bands of invariant mass distributions in data. As an example of the discriminating

impact, Figure 6.9 shows the signal and background input distributions for the variables $\left|\frac{L_{\mathrm{xy}}}{\sigma_{L_{\mathrm{xy}}}}\right|$ and $\left|\frac{P_{\mathrm{T}}}{\sigma_{P_{\mathrm{T}}}}\right|$ in a specific bin p_{T}: [1.0, 1.2] GeV and y: [-0.8,0.0] of K^0_{S} candidate.

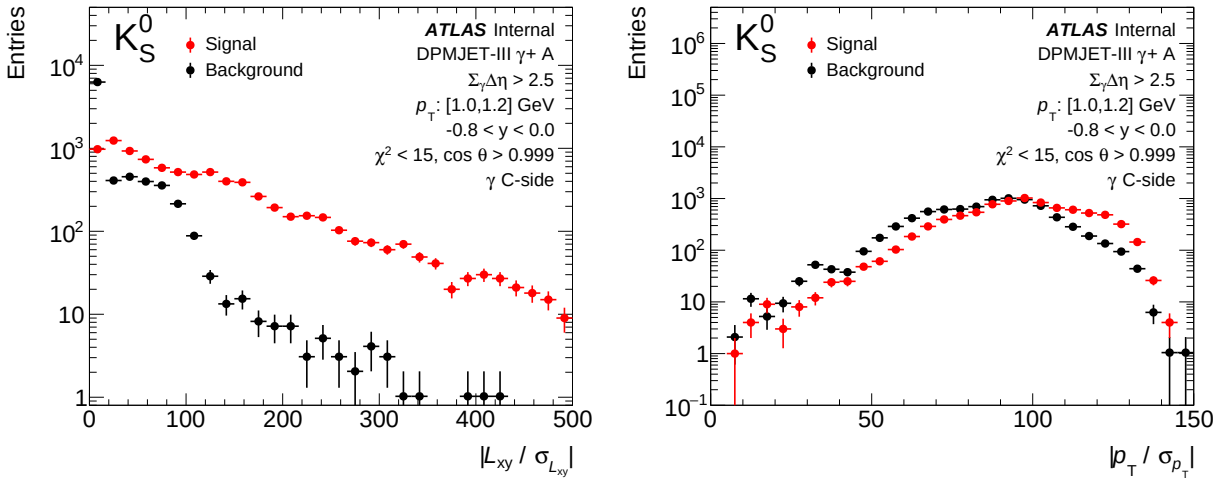

Figure 6.9: Shown are the signal and background distributions of $\left|\frac{L_{\mathrm{xy}}}{\sigma_{L_{\mathrm{xy}}}}\right|$ (left) and $\left|\frac{P_{\mathrm{T}}}{\sigma_{P_{\mathrm{T}}}}\right|$ (right) of K^0_{S} candidate in a specific p_{T}-y bin.

For signal inputs, particles are defined as non-secondary, and their masses fall within the specified ranges: [475,520] MeV for K^0_{S}, [1107,1127] MeV for Λ, and [1310,1335] MeV for Ξ^-. Additionally, they follow the pre-selection cuts for χ^2 and $\cos\theta$ defined in Section 6.2.1. A normalization factor is utilized for S by applying a ratio derived from signal counts in MC and data, corresponding to signal efficiency 0.99, for a specific p_{T}-y bin. To determine the signal counts in data, a double Gaussian is fitted as the signal function, and a second-order polynomial is used as the background function. This normalization accounts for the difference in signal magnitude between MC simulations and actual data.

For background inputs, sidebands of invariant mass distributions in data are utilized. The left side-band is defined using the specified ranges: [430,475] MeV for K^0_{S}, [1097,1107] MeV for Λ, and [1290,1310] MeV for Ξ^-. The right side-band is defined using the specified ranges: [520,565] MeV for K^0_{S}, [1127,1137] MeV for Λ, and [1335,1350] MeV for Ξ^-. A normalization factor is utilized for B by applying the ratio of mass range difference in the signal region to that of the sidebands. This normalization accounts for the difference in background magnitude between the signal region

and the sideband region.

The optimization performed by TMVA maximizes the background rejection at a given signal efficiency and scans over the full range of the latter quantity. TMVA machinery generates minimum cuts for $\left|\frac{L_{\rm xy}}{\sigma_{L_{\rm xy}}}\right|$ and $\left|\frac{P_{\rm T}}{\sigma_{P_{\rm T}}}\right|$ for each of the hundred signal efficiency values spanning from 0.00 to 0.99. Figure 6.10 shows a series of invariant mass distributions for $K^0_{\rm S}$ in the y-bin [-2.5,-1.6] and $p_{\rm T}$ bin [1000,1100] MeV in Pb+Pb UPC. Each subplot shows the invariant mass distribution with cuts on $\left|\frac{L_{\rm xy}}{\sigma_{L_{\rm xy}}}\right|$ and $\left|\frac{P_{\rm T}}{\sigma_{P_{\rm T}}}\right|$ corresponding to each of the signal efficiency values, ranging from 0.00 to 0.99 from left to right, top to bottom.

Signal significance, $\mathrm{S}/\sqrt{\mathrm{S}+\mathrm{B}}$, is calculated for each of the hundred invariant mass distributions. The distribution with the highest signal significance is selected for a given $p_{\rm T}$-y differential bin, and for each V^0 candidate. An example set of optimized invariant mass distributions of $K^0_{\rm S}$, Λ and Ξ^- is shown in Figure 6.11, highlighting the signal and the side-band regions for a specific $p_{\rm T}$-y bin in Pb+Pb UPC. Figure 6.12 shows the $L_{\rm xy}$ distribution after implementing optimized selection cuts within a specific $p_{\rm T}$-y bin for $K^0_{\rm S}$ and Λ in Pb+Pb UPC data.

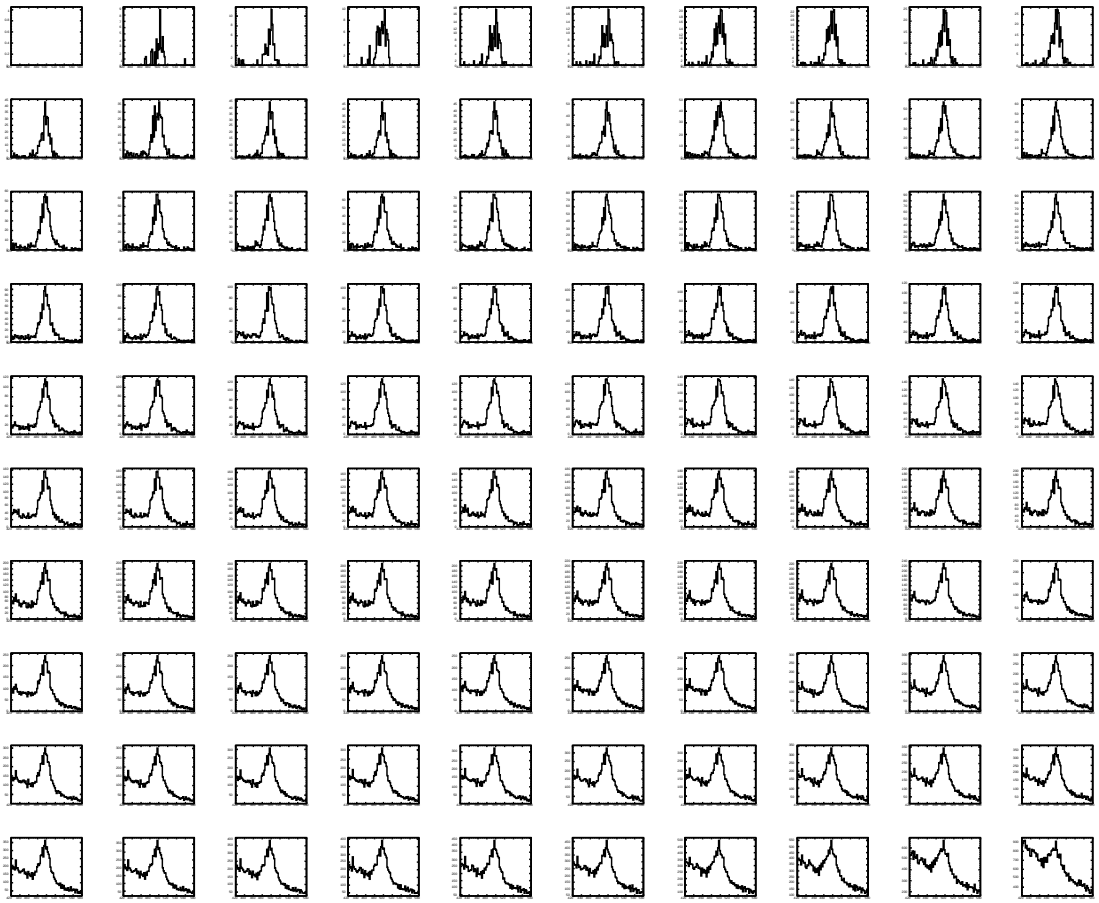

Figure 6.10: The invariant mass distributions in data, each associated with cuts on $\left|\frac{L_{\mathrm{xy}}}{\sigma_{L_{\mathrm{xy}}}}\right|$ and $\left|\frac{P_{\mathrm{T}}}{\sigma_{P_{\mathrm{T}}}}\right|$ corresponding to one of the hundred signal efficiency values, ranging from 0.00 to 0.99, arranged from left to right and top to bottom, for K^0_{S} in the y-bin [-2.5,-1.6] and p_{T} bin [1000,1100] MeV in Pb+Pb UPC.

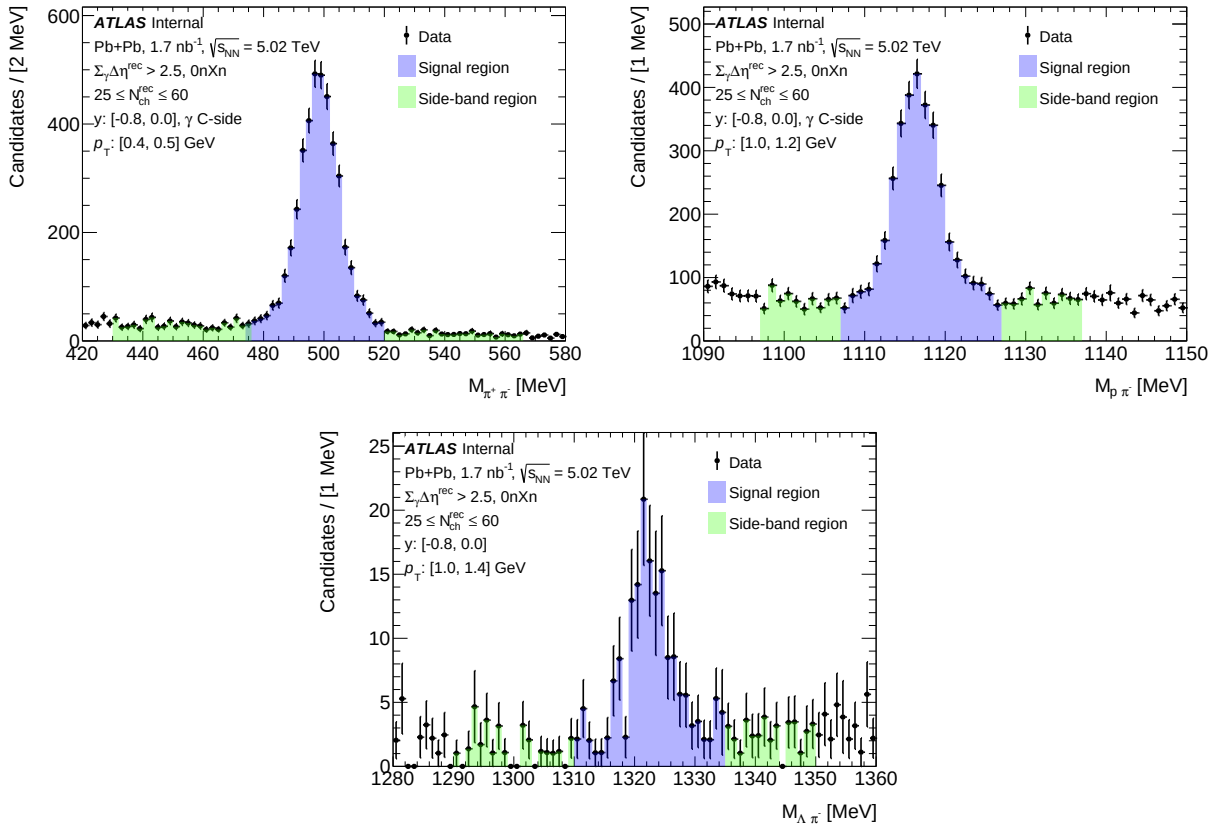

Figure 6.11: Shown are the invariant mass distributions of K^0_S, Λ and Ξ^- in Pb+Pb UPC highlighting the signal and the side-band region for a specific p_T-y bin.

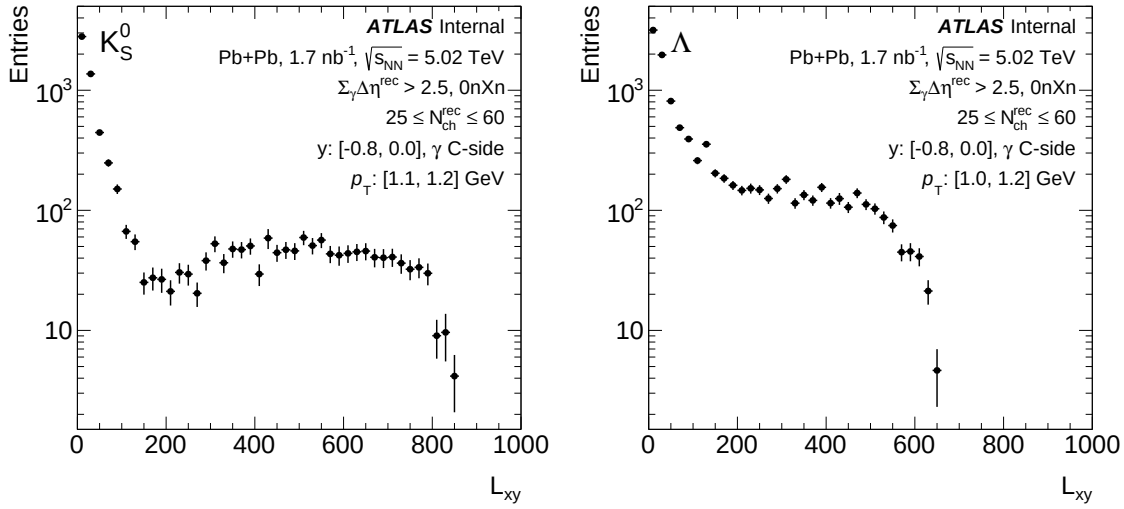

Figure 6.12: Shown are the L_{xy} distribution for a specific p_T-y bin in K^0_S (left) and Λ (right) in Pb+Pb UPC.

A fitting procedure is performed on the mass distribution to extract the corresponding yield. This yield is corrected using the reconstruction efficiency discussed in Section 6.2.3 and the signal efficiency discussed below in Section 6.2.5.

6.2.5 V^0 Signal Efficiency

The signal efficiency is defined as the ratio of the number of truth-matched particles that passed the optimized cuts from the TMVA procedure, to the number of truth-matched particles, as a function of both p_{T} and y:

$$\varepsilon_{\mathrm{sig}}(p_{\mathrm{T}}, y) = \frac{N_{\mathrm{truth}}^{\mathrm{matched,optimized}}(p_{\mathrm{T}}, y)}{N_{\mathrm{truth}^{\mathrm{matched}}}(p_{\mathrm{T}}, y)}. \tag{6.3}$$

Figures 6.13 and 6.14 show the signal efficiency as a function of $p_{\mathrm{T}}^{\mathrm{rec}}$ in each of the 6 y bins spanning from -2.5 to 2.5 in DPMJET-III for K_{S}^0 and Λ respectively. Figure 6.15 shows the same for HIJING. Figure 6.16 shows the signal efficiency of Ξ^- as a function of $p_{\mathrm{T}}^{\mathrm{rec}}$ in each of the 6 y bins spanning from -2.5 to 2.5 in DPMJET-III and in HIJING. These signal efficiency values are applied as a correction factor for each of the V^0 candidates, for each p_{T} and y bin.

The fluctuations in the signal efficiency values across different p_{T} bins arise from the approach of TMVA optimization performed on separate p_{T}-y bins. The lower values of signal efficiencies at the most backward y selection [-2.5,-1.6] in UPC indicate a relatively larger background in these bins. This is possible since the production of particles in UPC is highly asymmetric in rapidity and a larger number of particles are produced in the Pb-going direction, i.e., backward rapidity bins. In the case of p+Pb, similar values of signal efficiencies are obtained in the symmetric rapidity selections. This is due to the nearly symmetric distribution of particles in low multiplicity p+Pb collisions, thus influencing the contribution of the background.

6.2.6 V^0 Background Correction

The number of signal candidates for K_{S}^0 or Λ or Ξ^- in a given p_{T} and y bin is determined by fitting the invariant-mass spectrum of the corresponding candidates in that bin. The value and

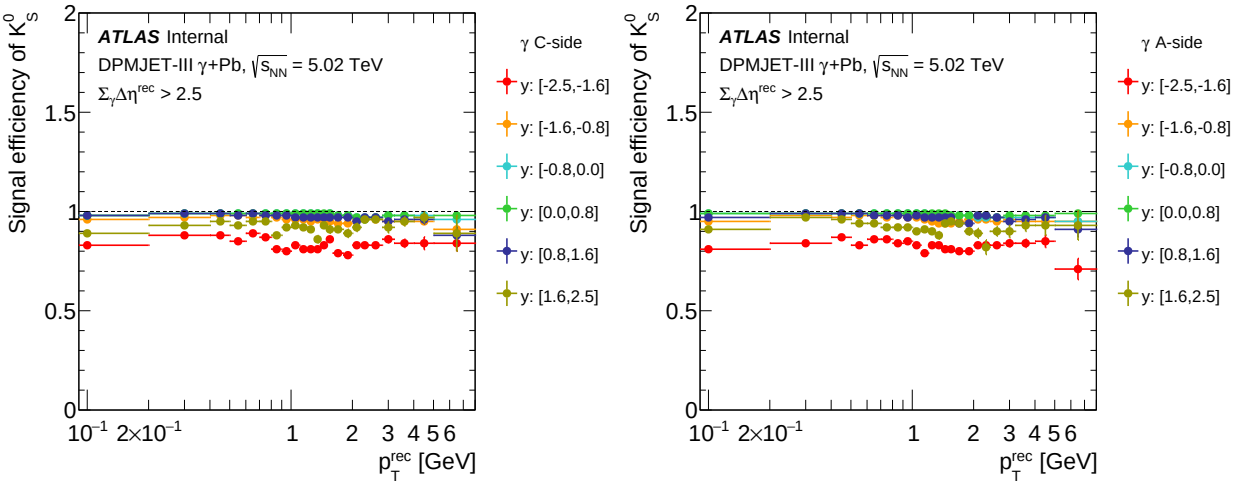

Figure 6.13: Shown are the signal efficiencies of K^0_S as a function of p_T^{rec} in selected y slices in DPMJET-III for photon C-side (left) and photon A-side (right).

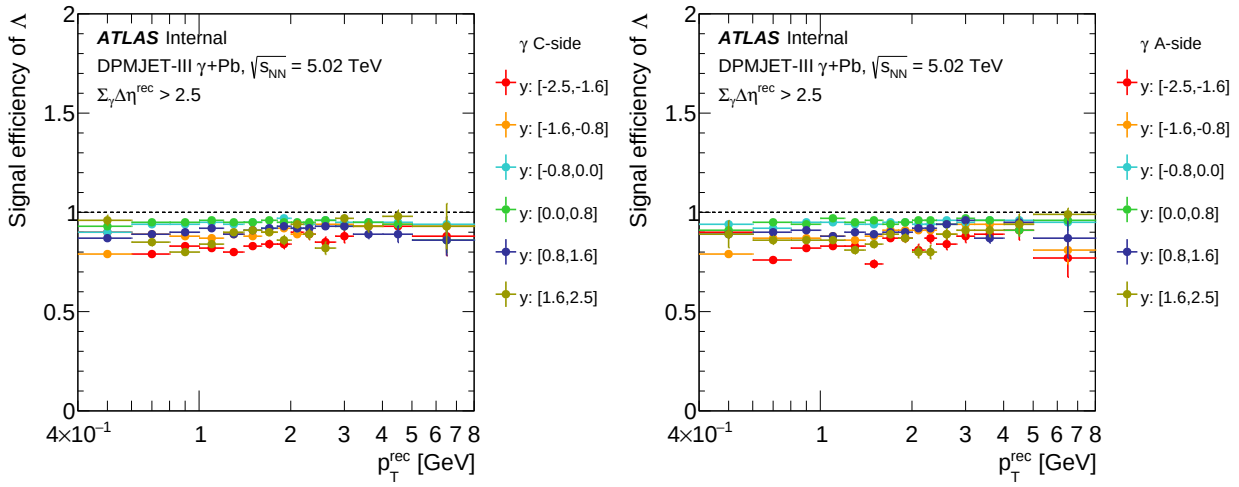

Figure 6.14: Shown are the signal efficiencies of Λ as a function of p_T^{rec} in selected y slices in DPMJET-III for photon C-side (left) and photon A-side (right).

statistical uncertainty on the bin are then determined from the fitted signal yield and its uncertainty. The fit utilizes a double Gaussian for the signal peak and a second-order polynomial for the combinatorial background. A single parameter is used for the mean of the two Gaussian distributions. The ratio of the widths and amplitudes of the two Gaussian distributions is constrained based on the MC truth-matched invariant-mass distributions for the corresponding p_T-y bin.

Example fits for K^0_S, Λ and Ξ^- candidates for different p_T, y bins in the event-class N_{ch}^{rec}:

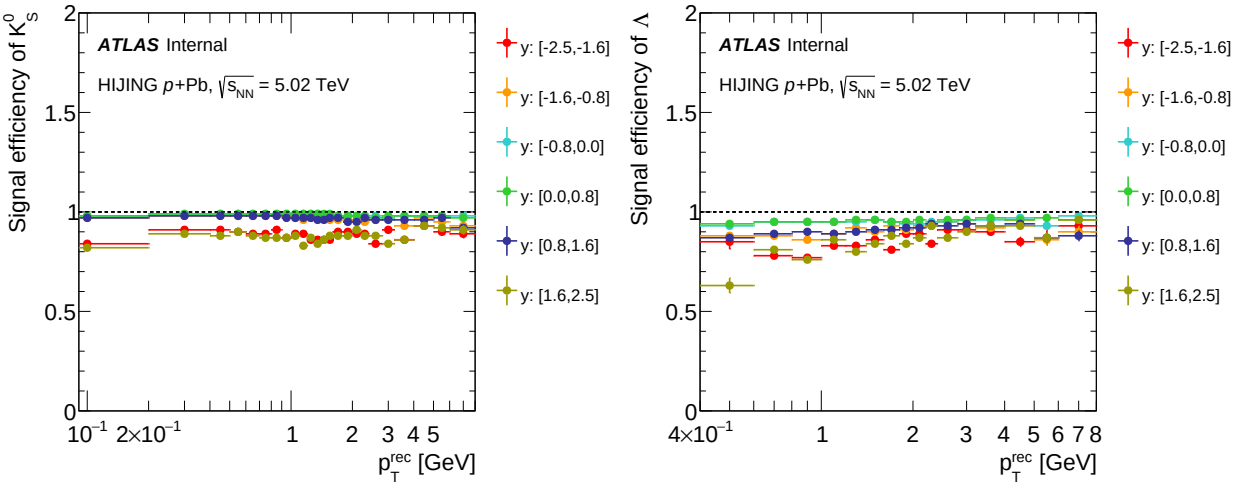

Figure 6.15: Shown are the signal efficiencies as a function of $p_{\mathrm{T}}^{\mathrm{rec}}$ in 6 y slices in HIJING for K_{S}^{0} (left) and Λ (right).

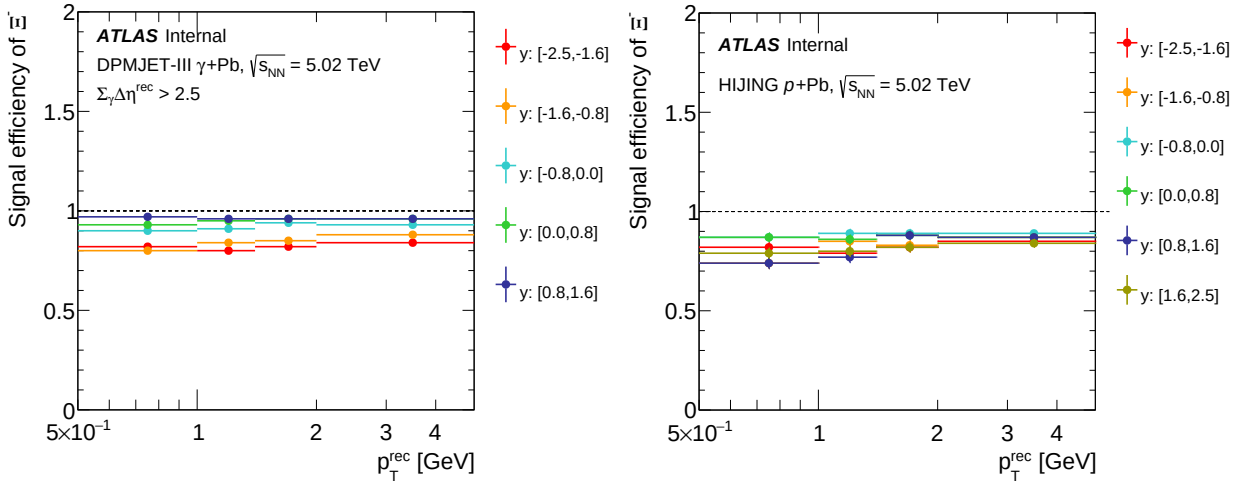

Figure 6.16: Shown are the signal efficiencies of Ξ^{-} as a function of $p_{\mathrm{T}}^{\mathrm{rec}}$ in 6 y slices in DPMJET-III (left) and in HIJING (right).

[25,60] in Pb+Pb UPC and p+Pb are shown in Figures 6.17 and 6.18 respectively. Figure 6.17 also includes the invariant mass distributions of Ω^{-} candidates in rapidity region y:[-2.5,2.5], within the p_{T} range of [1,5] GeV in Pb+Pb UPC utilizing the full statistics. Additional mass distributions are included in Appendix B.

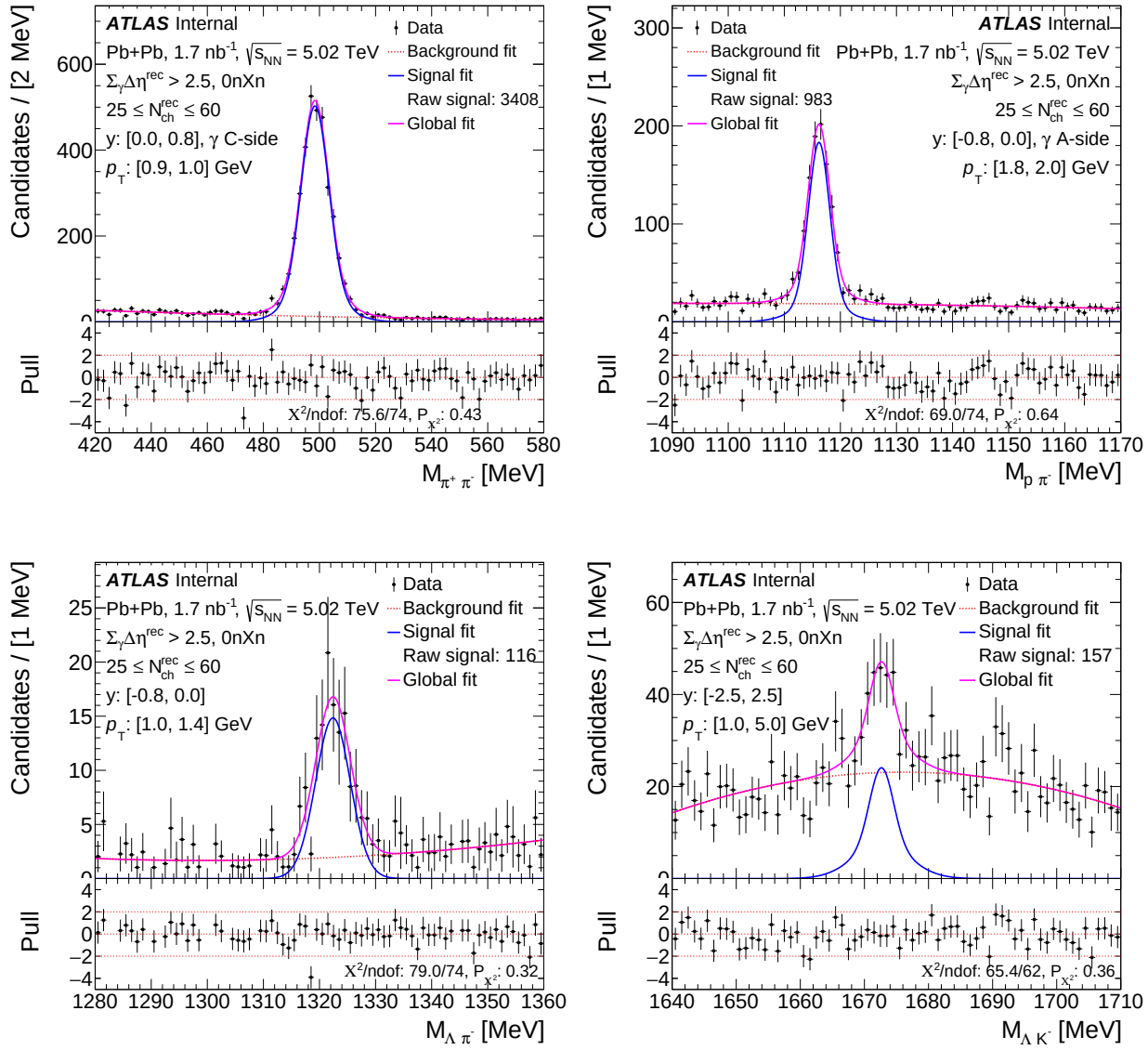

Figure 6.17: The invariant mass distributions of K^0_S (top left), Λ (top right), Ξ^- (bottom left) and Ω^- (bottom right) are shown for a specific p_T-y bin in Pb+Pb UPC, represented in black markers in the top panel. The global fit to the data is represented by a magenta solid line, utilizing a double Gaussian fit for signal (shown as a blue solid line), and a second-order polynomial (shown as a red dotted line). In the bottom panel, the pull distribution shows the difference between the data and fit value normalized to the data uncertainty.

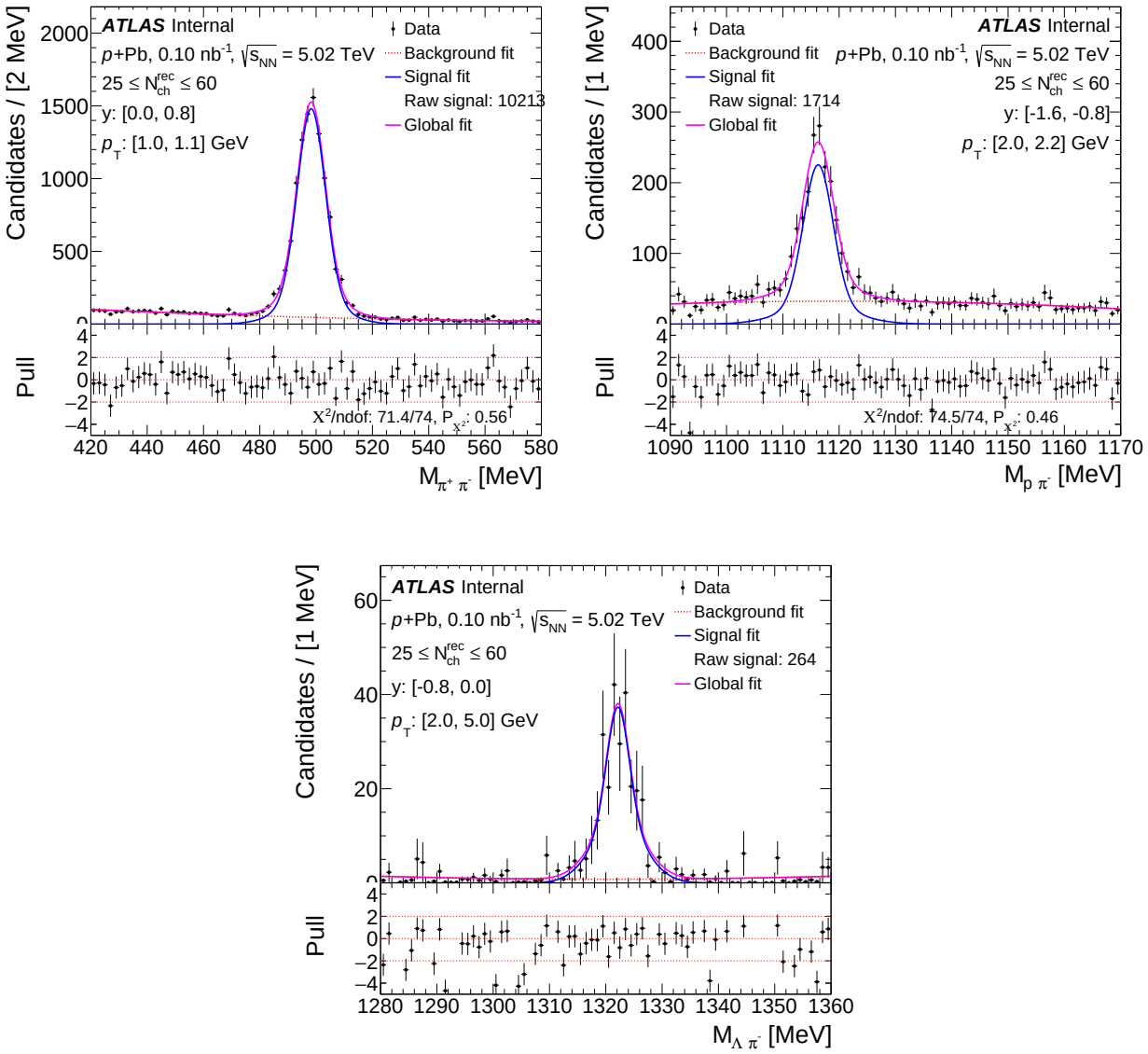

Figure 6.18: The invariant mass distributions of K^0_S (top), Λ (middle) and Ξ^- (bottom) are shown for a specific p_T-y bin in p+Pb. The global fit to the data is represented by a magenta solid line, utilizing a double Gaussian fit for signal (shown as a blue solid line), and a second-order polynomial (shown as a red dotted line). In the bottom panel, the pull distribution shows the difference between the data and fit value normalized to the data uncertainty.

6.2.7 Extrapolation to $p_{\mathrm{T}} = 0$ GeV

For the $\mathrm{d}N_{\mathrm{V}^0}/\mathrm{d}y$ and $\langle p_{\mathrm{T}} \rangle$ results, the final values reflect the yields integrated over the entire p_{T} range. Hence there is an extrapolation of the yield down to $p_{\mathrm{T}} = 0$ GeV, where there is no measurement. The minimum p_{T} values for measurements are 0 GeV for K^0_{S}, 0.4 GeV for Λ, and 0.5 GeV for Ξ^-.

The V^0 yields as a function of p_{T} are fit using the Modified Hagedorn function described in Equation 5.8. Here we set m_0 to the V^0 mass.

Figures 6.19 and 6.20 show the V^0 yield in Pb+Pb UPC and p+Pb as a function of p_{T} in six y selections with fit results for the Modified Hagedorn function on a linear p_{T} scale. The fits show reasonable agreement with the experimental data and show similar features in both Pb+Pb UPC and p+Pb. Roughly 13% of the total yield lies in the region of extrapolation ($p_{\mathrm{T}} < 0.4$ GeV) for Λ. Roughly 15% of the total yield lies in the region of extrapolation ($p_{\mathrm{T}} < 0.5$ GeV) for Ξ^-.

$\mathrm{d}N_{\mathrm{V}^0}/\mathrm{d}y$ in each y bin and each $N^{\mathrm{rec}}_{\mathrm{ch}}$ bin is calculated by integrating the fit results over the corresponding p_{T} range, i.e, $p_{\mathrm{T}} > 0$ GeV in the case of extrapolation and $p_{\mathrm{T}} >$ the corresponding minimum p_{T} values ($p_{\mathrm{T}} > 0$ GeV for K^0_{S}, 0.4 GeV for Λ, and 0.5 GeV for Ξ^-) in the case of non-extrapolation.

$\langle p_{\mathrm{T}} \rangle$ in each y bin and each $N^{\mathrm{rec}}_{\mathrm{ch}}$ bin is calculated by finding the mean value of the fit results over the corresponding p_{T} range, i.e, $p_{\mathrm{T}} > 0$ GeV in the case of extrapolation and $p_{\mathrm{T}} >$ the corresponding minimum p_{T} values ($p_{\mathrm{T}} > 0$ GeV for K^0_{S}, 0.4 GeV for Λ, and 0.5 GeV for Ξ^-) in the case of non-extrapolation.

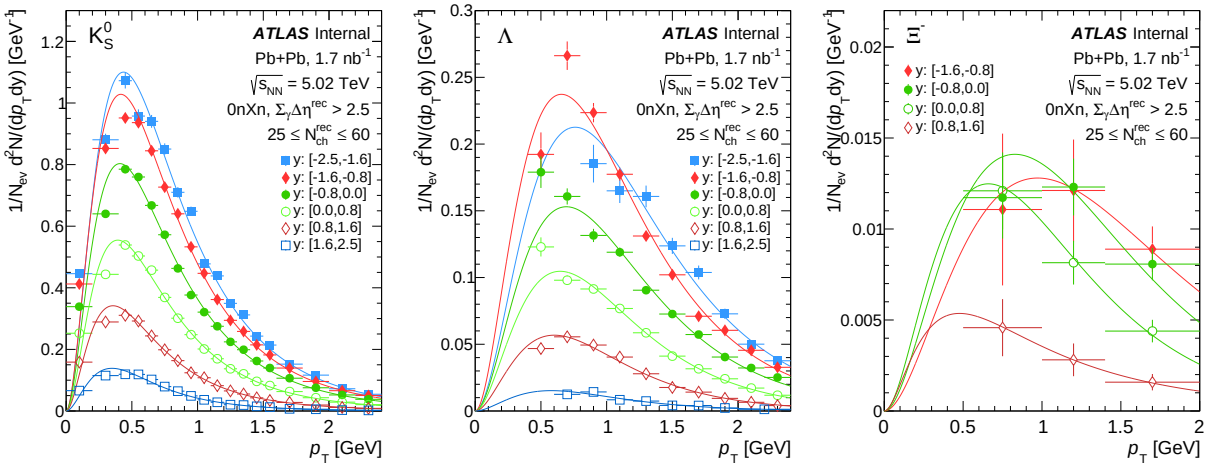

Figure 6.19: Shown are the yields of K^0_S (left), Λ (middle) and Ξ^- (right) as a function of p_T in different y selections in Pb+Pb UPC data, plotted on a linear p_T scale. The figure includes fit results to the Modified Hagedorn function.

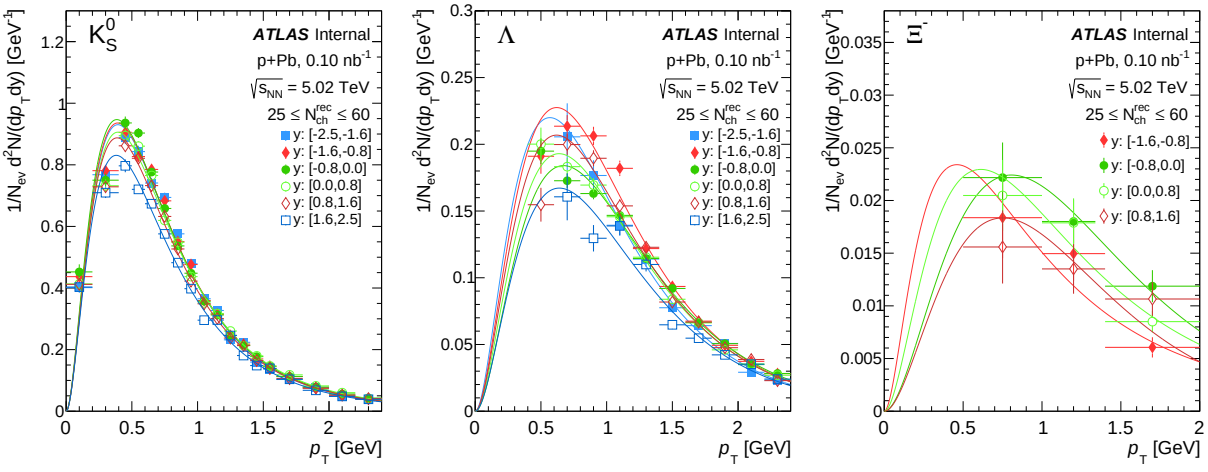

Figure 6.20: Shown are the yields of K^0_S (left), Λ (middle) and Ξ^- (right) a function of p_T in different y selections in p+Pb data, plotted on a linear p_T scale. The figure includes fit results to the Modified Hagedorn function.

6.2.8 Mis-Identification of Particles

Figure 6.21 shows the invariant mass distributions of truth-matched K^0_S (left) and Λ (right) are shown in DPMJET-III. The left plot additionally shows cases of truth-matched Λ particles, where the daughter proton is misidentified as a pion, leading to a contribution in the K^0_S mass range as background. The right plot additionally shows cases of truth-matched K^0_S particles, where one of the daughter pions is misidentified as a proton, leading to a contribution in the Λ mass range as the background. A systematic uncertainty is considered including the background shape from misidentification as an additional contribution to the invariant mass fit.

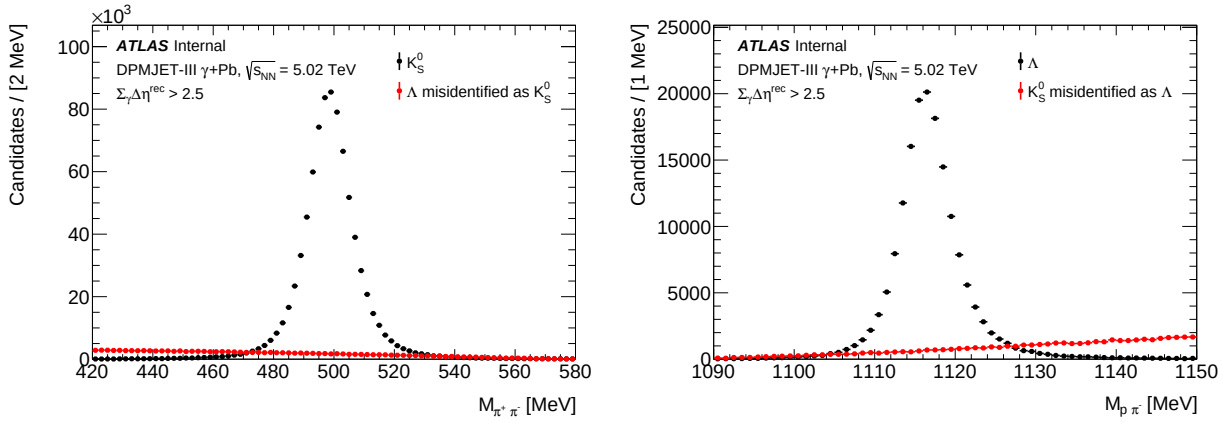

Figure 6.21: The invariant mass distributions of truth-matched K^0_S (left) and Λ (right) are shown in DPMJET-III. Also, shown are the misidentified cases.

6.3 Correction Factors

In this Section, the final measurement observables of the V^0 analysis are explained. The following observables are presented in this analysis.

- V^0 yields as a function of y:

$$Y(y) = \frac{1}{N_{\text{ev}}} \frac{\mathrm{d}N_{\text{V}^0}}{\mathrm{d}y} \tag{6.4}$$

- V^0 as a function of p_{T} in different y slices:

$$Y(y, p_{\text{T}}) = \frac{1}{N_{\text{ev}}} \frac{\mathrm{d}N^2_{\text{V}^0}}{\mathrm{d}p_{\text{T}}\mathrm{d}y} \tag{6.5}$$

- $\langle p_{\mathrm{T}} \rangle$ as a function of $N_{\mathrm{ch}}^{\mathrm{rec}}$

where p_{T} is the transverse momentum, y is the rapidity, $N_{\mathrm{V^0}}$ is the number of charged particles in an event, N_{ev} is the number of selected events in the event class, $\langle p_{\mathrm{T}} \rangle$ is the average p_{T} for a given number of V^0 candidate.

The correction factors are the following:

- In data, weights (w_{evt}) are applied event-by-event to correct for inefficiencies due to trigger selection:

$$w_{\mathrm{evt}} = f_{\mathrm{trigprescales}} \times \frac{1}{\varepsilon_{\mathrm{trigeff}}(N_{\mathrm{ch}}^{\mathrm{rec}}, \sum_{\gamma} \Delta\eta^{\mathrm{rec}})}, \tag{6.6}$$

  where $f_{\mathrm{trigprescales}}$ is the relevant trigger prescale and $\varepsilon_{\mathrm{trigeff}}(\mathrm{N}_{\mathrm{ch}}^{\mathrm{rec}}, \sum_{\gamma} \Delta\eta^{\mathrm{rec}})$ is the trigger efficiency.

- The V^0 yield is corrected with V^0 reconstruction efficiency, given by Equation 6.2 and signal efficiency, given by Equation 6.3.

- The $N_{\mathrm{ch}}^{\mathrm{rec}}$-dependent purity correction factor, PCF, is applied to the charged hadron yield as a function of y and p_{T}, detailed in Section 6.1.1.4.

- In the cases where yields and $\langle p_{\mathrm{T}} \rangle$ are reported over the full range of p_{T}, the $p_{\mathrm{T}} = 0$ GeV extrapolation down to $p_{\mathrm{T}} = 0$ GeV using the Modified Hagedorn fit, is applied to the V^0 yield, as detailed in Section 6.2.7.

Among the correction factors mentioned above, PCF is exclusively applied to Pb+Pb UPC events. All the other correction factors are applied to both Pb+Pb UPC and p+Pb.

6.4 Results

This Section presents the final physics results. The results are currently shown without incorporating systematic uncertainties, as this aspect is still a work in progress. Detailed physics discussions are included in the Chapter 7.

The V^0 results are presented in 5.02 TeV Pb+Pb UPC and p+Pb collisions both (i) as a function of p_{T} in six exclusive intervals of y and (ii) integrated over all p_{T} as a function of y. The yields are shown for the $N_{\mathrm{ch}}^{\mathrm{rec}}$ selection 25-60, where the p+Pb events are re-weighted to have effectively the same $N_{\mathrm{ch}}^{\mathrm{rec}}$ distribution as the Pb+Pb UPC events. Negative η corresponds to the Pb-going direction, and positive η corresponds to the photon-going and proton-going directions in Pb+Pb UPC and p+Pb, respectively.

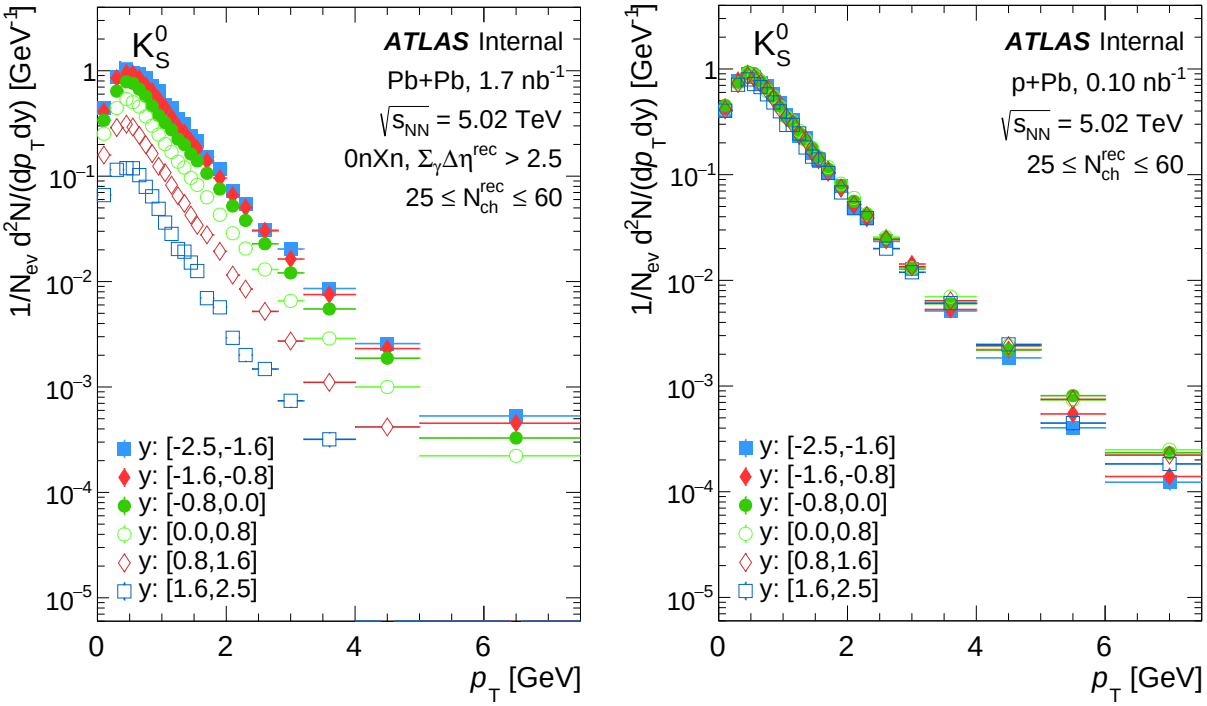

Figure 6.22: K^0_{S} yields as a function of p_{T} in six y selections. The left panel is for Pb+Pb UPC collisions and the right panel is for p+Pb collisions. Statistical uncertainties are shown as vertical lines.

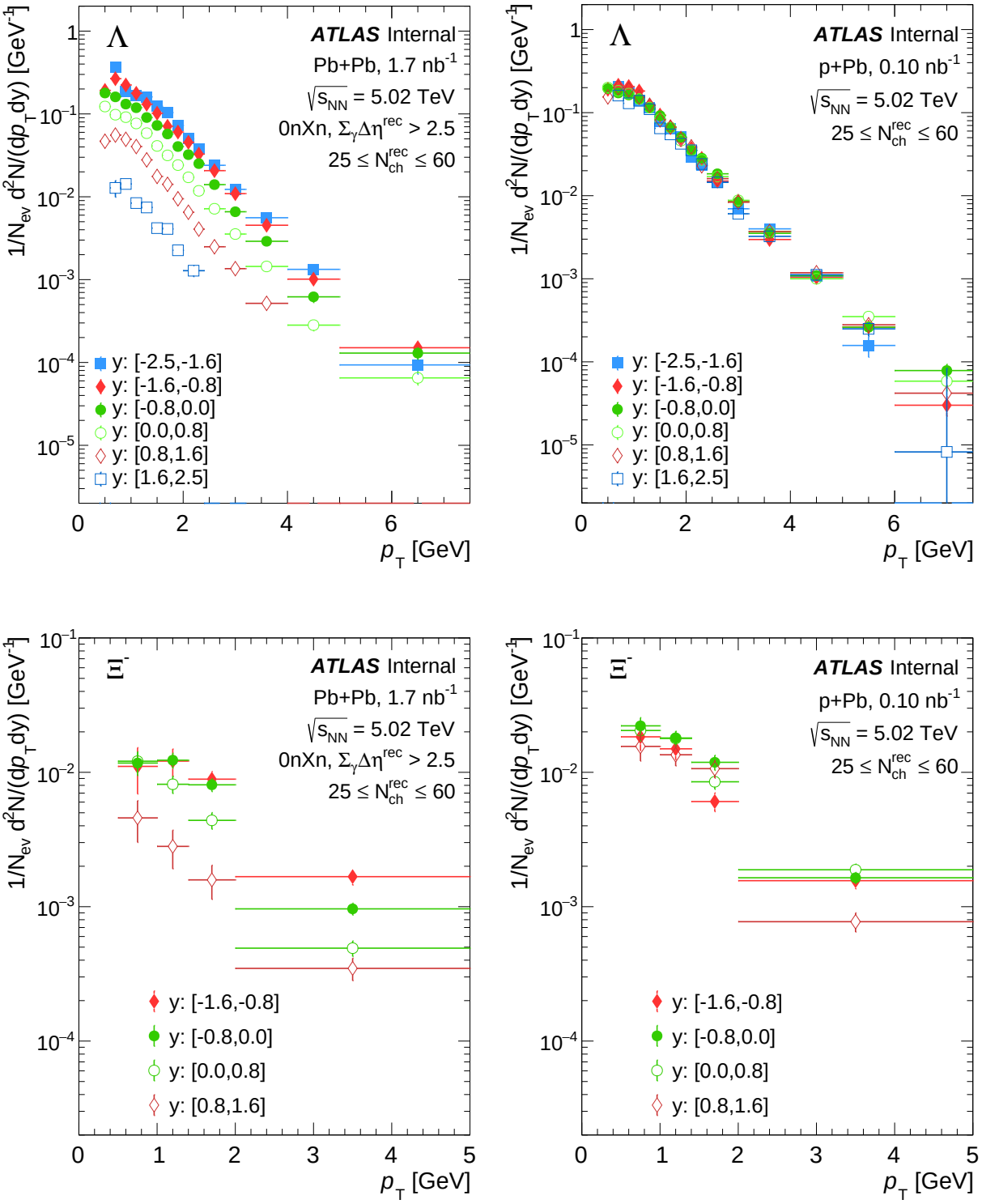

Figure 6.23: Λ (top) and Ξ^- (bottom) yields as a function of p_{T} in six y selections. The left panel is for Pb+Pb UPC collisions and the right panel is for p+Pb collisions. Statistical uncertainties are shown as vertical.

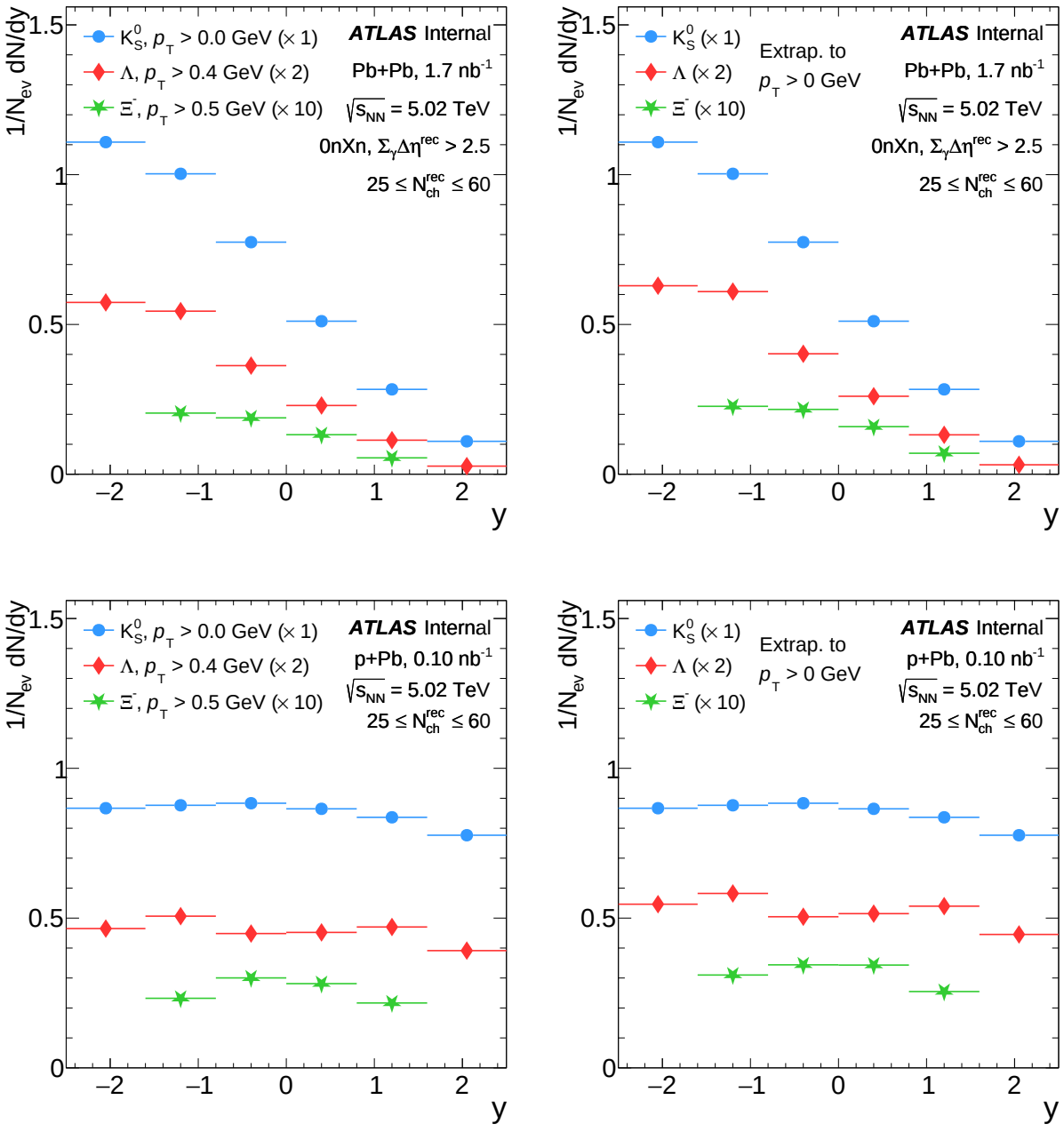

Figure 6.24: Shown are the V^0 yields as a function of y. The top panels are for Pb+Pb UPC and the bottom panels are for p+Pb collisions. The left panels correspond to yields integrated for p_{T} results integrated over the measured p_{T} range, i.e., $p_{\mathrm{T}} > 0$ GeV for K^0_{S}, $p_{\mathrm{T}} > 0.4$ GeV for Λ and $p_{\mathrm{T}} > 0.5$ GeV for Ξ^-, and the right panels correspond to results extrapolated down to $p_{\mathrm{T}} = 0$ GeV. Λ and Ξ^- are scaled for better visibility. The statistical uncertainties are shown as vertical lines.

Figure 6.22 and 6.23 show the yields of K^0_S, Λ and Ξ^- as a function of p_T in six y selections: [-2.5,-1.6], [-1.6,-0.8], [-0.8,0.0], [0,0.8], [0.8,1.6] and [1.6,2.5]. The left panel shows Pb+Pb UPC results and the right panel shows p+Pb results.

Figure 6.24 shows the V^0 yields as a function of y. The top panels show Pb+Pb UPC results and the bottom panels show p+Pb results. Two cases are included: (i) results integrated over the measured p_T range, i.e., $p_T > 0$ GeV for K^0_S and $p_T > 0.4$ GeV for Λ and $p_T > 0.5$ GeV for Ξ^- (ii) results extrapolated to include the yield over all p_T, i.e., $p_T > 0$. The yields are thus slightly higher in the $p_T > 0$ case.

Figure 6.25 shows the ratio of Λ to K^0_S yield and the ratio of Ξ^- to K^0_S yield as a function of p_T in six y selections: [-2.5,-1.6], [-1.6,-0.8], [-0.8,0.0], [0,0.8], [0.8,1.6], [1.6,2.5]. The left panels show Pb+Pb UPC results and the right panels show p+Pb results.

Figure 6.26 shows the $\langle p_T \rangle$ of V^0 yields and charged-hadron yields ($h^\pm$) as a function of N^{rec}_{ch} in six y selections for $p_T > 0$ GeV for K^0_S, $p_T > 0.1$ GeV for $h^\pm$, $p_T > 0.4$ GeV for Λ and $p_T > 0.5$ GeV for Ξ^-. The left panels are for Pb+Pb UPC and the right panels are for p+Pb collisions. Figure 6.27 shows the same in the case of extrapolation down to $p_T = 0$ GeV.

Figure 6.28 presents the ratio of V^0 yields to charged hadron yields as a function of multiplicity in Pb+Pb UPC and p+Pb collisions. The dependence of the ratio on multiplicity remains relatively constant within the presented multiplicity ranges. For extrapolated results, refer to Figure 6.29.

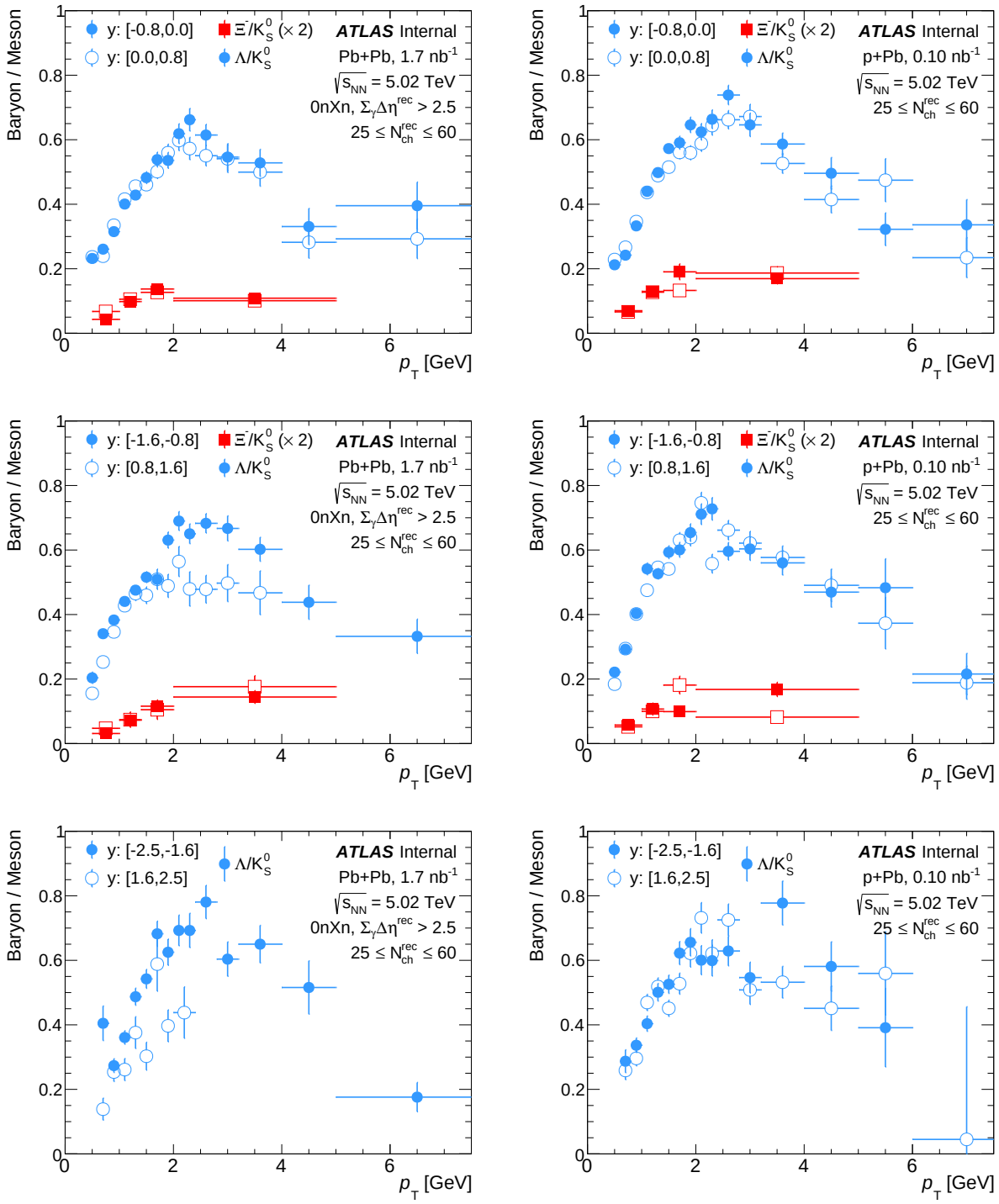

Figure 6.25: Shown is the ratio of Λ to K^0_S yield (blue markers) and the ratio of Ξ^- to K^0_S yield (red markers), as a function of p_T in six y selections. The closed markers show the Pb-going direction ($y < 0$) and the open markers show the proton-going direction ($y > 0$) in the case of p+Pb and γ-going direction ($y > 0$) in the case of Pb+Pb UPC. The left panels are for Pb+Pb UPC and the right panels are for p+Pb collisions. The ratio of Ξ^- to K^0_S yield is scaled for better visibility. Statistical uncertainties are shown as vertical lines.

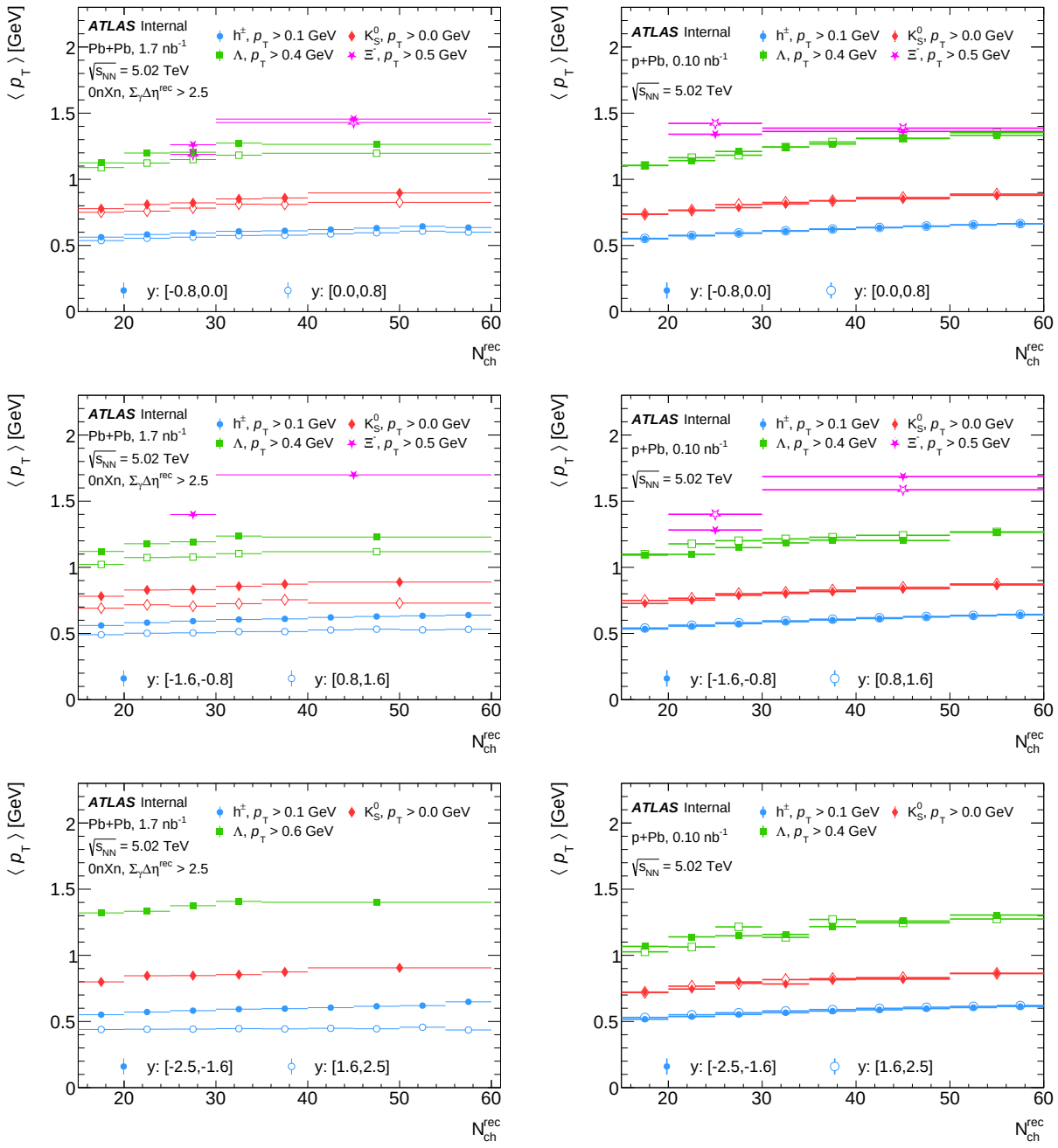

Figure 6.26: Shown are the $\langle p_{\mathrm{T}} \rangle$ of V^0 yields as a function of $N_{\mathrm{ch}}^{\mathrm{rec}}$ in six y selections in the p_{T} range: $p_{\mathrm{T}} > 0$ GeV for K_{S}^0, $p_{\mathrm{T}} > 0.4$ GeV for Λ and $p_{\mathrm{T}} > 0.5$ GeV for Ξ^-. The closed markers show the Pb-going direction ($y < 0$) and the open markers show the proton-going direction ($y > 0$) in the case of p+Pb and γ-going direction ($y > 0$) in the case of Pb+Pb UPC. The left panels are for Pb+Pb UPC and the right panels are for p+Pb collisions. Statistical and systematic uncertainties are yet to be determined.

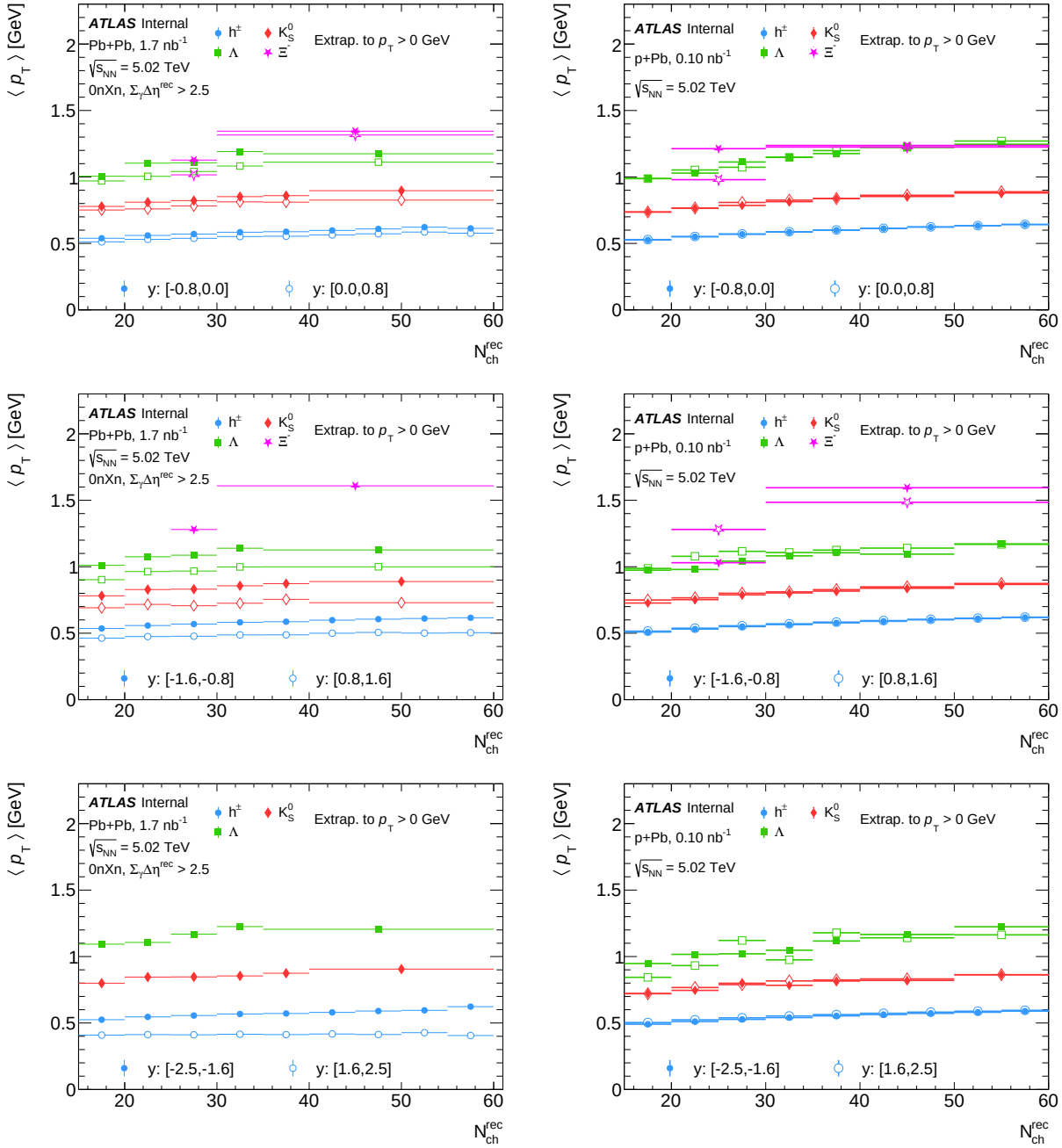

Figure 6.27: Shown are the $\langle p_{\mathrm{T}} \rangle$ of V^0 yields as a function of $N_{\mathrm{ch}}^{\mathrm{rec}}$ in six y selections for $p_{\mathrm{T}} >$ 0 GeV. The closed markers show the Pb-going direction ($y < 0$) and the open markers show the proton-going direction ($y > 0$) in the case of p+Pb and γ-going direction ($y > 0$) in the case of Pb+Pb UPC. The left panels are for Pb+Pb UPC and the right panels are for p+Pb collisions. Statistical and systematic uncertainties are yet to be determined.

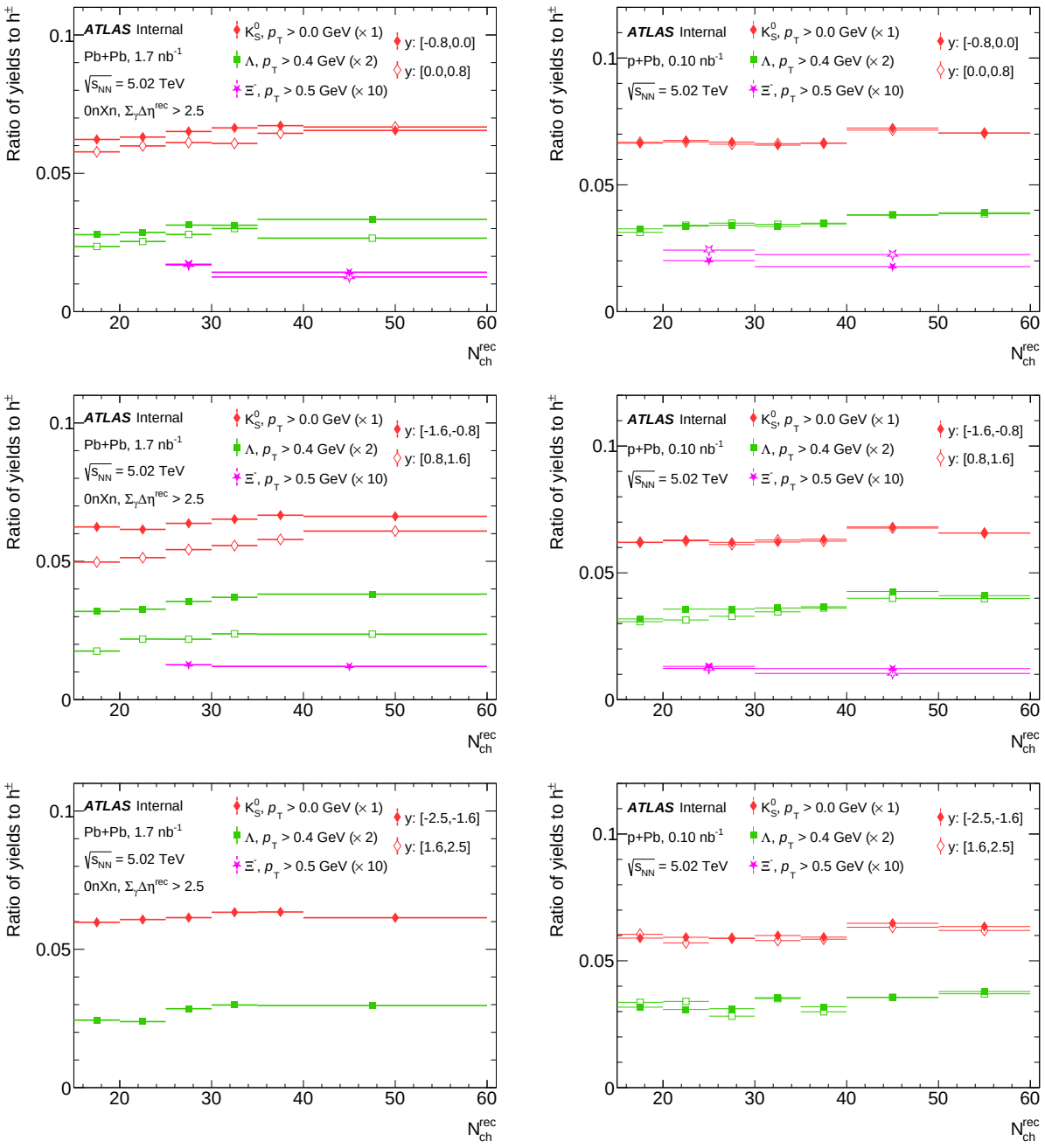

Figure 6.28: Shown are the ratio of V^0 yields to charged hadrons as a function of $N_{\mathrm{ch}}^{\mathrm{rec}}$ in six y selections in the p_{T} range: $p_{\mathrm{T}} > 0$ GeV for K_{S}^0, $p_{\mathrm{T}} > 0.4$ GeV for Λ and $p_{\mathrm{T}} > 0.5$ GeV for Ξ^-. The closed markers show the Pb-going direction ($y < 0$) and the open markers show the proton-going direction ($y > 0$) in the case of p+Pb and γ-going direction ($y > 0$) in the case of Pb+Pb UPC. The left panels are for Pb+Pb UPC and the right panels are for p+Pb collisions. Statistical and systematic uncertainties are yet to be determined.

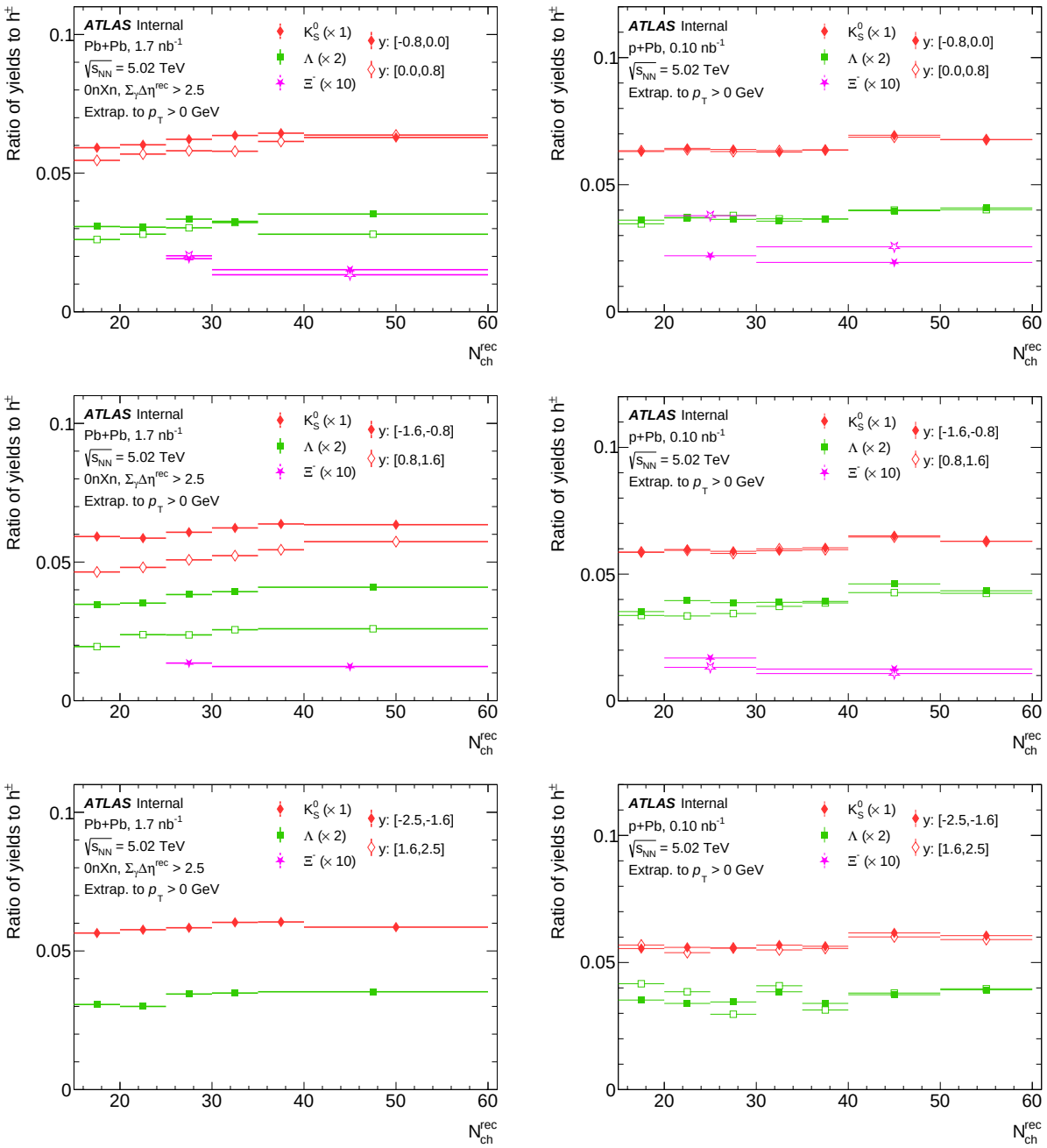

Figure 6.29: Shown are the ratio of V^0 yields to charged hadrons as a function of $N_{\mathrm{ch}}^{\mathrm{rec}}$ in six y selections for $p_{\mathrm{T}} > 0$ GeV. The closed markers show the Pb-going direction ($y < 0$) and the open markers show the proton-going direction ($y > 0$) in the case of p+Pb and γ-going direction ($y > 0$) in the case of Pb+Pb UPC. The left panels are for Pb+Pb UPC and the right panels are for p+Pb collisions. Statistical and systematic uncertainties are yet to be determined.

Chapter 7

Physics Discussion

This dissertation presents the characterization of photo-nuclear collisions using the 5.02 TeV Pb+Pb collision data recorded by ATLAS and the search of QGP droplets within the produced system. Characterizing photo-nuclear events is particularly interesting due to their highly asymmetric nature and the fluctuations in photon energy from event to event, both posing challenges to theoretical modeling. Furthermore, features of collective expansion have been observed in photo-nuclear collisions attributed to the perfect liquid nature of QGP [10]. Various other QGP signatures, such as radial flow, baryon anomaly, and strangeness enhancement, are also explored in this thesis. Additionally, the thesis delves into comparison studies using 5.02 p+Pb collision data recorded by ATLAS. The comparison with p+Pb aims to determine whether photo-nuclear collisions behave similarly to hadron-nucleus collisions and whether a comparable number of QGP signatures are observed between these collisions.

This Chapter discusses the physics implications of the results of charged hadron production, as presented in Chapter 5, and identified particle production, as reported in Chapter 6. Section 7.1 provides a detailed characterization of photo-nuclear events, including comparisons to p+Pb data and theoretical calculations. Section 7.2 details the QGP signatures studied in photo-nuclear events, including comparison to p+Pb data and theoretical calculations. For clarity, "Pb+Pb UPC" is used when discussing the photo-nuclear data, and "γ+Pb" is used when discussing the photo-nuclear models.

7.1 Characterization of Photo-Nuclear Events

This Section details the characterization of photo-nuclear events, including comparisons to p+Pb data and theoretical DPMJET-III and hydrodynamic calculations.

7.1.1 Comparison Between Pb+Pb UPC and p+Pb Data

The charged-hadron yields are presented in 5.02 TeV Pb+Pb UPC and p+Pb collisions both (i) as a function of p_{T} in six exclusive intervals of η and (ii) integrated over all p_{T} as a function of η. The yields are first shown for the $N_{\mathrm{ch}}^{\mathrm{rec}}$ selection, $25 < N_{\mathrm{ch}}^{\mathrm{rec}} \leq 60$, where the p+Pb events are re-weighted to have effectively the same $N_{\mathrm{ch}}^{\mathrm{rec}}$ distribution as the Pb+Pb UPC events. Additionally, the distribution in p+Pb is re-weighted to have the same integral of $\mathrm{d}N_{\mathrm{ch}}/\mathrm{d}\eta$ in Pb+Pb UPC over the η range, -2.5 to 2.5. Negative η corresponds to the Pb-going direction, and positive η corresponds to the photon-going and proton-going directions in Pb+Pb UPC and p+Pb, respectively.

Figure 7.1 shows the charged-hadron yields as a function of p_{T} in six η selections: [-2.5,-1.6], [-1.6,-0.8], [-0.8,0.0], [0,0.8], [0.8,1.6], and [1.6,2.5]. The left panel shows Pb+Pb UPC results, and the right panel shows p+Pb results. They have a qualitatively similar shape as a function of p_{T} for the two systems. Figure 7.2 shows the charged-hadron yields as a function of η for Pb+Pb UPC and p+Pb, extrapolated for $p_{\mathrm{T}} > 0$ GeV. The Pb+Pb UPC distribution is highly asymmetric, as expected, given the lower energy of the photon compared with the energy per nucleon in the opposing Pb nucleus. In contrast, the p+Pb distribution is nearly symmetric. In central p+Pb collisions, the distribution is asymmetric [157]. However, in this analysis, low multiplicity p+Pb events are selected, and hence, the η distribution is more pp like, i.e., symmetry.

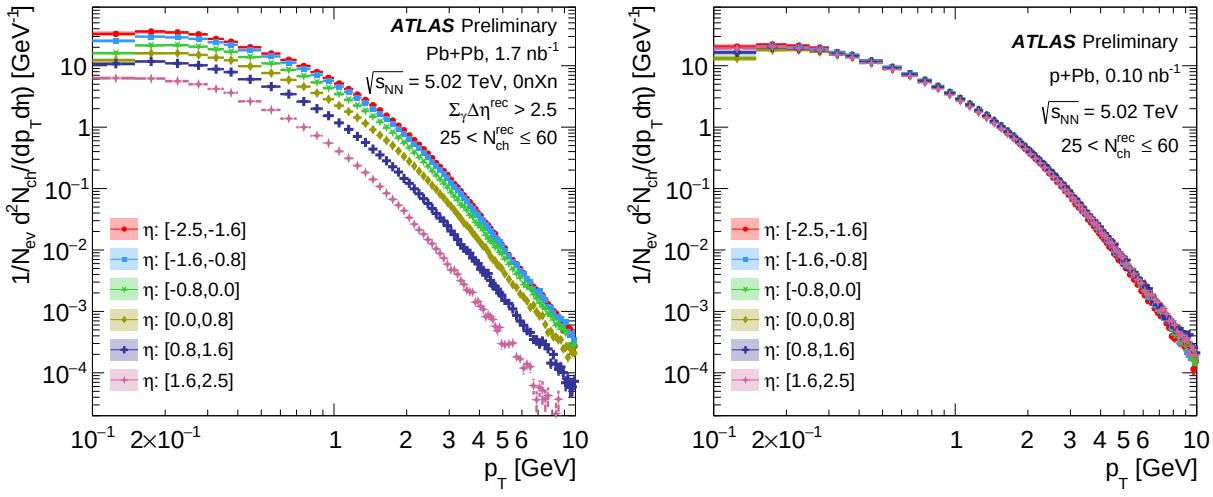

Figure 7.1: Shown are the charged-hadron yields as a function of p_{T} in six η selections. The left panel is for UPC Pb+Pb collisions, and the right panel is for p+Pb collisions. The statistical uncertainties are shown as vertical lines, and systematic uncertainties are shown as open boxes. For most data points, the systematic uncertainties are smaller than the markers.

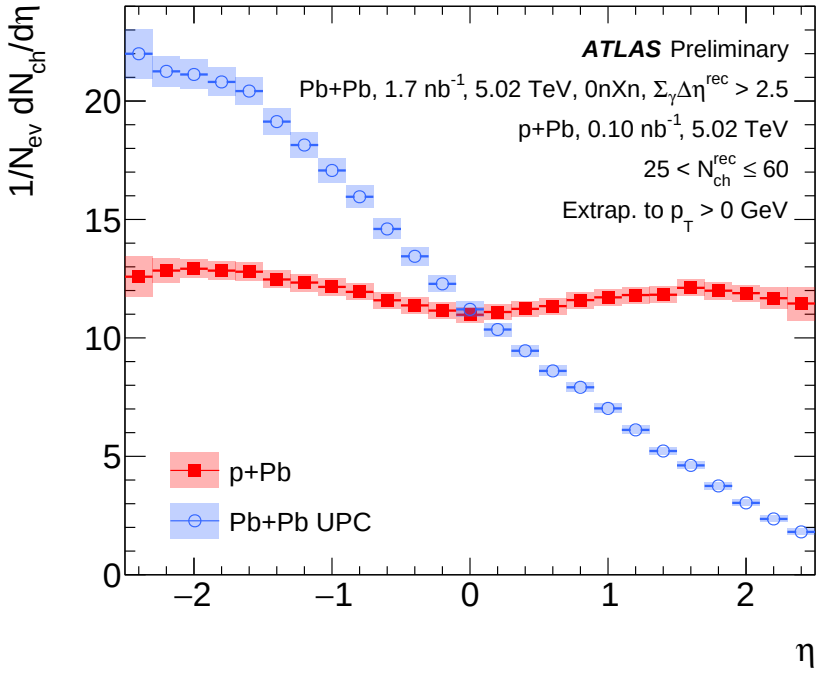

Figure 7.2: Shown are the charged-hadron yields as a function of η extrapolated to $p_{\mathrm{T}} > 0$ GeV for Pb+Pb UPC and p+Pb collisions. The statistical uncertainties are shown as vertical lines, and systematic uncertainties are shown as open boxes.

The identified hadron (so-called V^0) results are presented in 5.02 TeV Pb+Pb UPC and p+Pb collisions both (i) as a function of p_{T} in six exclusive intervals of y, depicted by Figures 7.3 and 7.4 and (ii) integrated over all p_{T} as a function of y, depicted by Figure 7.5. The yields are shown for the $N_{\mathrm{ch}}^{\mathrm{rec}}$ selection 25-60, where the p+Pb events are re-weighted to have effectively the same $N_{\mathrm{ch}}^{\mathrm{rec}}$ distribution as the Pb+Pb UPC events. Negative η corresponds to the Pb-going direction, and positive η corresponds to the photon-going and proton-going directions in Pb+Pb UPC and p+Pb, respectively.

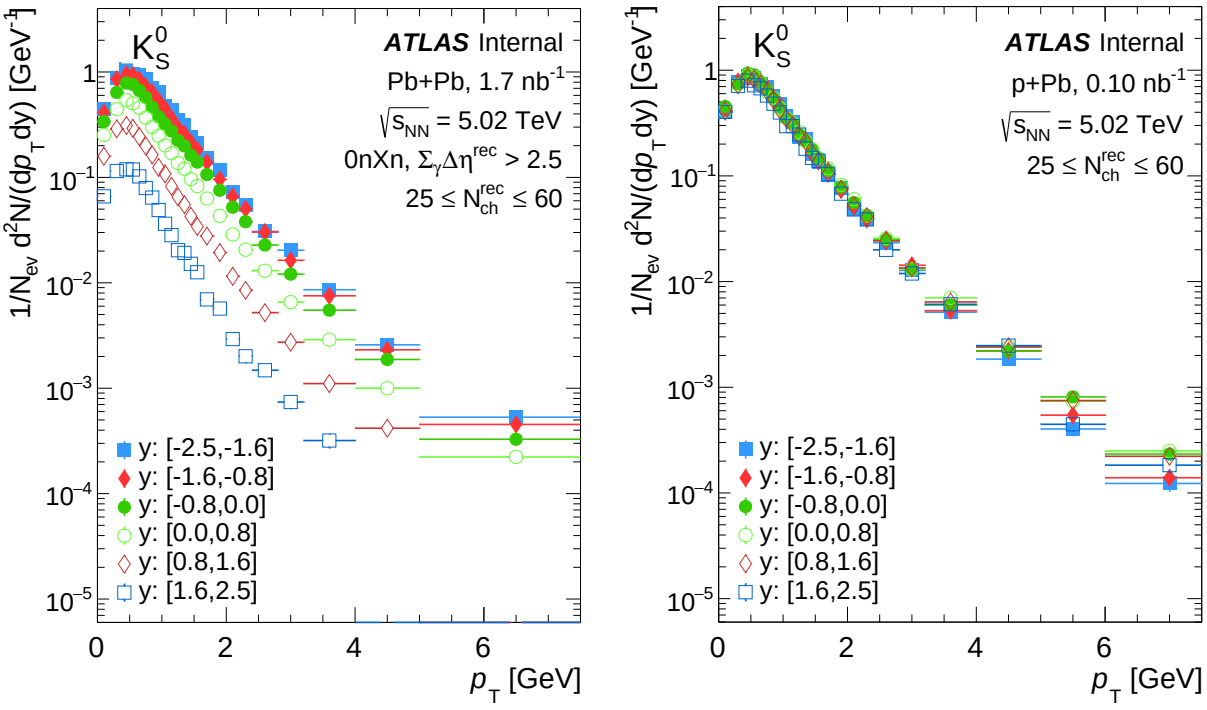

Figure 7.3: K^0_{S} yields as a function of p_{T} in six y selections. The left panel is for Pb+Pb UPC, and the right panel is for p+Pb collisions. Statistical uncertainties are shown as vertical lines, often smaller than the markers. No systematic uncertainties are shown.

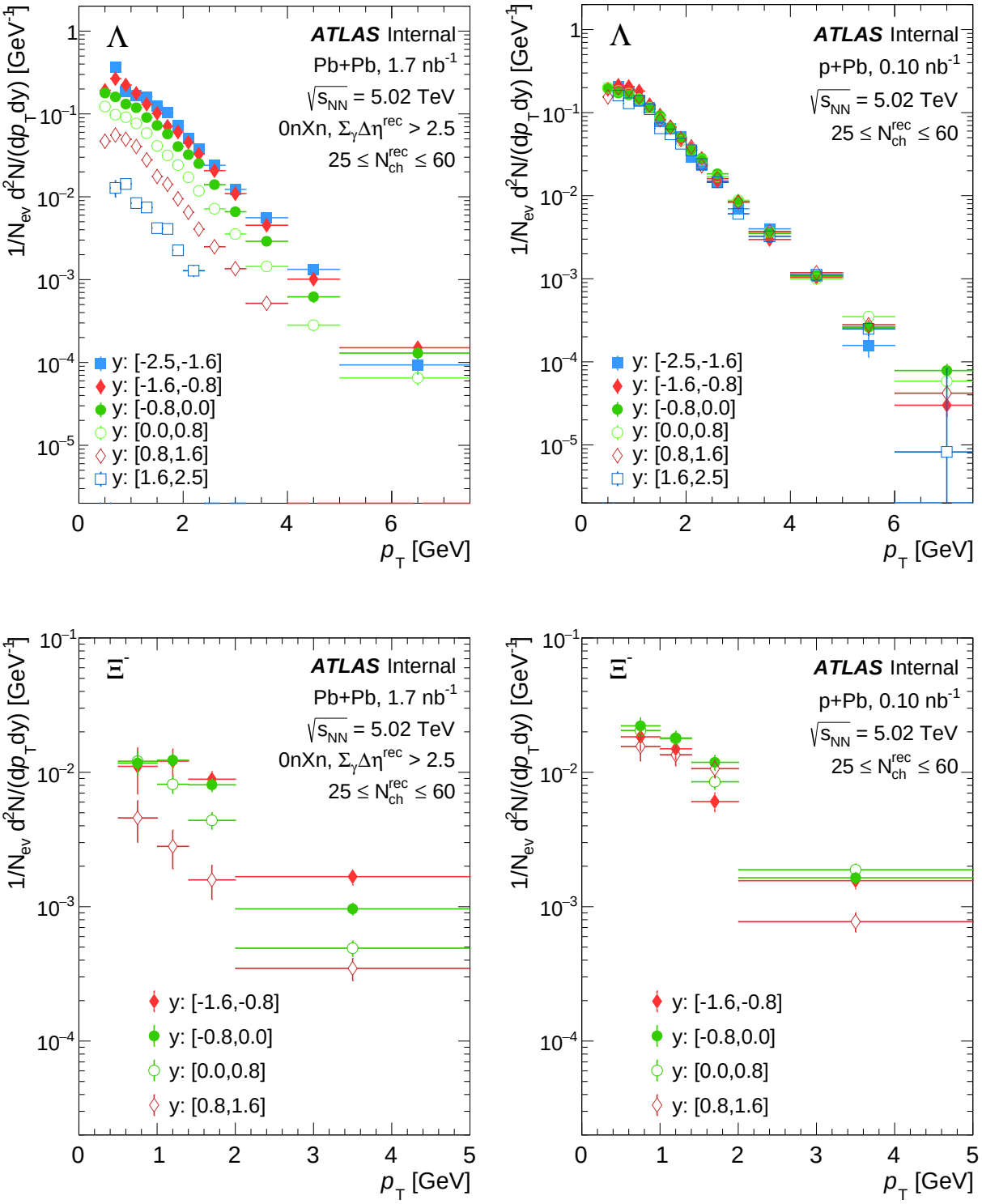

Figure 7.4: Λ (top) and Ξ^- (bottom) yields as a function of p_{T} in six y selections. The left panel is for Pb+Pb UPC, and the right panel is for p+Pb collisions. Statistical uncertainties are shown as vertical lines. No systematic uncertainties are shown.

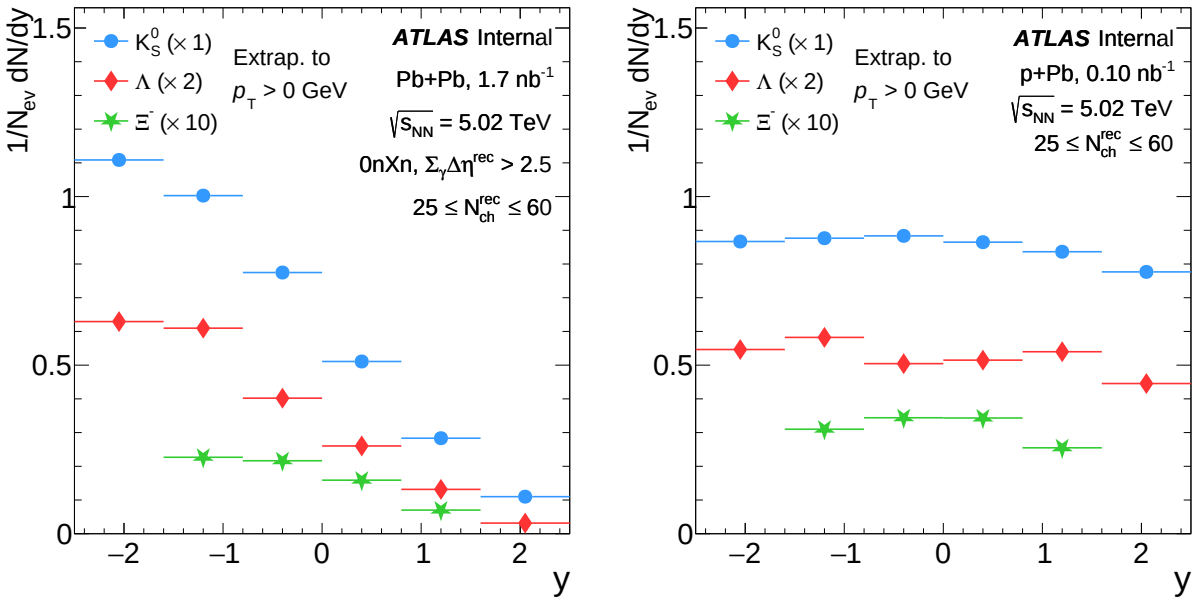

Figure 7.5: Shown are the V^0 yields as a function of y extrapolated to $p_{\mathrm{T}} > 0$ GeV for Pb+Pb UPC and p+Pb collisions. Λ and Ξ^- are scaled for better visibility. The statistical uncertainties are shown as vertical lines. No systematic uncertainties are shown.

The shape comparison between the Pb+Pb UPC and p+Pb $\mathrm{d}N_{V^0}/\mathrm{d}y$ is consistent with that of charged hadrons, i.e., the Pb+Pb UPC distribution exhibits a strong asymmetry attributed to the comparatively lower energy of the photon in contrast to the energy per nucleon in the opposing Pb nucleus, whereas the p+Pb distribution is nearly symmetric due to the selected low multiplicity p+Pb events. In both these collisions, there is a higher yield of K^0_{S}, followed by Λ and then Ξ^-.

7.1.2 DPMJET-III comparison

Figure 7.6 shows the charged-hadron yields as function of η, and Figure 7.7 displays the V^0 yields as a function of y, with comparisons to the Monte Carlo model DPMJET-III. Additionally, Figure 7.8 depicts the charged-hadron yields as a function of p_{T} in the same model and data comparison.

In the case of charged hadrons, DPMJET-III over-predicts the yield at forward rapidity by up to 50%, though with a reasonable description of the steeply falling p_{T} distribution. At backward rapidity, DPMJET-III reasonably predicts the yield well, with significantly steeper high p_{T} yields. However, when considering identified hadrons like K^0_{S}, Λ and Ξ^-, DPMJET-III further deviates from describing the shape of the data distribution, particularly for heavier hadrons.

A detailed comparison of charged-hadron yield in Pb+Pb UPC to the Monte Carlo DPMJET-III model, particularly investigating the relationship between particle production and photon energy, is discussed in Appendix A.1. These results serve as a valuable resource for benchmarking Monte Carlo models.

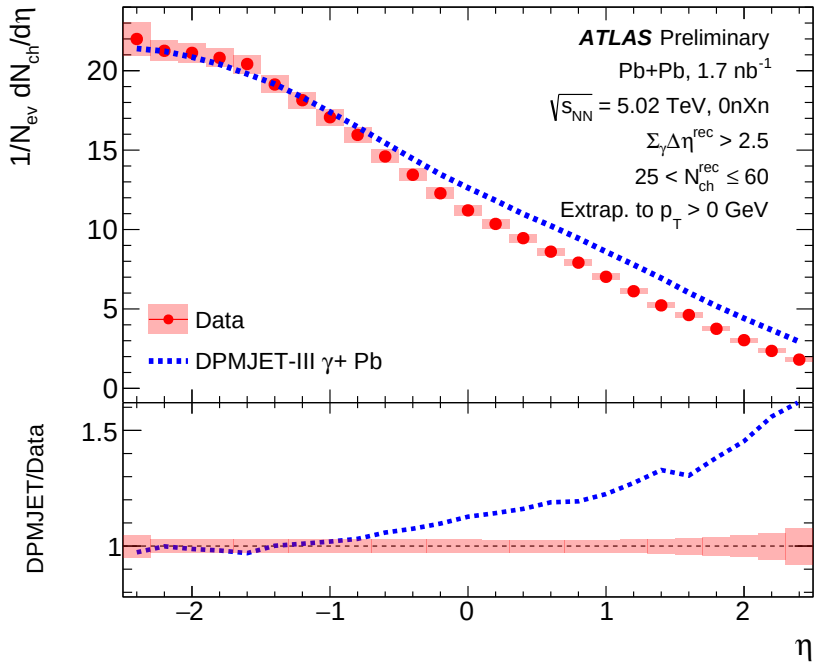

Figure 7.6: Shown are the charged hadron yields as a function of η in Pb+Pb UPC data and DPMJET-III γA generator results for $p_{\mathrm{T}} > 0$ GeV. The bottom panels show the ratio of DPMJET-III γ+Pb to data.

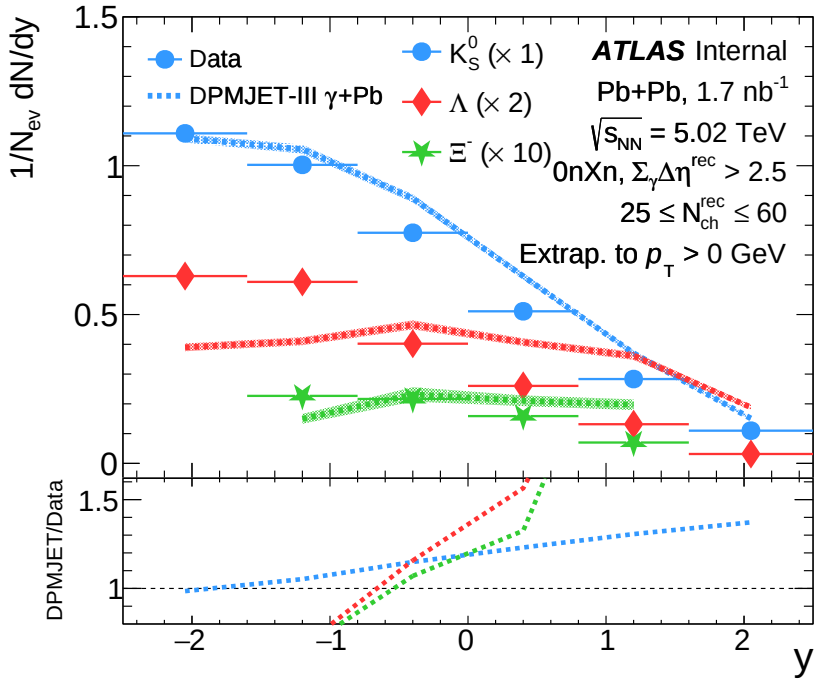

Figure 7.7: Shown are the V^0 yields as a function of y in Pb+Pb UPC data and DPMJET-III γA generator results for $p_{\mathrm{T}} > 0$ GeV. The bottom panels show the ratio of DPMJET-III γ+Pb to data.

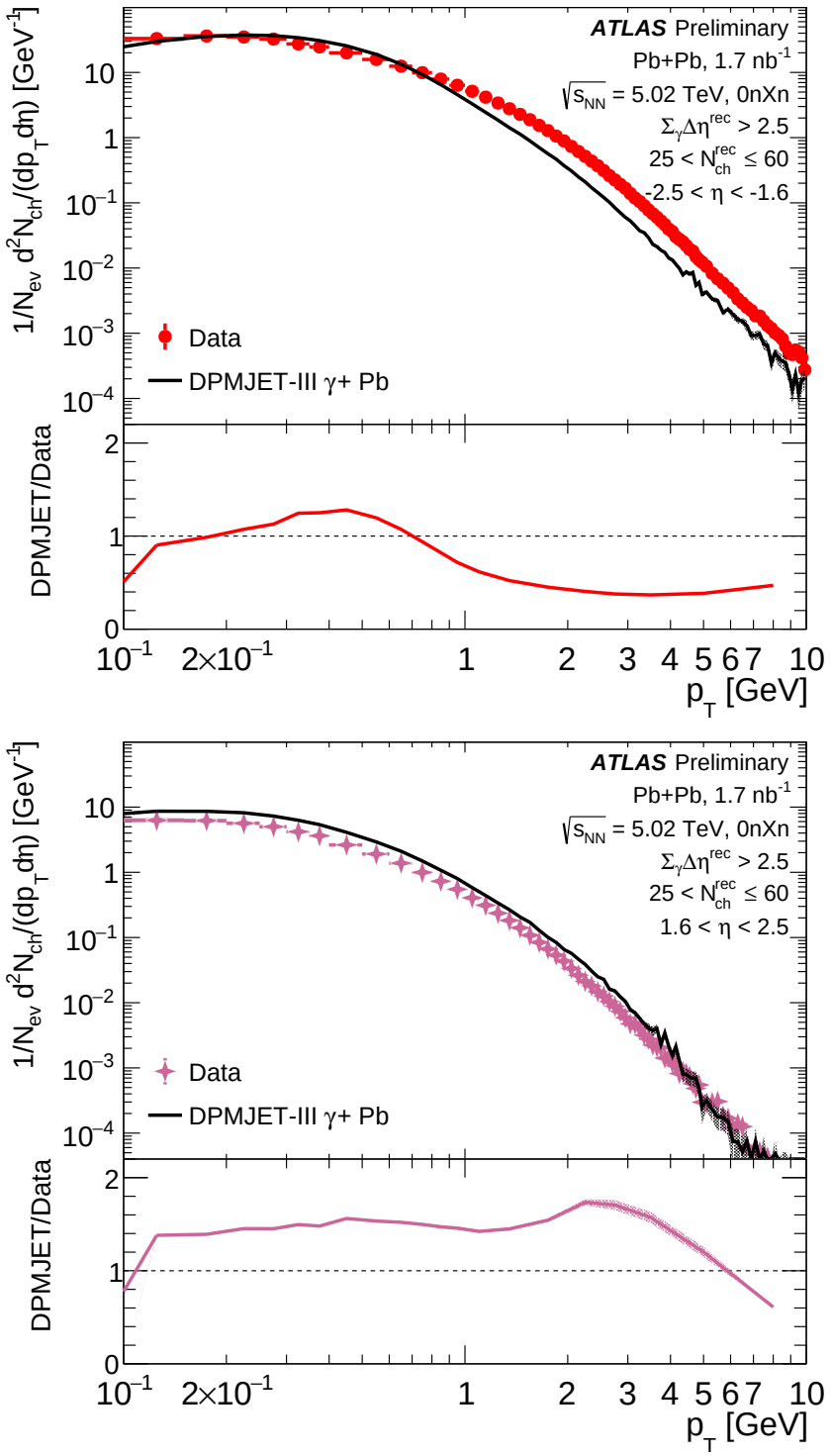

Figure 7.8: Shown are the charged hadron yields as a function of p_{T} in two η slices, $-2.5 < \eta < -1.6$ (top) and $1.6 < \eta < 2.5$ (bottom), in Pb+Pb UPC data and DPMJET-III γA model. The bottom panels show the ratio of DPMJET-III γ+Pb results to data.

7.1.3 Hydrodynamic Model

This Section presents the comparison of Pb+Pb UPC data to the hydrodynamic model, detailed in Section 2.5.1. Figure 7.9 illustrates the hydrodynamic model calculations for charged-hadron pseudorapidity distributions $\mathrm{d}N_{\mathrm{ch}}/\mathrm{d}\eta$ in γ+Pb and p+Pb collisions. The hydrodynamic results exhibit good agreement with Pb+Pb UPC data at the 10% level, indicating that the final-state-dominated framework can accurately predict experimental results. The charged-hadron pseudorapidity distribution has a strong asymmetry in the η direction, demonstrating a strong violation of longitudinal boost invariance. The Pb+Pb UPC data presented in this result is published as part of the event categorization in the ATLAS two-particle azimuthal correlation [10]. Thus, it does not have the correct normalization, and the hydrodynamic results only serve the shape comparison. A comparison with the results presented in this thesis, as shown in Figures 7.1 and 7.2, will be shown in the future.

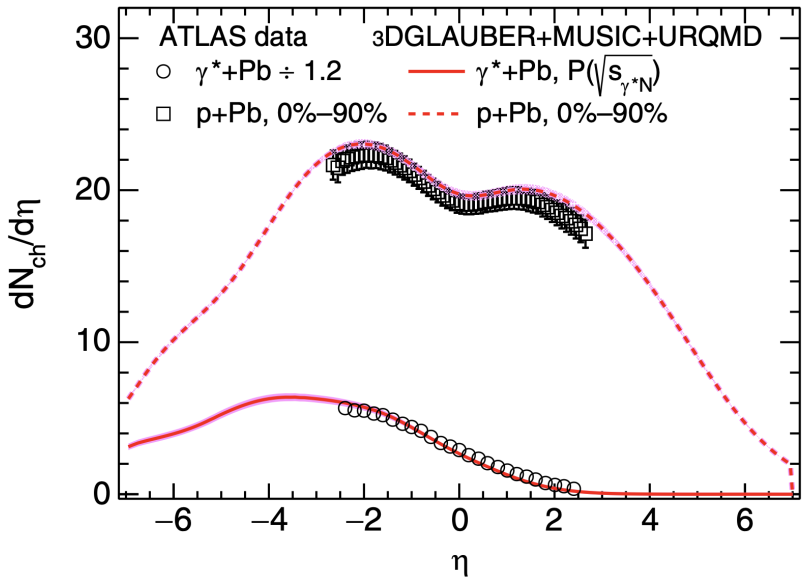

Figure 7.9: The charged hadron pseudorapidity distributions $\mathrm{d}N_{\mathrm{ch}}/\mathrm{d}\eta$ in γ+Pb and 0%-90% p+Pb collisions from the 3D-GLAUBER+MUSIC+URQMD simulations. The theoretical calculations are compared with experimental data from the ATLAS Collaboration in the laboratory frame. Reproduced from Ref [61].

7.2 Search for QGP signatures

This Section details the QGP signatures studied in photo-nuclear events, such as radial flow, baryon anomaly, and strangeness enhancement, including comparison to p+Pb data and theoretical calculations such as DPMJET-III and hydrodynamic simulations.

7.2.1 Radial Flow

Figure 7.10 shows the $\langle p_{\mathrm{T}} \rangle$ of charged hadrons for $p_{\mathrm{T}} > 0$ GeV as a function of $N_{\mathrm{ch}}^{\mathrm{rec}}$ in two η regions, [-1.6,-0.8] and [0.8,1.6], in Pb+Pb UPC and p+Pb collisions. At negative η, the $\langle p_{\mathrm{T}} \rangle$ value agree within uncertainties in the two collision systems, except a hint of difference in the lowest selection, $N_{\mathrm{ch}}^{\mathrm{rec}} < 30$. In contrast, on the photon/proton-going side ($\eta > 0$), there is a large difference in the $\langle p_{\mathrm{T}} \rangle$ between the two collision systems for all $N_{\mathrm{ch}}^{\mathrm{rec}}$. The smaller $\langle p_{\mathrm{T}} \rangle$ in the photon-going side ($\eta > 0$) in Pb+Pb UPC could be explained through the lower multiplicity, i.e., a smaller density of particles and shorter-lived QGP-like region compared to the p+Pb collisions. It is notable that DPMJET-III with no final-state interactions or hydrodynamic flow predicts a similar $\langle p_{\mathrm{T}} \rangle$ in Pb+Pb UPC at forward rapidity ($\eta > 0$), as detailed below.

Figure 7.11 shows the $\langle p_{\mathrm{T}} \rangle$ of charged hadrons for $p_{\mathrm{T}} > 0$ GeV as a function of $N_{\mathrm{ch}}^{\mathrm{rec}}$ in two η selections of interest, [-1.6,-0.8] and [0.8,1.6], in Pb+Pb UPC, compared to DPMJET-III calculations. DPMJET-III provides an excellent description of the $\langle p_{\mathrm{T}} \rangle$ at forward rapidity ($\eta > 0$) and significantly under-predicts the $\langle p_{\mathrm{T}} \rangle$ at backward rapidity ($\eta < 0$). The difference in $\langle p_{\mathrm{T}} \rangle$ between the data and DPMJET-III is further investigated by varying the photon energy distribution in DPMJET-III, as detailed in Appendix A.2. However, no significant difference was found between the $\langle p_{\mathrm{T}} \rangle$ obtained from nominal photon energy distribution compared to those obtained from re-weighted photon energy distribution. Thus this deviation cannot simply be attributed to a mismodeling of the photon energy distribution.

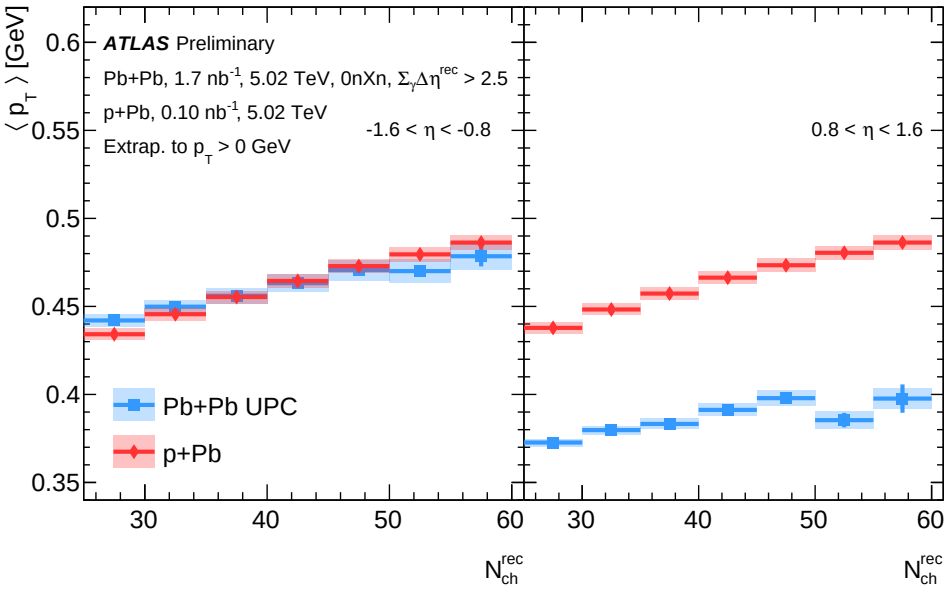

Figure 7.10: Shown are the $\langle p_{\mathrm{T}} \rangle$ of charged-hadron yields as a function of $N_{\mathrm{ch}}^{\mathrm{rec}}$ in Pb+Pb UPC and p+Pb collisions in two different η slices, [-1.6,-0.8] (left) and [0.8,1.6] (right). The charged-hadron yields are extrapolated to $p_{\mathrm{T}} > 0$ GeV. Vertical lines, often smaller than the markers, are statistical uncertainties, and shaded boxes are systematic uncertainties.

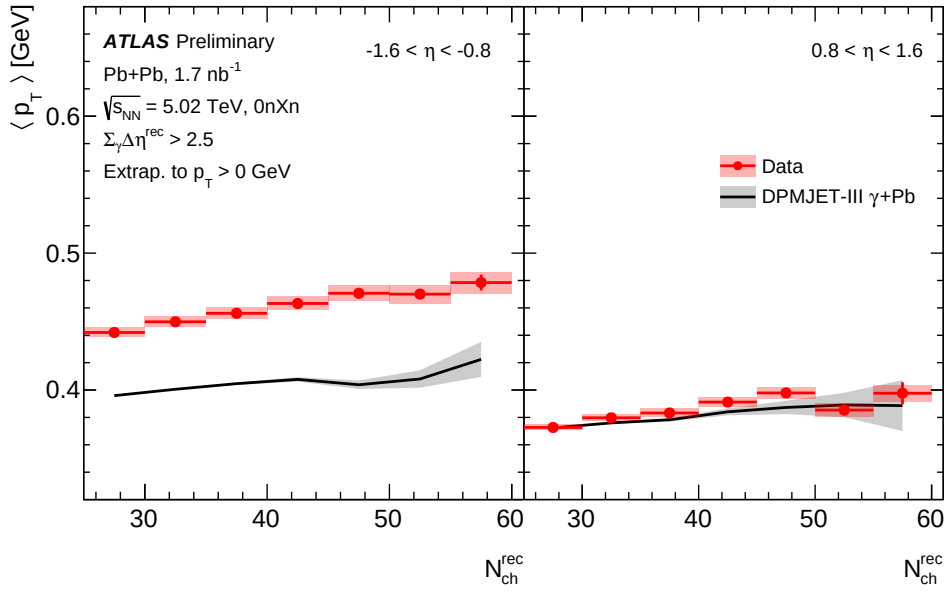

Figure 7.11: Shown are the $\langle p_{\mathrm{T}} \rangle$ of charged-hadron yields as a function of $N_{\mathrm{ch}}^{\mathrm{rec}}$ in Pb+Pb UPC and DPMJET-III model in two different η slices, [-1.6,-0.8] (left) and [0.8,1.6] (right). The charged-hadron yields are extrapolated to $p_{\mathrm{T}} > 0$ GeV. Vertical lines, often smaller than the markers, are statistical uncertainties, and shaded boxes are systematic uncertainties.

The substantially larger $\langle p_{\mathrm{T}} \rangle$ at negative η in Pb+Pb UPC, and its comparable magnitude in p+Pb, may already suggest a contribution from radial flow, detailed in Section 3.3.2. To confirm this hypothesis, further tests measuring the $\langle p_{\mathrm{T}} \rangle$ of identified hadrons are needed. Figure 7.12 shows the $\langle p_{\mathrm{T}} \rangle$ of V^0 yields as a function of $N_{\mathrm{ch}}^{\mathrm{rec}}$ in the two mid-rapidity selections. The $\langle p_{\mathrm{T}} \rangle$ values gradually increase as a function of multiplicity for both y selections in both Pb+Pb UPC and p+Pb collisions.

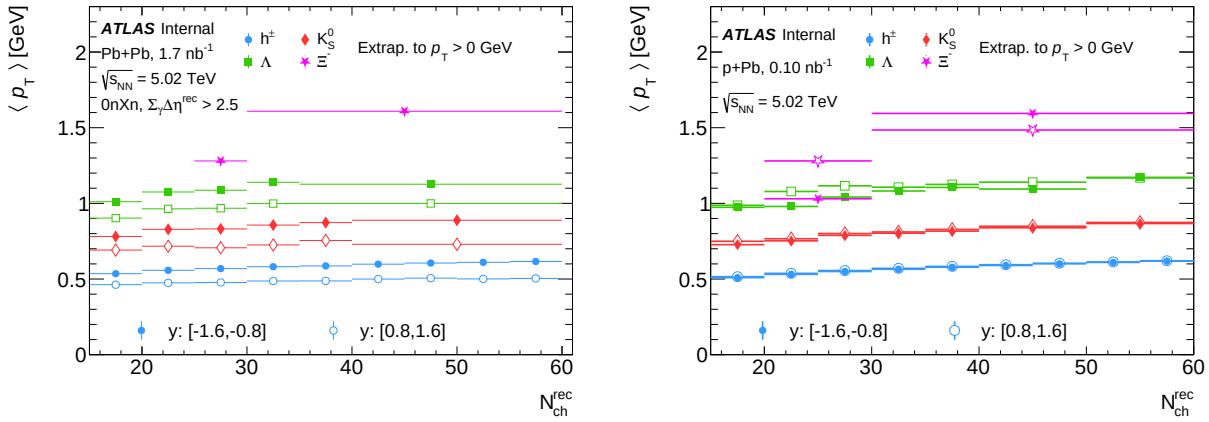

Figure 7.12: Shown are the $\langle p_{\mathrm{T}} \rangle$ of V^0 yields as a function of $N_{\mathrm{ch}}^{\mathrm{rec}}$ in the y selection, $0.8 < |y| < 1.6$ for $p_{\mathrm{T}} > 0$ GeV. The closed markers show the Pb-going direction ($y < 0$), and the open markers show the proton-going direction ($y > 0$) in the case of p+Pb and γ-going direction ($y > 0$) in the case of Pb+Pb UPC. The left panels are for Pb+Pb UPC, and the right panels are for p+Pb collisions. Statistical and systematic uncertainties are not shown and remain to be calculated.

The radial expansion of the fluid in the transverse plane significantly affects the shape of the p_{T} distribution of the particles and can be quantified by the $\langle p_{\mathrm{T}} \rangle$ of the distribution. As the fluid expands radially, driven by hydrodynamics, the momentum boost will be larger for massive particles that gain the same velocity boost. Consequently, the $\langle p_{\mathrm{T}} \rangle$ of massive particles is higher, as heavier hadrons are pushed to higher p_{T}, resulting in a comparatively flatter p_{T} distribution. This characteristic is evident in the figure, where $\langle p_{\mathrm{T}} \rangle$ is highest for massive particles such as Ξ^-, followed by Λ, then K_{S}^0, and finally by charged hadrons (dominated by light pions) in both Pb+Pb UPC and p+Pb collisions. In addition, heavier hadrons like Ξ^- shows a steeper dependence to $N_{\mathrm{ch}}^{\mathrm{rec}}$. Full hydrodynamic comparisons with data are forthcoming and will be needed to make

strong conclusions.

Furthermore, if one compares the $\langle p_{\mathrm{T}} \rangle$ between the forward ($y > 0$) and backward ($y < 0$) rapidity selections, there is a higher magnitude of $\langle p_{\mathrm{T}} \rangle$ in the backward rapidity compared to the forward rapidity, for charged hadrons and particle species, K^0_{S} and Λ, in Pb+Pb UPC. This indicates that the Pb-going rapidity region ($y < 0$) with larger multiplicity corresponds to a QGP-like region, exhibiting significant radial flow, quantified by a high $\langle p_{\mathrm{T}} \rangle$. In contrast, the photon-going rapidity region ($y > 0$) has a smaller multiplicity corresponding to a shorter-lived QGP-like region, featuring comparatively less radial flow. This effect is not visible in the $\langle p_{\mathrm{T}} \rangle$ of Ξ^- due to the statistical limitations of the Pb+Pb UPC data. In the case of p+Pb collisions, since the selected event class is peripheral, both the forward and backward rapidity selection correspond to similar multiplicities, leading to similar radial flow.

It has been established that QGP signatures, such as collective expansion, can be successfully explained through hydrodynamic models, as detailed in Section 2.5.1. The hydrodynamic paradigm, described in Section 3.3.1, suggests that the actual "flow" of the medium – indicating the hydrodynamic translation of initial state spatial anisotropy in the transverse plane – remains essentially the same in γ+Pb and p+Pb collisions. In other words, the radial flow, measured via the mean p_{T} of particles, should be similar for both systems at the same local multiplicity.

Figure 7.13 presents the mean transverse momentum, $\langle p_{\mathrm{T}} \rangle$, of identified particles such as π, K, and p as functions of charged hadron multiplicity in p+Pb collisions from the ALICE collaboration [116]. This data is compared to hydrodynamic model predictions in γ+Pb and p+Pb collisions. The model predicts that the identified particle $\langle p_{\mathrm{T}} \rangle$ measured in γ+Pb collisions are very similar to those in p+Pb collisions. Figure 7.14 presents the ATLAS measured $\langle p_{\mathrm{T}} \rangle$ of V^0 yields as a function of $N^{\mathrm{rec}}_{\mathrm{ch}}$ in the rapidity selection $0.0 < |y| < 0.8$ for γ+Pb and p+Pb collisions. In the two mid-rapidity regions, $0.0 < |y| < 0.8$, where there is similar multiplicity between Pb+Pb UPC and p+Pb collisions, a similar magnitude of $\langle p_{\mathrm{T}} \rangle$ is observed between different particle species. This experimental confirmation indicates that γ+Pb behaves like a hadron-nucleus interaction (p+Pb), experiencing strong final-state effects.

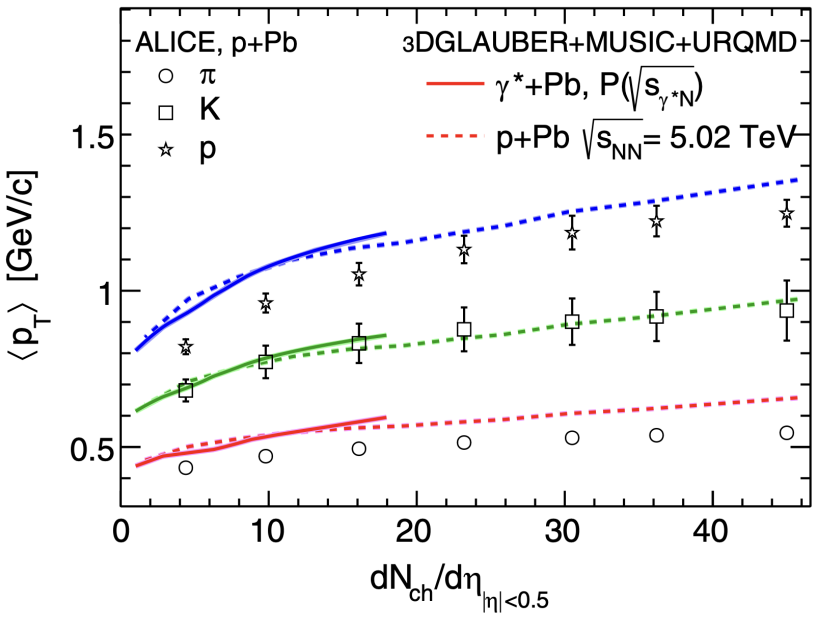

Figure 7.13: $\langle p_{\mathrm{T}} \rangle$ as a function of event multiplicity for various identified particles, $\pi^{\pm}$, $K^{\pm}$, and $p^{\pm}$, in p+Pb collisions measured by ALICE collaboration compared to hydrodynamic simulations. Reproduced from Ref [61].

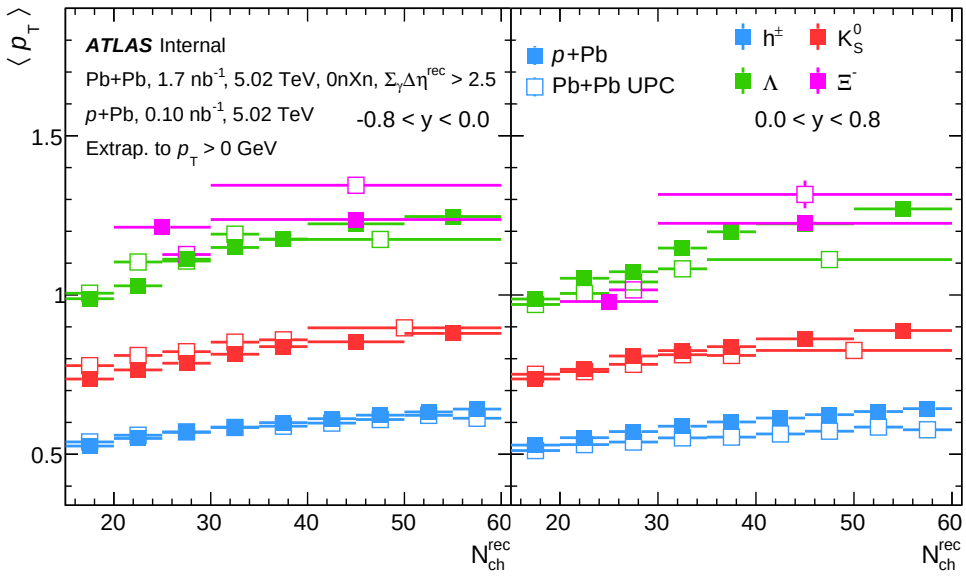

Figure 7.14: Shown are the $\langle p_{\mathrm{T}} \rangle$ of V^0 yields as a function of $N_{\mathrm{ch}}^{\mathrm{rec}}$ in the y selection, $0.0 < |y| < 0.8$ for $p_{\mathrm{T}} > 0$ GeV. The closed markers show p+Pb collisions and the open markers show Pb+Pb UPC. The left panel corresponds to the Pb-going direction ($y < 0$), and the right panel corresponds to the proton-going direction ($y > 0$) in the case of p+Pb and γ-going direction ($y > 0$) in the case of Pb+Pb UPC. Statistical and systematic uncertainties are yet to be determined.

7.2.2 Baryon Anomaly

The baryon anomaly, one of the QGP-like signals related to novel hadronization mechanisms, is closely connected to the radial flow discussed above. The hydrodynamically-driven radial expansion of the fluid leads to a shift of the p_{T} spectra towards higher values, resulting in a flatter distribution in the low-p_{T} range (up to approximately 2–3 GeV). The idea behind the baryon-to-meson ratio observable is that the momentum boost would be higher for massive hadrons in a radially expanding system, indicating an observation of an enhancement in the baryon-to-meson ratio at intermediate $p_{\mathrm{T}} \approx$ 2–3 GeV. Additionally, novel hadronization mechanisms, such as quark coalescence, have been proposed to explain this effect [72, 73]. This has been previously observed across collision systems with a wide range of sizes, with significant enhancement in central Pb+Pb collisions and a smaller enhancement in p+Pb collisions [158], as detailed in Section 2.5.3.

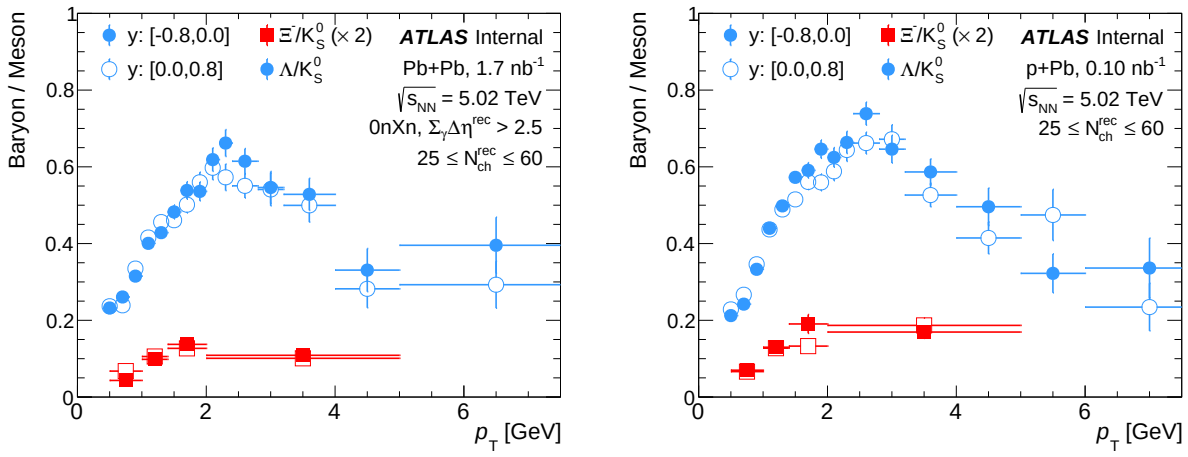

Figure 7.15: Shown is the ratio of Λ to K^0_{S} yield (blue markers), and the ratio of Ξ^- to K^0_{S} yield (red markers), as a function of p_{T} in the y selection, $0.0 < |y| < 0.8$. The closed markers show the Pb-going direction ($y < 0$), and the open markers show the proton-going direction ($y > 0$) in the case of p+Pb and γ-going direction ($y > 0$) in the case of Pb+Pb UPC. The left panels are for Pb+Pb UPC, and the right panels are for p+Pb collisions. The ratio of Ξ^- to K^0_{S} yield is scaled for better visibility. Statistical uncertainties are shown as vertical lines. No systematic uncertainties are shown.

Figure 7.15 shows the ratio of the Λ to K^0_S yields, and the ratio of the Ξ^- to K^0_S yields as functions of p_T in the two mid-rapidity selections $0.0 < |y| < 0.8$ for Pb+Pb UPC and p+Pb collisions. A significant enhancement of the Λ to K^0_S ratio in the intermediate p_T region, approximately at 2–3 GeV, is observed in both collisions. The strikingly similar magnitude of enhancement between Pb+Pb UPC and p+Pb collisions suggests that the system produced in γ+Pb collisions has important final-state interactions and behaves like a hadron-nucleus interaction.

The strongly asymmetric production of particles in rapidity in Pb+Pb UPC adds an interesting element to the observation of the baryon anomaly. As depicted in Figure 7.16, a significant enhancement of Λ to K^0_S ratio at the intermediate p_T region, approximately at 2–3 GeV, is observed in the most backward rapidity selection, $-1.6 < y < -0.8$, in Pb+Pb UPC. This enhancement gradually diminishes towards the forward rapidity direction, $0.8 < y < 1.6$. This trend aligns with the expectation, as there is a higher density of particles in the Pb-going direction ($y < 0$), contrasted by a smaller density of particles produced in the γ-going direction ($y > 0$). This observation suggests that the local density is driving these final-state interaction effects.

In p+Pb collisions, since the distribution of particles in y is nearly symmetric, a similar magnitude of enhancement is observed across y selections. A smaller enhancement in the Ξ^- to K^0_S yield at the intermediate p_T region, approximately at 2 GeV, is also present in Pb+Pb UPC and p+Pb collisions across y selections within limited statistics.

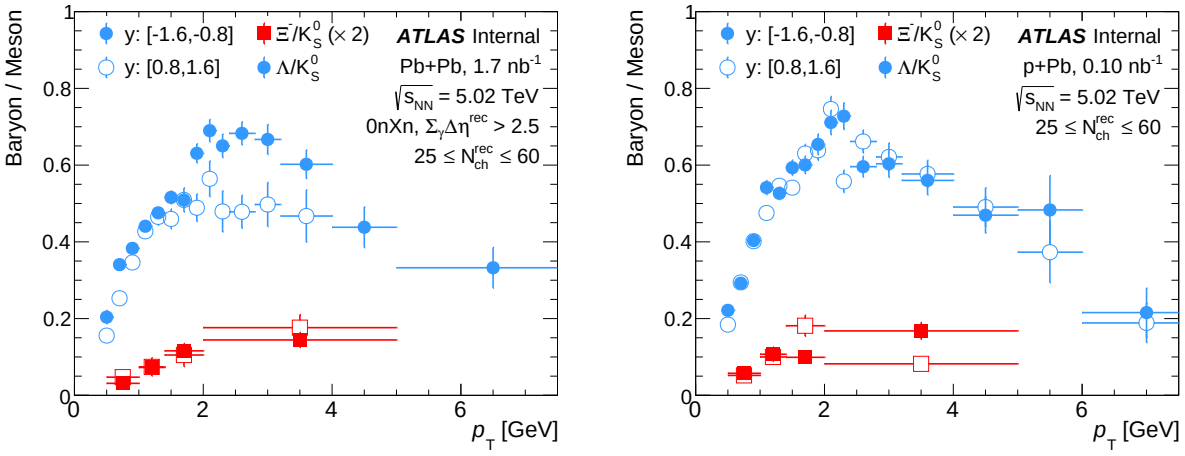

Figure 7.16: Shown is the ratio of Λ to K^0_S yield (blue markers), and the ratio of Ξ^- to K^0_S yield (red markers), as a function of p_T in the y selection, $0.8 < |y| < 1.6$. The closed markers show the Pb-going direction ($y < 0$), and the open markers show the proton-going direction ($y > 0$) in the case of p+Pb and γ-going direction ($y > 0$) in the case of Pb+Pb UPC. The left panels are for Pb+Pb UPC, and the right panels are for p+Pb collisions. The ratio of Ξ^- to K^0_S yield is scaled for better visibility. Statistical uncertainties are shown as vertical lines. No systematic uncertainties are shown.

The baryon-to-meson enhancement, specifically the ratio of Λ to K^0_S yields in the intermediate p_T region p_T = 2–3.2 GeV, as a function of y is shown in Figure 7.17. The magnitude of the enhancement in Pb+Pb UPC exhibits a strong asymmetry in rapidity, in contrast to the nearly symmetric enhancement observed in p+Pb collisions. The magnitude of enhancement is highest in the most backward rapidity selection, $-2.5 < y < -1.6$, where a large number of particles are produced. This enhancement gradually diminishes towards the forward direction, reducing by a factor of two in the most forward rapidity selection, $1.6 < y < 2.5$. In p+Pb collisions, since the distribution of particles in y is nearly symmetric, a similar magnitude of enhancement is observed across y selections. The magnitude of the enhancement in the rapidity selection $-1.6 < y < -0.8$ in Pb+Pb UPC has a similar magnitude to that of p+Pb collisions.

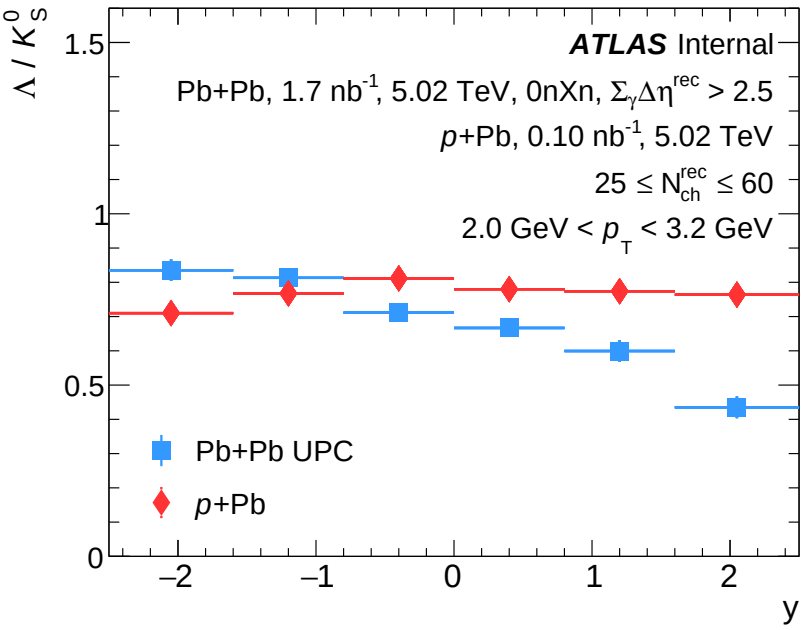

Figure 7.17: Shown are the ratio of Λ to K^0_S yield as a function of y, in the p_T region of baryon-to-meson enhancement, p_T: [2.0,3.2] GeV for Pb+Pb UPC and p+Pb collisions. Statistical uncertainties are shown as vertical lines. No systematic uncertainties are shown.

Figure 7.18 depicts the ratio of Λ to K^0_S yields in the intermediate p_T region $p_T = 2$– 3.2 GeV, as a function of y, in Pb+Pb UPC data compared to the DPMJET-III model. The DPMJET-III model, without final-state interactions or hydrodynamic flow, predicts the highest magnitude of enhancement in the most forward rapidity selection, $1.6 < y < 2.5$. However, this observation is opposite to what is seen in the Pb+Pb UPC data.

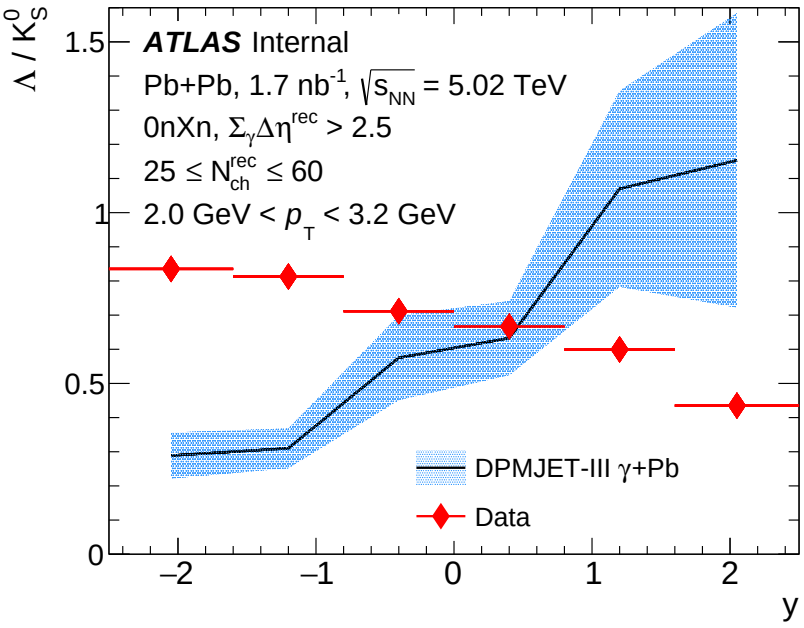

Figure 7.18: Shown are the ratio of Λ to K^0_S yield as a function of y, in the p_T region of baryon-to-meson enhancement, p_T: [2.0,3.2] GeV for Pb+Pb UPC and DPMJET-III model. Statistical uncertainties are shown as vertical lines in data, and as a band in DPMJET-III model. No systematic uncertainties are shown.

One can also study the behavior of baryon-to-meson enhancement as a function of multiplicity. Figure 7.19 shows the ratio of Λ to K^0_S yields, in the enhancement region p_T = 2.0–3.2 GeV, as a function of N^{rec}_{ch}, in Pb+Pb UPC compared to the p+Pb collisions. A gradual increase in the ratio of Λ to K^0_S yields is observed with increase in the multiplicity. This is consistent with what has been observed in the comparison of radial flow as a function of N^{rec}_{ch} between Pb+Pb UPC and p+Pb collisions, hinting at the formation of a QGP-like region when there is a dense production of particles, i.e., at higher multiplicities. Furthermore, a rapidity dependence of the enhancement is observed in Pb+Pb UPC, while a symmetric enhancement in rapidity is observed in p+Pb collisions.

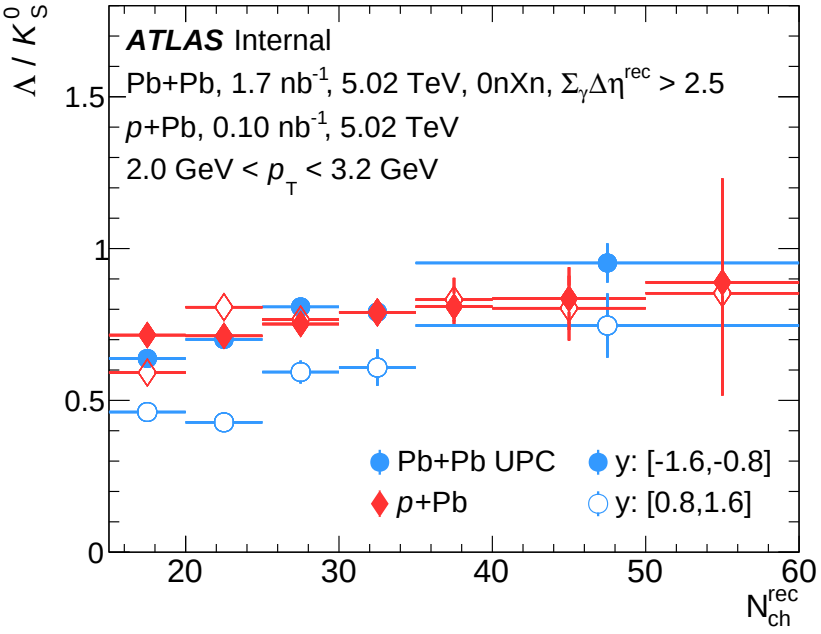

Figure 7.19: Shown are the ratio of Λ to K^0_S yield as a function of N^{rec}_{ch} for $0.8 < |y| < 1.6$ in the p_T region of baryon-to-meson enhancement, p_T: [2.0,3.2] GeV for Pb+Pb UPC and p+Pb collisions. Statistical uncertainties are shown as vertical lines. No systematic uncertainties are shown.

The baryon enhancement observed in Pb+Pb UPC, particularly in the most backward rapidity, might be attributed to the significant particle production in the Pb-going direction, $y < 0$. It is worth noting that, as established in Section 2.5.3, QGP signatures, including baryon-to-meson enhancement, are prominent in Pb+Pb collisions and diminish when moving towards small systems, such as p+Pb and pp. Similar to this trend, within Pb+Pb UPC, QGP-like signals are observed in the rapidity selection with the highest number of particles produced, then decrease when moving towards rapidity selections with a smaller number of particles produced. Detailed hydrodynamic model comparisons with the QGP equation of state are needed to confirm these conclusions.

7.2.3 Strangeness Enhancement

Strangeness enhancement, one of the earliest proposed QGP signatures, has been previously observed in various collision systems forming different QGP droplet sizes, including Pb+Pb, p+Pb and pp collisions [11], as discussed in Section 2.5.4. The strangeness enhancement is quantified via the ratio of the strange particle yield ($K^0_S, \Lambda, \Xi^-, \Omega^-$) to the pion yield and has been observed to be most enhanced for particles with the highest strange quark content, such as the Ω^-. In other words, the ratio of Ω^- to pions increases more steeply compared to other particles as a function of charged-particle multiplicity.

Figure 7.20 presents the ratio of V^0 yields to that for charged hadrons as a function of multiplicity in Pb+Pb UPC and p+Pb collisions. In both collision systems, the dependence of the ratio on multiplicity remains relatively constant within the presented multiplicity ranges. Strikingly, the magnitude of enhancement appears similar between Pb+Pb UPC and p+Pb collisions, suggesting that Pb+Pb UPC experience strong final-state effects and behave like a hadron-nucleus interaction. The mass ordering of the strangeness enhancement appears to be consistent with what has been reported in Pb+Pb, p+Pb, and pp collisions by the ALICE experimental collaboration at the LHC, as shown in Figure 2.25. Additionally, a rapidity dependence is observed in Pb+Pb UPC, with the strangeness ratios on the Pb-going side greater than those on the photon-going side, suggesting that the local density is driving the amount of QGP-like signals observed.

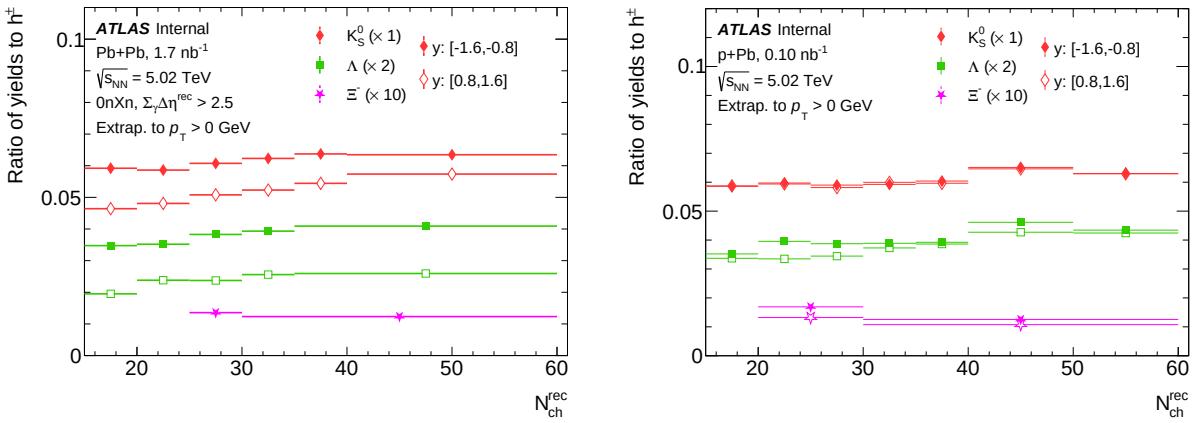

Figure 7.20: Shown are the ratio of V^0 yields to charged hadrons as a function of $N_{\mathrm{ch}}^{\mathrm{rec}}$ in in the y selection, $0.8 < |y| < 1.6$ for $p_{\mathrm{T}} > 0$ GeV. The closed markers show the Pb-going direction ($y < 0$), and the open markers show the proton-going direction ($y > 0$) in the case of p+Pb and γ-going direction ($y > 0$) in the case of Pb+Pb UPC. The left panels are for Pb+Pb UPC, and the right panels are for p+Pb collisions. Statistical and systematic uncertainties are yet to be determined.

Chapter 8

Conclusions

This dissertation includes two novel measurements in high-energy nuclear collisions using the 5.02 TeV Pb+Pb data collected in 2018 by the ATLAS detector at the CERN Large Hadron Collider. The first measurement, detailed in Chapter 5, presents the unidentified-charged-hadron yields in Pb+Pb Ultra-Peripheral Collisions (UPC), published as a preliminary result in Ref. [154]. The second measurement presents the identified-hadron yields, including K^0_S, Λ, and Ξ^-, as detailed in Chapter 6. These two measurements together delve into the characterization of photonuclear events and the investigation of the potential formation of tiny droplets of Quark-Gluon Plasma (QGP) in such collisions.

Theoretical modeling of UPC, *i.e.*, γ+A collisions, remains challenging due to the large variation in photon energy event-to-event, and the extreme asymmetry in particle production as a function of pseudorapidity. This thesis data provides key constraints by characterizing photonuclear collisions through a detailed analysis of charged hadron and identified particle yields as a function of pseudorapidity, transverse momentum, and event multiplicity.

There are numerous QGP signatures from heavy ion collisions. This thesis analysis looks into a suite of such signatures and finds hints of similar QGP-like behavior. Notable is that these QGP-like hints are consistently stronger in UPC events and specifically regions of pseudorapidity with larger particle production. The pronounced pseudorapidity asymmetry of these UPC events adds an intriguing dimension to observing these phenomena, reflecting the amount of QGP-like signals observed. Hydrodynamic model predictions have been successful in describing some features of

collisions, with more detailed comparisons to these data needed.

In the future, O+O collisions at the LHC will further measure QGP signatures in small collision systems, providing another opportunity to explore the limits of hydrodynamic modeling. Then the ATLAS detector is being upgraded and will have increased tracking coverage $|\eta| < 4.0$ for Run-4, which will enable exploring an even wider range of pseudorapidity asymmetry. These UPC collisions, also with increased statistics, will test the hydrodynamic model applicability by, for example, measuring the higher order anisotropic flow coefficients (v_4). Looking to the longer term future, additional theoretical efforts and experimental efforts from the Electron Ion Collider, where one has precise measure the virtuality of the colliding photon, will provide broader context for the experimental results presented in this thesis.

References

[1] Edward V. Shuryak, "Theory of Hadronic Plasma", Sov. Phys. JETP **47**, 212 (1978) (Cited on p. 1).

[2] Ulrich Heinz and Raimond Snellings, "Collective flow and viscosity in relativistic heavy-ion collisions", Ann. Rev. Nucl. Part. Sci. **63**, 123 (2013) (Cited on pp. 1, 5, 29, 85, 155).

[3] Paul Romatschke and Ulrike Romatschke, **Relativistic Fluid Dynamics In and Out of Equilibrium**, Cambridge Monographs on Mathematical Physics (Cambridge University Press, 2019), arXiv:1712.05815 [nucl-th] (Cited on p. 1).

[4] Nicolas Borghini, Phuong Mai Dinh, and Jean-Yves Ollitrault, "A New method for measuring azimuthal distributions in nucleus-nucleus collisions", Phys. Rev. C **63**, 054906 (2001) (Cited on p. 1).

[5] Johann Rafelski and R. Hagedorn, "From Hadron Gas to Quark Matter. 2.", in International Symposium on Statistical Mechanics of Quarks and Hadrons, CERN-TH-2969 (Oct, 1980) (Cited on p. 2).

[6] Eleazar Cuautle and Alejandro Ayala, "Strange Baryon to Meson Ratio", J. Phys. Conf. Ser. **509**, 012092 (2014) (Cited on p. 3).

[7] ATLAS Collaboration, "Observation of Associated Near-Side and Away-Side Long-Range Correlations in $\sqrt{s_{NN}}$=5.02 TeV Proton-Lead Collisions with the ATLAS Detector", Phys. Rev. Lett. **110**, 182302 (2013) (Cited on pp. 3, 28).

[8] Carlos A. Bertulani, Spencer R. Klein, and Joakim Nystrand, "Physics of ultra-peripheral nuclear collisions", Ann. Rev. Nucl. Part. Sci. **55**, 271 (2005) (Cited on pp. 4, 46, 48).

[9] Spencer R. Klein and Heikki Mäntysaari, "Imaging the nucleus with high-energy photons", Nature Rev. Phys. **1**, 662 (2019) (Cited on p. 4).

[10] ATLAS Collaboration, "Two-particle azimuthal correlations in photonuclear ultraperipheral Pb+Pb collisions at 5.02 TeV with ATLAS", Phys. Rev. C **104**, 014903 (2021) (Cited on pp. 5, 34, 56, 57, 59, 62, 85, 96, 100, 155, 192, 201).

[11] ALICE Collaboration, "Enhanced production of multi-strange hadrons in high-multiplicity proton-proton collisions", Nature Phys. **13**, 535 (2017) (Cited on pp. 5, 44, 45, 64, 155, 213).

[12] R. J. Fries, Berndt Muller, C. Nonaka, and S. A. Bass, "Hadronization in heavy ion collisions: Recombination and fragmentation of partons", Phys. Rev. Lett. **90**, 202303 (2003) (Cited on pp. 5, 64, 155).

[13] US Department of Energy, "DOE Explains...the Standard Model of Particle Physics", Office of Science (Cited on p. 7).

[14] R. L. Workman et al. (Particle Data Group), "Review of Particle Physics", PTEP **2022**, 083C01 (2022) (Cited on p. 9).

[15] C. Y. Wong, **Introduction to high-energy heavy ion collisions** (World Scientific, 1995) (Cited on pp. 10, 92).

[16] Florian Hebenstreit, "A space-time resolved view of the Schwinger effect", Frontiers of intense laser physics - KITP (2014) (Cited on p. 11).

[17] Siegfried Bethke, "Experimental tests of asymptotic freedom", Nucl. Phys. B Proc. Suppl. **54**, 314 (1997) (Cited on p. 12).

[18] Frank Geurts and Ralf-Arno Tripolt, "Electromagnetic probes: Theory and experiment", Prog. Part. Nucl. Phys. **128**, 104004 (2023) (Cited on p. 13).

[19] Y. Aoki, G. Endrodi, Z. Fodor, S. D. Katz, and K. K. Szabo, "The Order of the quantum chromodynamics transition predicted by the standard model of particle physics", Nature **443**, 675 (2006) (Cited on p. 14).

[20] Tanmoy Bhattacharya et al., "QCD Phase Transition with Chiral Quarks and Physical Quark Masses", Phys. Rev. Lett. **113**, 082001 (2014) (Cited on p. 14).

[21] K. Johnson, "The M.I.T. Bag Model", Acta Phys. Polon. B **6**, 865 (1975) (Cited on p. 17).

[22] Gergely Endrődi, "QCD phase diagram: overview of recent lattice results", J. Phys. Conf. Ser. **503**, 012009 (2014) (Cited on p. 19).

[23] HotQCD Collaboration, "The QCD equation of state", Nucl. Phys. A **931**, 867 (2014) (Cited on p. 19).

[24] Chun Shen, "The standard model for relativistic heavy-ion collisions and electromagnetic tomography", PhD thesis (Ohio State U., 2014) (Cited on p. 21).

[25] Michael L. Miller, Klaus Reygers, Stephen J. Sanders, and Peter Steinberg, "Glauber modeling in high energy nuclear collisions", Ann. Rev. Nucl. Part. Sci. **57**, 205 (2007) (Cited on pp. 21–24, 94).

[26] Sruthy Jyothi Das, Giuliano Giacalone, Pierre-Amaury Monard, and Jean-Yves Ollitrault, "Relating centrality to impact parameter in nucleus-nucleus collisions", Phys. Rev. C **97**, 014905 (2018) (Cited on p. 24).

[27] J. E. Parkkila, A. Onnerstad, and D. J. Kim, "Bayesian estimation of the specific shear and bulk viscosity of the quark-gluon plasma with additional flow harmonic observables", Phys. Rev. C **104**, 054904 (2021) (Cited on p. 26).

[28] P. Kovtun, Dan T. Son, and Andrei O. Starinets, "Viscosity in strongly interacting quantum field theories from black hole physics", Phys. Rev. Lett. **94**, 111601 (2005) (Cited on p. 26).

[29] Fred Cooper and Graham Frye, "Comment on the Single Particle Distribution in the Hydrodynamic and Statistical Thermodynamic Models of Multiparticle Production", Phys. Rev. D **10**, 186 (1974) (Cited on p. 27).

[30] PHENIX Collaboration, "Formation of dense partonic matter in relativistic nucleus-nucleus collisions at RHIC: Experimental evaluation by the PHENIX collaboration", Nucl. Phys. A **757**, 184 (2005) (Cited on p. 28).

[31] STAR Collaboration, "Experimental and theoretical challenges in the search for the quark gluon plasma: The STAR Collaboration's critical assessment of the evidence from RHIC collisions", Nucl. Phys. A **757**, 102 (2005) (Cited on p. 28).

[32] PHOBOS Collaboration, "The PHOBOS perspective on discoveries at RHIC", Nucl. Phys. A **757**, 28 (2005) (Cited on p. 28).

[33] BRAHMS Collaboration, "Quark gluon plasma and color glass condensate at RHIC? The Perspective from the BRAHMS experiment", Nucl. Phys. A **757**, 1 (2005) (Cited on p. 28).

[34] Berndt Muller, Jurgen Schukraft, and Boleslaw Wyslouch, "First Results from Pb+Pb collisions at the LHC", Ann. Rev. Nucl. Part. Sci. **62**, 361 (2012) (Cited on p. 28).

[35] CMS Collaboration, "Observation of Long-Range Near-Side Angular Correlations in Proton-Proton Collisions at the LHC", JHEP **09**, 091 (2010) (Cited on p. 28).

[36] PHENIX Collaboration, "Quadrupole Anisotropy in Dihadron Azimuthal Correlations in Central d+Au Collisions at $\sqrt{s_{NN}}$=200 GeV", Phys. Rev. Lett. **111**, 212301 (2013) (Cited on p. 28).

[37] ALICE Collaboration, "Long-range angular correlations on the near and away side in p-Pb collisions at $\sqrt{s_{NN}} = 5.02$ TeV", Phys. Lett. B **719**, 29 (2013) (Cited on p. 28).

[38] CMS Collaboration, "Observation of Long-Range Near-Side Angular Correlations in Proton-Lead Collisions at the LHC", Phys. Lett. B **718**, 795 (2013) (Cited on p. 28).

[39] Anthony Badea *et al.*, "Measurements of two-particle correlations in e^+e^- collisions at 91 GeV with ALEPH archived data", Phys. Rev. Lett. **123**, 212002 (2019) (Cited on pp. 28, 36).

[40] CMS Collaboration, **Observation of enhanced long-range elliptic anisotropies inside high-multiplicity jets in pp collisions at $\sqrt{s} = 13$ TeV**, (2023) arXiv:2312.17103 [hep-ex] (Cited on pp. 28, 36).

[41] Edwin Norbeck, Karel Šafařık, and Peter A. Steinberg, "Hard-Scattering Results in Heavy-Ion Collisions at the LHC", Ann. Rev. Nucl. Part. Sci. **64**, 383 (2014) (Cited on p. 29).

[42] Miklos Gyulassy, Ivan Vitev, Xin-Nian Wang, and Ben-Wei Zhang, **Jet quenching and radiative energy loss in dense nuclear matter**, (2004) arXiv:0302077 [nucl-th] (Cited on p. 29).

[43] Hannah Elfner and Berndt Müller, "The exploration of hot and dense nuclear matter: introduction to relativistic heavy-ion physics", J. Phys. G **50**, 103001 (2023) (Cited on p. 29).

[44] N. Herrmann, J. P. Wessels, and T. Wienold, "Collective flow in heavy ion collisions", Ann. Rev. Nucl. Part. Sci. **49**, 581 (1999) (Cited on p. 29).

[45] W. Reisdorf and H. G. Ritter, "Collective flow in heavy-ion collisions", Ann. Rev. Nucl. Part. Sci. **47**, 663 (1997) (Cited on p. 29).

[46] Jean-Yves Ollitrault, "Anisotropy as a signature of transverse collective flow", Phys. Rev. D **46**, 229 (1992) (Cited on p. 30).

[47] S. Voloshin and Y. Zhang, "Flow study in relativistic nuclear collisions by Fourier expansion of Azimuthal particle distributions", Z. Phys. C **70**, 665 (1996) (Cited on p. 30).

[48] B. Alver and G. Roland, "Collision geometry fluctuations and triangular flow in heavy-ion collisions", Phys. Rev. C **81**, 054905 (2010) (Cited on p. 31).

[49] CERNCOURIER, Going with the flow (Cited on p. 31).

[50] ATLAS Collaboration, "Measurement of the azimuthal anisotropy for charged particle production in $\sqrt{s_{NN}} = 2.76$ TeV lead-lead collisions with the ATLAS detector", Phys. Rev. C **86**, 014907 (2012) (Cited on p. 31).

[51] James L. Nagle and William A. Zajc, "Small System Collectivity in Relativistic Hadronic and Nuclear Collisions", Ann. Rev. Nucl. Part. Sci. **68**, 211 (2018) (Cited on p. 32).

[52] ATLAS Collaboration, "Measurement of the azimuthal anisotropy of charged particles produced in $\sqrt{s_{\mathrm{NN}}} = 5.02$ TeV Pb+Pb collisions with the ATLAS detector", Eur. Phys. J. C **78**, 997 (2018) (Cited on p. 32).

[53] ATLAS Collaboration, "Measurement of long-range pseudorapidity correlations and azimuthal harmonics in $\sqrt{s_{NN}} = 5.02$ TeV proton-lead collisions with the ATLAS detector", Phys. Rev. C **90**, 044906 (2014) (Cited on pp. 32, 34).

[54] ATLAS Collaboration, "Observation of Long-Range Elliptic Azimuthal Anisotropies in $\sqrt{s}$ = 13 and 2.76 TeV *pp* Collisions with the ATLAS Detector", Phys. Rev. Lett. **116**, 172301 (2016) (Cited on p. 32).

[55] Bjorn Schenke, Sangyong Jeon, and Charles Gale, "Higher flow harmonics from (3+1)D event-by-event viscous hydrodynamics", Phys. Rev. C **85**, 024901 (2012) (Cited on p. 34).

[56] CMS Collaboration, "Multiplicity and Transverse Momentum Dependence of Two- and Four-Particle Correlations in pPb and PbPb Collisions", Phys. Lett. B **724**, 213 (2013) (Cited on p. 34).

[57] CMS Collaboration, "Evidence for collectivity in pp collisions at the LHC", Phys. Lett. B **765**, 193 (2017) (Cited on pp. 34, 35).

[58] ALICE Collaboration, "Anisotropic flow of charged particles in Pb-Pb collisions at $\sqrt{s_{\mathrm{NN}}} =$ 5.02 TeV", Phys. Rev. Lett. **116**, 132302 (2016) (Cited on p. 34).

[59] Ryan D. Weller and Paul Romatschke, "One fluid to rule them all: viscous hydrodynamic description of event-by-event central p+p, p+Pb and Pb+Pb collisions at $\sqrt{s} = 5.02$ TeV", Phys. Lett. B **774**, 351 (2017) (Cited on pp. 34, 35).

[60] Chun Shen and Ulrich Heinz, "The road to precision: Extraction of the specific shear viscosity of the quark-gluon plasma", Nucl. Phys. News **25**, 6 (2015) (Cited on p. 34).

[61] Wenbin Zhao, Chun Shen, and Björn Schenke, "Collectivity in Ultraperipheral Pb+Pb Collisions at the Large Hadron Collider", Phys. Rev. Lett. **129**, 252302 (2022) (Cited on pp. 35, 58, 59, 61, 63, 64, 85, 86, 155, 201, 206).

[62] Yu-Chen Chen *et al.*, **Analysis note: two-particle correlation in e^+e^- collisions at 91-209 GeV with archived ALEPH data**, (2023) arXiv:2309.09874 [hep-ex] (Cited on pp. 35, 36).

[63] Wenbin Zhao, Zi-Wei Lin, and Xin-Nian Wang, **Collectivity inside high-multiplicity jets in high-energy proton-proton collisions**, (2024) arXiv:2401.13137 [hep-ph] (Cited on p. 36).

[64] Jean-Yves Ollitrault, "Flow systematics from SIS to SPS energies", Nucl. Phys. A **638**, 195 (1998) (Cited on p. 37).

[65] C. M. Hung and Edward V. Shuryak, "Equation of state, radial flow and freezeout in high-energy heavy ion collisions", Phys. Rev. C **57**, 1891 (1998) (Cited on p. 37).

[66] Kun Jiang *et al.*, "Onset of radial flow in p+p collisions", Phys. Rev. C **91**, 024910 (2015) (Cited on p. 37).

[67] ALICE Collaboration, "Centrality dependence of π, K, p production in Pb-Pb collisions at $\sqrt{s_{NN}} = 2.76$ TeV", Phys. Rev. C **88**, 044910 (2013) (Cited on pp. 37, 38).

[68] Ekkard Schnedermann, Josef Sollfrank, and Ulrich W. Heinz, "Thermal phenomenology of hadrons from 200-A/GeV S+S collisions", Phys. Rev. C **48**, 2462 (1993) (Cited on p. 38).

[69] STAR Collaboration, "Bulk Properties of the Medium Produced in Relativistic Heavy-Ion Collisions from the Beam Energy Scan Program", Phys. Rev. C **96**, 044904 (2017) (Cited on pp. 38, 39).

[70] **The ALICE experiment – A journey through QCD**, (2022) arXiv:2211.04384 [nucl-ex] (Cited on pp. 39, 40).

[71] ALICE Collaboration, "Strangeness production as a function of charged particle multiplicity in proton–proton collisions", Nucl. Phys. A **956**, 777 (2016) (Cited on pp. 39, 41, 42).

[72] Rainer J. Fries, Vincenzo Greco, and Paul Sorensen, "Coalescence Models For Hadron Formation From Quark Gluon Plasma", Ann. Rev. Nucl. Part. Sci. **58**, 177 (2008) (Cited on pp. 42, 207).

[73] Vincenzo Minissale, Francesco Scardina, and Vincenzo Greco, "Quark coalescence from RHIC to LHC", J. Phys. Conf. Ser. **636**, 012014 (2015) (Cited on pp. 42, 207).

[74] P. Koch, Berndt Muller, and Johann Rafelski, "Strangeness in Relativistic Heavy Ion Collisions", Phys. Rept. **142**, 167 (1986) (Cited on p. 43).

[75] WA97 Collaboration, "Strangeness enhancement at mid-rapidity in Pb Pb collisions at 158-A-GeV/c", Phys. Lett. B **449**, 401 (1999) (Cited on p. 43).

[76] A. J. Baltz, "The Physics of Ultraperipheral Collisions at the LHC", Phys. Rept. **458**, 1 (2008) (Cited on pp. 46, 60).

[77] Spencer R. Klein, "Ultra-peripheral collisions and hadronic structure", Nucl. Phys. A **967**, 249 (2017) (Cited on p. 46).

[78] Peter A. Steinberg, "Ultraperipheral Collisions at RHIC and the LHC", Nucl. Phys. A **1005**, 122007 (2021) (Cited on p. 46).

[79] Carlos A. Bertulani, "Ultra-peripheral nuclear collisions", J. Phys. Conf. Ser. **2619**, 012003 (2023) (Cited on pp. 46, 50, 55).

[80] Carlos A. Bertulani and Gerhard Baur, "Electromagnetic Processes in Relativistic Heavy Ion Collisions", Phys. Rept. **163**, 299 (1988) (Cited on p. 47).

[81] E. J. Williams, "Correlation of certain collision problems with radiation theory", Kong. Dan. Vid. Sel. Mat. Fys. Med. **13N4**, 1 (1935) (Cited on p. 47).

[82] C. F. von Weizsacker, "Radiation emitted in collisions of very fast electrons", Z. Phys. **88**, 612 (1934) (Cited on p. 47).

[83] **Measurement of high-mass dimuon pairs from ultraperipheral lead-lead collisions at $\sqrt{s_{\mathrm{NN}}} = 5.02$ TeV with the ATLAS detector at the LHC**, tech. rep., https://cds.cern.ch/record/2157689 (CERN, Geneva, 2016) (Cited on p. 50).

[84] ATLAS Collaboration, "Evidence for light-by-light scattering in heavy-ion collisions with the ATLAS detector at the LHC", Nature Phys. **13**, 852 (2017) (Cited on pp. 50–52).

[85] ATLAS Collaboration, "Observation of light-by-light scattering in ultraperipheral Pb+Pb collisions with the ATLAS detector", Phys. Rev. Lett. **123**, 052001 (2019) (Cited on p. 50).

[86] CMS Collaboration, "Evidence for light-by-light scattering and searches for axion-like particles in ultraperipheral PbPb collisions at $\sqrt{s_{\mathrm{NN}}} = 5.02$ TeV", Phys. Lett. B **797**, 134826 (2019) (Cited on p. 51).

[87] G. Baur and C. A. Bertulani, "$\gamma\gamma$ Physics With Peripheral Relativistic Heavy Ion Collisions", Z. Phys. A **330**, 77 (1988) (Cited on p. 51).

[88] Mariola Kłusek-Gawenda, "Importance of mesons in light-by-light scattering in ultraperipheral lead-lead collisions at the LHC", EPJ Web Conf. **199**, 05004 (2019) (Cited on p. 52).

[89] V. P. Goncalves and W. K. Sauter, "Exclusive axionlike particle production by gluon – induced interactions in hadronic collisions", Phys. Lett. B **811**, 135981 (2020) (Cited on p. 52).

[90] V. P. Goncalves, D. E. Martins, and M. S. Rangel, "Searching for axionlike particles with low masses in pPb and PbPb collisions", Eur. Phys. J. C **81**, 522 (2021) (Cited on p. 52).

[91] Martin Greiner, Mario Vidovic, Christian Hofmann, Andreas Schafer, and G. Soff, "Deduction of the in-medium gluon distribution from photon - gluon fusion processes in peripheral ultrarelativistic heavy ion collisions", Phys. Rev. C **51**, 911 (1995) (Cited on p. 52).

[92] Spencer R. Klein, Joakim Nystrand, and Ramona Vogt, "Photoproduction of top in peripheral heavy ion collisions", Eur. Phys. J. C **21**, 563 (2001) (Cited on p. 52).

[93] Benjamin Jacob Gilbert, Aaron Angerami, and Brian Andrew Cole, **Photonuclear Dijet Production in Ultra-Peripheral Pb+Pb Collisions**, tech. rep., https://cds.cern.ch/record/2886390 (CERN, Geneva, 2024) (Cited on pp. 52, 56, 100).

[94] Jon Pumplin, **Diffractive photoproduction of Z0**, (1996) arXiv:hep-ph/9612356 (Cited on p. 52).

[95] STAR Collaboration, "Coherent rho0 production in ultraperipheral heavy ion collisions", Phys. Rev. Lett. **89**, 272302 (2002) (Cited on p. 52).

[96] G. Baur and C. A. Bertulani, "Multiple electromagnetic excitation of giant dipole phonons in relativistic heavy ion collisions", Phys. Lett. B **174**, 23 (1986) (Cited on p. 52).

[97] G. Baur and C. A. Bertulani, "Multistep Fragmentation of Heavy Ions in Peripheral Collisions at Relativistic Energies", Phys. Rev. C **34**, 1654 (1986) (Cited on p. 52).

[98] J. Ritman et al., "First observation of the Coulomb-excited double giant dipole resonance in Pb-208 via double-gamma decay", Phys. Rev. Lett. **70**, 533 (1993) (Cited on p. 53).

[99] T. H. Bauer, R. D. Spital, D. R. Yennie, and F. M. Pipkin, "The Hadronic Properties of the Photon in High-Energy Interactions", Rev. Mod. Phys. **50**, 261 (1978) (Cited on p. 53).

[100] J. A. Crittenden, **Exclusive production of neutral vector mesons at the electron - proton collider HERA**, (1997) arXiv:hep-ex/9704009 (Cited on p. 53).

[101] V. P. Goncalves and C. A. Bertulani, "Peripheral heavy ion collisions as a probe of the nuclear gluon distribution", Phys. Rev. C **65**, 054905 (2002) (Cited on p. 54).

[102] Nestor Armesto, "Nuclear shadowing", J. Phys. G **32**, R367 (2006) (Cited on p. 54).

[103] LHCb Collaboration, "Central exclusive production of J/ψ and $\psi(2S)$ mesons in pp collisions at $\sqrt{s} = 13$ TeV", JHEP **10**, 167 (2018) (Cited on p. 56).

[104] H1 Collaboration, "Elastic and Proton-Dissociative Photoproduction of J/psi Mesons at HERA", Eur. Phys. J. C **73**, 2466 (2013) (Cited on p. 56).

[105] ZEUS Collaboration, "Exclusive photoproduction of J/psi mesons at HERA", Eur. Phys. J. C **24**, 345 (2002) (Cited on p. 56).

[106] ALICE Collaboration, "Coherent J/ψ photoproduction in ultra-peripheral Pb-Pb collisions at $\sqrt{s_{NN}} = 2.76$ TeV", Phys. Lett. B **718**, 1273 (2013) (Cited on p. 56).

[107] ATLAS Collaboration, "Rapidity gap cross sections measured with the ATLAS detector in pp collisions at $\sqrt{s_{NN}} = 7$ GeV", Eur. Phys. J. C **72**, 1926 (2012) (Cited on pp. 57, 98).

[108] Fábio S. Bemfica, Marcelo M. Disconzi, Vu Hoang, Jorge Noronha, and Maria Radosz, "Nonlinear Constraints on Relativistic Fluids Far from Equilibrium", Phys. Rev. Lett. **126**, 222301 (2021) (Cited on p. 58).

[109] Cheng Chiu and Chun Shen, "Exploring theoretical uncertainties in the hydrodynamic description of relativistic heavy-ion collisions", Phys. Rev. C **103**, 064901 (2021) (Cited on p. 58).

[110] Piotr Bozek, Adam Bzdak, and Guo-Liang Ma, "Rapidity dependence of elliptic and triangular flow in proton–nucleus collisions from collective dynamics", Phys. Lett. B **748**, 301 (2015) (Cited on p. 58).

[111] Weiyao Ke, J. Scott Moreland, Jonah E. Bernhard, and Steffen A. Bass, "Constraints on rapidity-dependent initial conditions from charged particle pseudorapidity densities and two-particle correlations", Phys. Rev. C **96**, 044912 (2017) (Cited on p. 58).

[112] Chun Shen and Björn Schenke, "Longitudinal dynamics and particle production in relativistic nuclear collisions", Phys. Rev. C **105**, 064905 (2022) (Cited on p. 60).

[113] Yu Shi, Lei Wang, Shu-Yi Wei, Bo-Wen Xiao, and Liang Zheng, "Exploring collective phenomena at the electron-ion collider", Phys. Rev. D **103**, 054017 (2021) (Cited on pp. 60–62, 85).

[114] Kevin Dusling and Raju Venugopalan, "Evidence for BFKL and saturation dynamics from dihadron spectra at the LHC", Phys. Rev. D **87**, 051502 (2013) (Cited on p. 61).

[115] ATLAS Collaboration, "Measurements of long-range azimuthal anisotropies and associated Fourier coefficients for pp collisions at $\sqrt{s} = 5.02$ and 13 TeV and p+Pb collisions at $\sqrt{s_{\mathrm{NN}}} = 5.02$ TeV with the ATLAS detector", Phys. Rev. C **96**, 024908 (2017) (Cited on pp. 62, 96).

[116] ALICE Collaboration, "Multiplicity Dependence of Pion, Kaon, Proton and Lambda Production in p-Pb Collisions at $\sqrt{s_{NN}} = 5.02$ TeV", Phys. Lett. B **728**, 25 (2014) (Cited on pp. 63, 205).

[117] Lyndon Evans and Philip Bryant, "LHC Machine", JINST **3**, S08001 (2008) (Cited on p. 65).

[118] **LEP design report**, Report, https://cds.cern.ch/record/102083, Copies shelved as reports in LEP, PS and SPS libraries (CERN, Geneva, 1984) (Cited on p. 65).

[119] ATLAS Collaboration, "Observation of a new particle in the search for the Standard Model Higgs boson with the ATLAS detector at the LHC", Phys. Lett. B **716**, 1 (2012) (Cited on p. 65).

[120] CMS Collaboration, "Observation of a New Boson at a Mass of 125 GeV with the CMS Experiment at the LHC", Phys. Lett. B **716**, 30 (2012) (Cited on p. 65).

[121] Esma Mobs, "The CERN accelerator complex in 2019. Complexe des accélérateurs du CERN en 2019", General Photo (2019) (Cited on p. 66).

[122] Jean-Luc Caron, "Magnetic field induced by the LHC dipole's superconducting coils.", AC Collection. Legacy of AC. Pictures from 1992 to 2002. (1998) (Cited on p. 68).

[123] Werner Herr and B Muratori, "Concept of luminosity", 10.5170/CERN-2006-002.361 (2006) (Cited on p. 68).

[124] ATLAS Collaboration, "The ATLAS Experiment at the CERN Large Hadron Collider", JINST **3**, S08003 (2008) (Cited on pp. 70, 73, 74, 78, 81, 82).

[125] Joao Pequenao and Paul Schaffner, "How ATLAS detects particles: diagram of particle paths in the detector", https://cds.cern.ch/record/1505342 (2013) (Cited on p. 71).

[126] ATLAS Collaboration, "ATLAS Insertable B-Layer Technical Design Report", https://cds.cern.ch/record/1291633 (2010) (Cited on p. 75).

[127] ATLAS Collaboration, "Performance of the ATLAS Track Reconstruction Algorithms in Dense Environments in LHC Run 2", Eur. Phys. J. C **77**, 673 (2017) (Cited on p. 75).

[128] R. Fruhwirth, "Application of Kalman filtering to track and vertex fitting", Nucl. Instrum. Meth. A **262**, 444 (1987) (Cited on p. 76).

[129] ATLAS Collaboration, "Reconstruction of primary vertices at the ATLAS experiment in Run 1 proton–proton collisions at the LHC", Eur. Phys. J. C **77**, 332 (2017) (Cited on p. 77).

[130] ATLAS Collaboration, "Topological cell clustering in the ATLAS calorimeters and its performance in LHC Run 1", Eur. Phys. J. C **77**, 490 (2017) (Cited on p. 79).

[131] Peter Jenni, **ATLAS forward detectors for measurement of elastic scattering and luminosity**, tech. rep., https://cds.cern.ch/record/1095847 (ATLAS-TDR-018, 2008) (Cited on p. 80).

[132] ATLAS Collaboration, "Performance of the ATLAS Zero Degree Calorimeter", in 2013 IEEE Nuclear Science Symposium and Medical Imaging Conference and Workshop on Room-Temperature Semiconductor Detectors (2013) (Cited on p. 80).

[133] ATLAS Collaboration, **Trigger menu in 2018**, tech. rep., https://cds.cern.ch/record/2693402 (CERN, Geneva, 2019) (Cited on pp. 82, 84).

[134] ATLAS Collaboration, "The ATLAS Data Acquisition System: from Run 1 to Run 2", Nucl. Part. Phys. Proc. **273-275**, 939 (2016) (Cited on p. 83).

[135] R. Engel, "Photoproduction within the two component Dual Parton Model: Amplitudes and cross sections", Z. Phys. C **66**, 203 (1995) (Cited on pp. 86, 92, 227).

[136] Stefan Roesler, Ralph Engel, and Johannes Ranft, "The Monte Carlo Event Generator DPMJET-III", in International Conference on Advanced Monte Carlo for Radiation Physics (2000), pp. 1033–1038 (Cited on pp. 86, 92, 93, 227).

[137] ATLAS Collaboration, **Two-particle azimuthal correlations in photo-nuclear ultra-peripheral Pb+Pb collisions at** 5.02 **TeV with ATLAS**, ATLAS-CONF-2019-022, https://cds.cern.ch/record/2679473, 2019 (Cited on pp. 86, 95, 98, 100, 156, 157).

[138] Spencer R. Klein, Joakim Nystrand, Janet Seger, Yuri Gorbunov, and Joey Butterworth, "STARlight: A Monte Carlo simulation program for ultra-peripheral collisions of relativistic ions", Comput. Phys. Commun. **212**, 258 (2017) (Cited on p. 92).

[139] Z. Koba and Holger Bech Nielsen, "Reaction amplitude for n mesons: A Generalization of the Veneziano-Bardakci-Ruegg-Virasora model", Nucl. Phys. B **10**, 633 (1969) (Cited on p. 92).

[140] Xin-Nian Wang and Miklos Gyulassy, "HIJING: A Monte Carlo model for multiple jet production in pp, pA and AA collisions", Phys. Rev. D **44**, 3501 (1991) (Cited on p. 94).

[141] Miklos Gyulassy and Xin-Nian Wang, "HIJING 1.0: A Monte Carlo program for parton and particle production in high-energy hadronic and nuclear collisions", Comput. Phys. Commun. **83**, 307 (1994) (Cited on p. 95).

[142] S. Agostinelli et al., "GEANT4 – a simulation toolkit", Nucl. Instrum. Meth. A **506**, 250 (2003) (Cited on p. 95).

[143] ATLAS Collaboration, "Measurement of the Sensitivity of Two-Particle Correlations in pp Collisions to the Presence of Hard Scatterings", Phys. Rev. Lett. **131**, 162301 (2023) (Cited on p. 96).

[144] ATLAS Collaboration, "Measurement of long-range two-particle azimuthal correlations in Z-boson tagged pp collisions at $\sqrt{s}$=8 and 13 TeV", Eur. Phys. J. C **80**, 64 (2020) (Cited on p. 96).

[145] ATLAS Collaboration, "Measurement of forward-backward multiplicity correlations in lead-lead, proton-lead, and proton-proton collisions with the ATLAS detector", Phys. Rev. C **95**, 064914 (2017) (Cited on p. 96).

[146] Blair Daniel Seidlitz, Qipeng Hu, Dennis Perepelitsa, James Lawrence Nagle, Aaron Angerami, and Kurt Keys Hill, **Supporting note for two particle azimuthal correlation analysis in UPC events with ATLAS**, tech. rep., https://cds.cern.ch/record/2668489 (CERN, Geneva, 2019) (Cited on pp. 100, 101, 127).

[147] ATLAS Collaboration, **Modelling of Track Reconstruction Inside Jets with the 2016 ATLAS $\sqrt{s} = 13$ TeV pp Dataset**, ATL-PHYS-PUB-2017-016, https://cds.cern.ch/record/2275639, 2017 (Cited on pp. 112, 165).

[148] Petr Balek and Alexander Milov, **Supporting note for the measurement of the charged hadron spectra in heavy-ion collisions at $\sqrt{s_{NN}} = 5.02$ TeV with the ATLAS detector at the LHC**, ATL-COM-PHYS-2019-1424, https://cds.cern.ch/record/2702964 (2019) (Cited on p. 118).

[149] ATLAS Collaboration, "Charged-particle multiplicities in pp interactions measured with the ATLAS detector at the LHC", New J. Phys. **13**, 053033 (2011) (Cited on p. 119).

[150] M. Biyajima, T. Mizoguchi, N. Nakajima, N. Suzuki, and G. Wilk, "Modified Hagedorn formula including temperature fluctuation - Estimation of temperatures at RHIC experiments -", Eur. Phys. J. C **48**, 597 (2006) (Cited on p. 122).

[151] Cheuk-Yin Wong and Grzegorz Wilk, "Tsallis Fits to p_T Spectra for pp Collisions at LHC", Acta Phys. Polon. B **43**, 2047 (2012) (Cited on p. 122).

[152] Constantino Tsallis, "Possible Generalization of Boltzmann-Gibbs Statistics", J. Statist. Phys. **52**, 479 (1988) (Cited on p. 122).

[153] ATLAS Collaboration, "Early Inner Detector Tracking Performance in the 2015 Data at $\sqrt{s} = 13$ TeV", https://cds.cern.ch/record/2110140 (2015) (Cited on p. 140).

[154] ATLAS Collaboration, "Charged-hadron yield measurements in photo-nuclear collisions using 5.02 TeV Pb+Pb data with ATLAS", https://cds.cern.ch/record/2871729 (Cited on pp. 155, 158, 215).

[155] ATLAS Collaboration, "K_s^0 and Λ production in pp interactions at $\sqrt{s}$=0.9 and 7 TeV measured with the ATLAS detector at the LHC", Phys. Rev. D **85**, 012001 (2012) (Cited on p. 162).

[156] Andreas Hocker et al. (TMVA), **TMVA - Toolkit for Multivariate Data Analysis**, (2007) arXiv:physics/0703039 (Cited on p. 169).

[157] ATLAS Collaboration, "Transverse momentum, rapidity, and centrality dependence of inclusive charged-particle production in $\sqrt{s_{NN}} = 5.02$ TeV p+Pb collisions measured by the ATLAS experiment", Phys. Lett. B **763**, 313 (2016) (Cited on p. 193).

[158] ALICE Collaboration, "K_S^0 and Λ Production in Pb-Pb Collisions at $\sqrt{s_{NN}}$=2.76 TeV", Phys. Rev. Lett. **111**, 222301 (2013) (Cited on p. 207).

[159] T. Adye, "Unfolding algorithms and tests using RooUnfold", physics.data-an, 313 (2011) (Cited on p. 246).

Appendix A

Measurement of Charged Hadrons Production

A.1 Monte Carlo DPMJET-III Comparisons

The DPMJET-III Monte Carlo [135, 136] is used to model various UPC processes and is compared to experimental data in this note. In this Appendix, we include specific calculations from DPMJET-III with kinematics beyond what is measured with in ATLAS for reference.

In this Section we detail data to theory comparisons of the Pb+Pb UPC with the DPMJET-III Monte Carlo. The DPMJET-III model is detailed in Section 5.1.3.1. We highlight here that the DPMJET-III generator results are run through the ATLAS reconstruction and utilizing the identical reconstructed-level $N_{\mathrm{ch}}^{\mathrm{rec}}$ and $\sum_{\gamma} \Delta\eta^{\mathrm{rec}}$ selection criteria as with experimental data. However, DPMJET-III does not model the detailed nuclear breakup and hence the ZDC selections are not matched.

Figures A.1 and A.2 show the DPMJET-III calculations compared to the experimental results in Pb+Pb UPC for $N_{\mathrm{ch}}^{\mathrm{rec}}$ = 25-60 for the yields as a function of p_{T} and η, respectively. DPMJET-III over-predicts the yield at forward rapidity, though with a reasonable description of the steeply falling p_{T} distribution. At backward rapidity, DPMJET-III slightly under-predicts the yield and with a significant under-estimate of the high p_{T} yields.

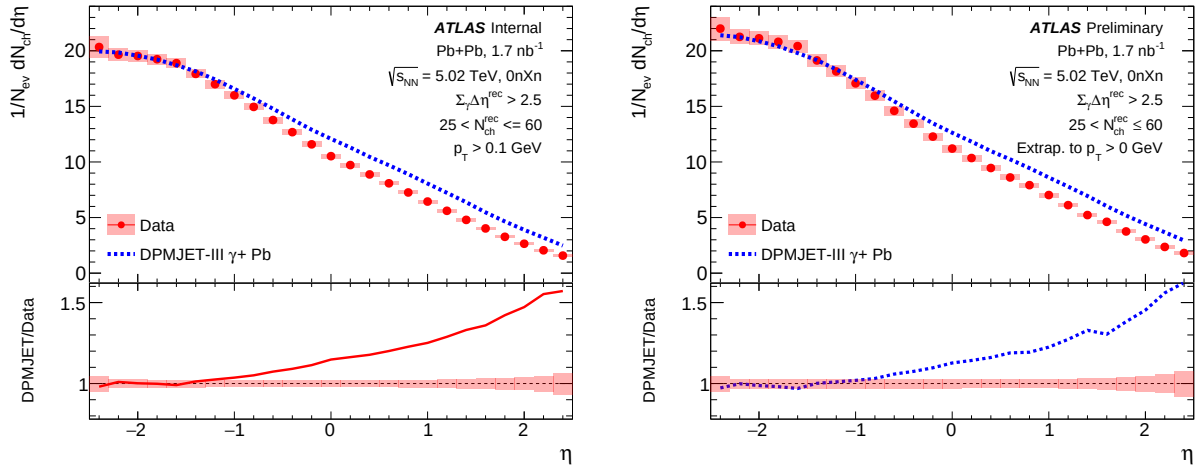

Figure A.1: Shown are the charged-hadron yields as a function of η in Pb+Pb UPC data and DPMJET-III γA generator results for $p_{\mathrm{T}} > 0.1$ GeV (left panel) and $p_{\mathrm{T}} > 0$ GeV (right panel). The bottom panels show the ratio of DPMJET-III γ+Pb to data.

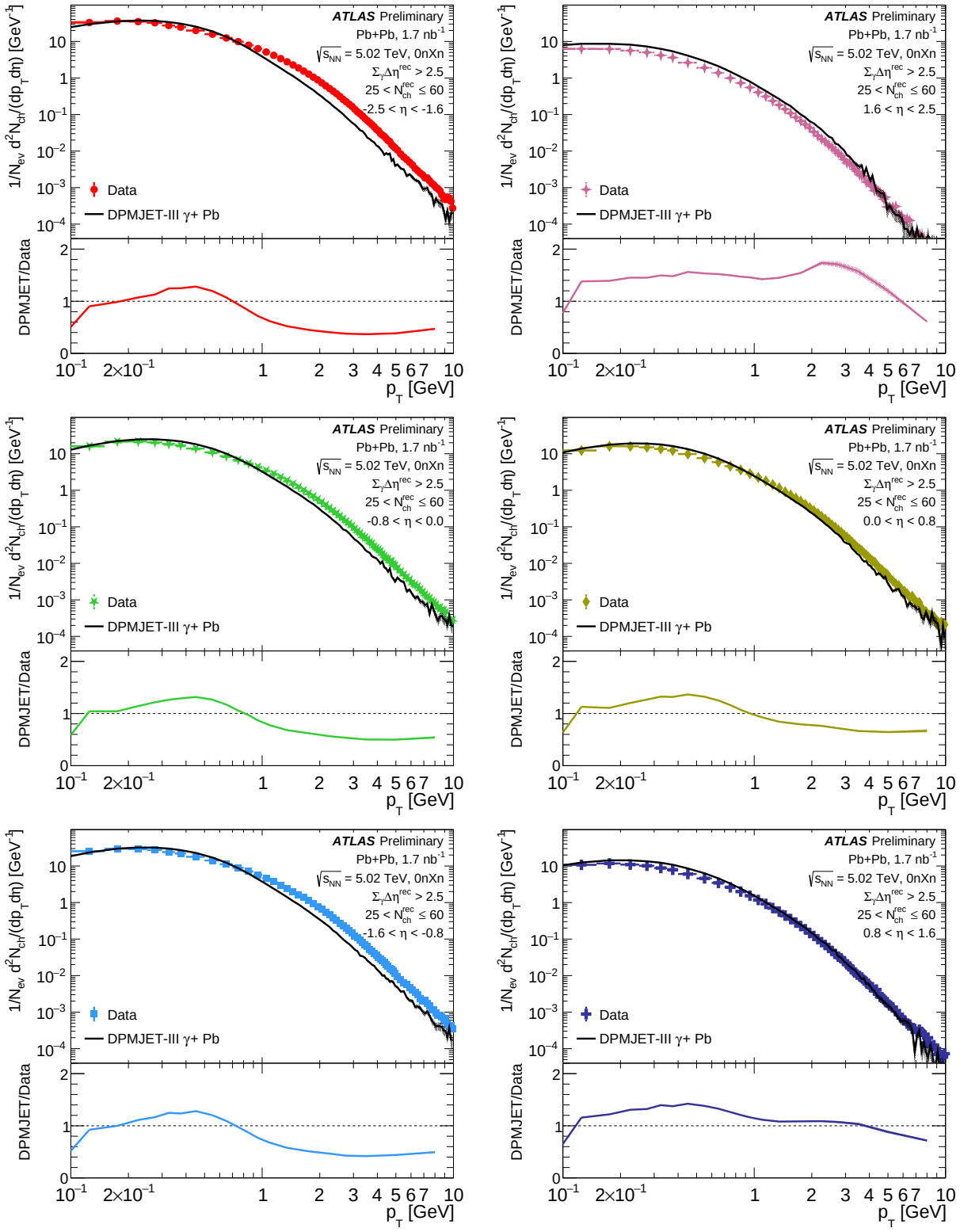

Figure A.2: Shown are the charged-hadron yields as a function of p_T in three different η slices in Pb+Pb UPC data and DPMJET-III γA Monte Carlo. The bottom panels show the ratio of DPMJET-III γ+Pb to data.

Examining the comparison more differentially in $N_{\mathrm{ch}}^{\mathrm{rec}}$, Figure A.3 shows four specific $N_{\mathrm{ch}}^{\mathrm{rec}}$ bins with comparison to DPMJET-III calculations. The $\mathrm{d}N_{\mathrm{ch}}/\mathrm{d}\eta$ distribution in DPMJET-III gives a reasonable description of the particle yield at backward rapidity, while consistently over-predicting the yield at forward rapidity in all $N_{\mathrm{ch}}^{\mathrm{rec}}$ selections.

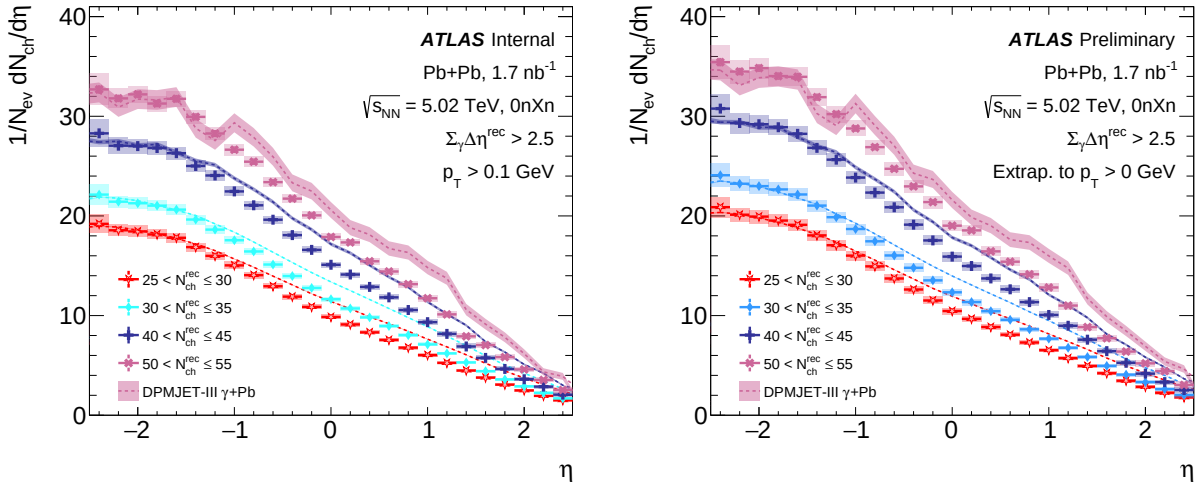

Figure A.3: Shown are the charged-hadron yields as a function of η in different $N_{\mathrm{ch}}^{\mathrm{rec}}$ bins in Pb+Pb UPC collisions and DPMJET-III γA Monte Carlo. The left panel shows the result for $p_{\mathrm{T}} > 0.1$ GeV and the right panel shows the extrapolated result, $p_{\mathrm{T}} > 0$ GeV. Vertical lines are statistical uncertainties and open boxes are systematic uncertainties.

Figure A.4 shows $\langle\eta\rangle$ as a function of $N_{\mathrm{ch}}^{\mathrm{rec}}$ in both UPC data and the DPMJET-III model. A constant difference in $\langle\eta\rangle$ is observed between UPC data and DPMJET-III model. The DPMJET-III over-prediction of the yield at forward-rapidity leads to a smaller rapidity shift that seen in data.

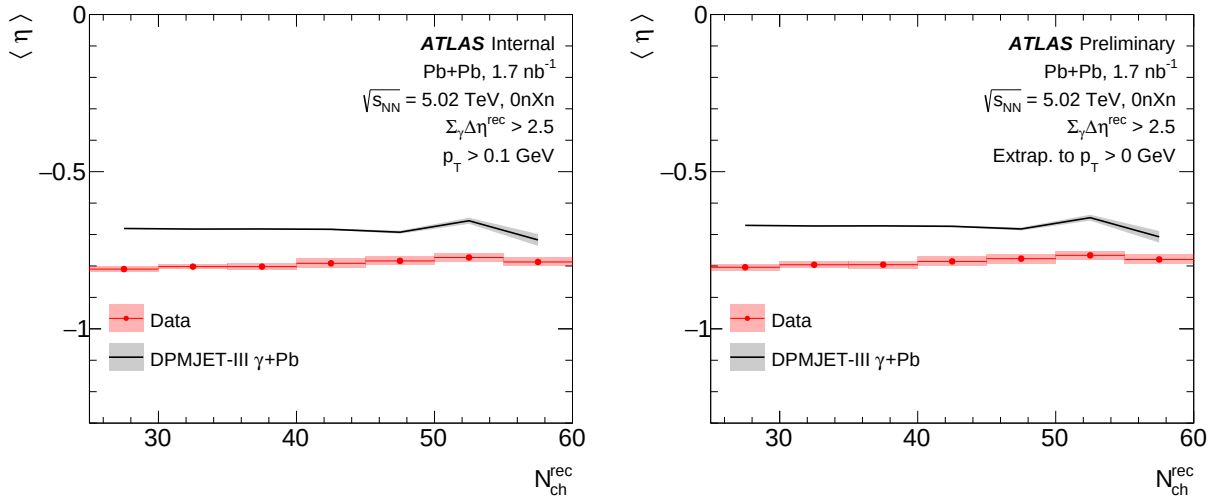

Figure A.4: Shown are the calculated $\langle\eta\rangle$ values within the window $-2.5 < \eta < +2.5$ of charged-hadron yields as a function of $N_{\mathrm{ch}}^{\mathrm{rec}}$ in Pb+Pb UPC collisions and DPMJET-III γA Monte Carlo. The left panel shows the result for $p_{\mathrm{T}} > 0.1$ GeV and the right panel shows the extrapolated result, $p_{\mathrm{T}} > 0$ GeV.

Figure A.5 shows the calculated $\langle p_{\mathrm{T}}\rangle$ for $p_{\mathrm{T}} > 0.1$ GeV in the top panels and $\langle p_{\mathrm{T}}\rangle$ for $p_{\mathrm{T}} > 0$ GeV in the bottom panels as a function of $N_{\mathrm{ch}}^{\mathrm{rec}}$ in two η selections of interest, [-1.6,-0.8] and [0.8,1.6], in Pb+Pb UPC collisions. DPMJET-III provides an excellent description of the $\langle p_{\mathrm{T}}\rangle$ at forward rapidity, despite over-predicting the yield in this region, and significantly under-predicts the $\langle p_{\mathrm{T}}\rangle$ at backward rapidity, despite describing the yield in this region.

We highlight that the typical UPC photon energy is lower than the individual nucleon energy in the opposing Pb nucleus, and hence the rapidity distribution is shifted towards the Pb-going direction, i.e., backward rapidity. However, for higher energy photons, one expects a smaller rapidity shift and hence the $\langle\eta\rangle$ value increases towards zero. Thus, one possibility is a mis-modeling of the photon energy distribution at input to DPMJET-III. A detailed study of this mis-modeling by reweighing photon energy distribution in DPMJET-III is discussed in the next section.

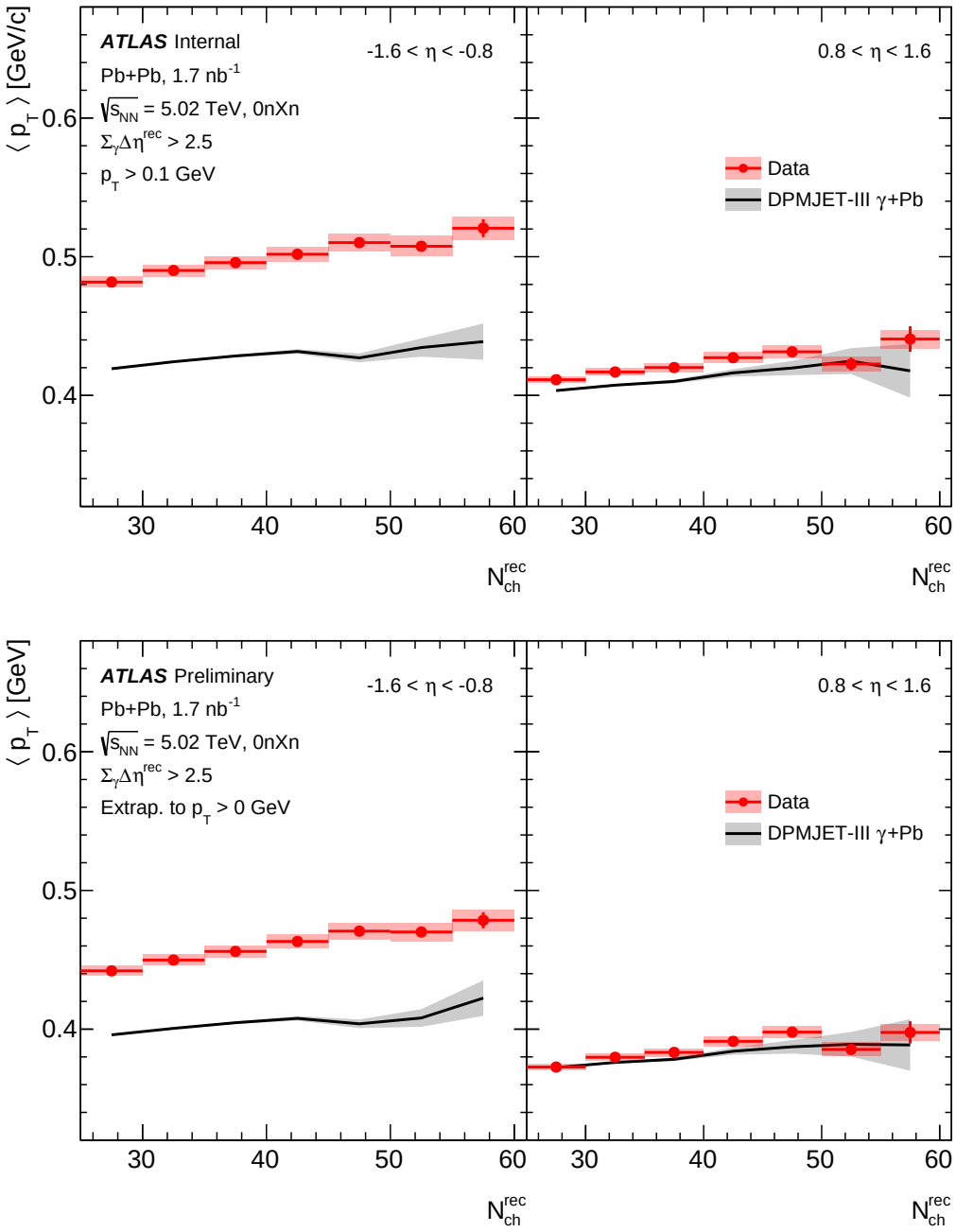

Figure A.5: Shown are the $\langle p_{\mathrm{T}} \rangle$ of charged-hadron yields as a function of $N_{\mathrm{ch}}^{\mathrm{rec}}$ in Pb+Pb UPC collisions in two different η slices, [-1.6,-0.8] (left) and [0.8,1.6] (right). Also shown are DPMJET-III generator results are run through the ATLAS reconstruction and utilizing the identical $N_{\mathrm{ch}}^{\mathrm{rec}}$ and $\sum_{\gamma} \Delta\eta^{\mathrm{rec}}$ selection criteria as with experimental data. The top panel shows the result for p_{T} > 0.1 GeV and the bottom panel shows the extrapolated result, $p_{\mathrm{T}} > 0$ GeV.

A.2 Reweighing Photon-Energy Distribution in DPMJET-III

In order to further examine the relationship between particle production and photon energy, Figure A.6 (left) shows the photon energy distribution in the DPMJET-III model with different $N_{\mathrm{ch}}^{\mathrm{rec}}$ selections. A very large number of events have extremely low E_γ ($E_\gamma < 10$ GeV) for the lowest $N_{\mathrm{ch}}^{\mathrm{rec}}$ selection (which is below the range used in this analysis). Figure A.6 (right) shows the correlation between photon energy and $N_{\mathrm{ch}}^{\mathrm{rec}}$ in DPMJET-III events. Events with larger $N_{\mathrm{ch}}^{\mathrm{rec}}$ select cases where the emitted photon has larger energy. The figure also presents $W_{\gamma\mathrm{A}}$, the effective center-of-mass energy of the photon-nucleus system (per nucleon), in a secondary axis to highlight the energy-dependence of the multiplicities.

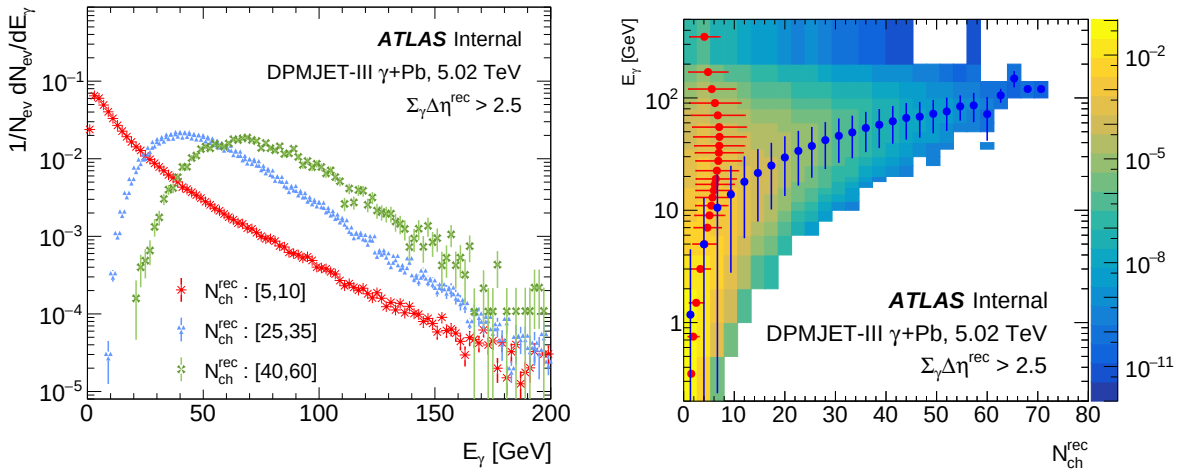

Figure A.6: (left) Truth photon energy distribution from the Monte Carlo model DPMJET-III. The DPMJET-III results are shown with three selections on $N_{\mathrm{ch}}^{\mathrm{rec}}$. (right) Correlation between photon energy and $N_{\mathrm{ch}}^{\mathrm{rec}}$ in DPMJET-III. The blue points represent the mean photon energy value in each $N_{\mathrm{ch}}^{\mathrm{rec}}$ bin and the red points represent the mean $N_{\mathrm{ch}}^{\mathrm{rec}}$ in each E_γ bin. The vertical/horizontal error bars represent the standard deviation. Additionally, $W_{\gamma A}$ is presented in the right y-axis.

A possible explanation for the difference observed between DPMJET-III and Pb+Pb UPC data is the mis-modeling of the photon energy distribution coupled into DPMJET-III. Figure A.7 shows the DPMJET-III truth photon energy distribution for events with the generator level $\sum_\gamma \Delta\eta^{\mathrm{rec}} > 2.5$ selection and no selection on $N_{\mathrm{ch}}^{\mathrm{rec}}$. Additionally, two re-weightings of the photon energy distribution are shown, referred to as "higher" and "lower", that increase (decrease) the

relative contribution of high-energy photons. These re-weightings are not motivated for example by expected uncertainties in the STARLIGHT flux calculation and rather are selected as extremes just to test the impact on the $\langle\eta\rangle$ and $\langle p_{\mathrm{T}}\rangle$.

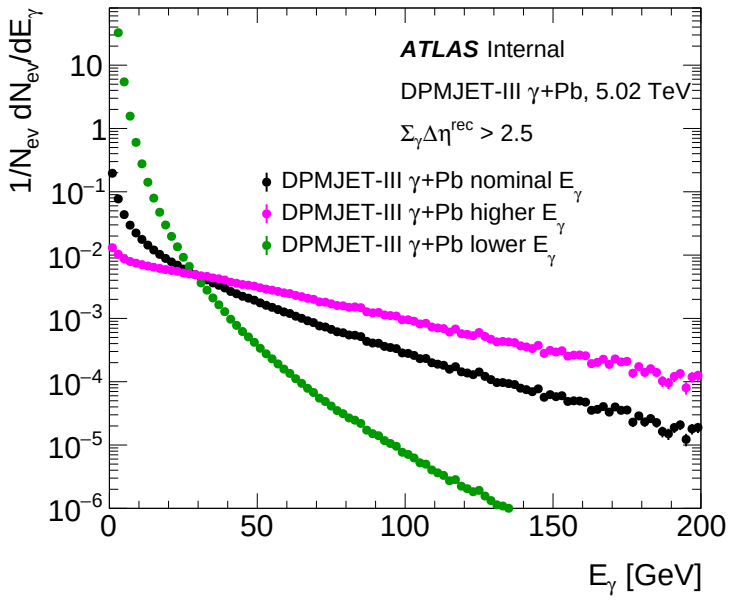

Figure A.7: Shown are the DPMJET-III truth photon energy distribution for events with the generator level $\sum_\gamma \Delta\eta^{\mathrm{rec}} > 2.5$ selection and no selection on $N_{\mathrm{ch}}^{\mathrm{rec}}$. Additionally, two re-weightings of the photon energy distribution are shown, referred to as "higher" and "lower", that increase (decrease) the relative contribution of high-energy photons.

Any change in the photon energy distribution shifts the particle production in pseudorapidity. The typical UPC photon energy is lower than the individual nucleon energy in the opposing Pb nucleus, and hence the rapidity distribution is shifted towards the Pb-going direction, i.e., backward rapidity. However, for higher energy photons, one expects a smaller rapidity shift and hence the $\langle\eta\rangle$ value increases towards zero. The change in photon energy concordantly shifts the $\sum_\gamma \Delta\eta^{\mathrm{rec}}$ distribution too.

Figure A.8 and A.9 show the $\sum_\gamma \Delta\eta^{\mathrm{rec}}$ distribution for $25 < N_{\mathrm{ch}}^{\mathrm{rec}} \leq 60$ and $\langle\eta\rangle$ as a function of $N_{\mathrm{ch}}^{\mathrm{rec}}$ for each of the three photon energy distributions respectively. The distribution with more low-energy photons, shown by the green lines, yields $\sum_\gamma \Delta\eta^{\mathrm{rec}}$ distribution and $\langle\eta\rangle$ in closer agreement with data. Conversely, the distribution with more high-energy photons, shown by the magenta

lines, yields $\sum_\gamma \Delta\eta^{\rm rec}$ distribution and $\langle\eta\rangle$ results in greater disagreement with Pb+Pb UPC data.

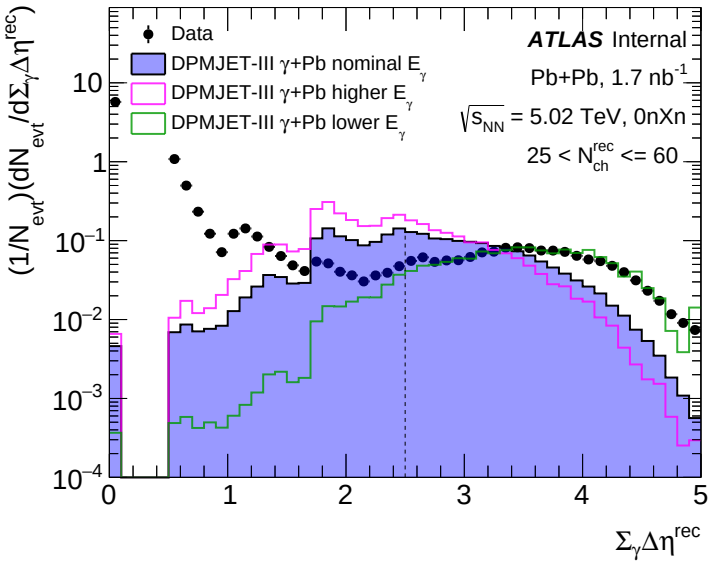

Figure A.8: Shown is the $\sum_\gamma \Delta\eta^{\rm rec}$ distribution for data events corresponding to $N_{\rm ch}^{\rm rec}$ = 25-60. Also, shown are the results from reconstructed event generated by DPMJET-III not corrected for detector effects utilizing the identical $N_{\rm ch}^{\rm rec}$ and $\sum_\gamma \Delta\eta^{\rm rec}$ selection criteria as with experimental data for the nominal DPMJET-III and the two variations in the photon energy distribution, i.e., "higher" and "lower". The black dashed line corresponds to the $\sum_\gamma \Delta\eta^{\rm rec}$ selection cut.

Figure A.10 shows the $\langle p_{\rm T}\rangle$ as a function of $N_{\rm ch}^{\rm rec}$ for each of the three photon energy distributions. There is no significant difference between the $\langle p_{\rm T}\rangle$ obtained from nominal photon energy distribution compared to those obtained from re-weighted photon energy distribution.

The very substantial energy re-weighting applied to DPMJET-III that emphasizes lower energy photons, referred to as "lower", is quite likely ruled out by other Pb+Pb UPC measurements. It is notable that such a large change does naturally shift the $\langle\eta\rangle$ and $\sum_\gamma \Delta\eta^{\rm rec}$ distributions, while having a very modest impact on the $\langle p_{\rm T}\rangle$.

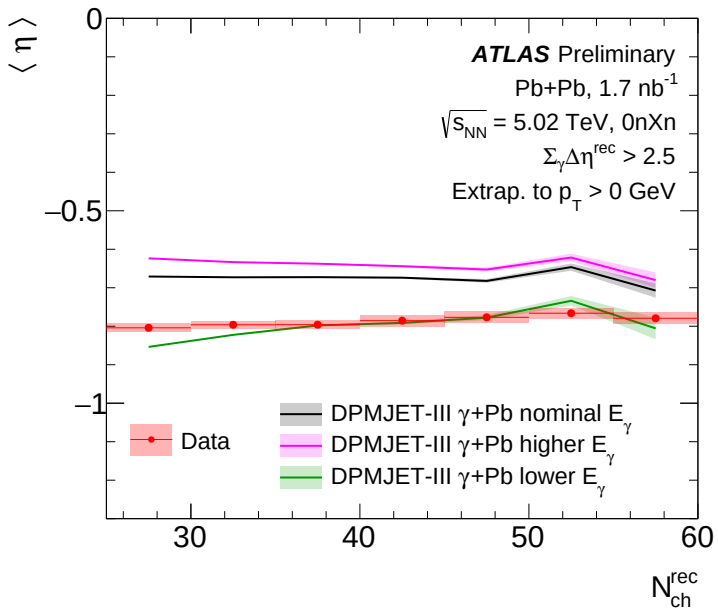

Figure A.9: Shown is the $\langle\eta\rangle$ as a function of $N_{\mathrm{ch}}^{\mathrm{rec}}$ compared to the nominal truth-level yield result in DPMJET-III and two variations.

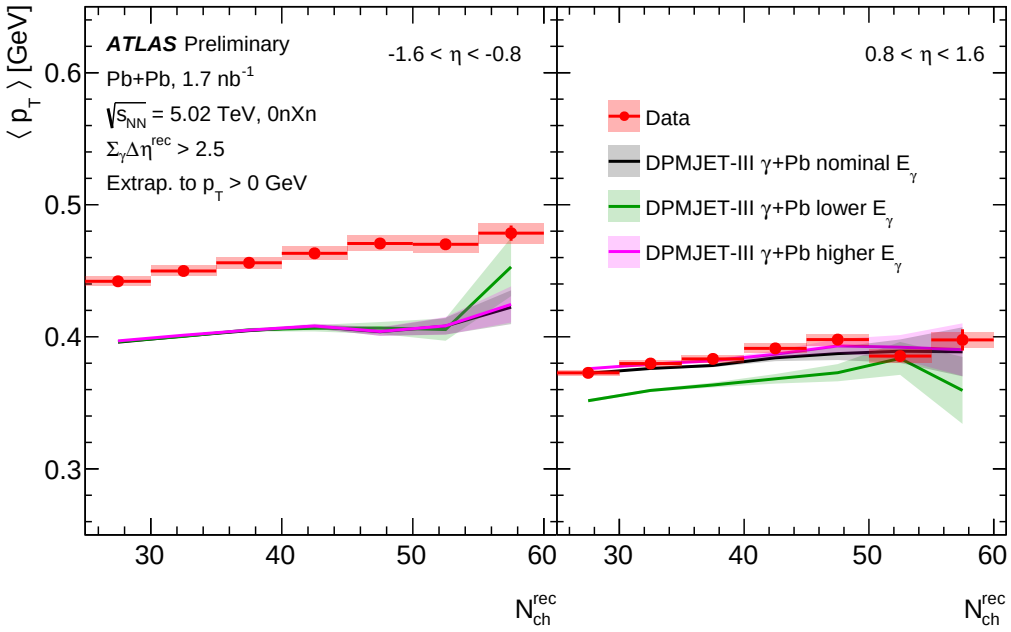

Figure A.10: Shown are the $\langle p_{\mathrm{T}}\rangle$ as a function of $N_{\mathrm{ch}}^{\mathrm{rec}}$. The left panel shows the result for the backward rapidity slice [-1.6,-0.8] and the right panel shows the result for the forward rapidity slice [0.8,1.6] utilizing results extrapolated to $p_{\mathrm{T}} > 0$ GeV. Also, shown are the truth-level yield result from reconstructed event generated by DPMJET-III utilizing the identical $N_{\mathrm{ch}}^{\mathrm{rec}}$ and $\sum_{\gamma}\Delta\eta^{\mathrm{rec}}$ selection criteria as with experimental data for the nominal DPMJET-III and the two variations in the photon energy distribution, i.e., "higher" and "lower".

A.3 Additional DPMJET-III Details

Figure A.11 shows $\langle\eta\rangle$ within the range $-2.5 < \eta < +2.5$ as a function of E_γ. The $\langle\eta\rangle$ value increases as a function of E_γ, with $\langle\eta\rangle \to 0$ for large photon energies, i.e., $E_\gamma > 100$ GeV. It is striking that the $\langle\eta\rangle$ from DPMJET-III shown as a function of $N_{\rm ch}^{\rm rec}$– see Figure A.4 – is almost flat with $\langle\eta\rangle \approx -0.6$. This is the result of a rather loose correspondence between E_γ and $N_{\rm ch}^{\rm rec}$.

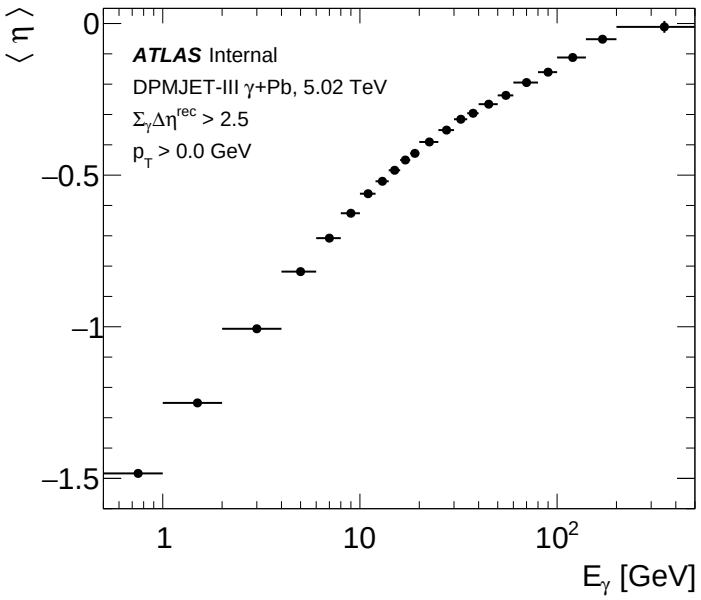

Figure A.11: Shown are the $\langle\eta\rangle$ of charged-hadron yields as a function of E_γ from the DPMJET-III model.

Figure A.12 shows $\langle p_{\rm T}\rangle$ as a function of E_γ for two different η slices, [-1.6,-0.8] and [0.8,1.6], in the DPMJET-III model. The η bin on the Pb-going side ($\eta < 0$) shows a nearly constant $\langle p_{\rm T}\rangle$ as a function of E_γ, whereas on the photon-going side ($\eta > 0$), the $\langle p_{\rm T}\rangle$ slowly increase until $E_\gamma =$ 10 GeV, then decreases slightly.

Figures A.13 shows the correlation between $\sum_\gamma \Delta\eta^{\rm rec}$ and $\Delta\eta_{\rm edge}$ in the DPMJET-III (left) and Pb+Pb UPC data (right). $\Delta\eta_{\rm edge}$ is defined as the $|\Delta\eta|$ between photon-going edge of the detector (eg: $\eta = 4.9$) and the closest cluster to the photon-going edge.

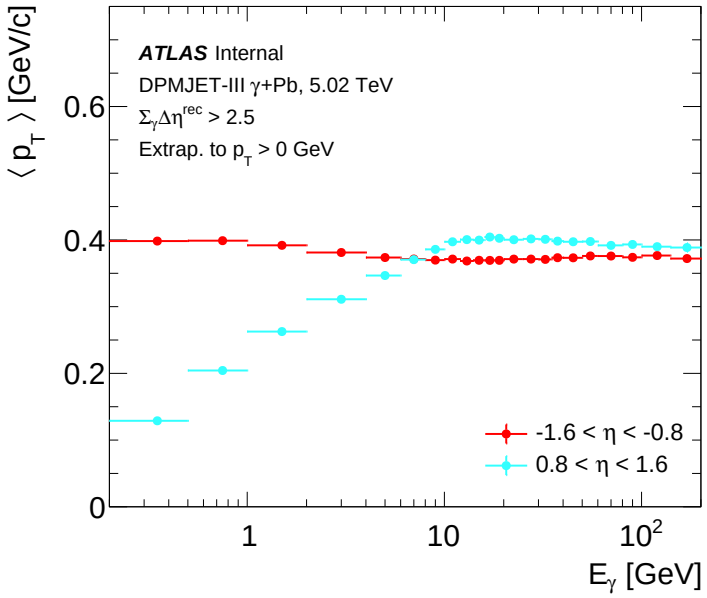

Figure A.12: Shown are the $\langle p_{\mathrm{T}} \rangle$ of charged-hadron yields as a function of E_γ from the DPMJET-III model in two different η slices, [-1.6,-0.8] and [0.8,1.6] for $p_{\mathrm{T}} > 0$ GeV.

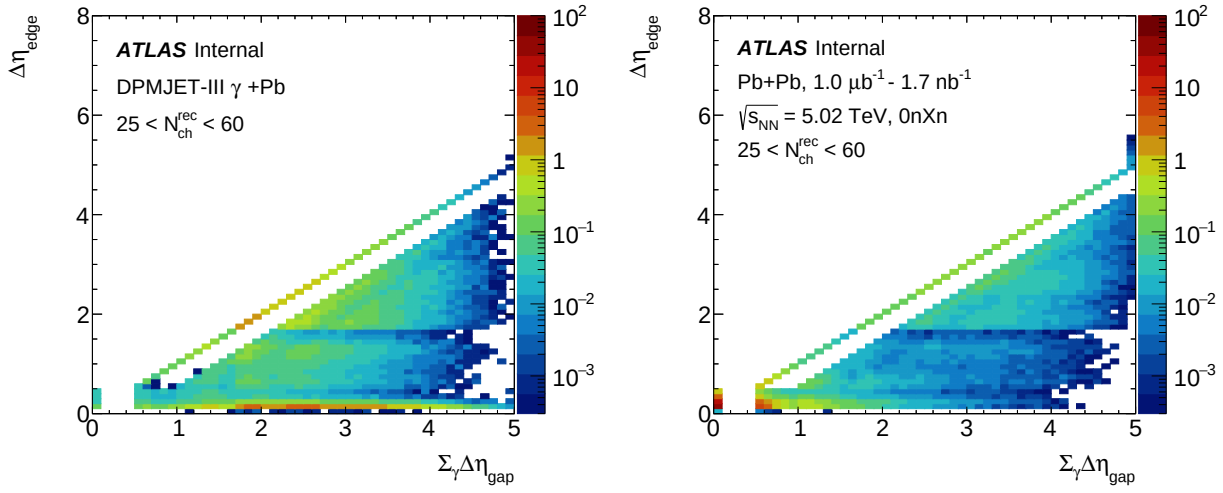

Figure A.13: Shown are the correlation between $\sum_\gamma \Delta\eta^{\mathrm{rec}}$ and $\Delta\eta_{\mathrm{edge}}$ in the DPMJET-III (left) and Pb+Pb UPC data (right).

Figures A.14 and A.15 show the DPMJET-III particle pseudorapidity distribution for different $N_{\mathrm{ch}}^{\mathrm{rec}}$ selections, both within the ATLAS tracking region $-2.5 < \eta < +2.5$ and over the entire η range.

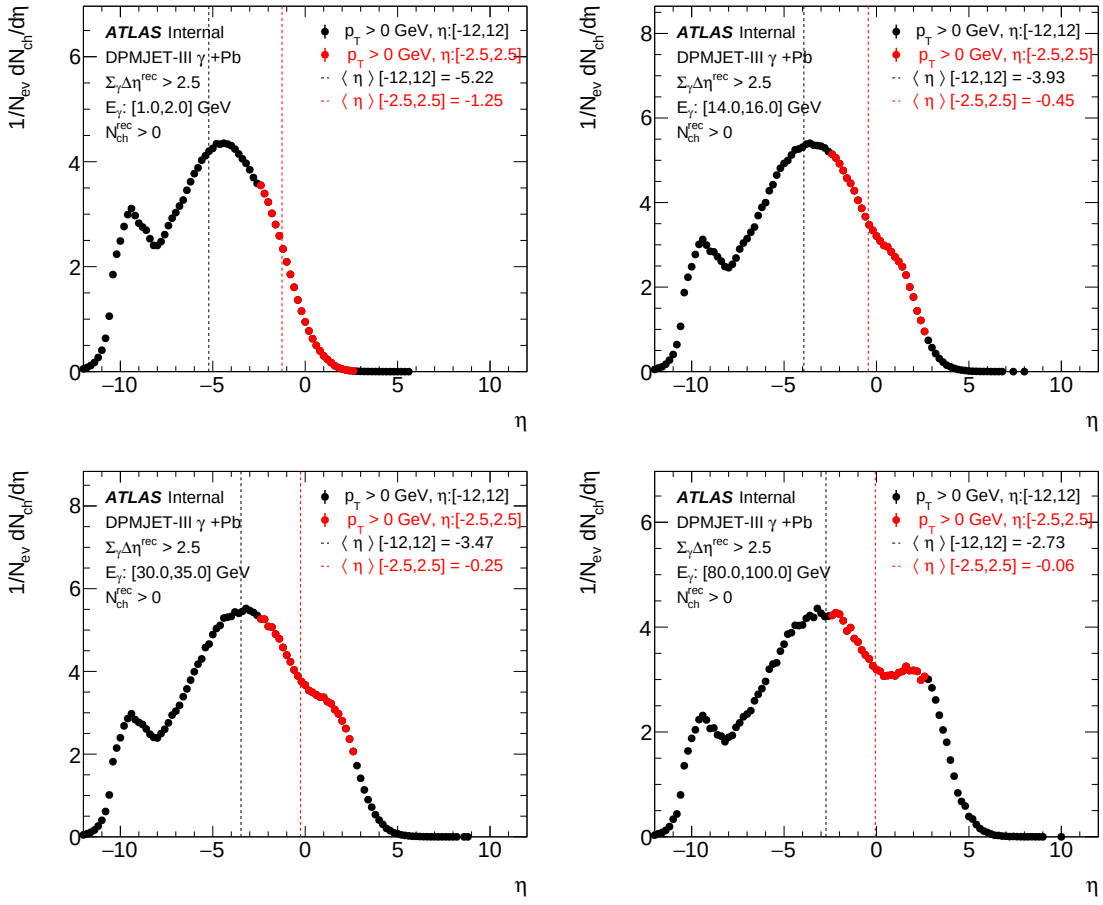

Figure A.14: Shown are the fully normalized yield as a function of η from -12.0 to 12.0 for $p_{\mathrm{T}} > 0$ GeV in different photon energy slices. Red markers/lines highlight the η region: [-2.5,2.5] while black markers/lines highlight the entire η region: [-12.0,12.0].

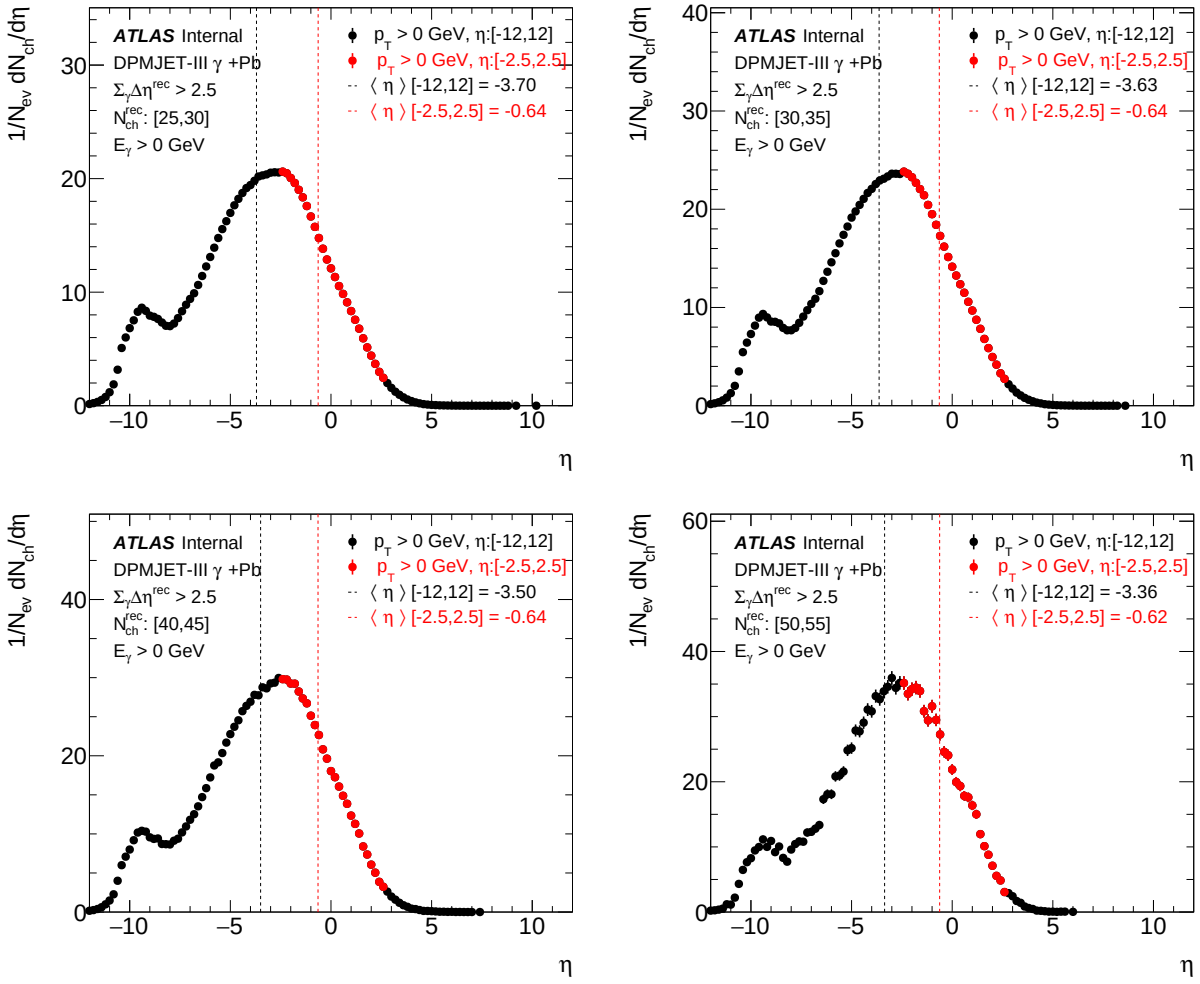

Figure A.15: Shown are the fully normalized yield as a function of η from -12.0 to 12.0 for p_{T} > 0 GeV in different $N_{\mathrm{ch}}^{\mathrm{rec}}$ slices. Red markers/lines highlight the η region: [-2.5,2.5] while black markers/lines highlight the entire η region: [-12.0,12.0].

A.4 DPMJET and PYTHIA Truth vs Reconstructed Definition Comparisons

This section discusses the comparison of yield in Monte Carlo simulations with the nominal definitions at reconstructed level such as $\sum_\gamma \Delta\eta^{\mathrm{rec}}$ and $N_{\mathrm{ch}}^{\mathrm{rec}}$ to that of truth definitions.

A.4.1 Truth vs Reconstructed $\sum_\gamma \Delta\eta$ Definition

Figure A.16 compares the charged hadron yield as a function of η in DPMJET-III, using separate $\sum_\gamma \Delta\eta$ definitions based on reconstructed tracks and truth particles. Figure A.17 compare the same, but weighed with the lower energy favored photon distribution discussed in Appendix A.2. We note that the $\sum_\gamma \Delta\eta^{\mathrm{rec}}$ defined at the reconstructed level utilizes tracks with $p_{\mathrm{T}} > 0.4$ GeV, $|\eta| < 2.5$ and clusters with $p_{\mathrm{T}} > 0.2$ GeV, $|\eta| < 4.9$, while for the truth-level $\sum_\gamma \Delta\eta^{\mathrm{truth}}$ definition, particles with $p_{\mathrm{T}} > 0.33$ GeV, $|\eta| < 4.9$ are utilized to achieve better agreement with the reconstructed level gap definition. The kink feature appear at $p_{\mathrm{T}} \approx 0.3$ GeV is simply due to the auto-correlation bias between the particles included in the $\sum_\gamma \Delta\eta$ definition and those included in the yield.

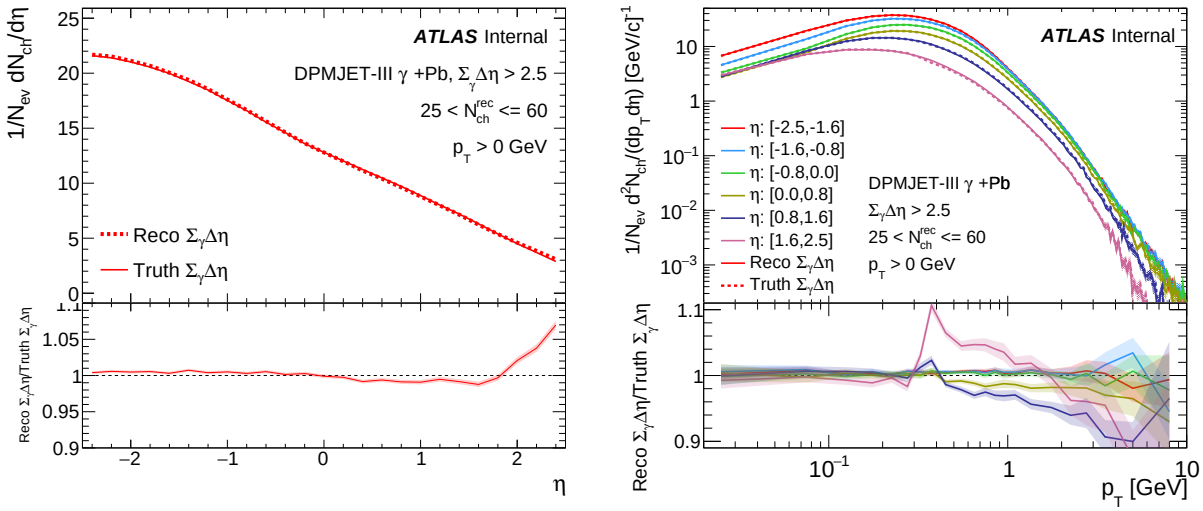

Figure A.16: Shown are the charged hadron yield as a function of η in DPMJET-III, utilizing $\sum_\gamma \Delta\eta$ defined using reconstructed tracks, shown as dotted line and truth particles, shown as solid line. The bottom panel shows the ratio of the two distributions.

In Figure A.16, in the forward rapidity region $0.8 < \eta < 2.5$, and in the highest p_{T} region above 0.4 GeV, there is an observed difference of $< 10\%$ between the two distributions. This difference is significantly reduced to $< 5\%$ when comparing the charged hadron yield between truth-level and reconstructed-level $\sum_{\gamma} \Delta\eta$ definitions in Figure A.17. We note that the $\sum_{\gamma} \Delta\eta^{\mathrm{rec}}$ distribution, when weighed with the lower energy favored photon distribution, closely matches that of the data in the signal region $\sum_{\gamma} \Delta\eta^{\mathrm{rec}} > 2.5$, as shown in Figure A.8.

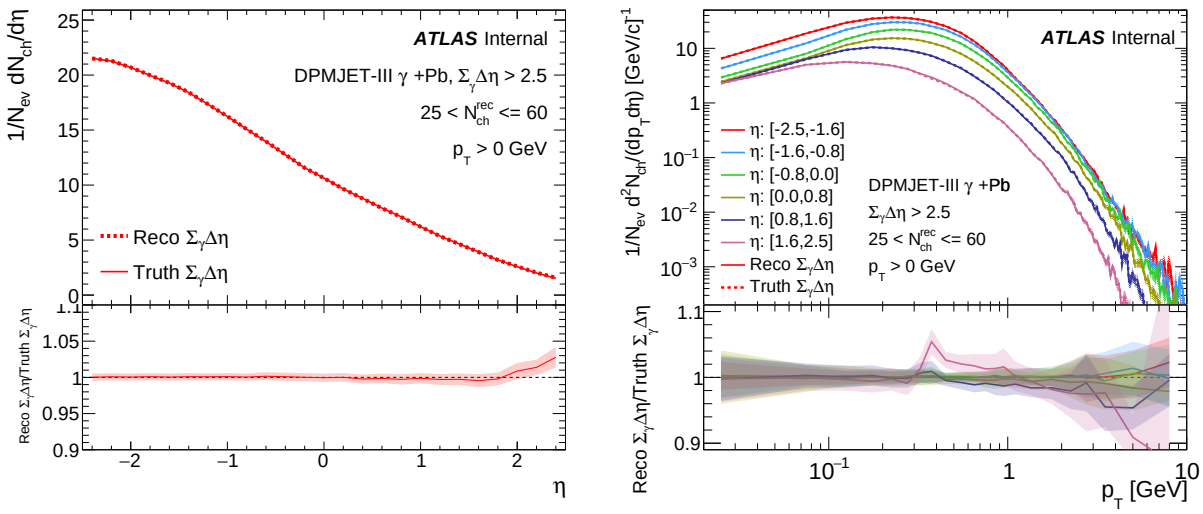

Figure A.17: Shown are the charged hadron yield as a function of η in DPMJET-III reweighed with lower photon energy distribution, utilizing $\sum_{\gamma} \Delta\eta$ defined using reconstructed tracks, shown as dotted line and truth particles, shown as solid line. The bottom panel shows the ratio of the two distributions.

Figure A.18 compares the charged hadron yield as a function of η in PYTHIA, using separate $\sum_{\gamma} \Delta\eta$ definitions based on reconstructed tracks and truth particles. We note that the $\sum_{\gamma} \Delta\eta^{\mathrm{rec}}$ defined at the reconstructed level utilizes tracks with $p_{\mathrm{T}} > 0.4$ GeV, $|\eta| < 2.5$, and clusters with $p_{\mathrm{T}} > 0.2$ GeV, $|\eta| < 4.9$,, while for the truth-level $\sum_{\gamma} \Delta\eta^{\mathrm{truth}}$ definition, particles with $p_{\mathrm{T}} > 0.45$ GeV, $|\eta| < 4.9$, are utilized to achieve better agreement with the reconstructed level gap definition. Remarkably, PYTHIA exhibits excellent agreement in $\mathrm{d}N_{\mathrm{ch}}/\mathrm{d}\eta$ between truth and reconstructed level $\sum_{\gamma} \Delta\eta$ definitions.

However, in the most forward rapidity region η:[1.6,2.5], and in the highest p_{T} region above 2 GeV, there is an observed difference of $< 5\%$ between the two distributions. This difference is fitted using a log polynomial of 2$^{\mathrm{nd}}$ order and the fit values are assigned as a systematic uncertainty.

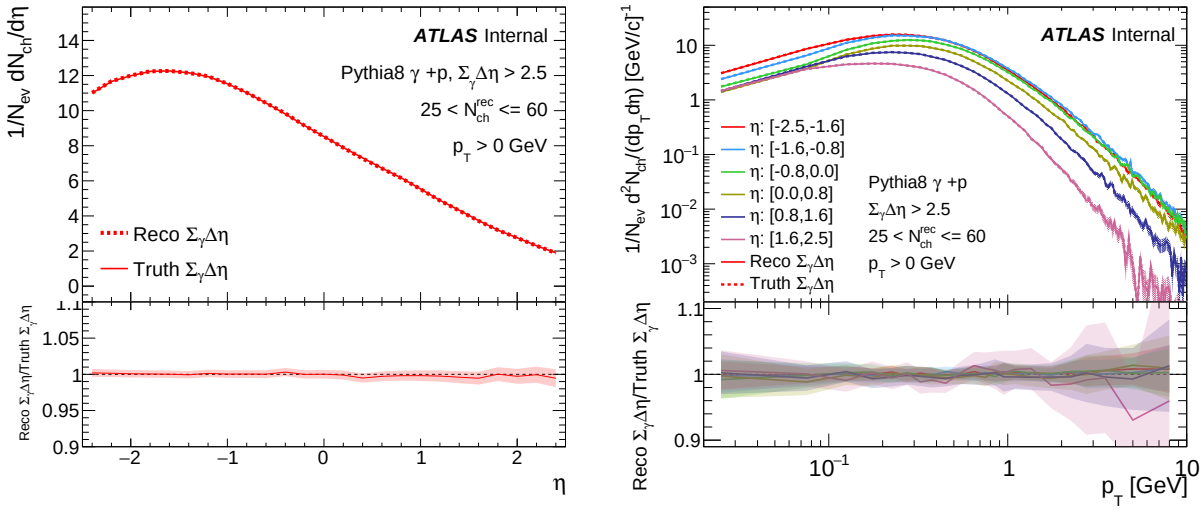

Figure A.18: Shown are the charged hadron yield as a function of η in PYTHIA, utilizing $\sum_{\gamma} \Delta\eta$ defined using reconstructed tracks, shown as dotted line and truth particles, shown as solid line. The bottom panel shows the ratio of the two distributions.

A.4.2 Truth vs Reconstructed N_{ch} Definition

The DPMJET-III plots shows in this section are not weighed with the lower energy favored photon distribution discussed in Appendix A.2.

Figure A.19 shows the correlation between $N_{\mathrm{ch}}^{\mathrm{truth}}$ defined using reconstructed tracks and truth particles in DPMJET-III. The $N_{\mathrm{ch}}^{\mathrm{truth}}$ values corresponds to the event-class selection, $25 < N_{\mathrm{ch}}^{\mathrm{rec}} \leq 60$ are $N_{\mathrm{ch}}^{\mathrm{truth}}$: [31,73], which makes sense since the track reconstruction efficiency of 80% is not accounted in the definition of $N_{\mathrm{ch}}^{\mathrm{rec}}$. Table A.1 shows the corresponding $N_{\mathrm{ch}}^{\mathrm{truth}}$ range for event-class selection, $25 < N_{\mathrm{ch}}^{\mathrm{rec}} \leq 60$ and its subdivisions.

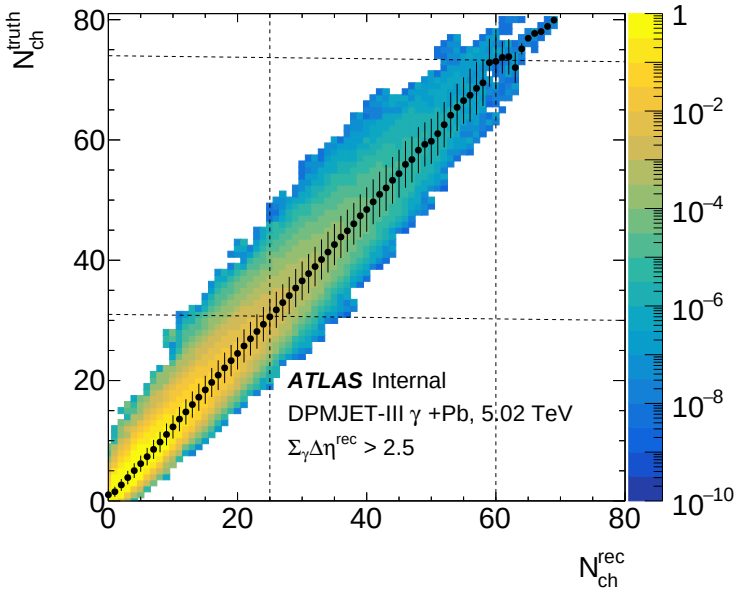

Figure A.19: Shown are the correlation between N_{ch} defined using reconstructed tracks, in x axis and truth particles, in y axis in DPMJET-III. The black markers represent the mean $N_{\mathrm{ch}}^{\mathrm{truth}}$ value in each $N_{\mathrm{ch}}^{\mathrm{rec}}$ bins. The corresponding $N_{\mathrm{ch}}^{\mathrm{truth}}$ to event-class selection, $N_{\mathrm{ch}}^{\mathrm{rec}}$: [25,60] are highlighted in dotted lines.

$N_{\mathrm{ch}}^{\mathrm{rec}}$	$N_{\mathrm{ch}}^{\mathrm{truth}}$
$25 < N_{\mathrm{ch}}^{\mathrm{rec}} \leq 60$	$31 < N_{\mathrm{ch}}^{\mathrm{truth}} \leq 73$
$25 < N_{\mathrm{ch}}^{\mathrm{rec}} \leq 30$	$31 < N_{\mathrm{ch}}^{\mathrm{truth}} \leq 37$
$30 < N_{\mathrm{ch}}^{\mathrm{rec}} \leq 35$	$37 < N_{\mathrm{ch}}^{\mathrm{truth}} \leq 43$
$35 < N_{\mathrm{ch}}^{\mathrm{rec}} \leq 40$	$43 < N_{\mathrm{ch}}^{\mathrm{truth}} \leq 48$
$40 < N_{\mathrm{ch}}^{\mathrm{rec}} \leq 45$	$48 < N_{\mathrm{ch}}^{\mathrm{truth}} \leq 54$
$45 < N_{\mathrm{ch}}^{\mathrm{rec}} \leq 50$	$54 < N_{\mathrm{ch}}^{\mathrm{truth}} \leq 60$
$50 < N_{\mathrm{ch}}^{\mathrm{rec}} \leq 55$	$60 < N_{\mathrm{ch}}^{\mathrm{truth}} \leq 67$
$55 < N_{\mathrm{ch}}^{\mathrm{rec}} \leq 60$	$67 < N_{\mathrm{ch}}^{\mathrm{truth}} \leq 73$

Table A.1: Shown are the corresponding $N_{\mathrm{ch}}^{\mathrm{truth}}$ range for event-class selection, $25 < N_{\mathrm{ch}}^{\mathrm{rec}} \leq 60$ and its subdivisions.

Figure A.20 compares the charged hadron yield as a function of η in DPMJET-III, using separate N_{ch} definitions based on reconstructed tracks and truth particles. We note that both reconstructed and truth-level N_{ch} definitions utilizes charged particles with $p_{\mathrm{T}} > 0.4$ GeV, $|\eta| < 2.5$. There is an observed difference of $< 1\%$ between the two distributions.

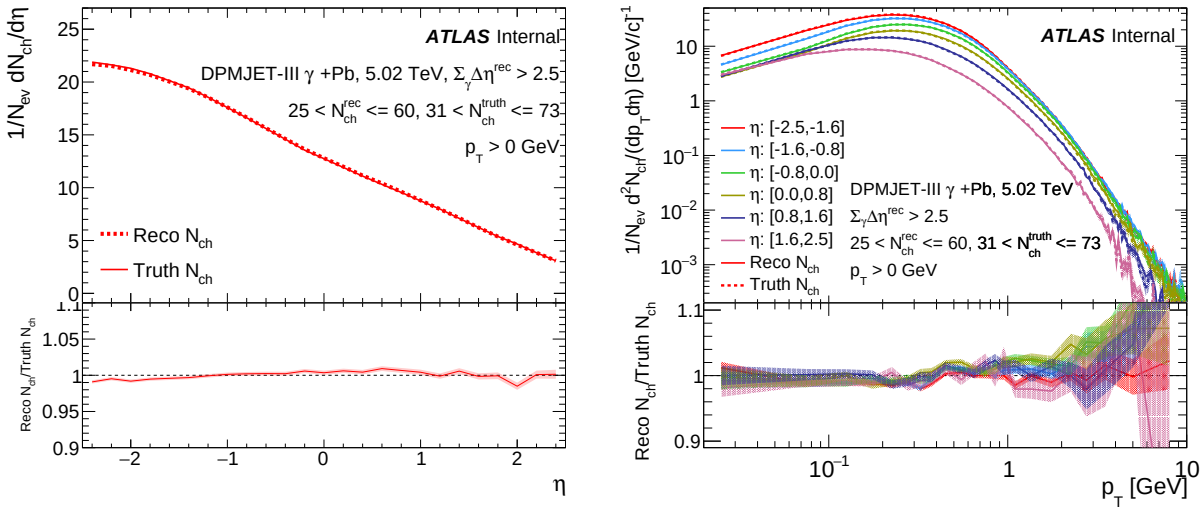

Figure A.20: Shown are the charged hadron yield as a function of η (left) and p_{T} in different η slices (right) in DPMJET-III, utilizing N_{ch} defined using reconstructed tracks, shown as dotted line and truth particles, shown as solid line. The bottom panel shows the ratio of the two distributions.

A.5 Unfolding

Figures A.21 and A.22 show the unfolded charged hadrons yield as a function of p_{T} in different η slices from Pb+Pb UPC data. This is performed as a cross-check to the bin migration effects as detailed in Section 5.3.5. RooUnfold software package, with the Bayesian unfolding method, is utilized to perform the unfolding procedure [159]. We highlight that the ratio of the distributions with and without unfolding is within 1% as a function of p_{T}. Thus, it is optimal to utilize the bin migration procedure and not incur additional unfolding systematics and bin-to-bin correlations in the final yields.

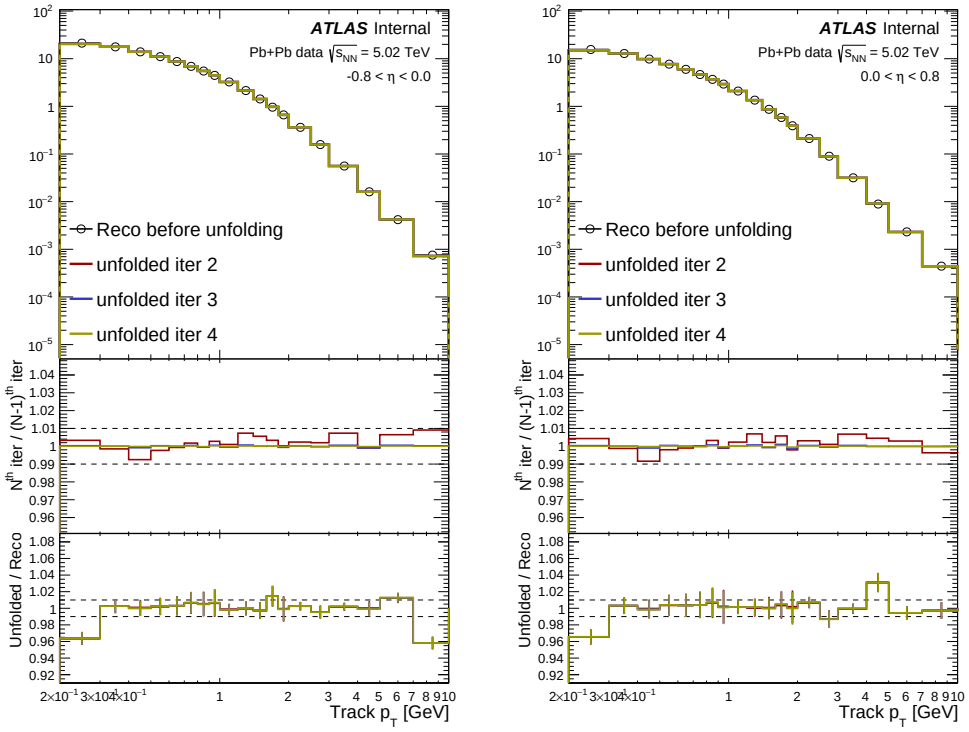

Figure A.21: Shown are the charged hadron yield in Pb+Pb UPC as a function of p_{T}, with unfolded distributions up to 4 iterations. The bottom panel shows the ratio of the distributions with and without unfolding.

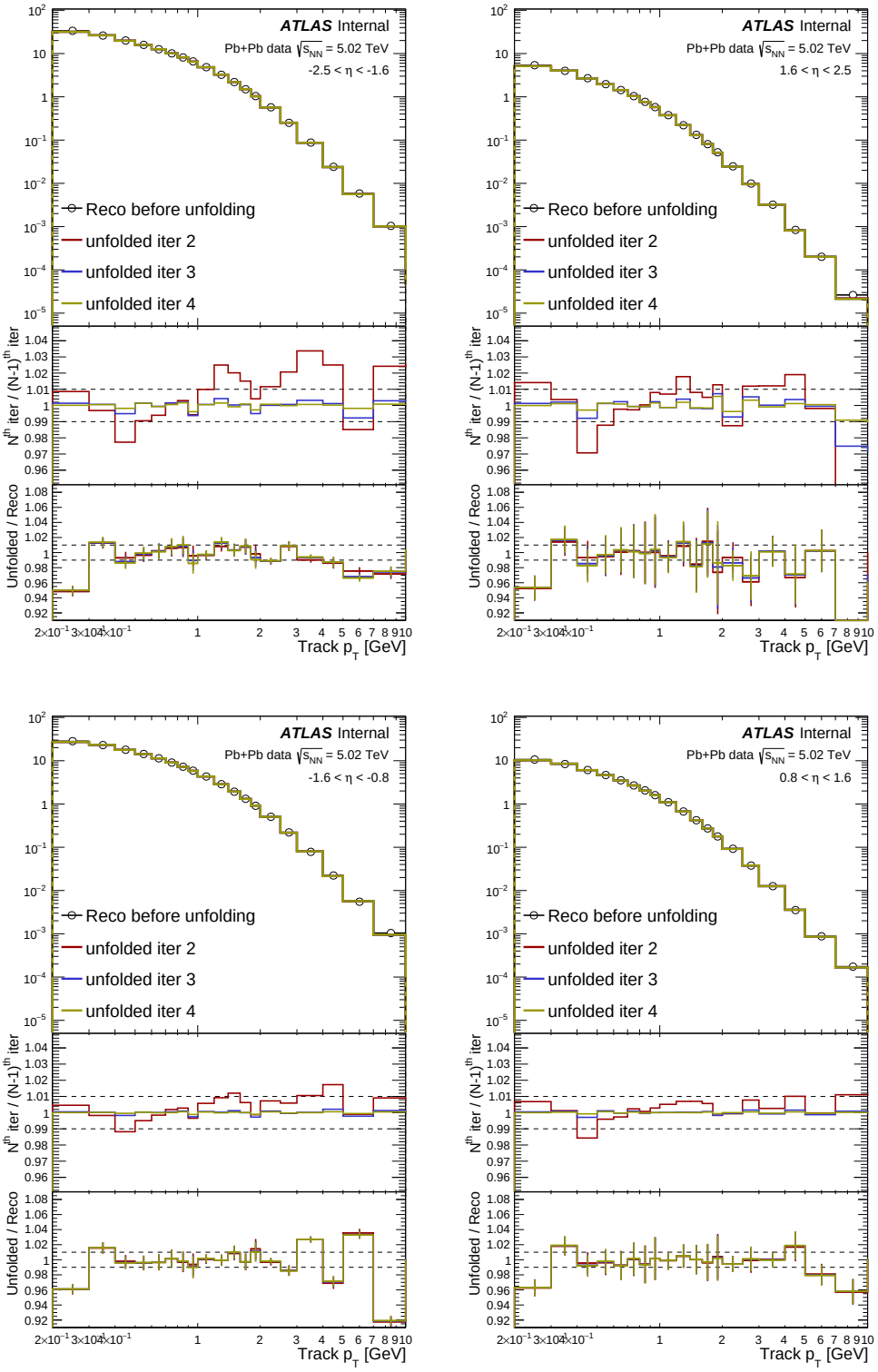

Figure A.22: Shown are the charged hadron yield in Pb+Pb UPC as a function of p_{T}, with unfolded distributions up to 4 iterations. The bottom panel shows the ratio of the distributions with and without unfolding.

A.6 Additional Purity Estimation Details

This section shows the two-component fit plots utilized in the purity estimation procedure, namely DPMJET-III +HIJING $\sum_\gamma \Delta\eta^{\rm rec}$ derived result and PYTHIA +HIJING $\sum_\gamma \Delta\eta^{\rm rec}$ derived result.

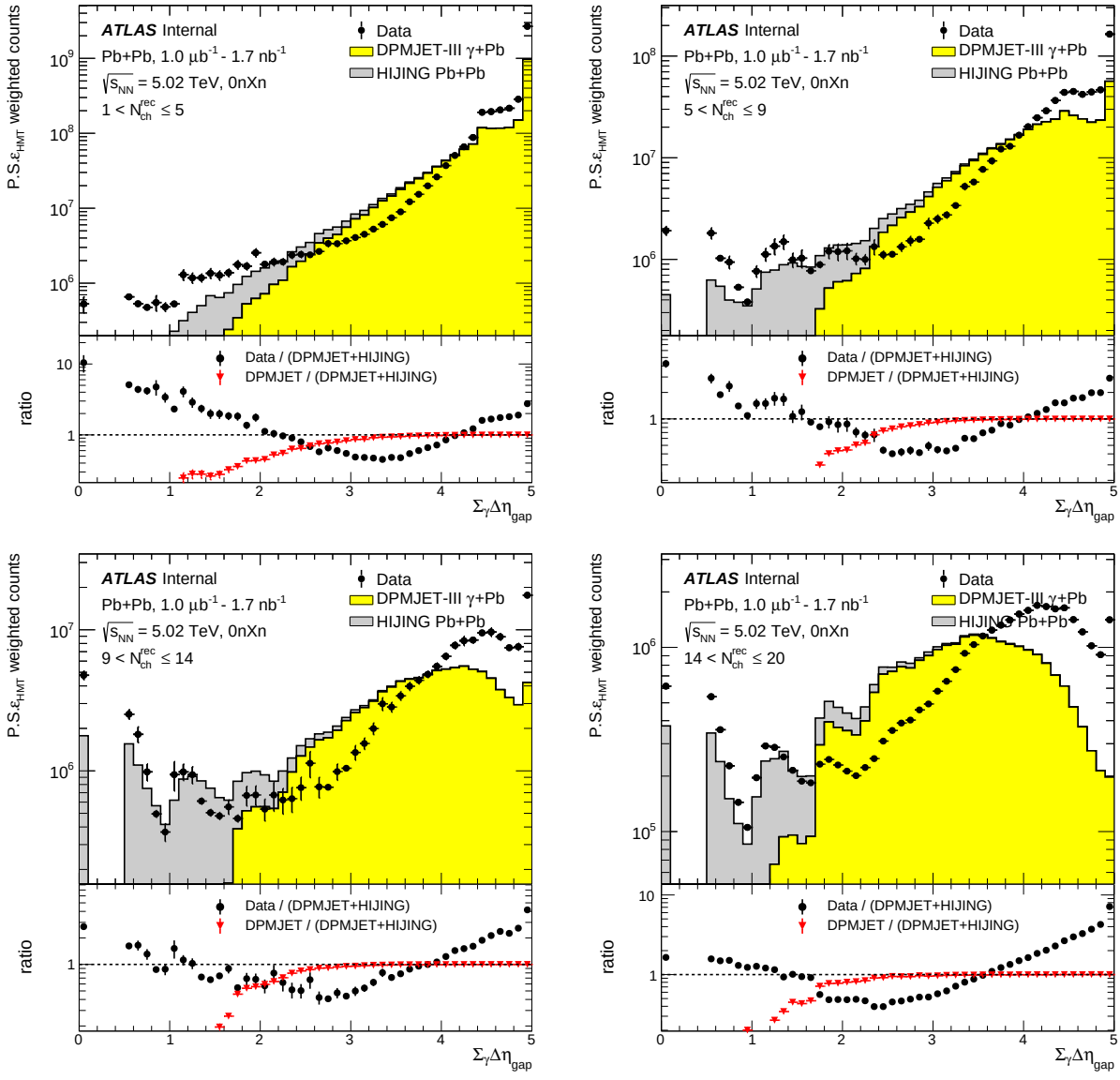

Figure A.23: Shown in the top panel are the signal (DPMJET-III) and background (HIJING) utilized in the two-component fit, DPMJET-III +HIJING $\sum_\gamma \Delta\eta^{\rm rec}$ derived result, along with Pb+Pb UPC data as a function of $\sum_\gamma \Delta\eta^{\rm rec}$ in several $N_{\rm ch}^{\rm rec}$ slices up to $N_{\rm ch}^{\rm rec} = 20$. The bottom panel shows the ratio of data to the two-component fit in black markers and the ratio of DPMJET-III to the two-component fit, referred to as purity, in red markers.

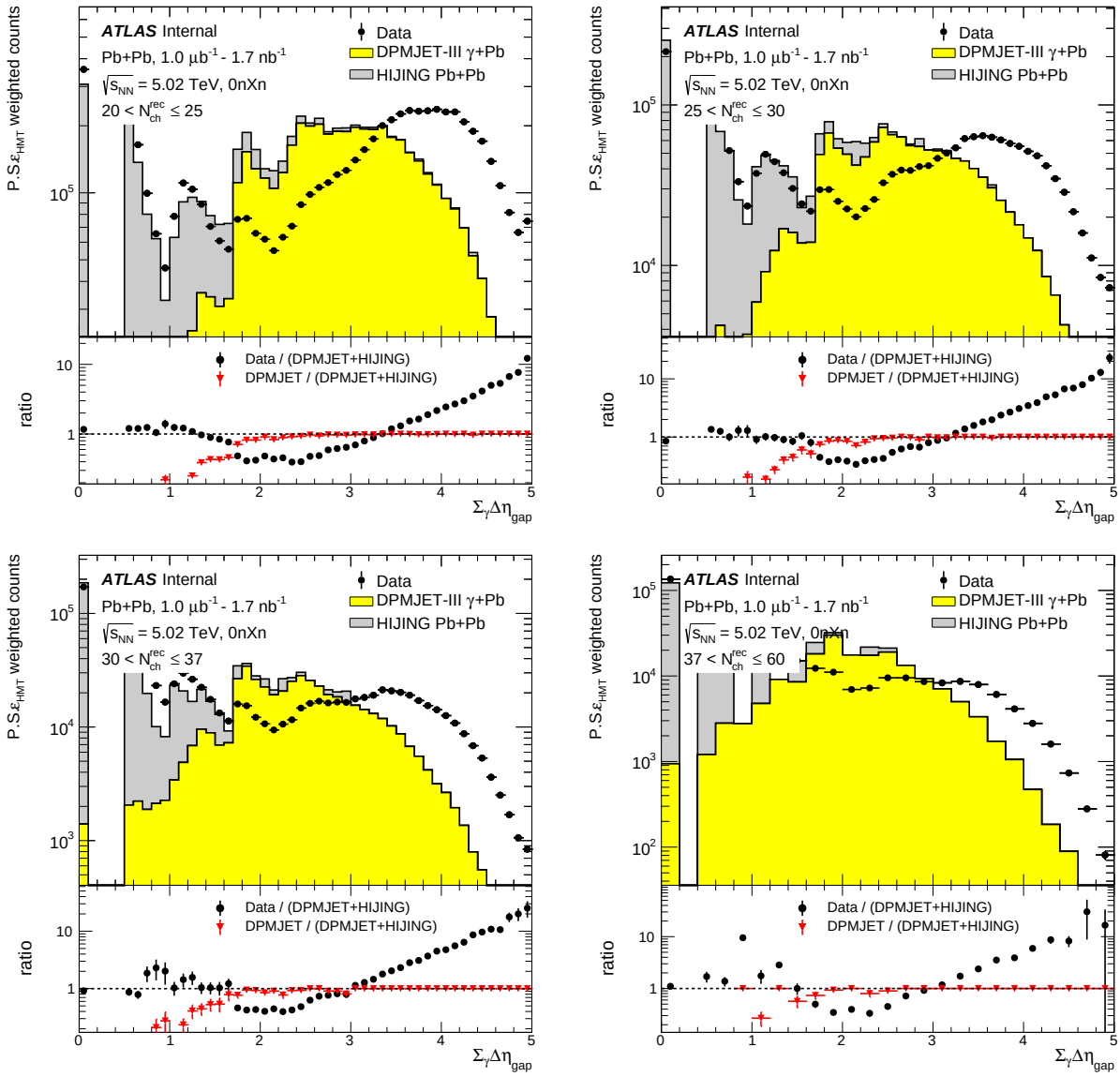

Figure A.24: Shown in the top panel are the signal (DPMJET-III) and background (HIJING) utilized in the two-component fit, DPMJET-III +HIJING $\sum_{\gamma} \Delta\eta^{\mathrm{rec}}$ derived result, along with Pb+Pb UPC data as a function of $\sum_{\gamma} \Delta\eta^{\mathrm{rec}}$ in several $N_{\mathrm{ch}}^{\mathrm{rec}}$ slices, $N_{\mathrm{ch}}^{\mathrm{rec}}$ = 20-60. The bottom panel shows the ratio of data to the two-component fit in black markers and the ratio of DPMJET-III to the two-component fit, referred to as purity, in red markers.

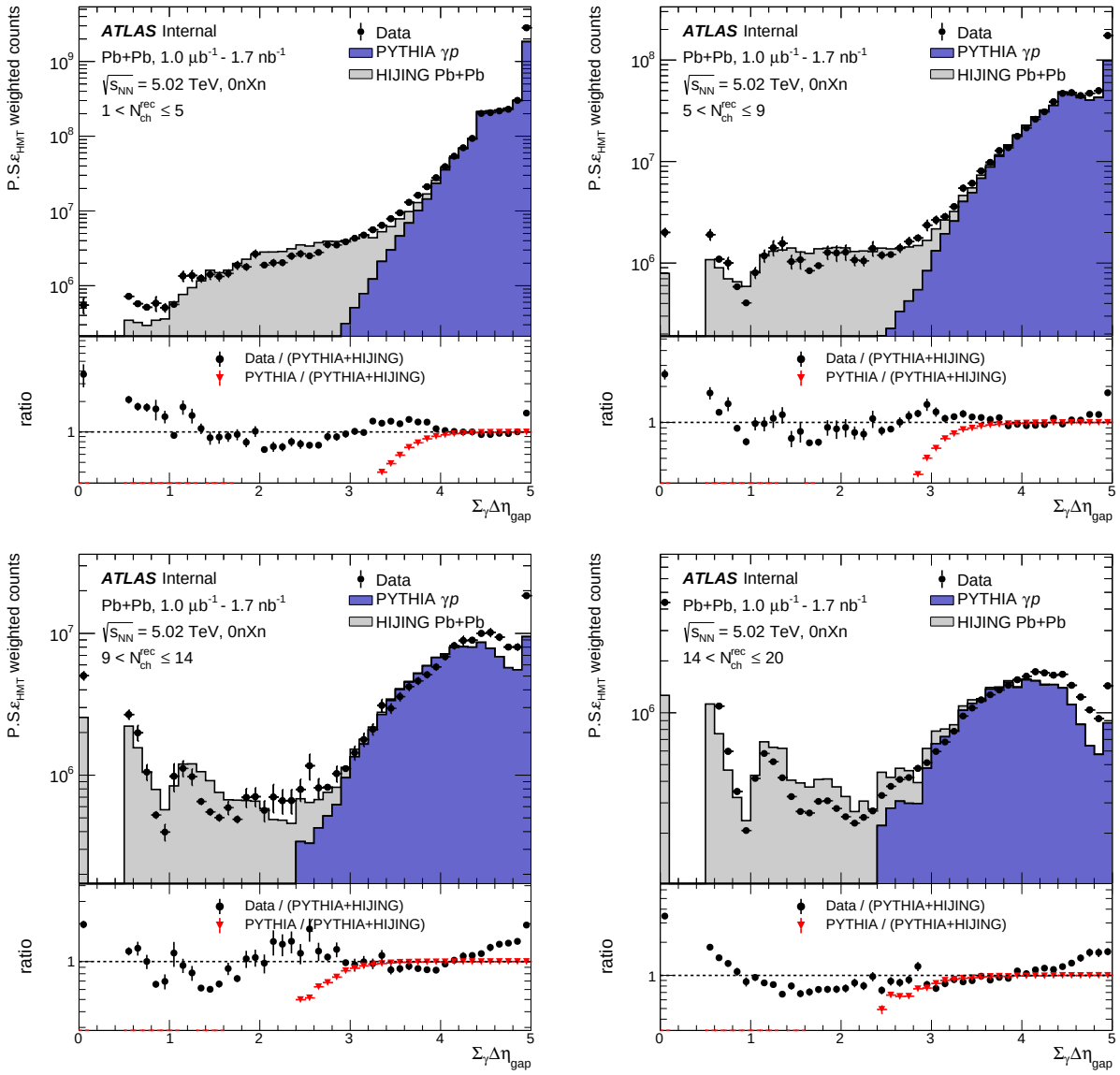

Figure A.25: Shown in the top panel are the signal (PYTHIA) and background (HIJING) utilized in the two-component fit, PYTHIA +HIJING $\sum_\gamma \Delta\eta^{\rm rec}$ derived result, along with Pb+Pb UPC data as a function of $\sum_\gamma \Delta\eta^{\rm rec}$ in several $N_{\rm ch}^{\rm rec}$ slices up to $N_{\rm ch}^{\rm rec} = 20$. The bottom panel shows the ratio of data to the two-component fit in black markers and the ratio of PYTHIA to the two-component fit, referred to as purity, in red markers.

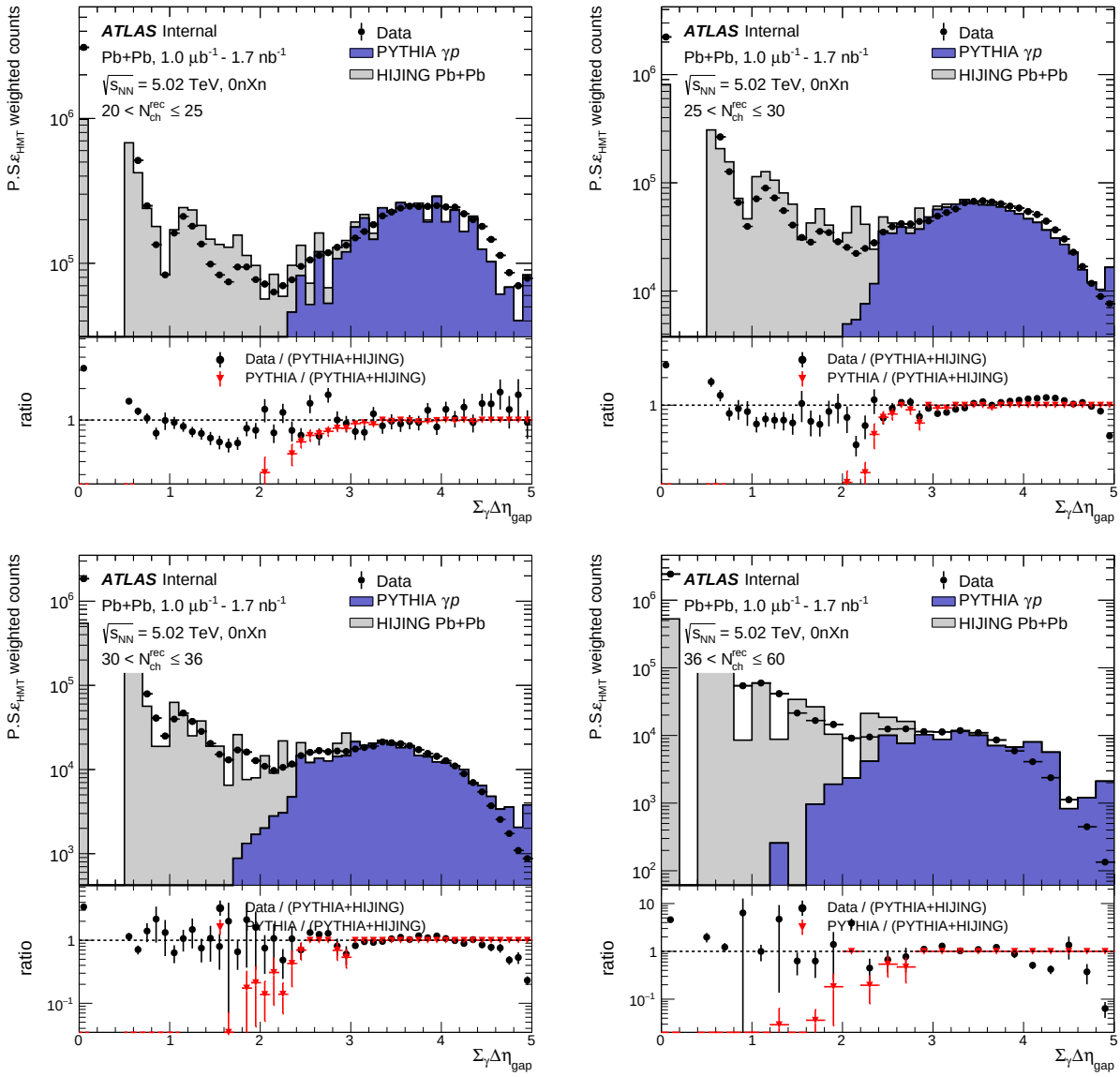

Figure A.26: Shown in the top panel are the signal (PYTHIA) and background (HIJING) utilized in the two-component fit, PYTHIA +HIJING $\sum_{\gamma} \Delta\eta^{\mathrm{rec}}$ derived result, along with Pb+Pb UPC data as a function of $\sum_{\gamma} \Delta\eta^{\mathrm{rec}}$ in several $N_{\mathrm{ch}}^{\mathrm{rec}}$ slices, $N_{\mathrm{ch}}^{\mathrm{rec}}$ = 20-60. The bottom panel shows the ratio of data to the two-component fit in black markers and the ratio of PYTHIA to the two-component fit, referred to as purity, in red markers.

A.7 Additional Systematic Uncertainty Details

This section shows the systematic uncertainty estimation of charged hadron yield as a function of η in Pb+Pb UPC and p+Pb.

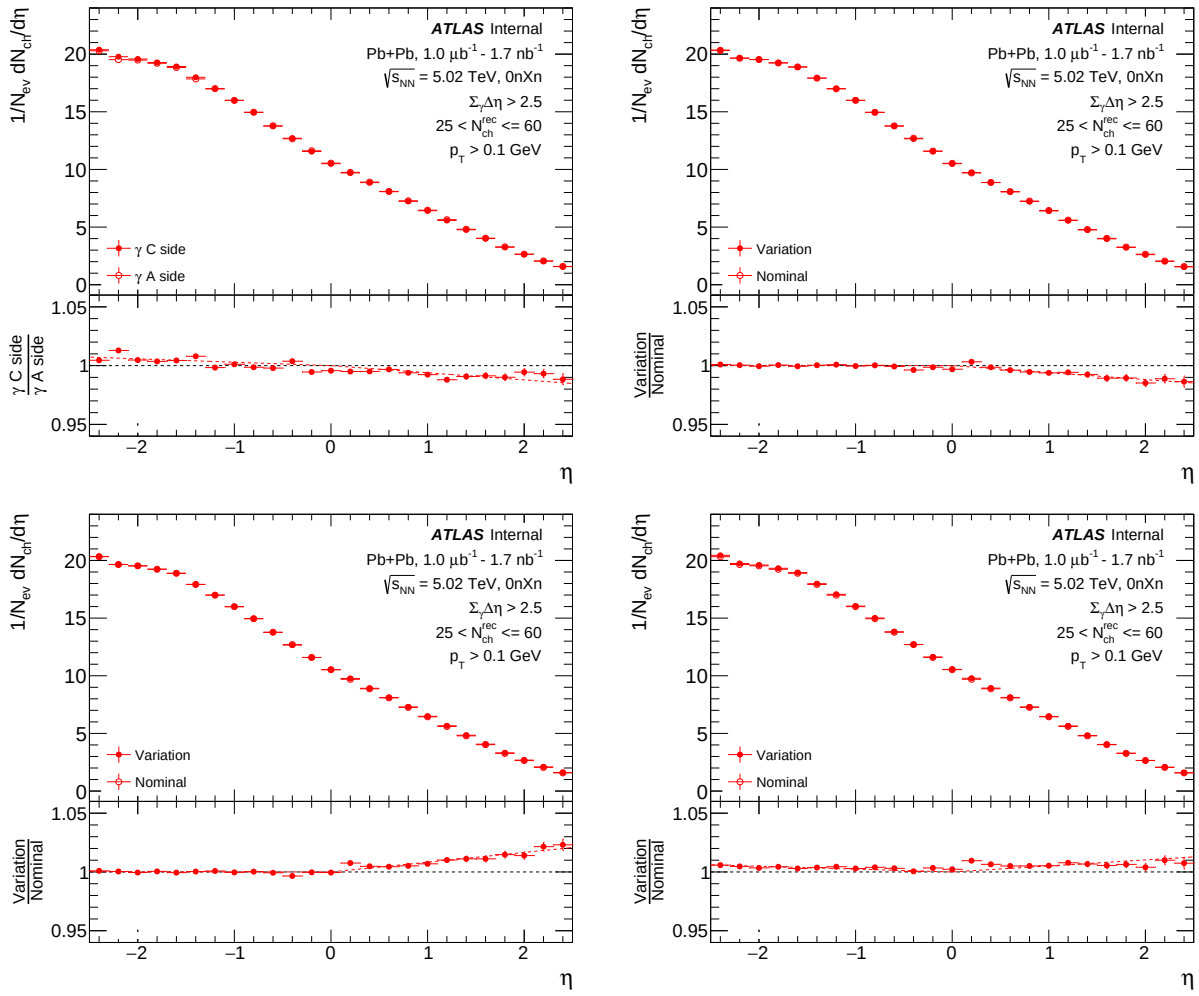

Figure A.27: Shown are the charged hadron yield in Pb+Pb UPC as a function of η, with nominal and varied results. From left to right: 1. Photon A-side vs C-side. 2. Purity sensitivity - Variation up. 3. Purity sensitivity - Variation down. 4. $N_{\mathrm{ch}}^{\mathrm{rec}}$ definition. The bottom panel shows the ratio of the nominal to the varied distributions.

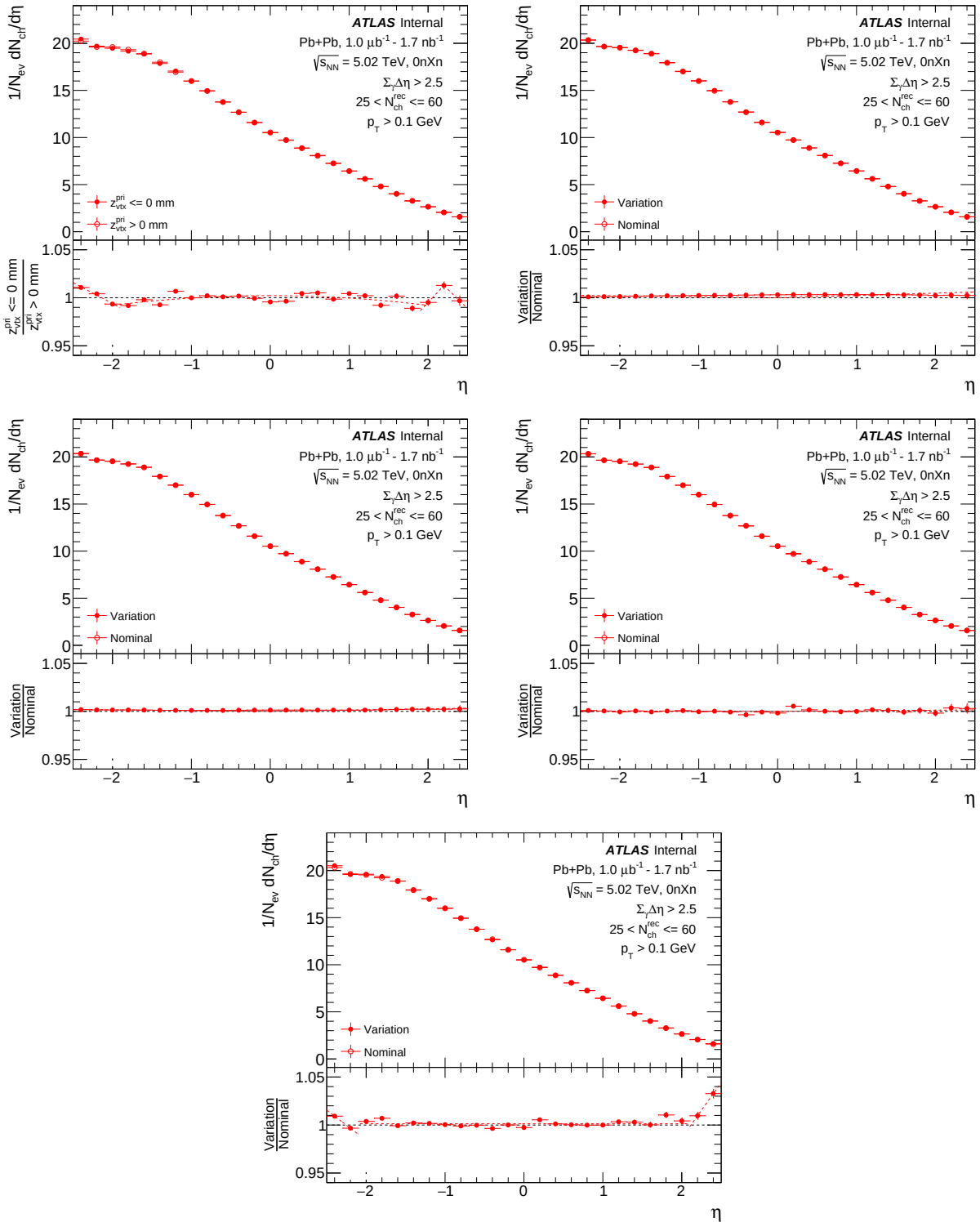

Figure A.28: Shown are the charged hadron yield in Pb+Pb UPC as a function of η, with nominal and varied results. From left to right: 1. Z-vertex dependence. 2. Charged particle composition - K/π. 3. Charged particle composition - p/π. 4. Track selection - Eliminating pixel requirement. 5. Track selection - Eliminating SCT requirement. The bottom panel shows the ratio of the nominal to the varied distributions.

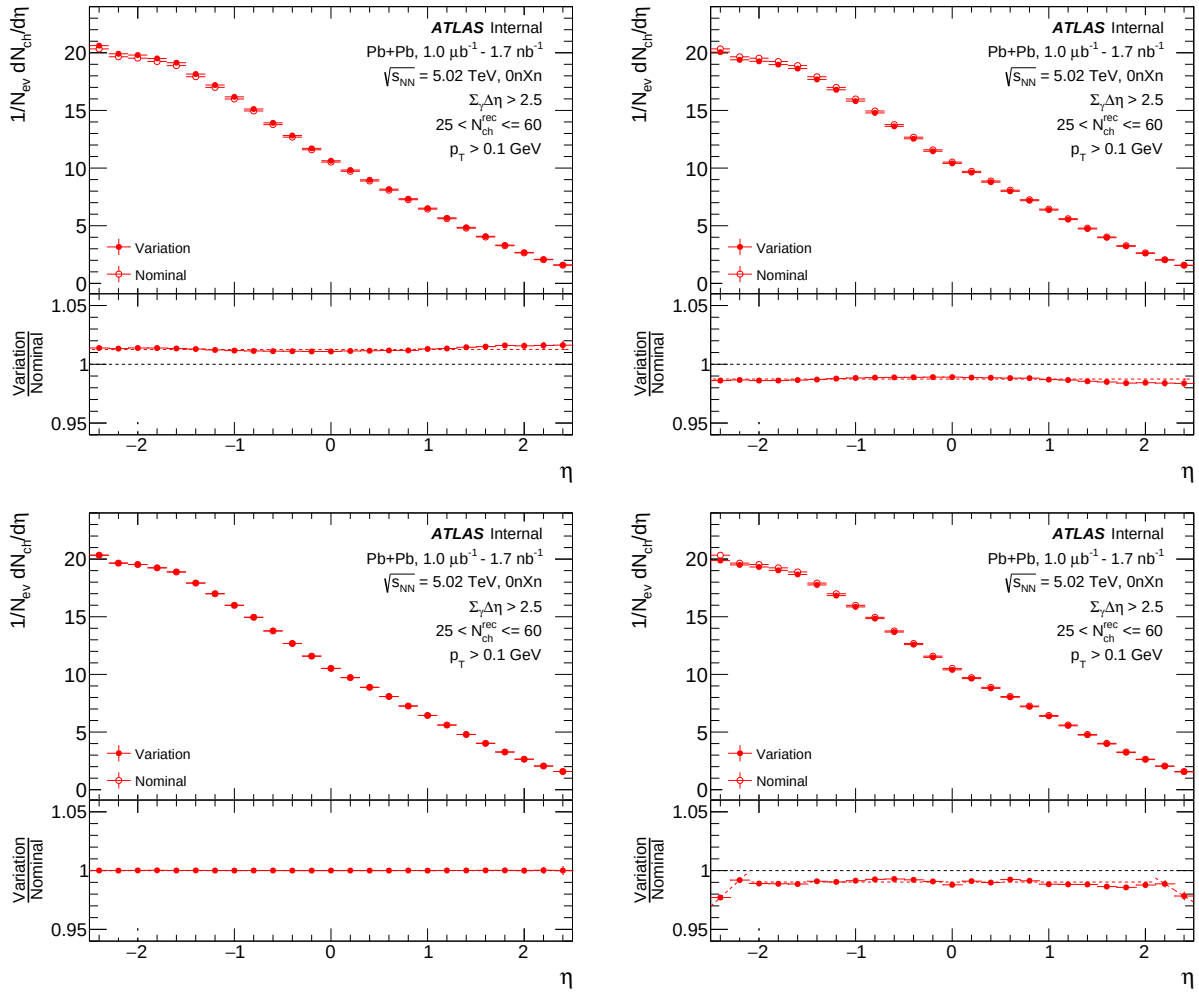

Figure A.29: Shown are the charged hadron yield in Pb+Pb UPC as a function of η, with nominal and varied results. From left to right: 1. Fakes and secondary tracks - Variation up. 2. Fakes and secondary tracks - Variation down. 3. Track-to-particle match. 4. Track bin migration. The bottom panel shows the ratio of the nominal to the varied distributions.

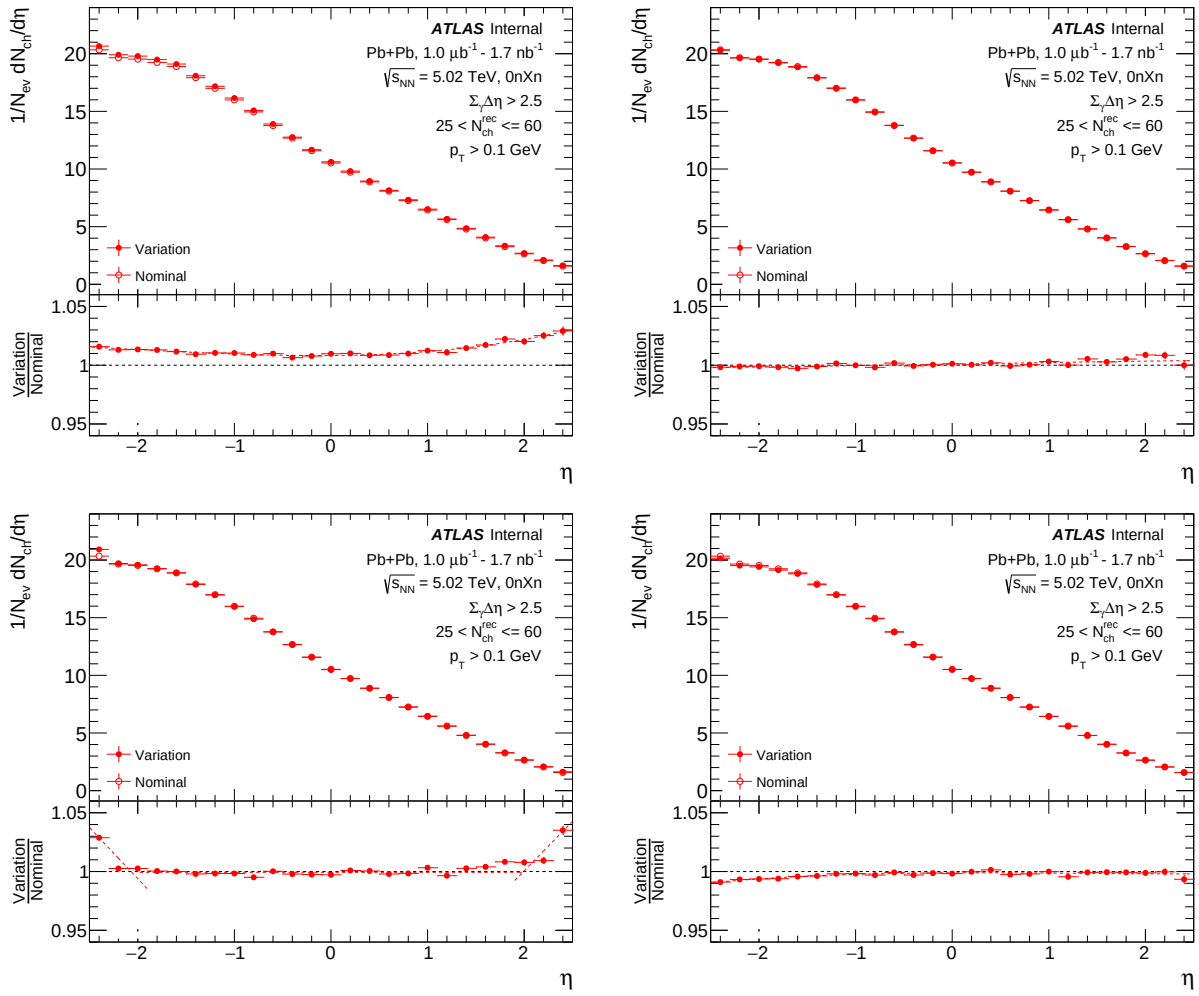

Figure A.30: Shown are the charged hadron yield in Pb+Pb UPC as a function of η, with nominal and varied results. From left to right: 1. Detector material/physics model - Material ID 5%. 2. Detector material/physics model - Material IBL 10%. 3. Detector material/physics model - Material PP0 25%. 4. Detector material/physics model - GEANT4 Physics model. The bottom panel shows the ratio of the nominal to the varied distributions.

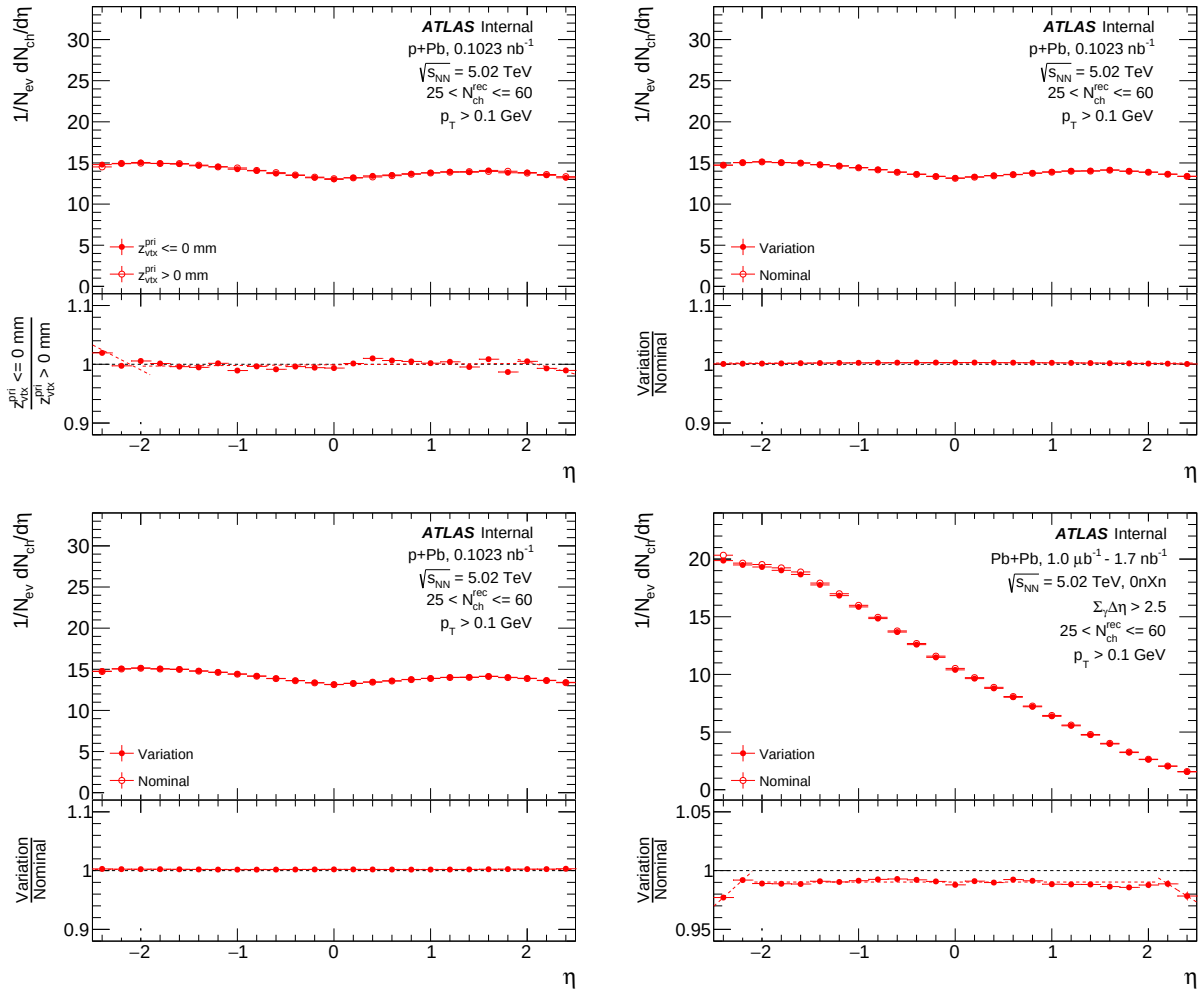

Figure A.31: Shown are the charged hadron yield in p+Pb as a function of η, with nominal and varied results. From left to right: 1. Z-vertex dependence. 2. Charged particle composition - K/π. 3. Charged particle composition - p/π. 4. Track bin migration. The bottom panel shows the ratio of the nominal to the varied distributions.

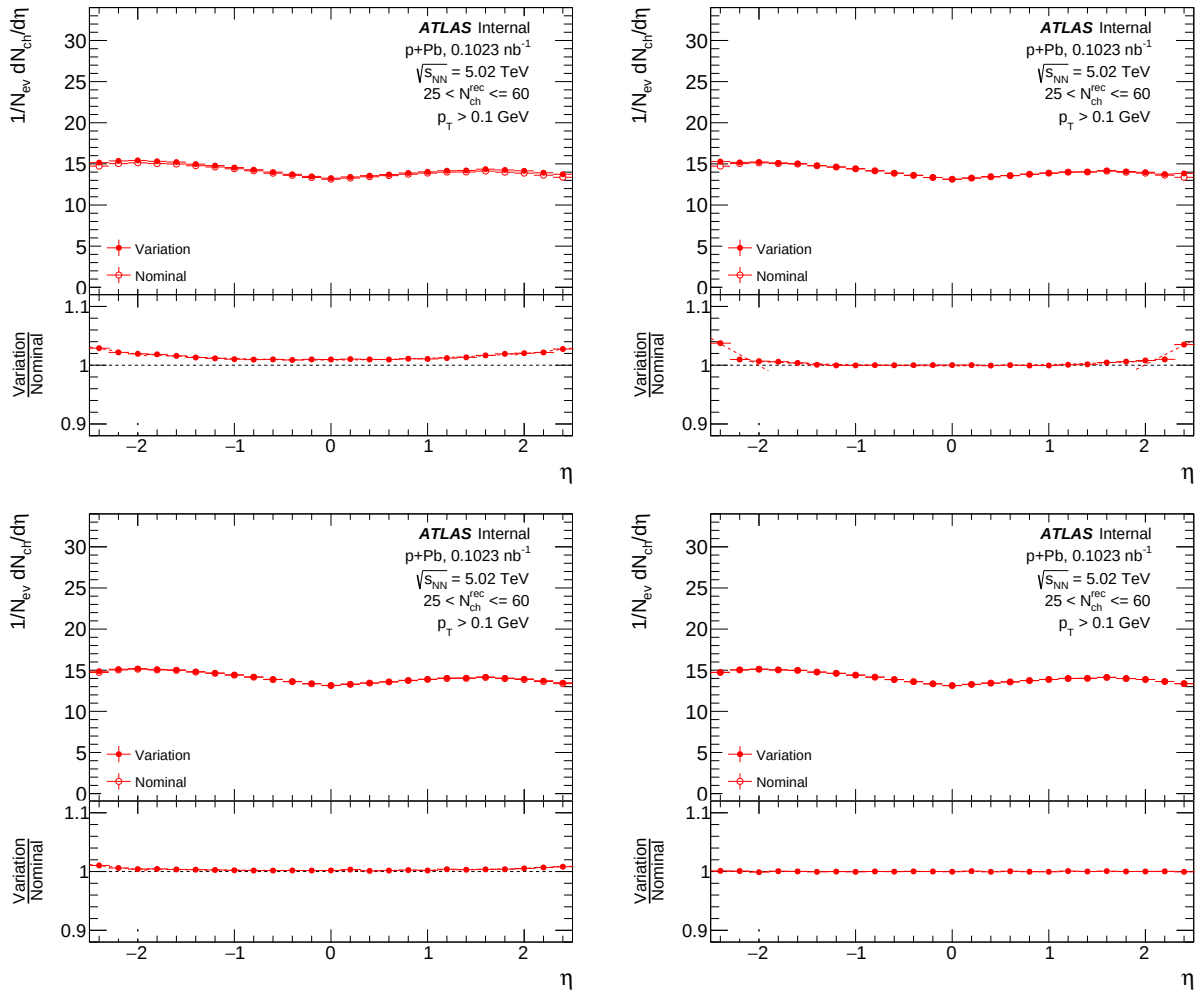

Figure A.32: Shown are the charged hadron yield in p+Pb as a function of η, with nominal and varied results. From left to right: 1. Detector material/physics model - Material ID 5%. 2. Detector material/physics model - Material IBL 10%. 3. Detector material/physics model - Material PP0 25%. 4. Detector material/physics model - GEANT4 Physics model. The bottom panel shows the ratio of the nominal to the varied distributions.

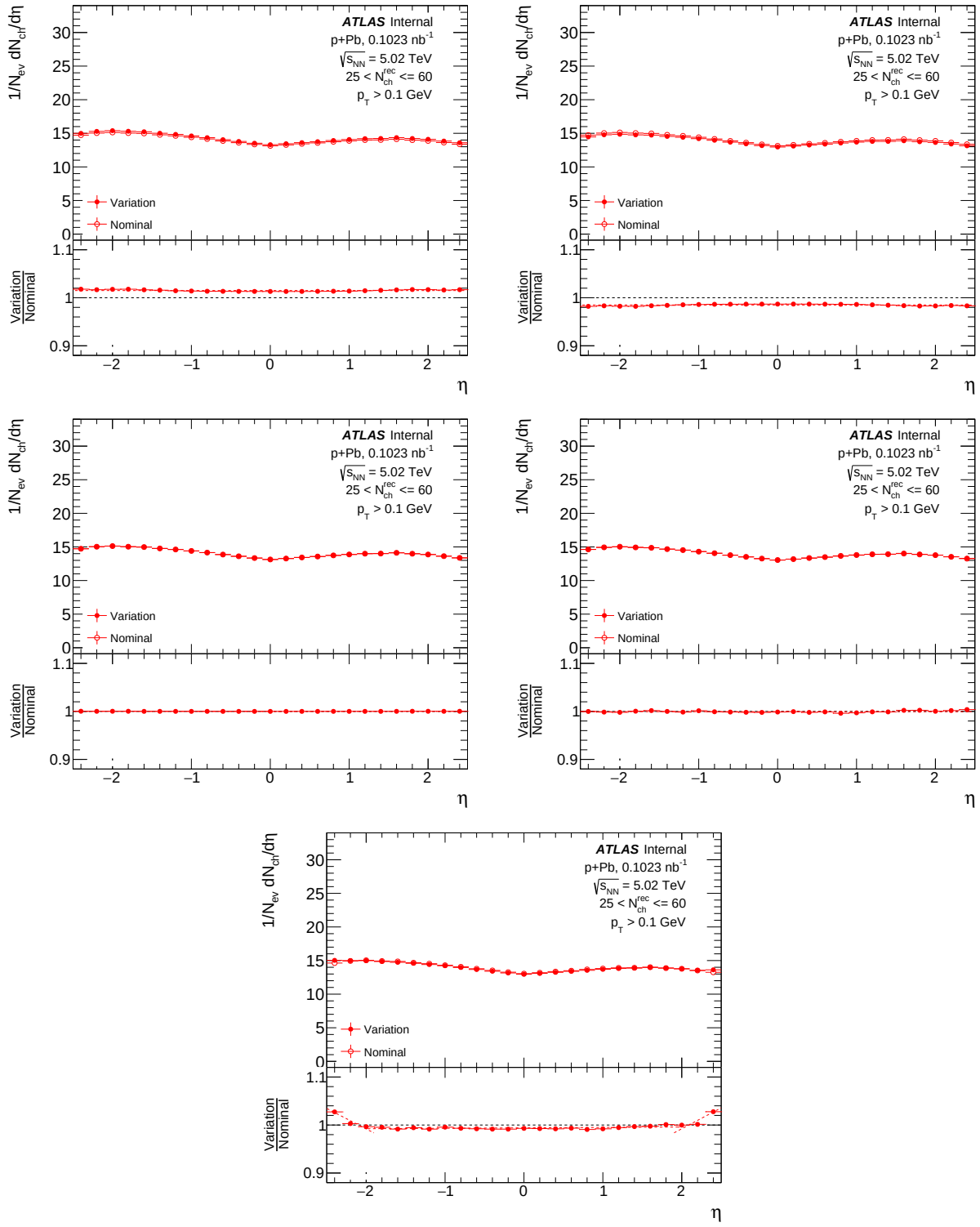

Figure A.33: Shown are the charged hadron yield in p+Pb as a function of η, with nominal and varied results. From left to right: 1. Fakes and secondary tracks - Variation up. 2. Fakes and secondary tracks - Variation down. 3. Track-to-particle match. 4. Track selection - Eliminating pixel requirement. 5. Track selection - Eliminating SCT requirement. The bottom panel shows the ratio of the nominal to the varied distributions.

Appendix B

Measurement of Identified Particle Production

This Chapter includes the additional invariant mass distributions of identified particles.

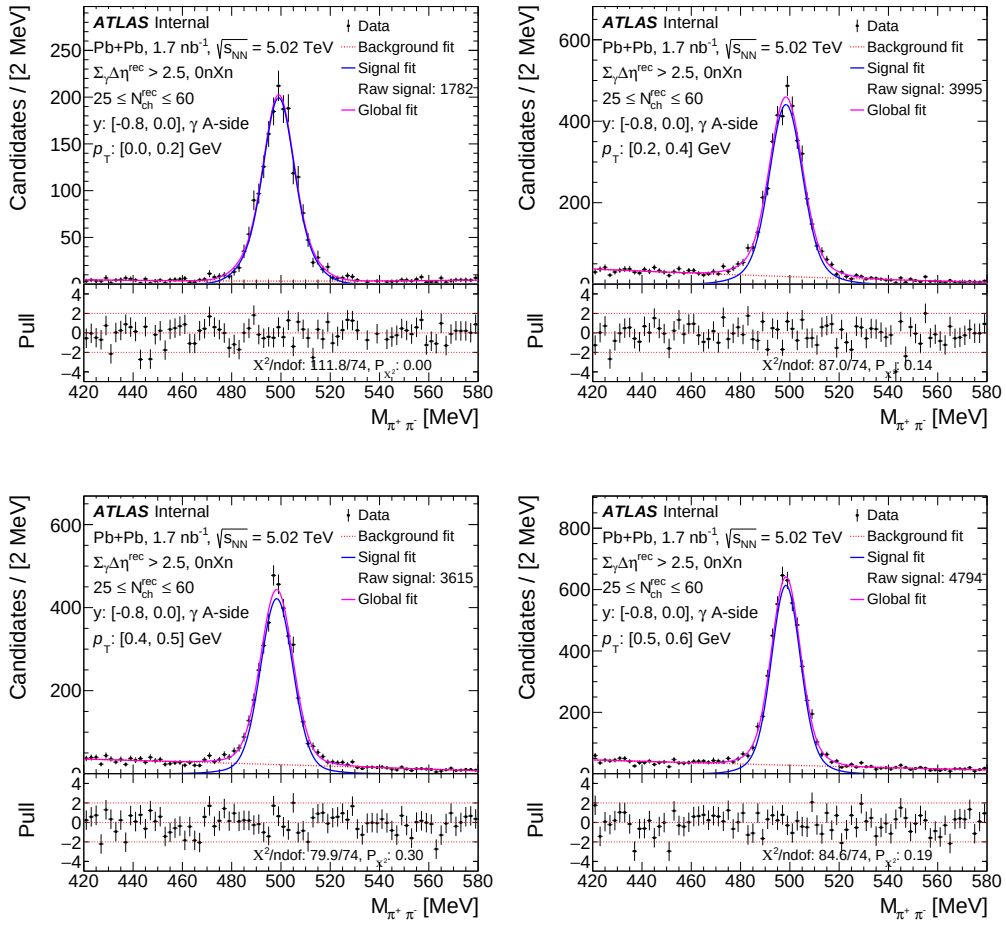

Figure B.1: The invariant mass distributions of K^0_S shown for a set of p_T-y bins in Pb+Pb UPC, represented along with the fit curves.

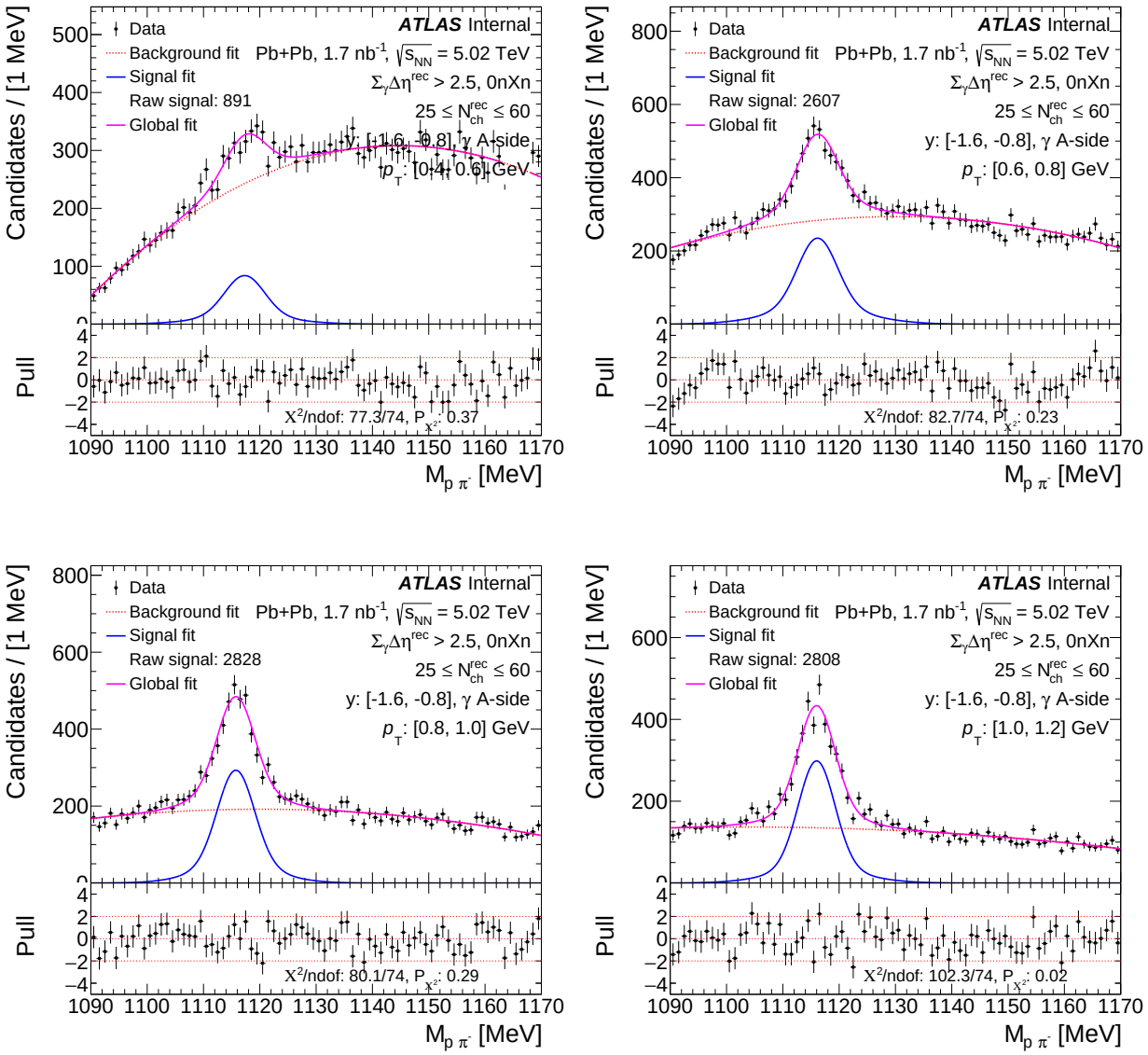

Figure B.2: The invariant mass distributions of Λ shown for a specific p_T-y bin in Pb+Pb UPC, represented in black markers in the top panel. The global fit to the data is represented by a magenta solid line, utilizing a double Gaussian fit for signal (shown as a blue solid line), and a second-order polynomial (shown as a red dotted line). In the bottom panel, the pull distribution shows the difference between the data and fit value normalized to the data uncertainty.